

Mission Design and Technology for a Titan Aerobot Balloon System (TABS)

Mission Design und Technologie für ein Titan Aerobot Ballon-System (TABS)

A thesis accepted by the Faculty of Aerospace Engineering and Geodesy of the
Universität Stuttgart in partial fulfillment of the requirements for the degree of
Doctor of Engineering Sciences (Dr.-Ing.)

By

Jaime Esper

Born in Colombia

Main referee: Prof. Dr. rer. nat. Hans-Peter Röser
Co-referees: Prof. Michael W. Plesniak, Ph.D.
Prof. Dr. -Ing. Stefanos Fasoulas

Date of Defense: 28 March 2012

Institute of Space Systems
University of Stuttgart
2012

Dedication

In living memory of my father Dr. Alfredo Esper, who instilled in me a deep sense of awe and admiration for nature, and a curiosity to always reach for the stars. To my family, whose love gives warmth and meaning to my journey.

Table of Contents

Dedication	ii
List of Figures	v
List of Tables	vi
Acronyms	vi
Abstract / Kurzfassung	vii
1.0 Introduction and Background	1
1.1 Research Plan	1
1.2 Technology Functional Areas	1
1.3 Dissertation Methodology/Outline	6
2.0 Scientific Objectives and Science Instruments	7
3.0 Mission Design	7
3.1 Design Approach	7
3.2 Trajectory Design	7
3.3 Trajectory Computation	9
3.4 Trajectory Correction Maneuvers	18
3.5 Entry Flight Path Angle	18
4.0 Communications	19
4.1 Link Analysis and TABS Antenna Sizing	19
4.2 Onboard Storage, Downlink Duty Cycle, and Total Data	22
4.3 Carrier Spacecraft Flyby and Relay Communications	24
4.4 Communications Summary	25
5.0 TABS Buoyant Gas System	26
5.1 Hydrogen Balloon (baseline)	26
5.2 Montgolfier Balloon	28
5.3 Comparison of Different Balloon Types	29
5.3.1 Super Pressure Hydrogen versus Montgolfier Balloons	29
5.3.2 Super Pressure Hydrogen versus Helium Balloons	31
5.4 TABS H ₂ Tank Sizing	33
5.4.1 Primary Spherical Tank Sizing	33
5.4.2 Primary Toroidal Tank Sizing	35
5.4.3 Auxiliary Toroidal Tank Sizing	36
5.5 Tank Gas Flow Rate and Balloon Inflation Time	37
6.0 Entry Probe	40
6.1 Instrument Platform Size	40
6.2 High Gain Antenna	40
6.3 Aeroshell Geometry and Size	41
6.4 Payload Thermal Control	42
6.5 Aft Component Accommodation	42
6.6 Probe Layout and Overall Dimension	43
6.7 Vehicle Aerodynamic Stability Considerations	43
6.8 Deployment Scheme and Operational Configuration	45
6.9 Entry Probe Equipment List	48
7.0 Aerothermodynamic Entry Analysis	51
7.1 Titan's Atmospheric Model	52
7.1.1 Atmospheric Scale Height	52
7.1.2 Exponential Atmospheric Model	53

7.1.3 Atmospheric Model Comparisons	55
7.1.4 Flow Regime Estimation	56
7.2 Aerodynamics	57
7.2.1 Aerodynamic Loading and Velocity Evolution	57
7.2.2 Dynamic Pressure	58
7.2.3 Entry Flight Time	59
7.3 Aerothermodynamics	60
7.3.1 Total Convective Heat Load and Body Average Heating Rate	61
7.3.2 Stagnation Point Heating – Convective	62
7.3.3 Stagnation Point Heating – Radiative	64
7.3.4 Total Heat Input at the Stagnation Point	67
7.3.5 Thermal Protection System (TPS) Requirements	68
7.4 Aerothermodynamic Model Validation Based on Huygens Results	72
7.4.1 Entry Aerodynamics	72
7.4.2 Entry Aerothermodynamics	75
7.4.3 Summary Results and Comparison	81
8.0 Decelerator System Sizing and Balloon Inflation	83
8.1 Drogue Decelerator Sizing	83
8.2 Main Parachute Sizing and Balloon Inflation	87
9.0 Carrier Spacecraft	93
9.1 Interface Structure and TABS Accommodation	93
9.2 Carrier Spacecraft (CS) Sizing	93
9.3 Chemical Propulsion System (CHEM)	98
9.4 Solar Electric Propulsion (SEP) Module	100
9.5 Solar Array	105
10.0 Integrated Space System and Launch Vehicle Selection	108
11.0 Conclusion and Future Prospect	112
12.0 References	114
Appendix A (separate volume): TABS Thermal Protection System Material Selection, Manufacturing, and Test	
A.1 Boundary Conditions: the Flight Environment	A3
A.2 Aeroshell Characteristics and Heat Shield Structure	A5
A.3 Raw Material Selection	A5
A.3.1 Shield Structure Honeycomb Core Selection	
A.3.2 Composite Facesheet Selection	
A.3.3 Adhesive Selection	
A.3.4 TPS Carbon Fiber Selection	
A.3.5 TPS Resin Selection: Phenol Formaldehyde	
A.4 Carbon/Phenolic Composite Manufacturing	A10
A.4.1 Vacuum Assisted Process (VAP)	
A.4.2 Curing Process	
A.4.3 Manufacturing Results	
A.5 Plasma Wind Tunnel Tests	A23
A.5.1 Sample Preparation	
A.5.2 Test Set-up	
A.5.3 PWK1 Boundary Conditions	
A.5.4 Test Results	
A.5.5 Comparative Assessment of RICA TPS Samples	
A.6 Appendix References	A44

List of Figures

1-1	Performance of past, present, and future radioisotope power systems	2
1-2	Deployment and inflation of Goddard/Wallops prototype Mars pumpkin balloon	3
1-3	Titan's atmospheric structure and TABS balloon operating conditions	4
1-4	Dissertation structure and areas of emphasis	6
3-1	TABS SEEGA trajectory to Titan	9
3-2	Titan inertial entry velocities at 1000 km as a function of flight time	17
3-3	Flight path angle assessment for 1000 km entry interface	18
4-1	Carrier Spacecraft relay geometry	24
5-1	Comparison of TABS balloon design baseline and Montgolfier	30
5-2	Comparison of time required to inflate balloon	30
5-3	SP H ₂ mass efficiency	31
5-4	Comparison of payload carrying capacity versus balloon envelope for H ₂ and He balloons	32
5-5	SP H ₂ mass efficiency over He proves enabling for TABS	32
5-6	Mass flow rate decreases asymptotically as differential pressure approaches zero	39
6-1	TSSM and TABS instrument area and volume allocations	40
6-2	1-meter parabolic dish in stowed and deployed configurations	41
6-3	TABS and Galileo Aeroshell cross-sections	41
6-4	The ASRG provides enough heat to safely operate components	42
6-5	Aft Component Identification and Accommodation	43
6-6	TABS entry probe, Aeroshell, and Gondola	44
6-7	TABS aerodynamic stability consideration	44
6-8	TABS entry and deployment sequence	46
6-9	TABS configuration changes during descent	47
6-10	Load path lanyard for balloon deployment ensures fabric will not be unduly stressed	48
7-1	Estimation of atmospheric temperature for ballistic corridor	52
7-2	Titan exponential atmospheric model for high altitudes (>~40 km)	53
7-3	Titan exponential atmospheric model for low altitudes (<~120 km)	54
7-4	Titan exponential pressure-altitude model for low altitudes (<~120 km)	55
7-5	Comparison of different exponential atmospheric models	56
7-6	Velocity evolution over the ballistic trajectory with the critical locus of maximum deceleration	58
7-7	Dynamic pressure and speed versus altitude	59
7-8	Time evolution of the entry trajectory	60
7-9	Convective stagnation point heat flux versus altitude	63
7-10	Radiative stagnation point heat flux versus altitude	65
7-11	Developing a correlation between convective and radiative heating rate at the stagnation point	66
7-12	Stagnation point heating rate versus altitude derived from power curve correlation	67
7-13	Ablative TPS material density requirement based on pressure and peak heat flux environment	69
7-14	Front Shield maximum surface temperature assuming radiation cooling alone	70
7-15	Huygens Probe Aeroshell geometry and dimensions	72
7-16	Predicted Huygens stagnation point (convective) heating rate	77
7-17	Radiative stagnation point heat flux versus altitude	78
7-18	Convective heating rate and range of radiative heating rates for Huygens	79
8-1	Drogue gore layout and approximate dimensions	85
8-2	Correlation of parachute system mass with nominal diameter	86
8-3	Main parachute descent rate versus altitude	89
8-4	Main parachute approximate size next to Drogue	91
9-1	TABS interface and carrier spacecraft structures	93
9-2	Geometry used in thermal energy balance estimation	95
9-3	Spacecraft equilibrium temperature at different distances in its trajectory to Saturn	97
9-4	CHEM propulsion system payload, with TABS probe and CS	97
9-5	Finding the optimum specific impulse	101
9-6	SEP Propulsion module (solar arrays not shown)	105
9-7	IPS "on" time required to provide 2.3 km/s, and maximum array operating distance	105
9-8	SEP Module	107
10-1	NASA ELV and Falcon 9 launch energy performance curves	109
10-2	Complete Space System perspective views	110
10-3	Deployed and launch vehicle configurations and dimensions	110
10-4	The TABS Space System fits well within the volume allocations of Falcon 9	111

11-1	Layout and aeroshell configurations leading to the baseline	112
11-2	Size and mass comparisons for Titan entry systems	113

List of Tables

2-1	TABS science objectives define instruments and mission requirements	8
3-1	Cassini's TCM flight data	18
4-1	Mission Communications Characteristics	25
5-1	Axial height comparison for spherical versus toroidal tanks	35
6-1	Mass distribution used in CG estimation	45
6-2	TABS Floating System Mass and Power Budgets	49
6-3	Entry System Mass Budget Estimation	50
7-1	Summary of Aerothermodynamic entry calculations and comparison with Huygens values	82
9-1	Mass allocations for TABS interface and carrier spacecraft structures	93
9-2	Mass and power allocations for CS sizing	94
9-3	SEP System structure mass allocations	100
10-1	Space system mass and power summary	108

Acronyms

TABS	Titan Aerobot Balloon System
TPS	Thermal Protection System
CS	Carrier Spacecraft
CHEM	Chemical Propulsion System
SEP	Solar Electric Propulsion
IRS	Institut für Raumfahrtssysteme
OPAG	Outer Planets Assessment Group
RPS	Radioactive Power System
ASRG	Advanced Stirling Radioisotope Generator
MMRTG	Multi-Mission Radioisotope Thermoelectric Generator
TSSM	Titan Saturn System Mission
SEEGA	Solar Electric Earth Gravity Assist
EP	Electric Propulsion
EGA	Earth Gravity Assist
DTE	Direct to Earth (communications)
RF	Radio Frequency
SNR	Signal-to-noise ratio
VHC	Volumetric Heat Capacity
SP	Super Pressure (balloon)
COPV	Composite Overwrapped Pressure Vessel
HM	High Modulus (material)
UD	Unidirectional (fiber)
MEOP	Maximum Expected Operating Pressure
STA	Station (reference location on vehicle)
CBE	Current Best Estimate
HASI	Huygens Atmospheric Structure Instrument
DISR	Descent Imager / Spectral Radiometer
GRAM	Global Reference Atmospheric Model
EM	Jaime Esper (Titan atmospheric) Model
FWHM	Full Width at Half Maximum
CAD	Computer Aided Design
RICA	Resin Impregnated Carbon Ablator

Abstract

An alternative implementation to a Titan aerobot mission is presented that uses tried (by similarity) and relatively low-risk methods for designing and deploying a Hydrogen-filled balloon in Titan's atmosphere. This is a departure from the current consensus approach of using a Montgolfier (hot air) balloon for in-situ exploration. It was demonstrated that this mission implementation is not only feasible, but also presents a risk advantage in the deployment (the most critical part of operations) of this system, without the need for a complicated scheme of lines and ties that can snatch or rupture the material. With on-board Hydrogen, and an auxiliary tank for replenishment during a six-month mission, the Titan Aerobot Balloon System (TABS) is capable of gathering up to 892 Mbits of data per day, that includes optical, spectroscopy, and atmospheric remote and in-situ sensing. This data is transmitted directly to Earth with a steerable 1-meter parabolic dish antenna. During the course of formulating mission enablers, a new Thermal Protection System (TPS) material was also designed, manufactured, and tested at the Institut für Raumfahrtssysteme of the Universität Stuttgart. This new carbon/Phenolic ablator was successfully demonstrated at the IRS' Plasma Wind tunnel. Two out of three sample types proved to be viable ablators, with no sign of delamination, and with thermal properties that enable high-speed entry not only in Titan's atmosphere, but also for Earth re-entry and planetary sample return missions. TABS entry vehicle is 628 kg with a total floating mass including gondola and buoyant system of 242 kg (both numbers include a 30% contingency). TABS can be launched in a Space X Falcon 9 rocket, with a 30% performance margin (on top of the 30% contingency). There is enough mass and volume reserve left in the launch vehicle for co-manifested spacecraft, so international cooperation is not only built-into TABS, the flight can also accommodate the addition of separate contributions with the potential for individual partner cost-sharing and savings.

Kurzfassung

Diese Arbeit präsentiert eine Variante einer robotischen Raumsonde zur Erkundung des Saturnmondes Titan unter Nutzung von Analogie- und Risikominderungsmethoden zum Entwurf eines wasserstoffgefüllten Ballons, der sich in Titans Atmosphäre entfaltet. Dies ist ein Umdenken, weg vom gegenwärtig akzeptierten Vorgehen, wo ein Heißluftballon (Montgolfiere) zur In-Situ-Erforschung verwendet wird. Es hat sich gezeigt, dass die Umsetzung einer solchen Mission nicht nur durchführbar ist, sondern auch Vorteile durch Risikoverringerung während der Entfaltungsphase bietet – dem kritischsten Teil des Ablaufes. Das System kommt dabei ohne ein kompliziertes Geflecht aus Leinen und Verbindungen aus, die reißen und andere Komponenten oder Materialien beschädigen können. Mit an Bord gelagertem Wasserstoff sowie einem Hilfstank zum Nachfüllen während einer sechsmonatigen Mission ist TABS (Titan Aerobot Balloon System) in der Lage bis zu 892 Mbits an Daten pro Tag zu sammeln (aus optischer, spektroskopischer und atmosphärischer Fernerkundung sowie aus In-Situ-Messungen). Diese Daten werden mittels einer steuerbaren 1 m Parabolantenne direkt zur Erde gesendet. Im Verlauf der Arbeit wurde ein neues Karbon-Phenol-Hitzeschildmaterial am Institut für Raumfahrtssysteme (IRS) der Universität Stuttgart entwickelt, gefertigt und getestet und daraufhin erfolgreich im IRS-Plasmawindkanal validiert. Zwei der drei untersuchten Konzepte erwiesen sich als realisierbar – ohne Anzeichen von Ablösung und mit Thermaleigenschaften, die nicht nur einen atmosphärischen Hochgeschwindigkeitseintritt am Titan ermöglichen sondern auch einen Wiedereintritt an der Erde sowie zukünftige planetare Probenrückführungsmissionen. Das TABS-Eintrittsfahrzeug hat eine Masse von 628 kg mit einer Masse des Ballonfahrzeuges von 242 kg inklusive Gondel und Auftriebskörper (jeweils einschließlich 30% Sicherheitsreserve). Ein Start von TABS an der Spitze der SpaceX Falcon 9 Rakete bietet einen Leistungsspielraum von 30% zusätzlich zur bereits vorhandenen 30% Sicherheitsreserve. Die verfügbare Masse- und Volumenreserve eröffnet daher die Möglichkeit eines kombinierten Starts mit weiteren Raumsonden/Satelliten. Internationale Zusammenarbeit ist also nicht nur innerhalb des TABS-Projektes durchführbar, sondern auch im Rahmen der Kostenteilung eines gemeinsamen Starts.

1.0 Introduction and Background

During the week of February 9th 2009, NASA and ESA officials decided to “...plan for another potential mission to visit Saturn's largest moon Titan and Enceladus”. On the heels of a joint report, the “Titan Saturn System Mission (TSSM)”¹, NASA and ESA decided to undertake several more steps and detailed studies before officially moving forward. It was considered that such complex mission faced several technical challenges and required significant study and technology development. This dissertation takes a new look at the challenges facing such a mission, and provides an alternative implementation that goes somewhat contrary to the consensus approach of using a Montgolfier balloon as the choice technology for a long duration buoyant flight in Titan's atmosphere. During the course of this research however, and from a pragmatic perspective, emphasis is centered not on balloon technology development or test (enough resources are being spent in this area by CNES and JPL), but rather on a capability that is well suited to the Institute of Space Systems (Institut für Raumfahrtssysteme or IRS), with its world-class plasma wind tunnel facilities. Considering that IRS' facilities have been used in the past for (among other important projects) the qualification of the Thermal Protection System (TPS) material used in the Cassini-Huygens Titan's entry probe heat shield, the experimental leg of this research was then focused on the development and test of a new hyperbolic entry speed, TPS ablative material. Nonetheless, this development is put in the context of an overall mission design, which forms the basis of the Titan Aerobot Balloon System (TABS) reference mission approach, the thread that ties all the different sections of this dissertation.

1.1 Research Plan

The sheer number of areas that require research and development to enable a Titan balloon mission necessitated the choice of a few elements that could be effectively tackled through this work. The discourse of an end-to-end mission in turn allows these key elements to be placed within a contextual background. In particular, the objectives of this dissertation are:

1. Develop an end-to-end mission concept that includes a direct entry trajectory at Titan. This preserves options for coordinated / international mission execution with an orbiter and Lander, but maintains required independence for budgetary constraints. The operational life of the buoyant system is set to 6 months, to allow for proper coverage through seasonal changes.
2. Focus on systems and technologies that both **enable** and **enhance** a successful Titan Balloon Aerobot.
 - a. Develop a mission implementation that uses a lighter-than-air buoyant gas, as an alternative approach to the common consensus using a Montgolfier (hot air balloon).
 - b. Carry out experimental research in short term to assess system feasibility of certain key technology. In particular, the development of a TPS ablative material using current commercial and available materials.

1.2 Technology Functional Areas

This dissertation uses previous studies, reports, and assessments as starting point for key mission areas. In the technology area, this research follows the Outer Planets Assessment Group (OPAG) recommendations for technology development². This report recommends the following emphasis for a Titan in-situ sampler (E=enabling; e=enhancing):

- Electric Propulsion (e)
- Radioactive Power System – RPS (E)
- Expanded Ka capability (OPAG = e) – for our purposes, and given a stand-alone mission, this is an *enabling* capability (E)
- Planetary mobility (E)
- Autonomy (OPAG = e) – without autonomy, TABS could not be flown given the great distances involved. Hence it is considered an *enabling capability* (E)
- Extreme environments (OPAG = e) – for a balloon mission this technology capability remains a mission *enabling capability* (E)
- Entry systems (includes TPS) (OPAG = e) – for certain application/system combinations (such as TABS TPS material), entry systems may also represent an *enabling capability* (E)
- In situ sensing of surface and atmospheres (E)
- Components and miniaturization (E)
- Remote sensing (e)

1.2.1 Electric Propulsion – mission enhancing technology

Maximizes payload and reduces flight times. From a Neptune/Triton mission study³, the most effective approach to reaching an outer planet is to design a two-stage system, with SEP in the inner solar system, and chemical propulsion beyond the orbit of Mars. This payload optimization will be demonstrated for TABS in subsequent sections.

1.2.2 Radioactive Power System (RPS) – mission enabling technology

TABS would leverage current US Department of Energy (DOE) and NASA work in this enabling technology. Figure 1-1 shows the performance of past, present, and future radioisotope power systems ⁴. In particular, an Advanced Stirling Radioisotope Generator (ASRG) will be used as the primary power source in TABS.

	 GPHS-RTG Past	 MMRTG Present	 ASRG In Development	 ARTG Future	 TPV Future
Electric Output, BOM, W _e	285	125	~140-150	~280 to 420	~38-50
Heat Input, BOM, W _e	4500	2000	500	3000	250
RPS System Efficiency, BOM, %	6.3	6.3	~28-30	~9-14	~15-20
Total System Weight, kg	56	44.2	~19-21	~40	~7
Specific Power, W _e /kg	5.1	2.8	~7-8	~7-10	~6-7
Number of GPHS Modules	18	8	2	12	1
GPHS Module Weight, kg	25.7	12.9	3.2	19.3	1.6
²³⁸ Pu Weight, kg	7.6	3.5	0.88	5.3	0.44

Figure 1-1: Performance of past, present, and future radioisotope power systems. Acronym Key: ARTG, Advanced Radioisotope Thermal Generator; ASRG, Advanced Stirling Radioisotope Generator; BOM, Beginning of Mission; GPHS, General Purpose Heat Source; MMRTG, Multi-Mission Radioisotope Thermoelectric Generator; RTG, Radioisotope Thermal Generator; TPV, Thermophotovoltaic.

1.2.3 Expanded Ka Capability – mission enabling technology

Direct-to-Earth link requires the use of Ka-band and higher frequencies in order to effectively transfer relatively large amounts of information over vast distances typical of to the outer planets. Inflatable / small package antenna technology is one consideration, but was not required in this research based on the link analysis for a one-meter aperture parabolic antenna. Relevant selections from OPAG are included here as they were used in the mission implementation approach:

- Mature and advance *higher-power transmitters*
- Invest in maturing the next generation transponder supporting: 10 Mbps uplink; 100 Mbps downlink; integrated proximity and direct-to-Earth communications (currently requires two devices); integrated radio science for atmospheric and gravity experiments with few micron/sec two-way Doppler capabilities.
- Implement advances in data compression to more efficiently transmit science data to Earth.

1.2.4 Planetary Mobility – mission enabling technology

A hot air balloon was identified by a joint NASA/ESA study group as a key element in a comprehensive Titan exploration plan. However, a balloon has not been flown in conditions present at Titan and thus requires a focus effort of risk reduction. CNES is currently spending resources to develop a Montgolfier concept for Titan, based on the work reported in the joint NASA/ESA TSSM study report. Main argument put forth in favor of a Montgolfier concept as opposed to others (e.g., Helium/Hydrogen filled balloon) is summarized in the TSSM in Situ Elements ESA contribution ⁵: “Considering the deployment, reliability and most importantly the longer operational lifetime (6 months) in the cold environment.” An MMRTG would be used to heat the air inside the balloon, and it would be “hanging from cables which are attached to the skin of the balloon”.

Although a Montgolfier-based architecture represents a good implementation approach, the deployment and arrangement of the MMRTG inside the balloon represents an operational complication difficult to ignore. Deployment of the balloon material around the MMRTG and dynamic loads due to winds, among other factors, exacerbate the potential for material rupture or entanglement on deployment. The research at hand will explore a Helium/Hydrogen-filled balloon alternative that can leverage extensive experience and simplifies the balloon system. A choice of gas will be made based on a trade analysis. The He/H₂ tanks mass and their accommodation are problems that require careful planning. Areas of balloon research include:

- Material choice and properties
- Rigidity
- Packaging and long-term storage
- Helium/Hydrogen leakage and seals
- Structural mock-up of aeroshell, balloon, and gondola
- Deployment under simulated wind and cold conditions (not cryogenic temperatures)
- Deployment in cryogenic environment with simulated aerodynamic forces
- Drop test

Only theoretical considerations will be included in this dissertation, as experimental proof-of-concept activities were beyond the scope and material resources herein.

Nonetheless, in-air balloon deployment data is available under low-density conditions. Figure 1-2 shows photographs of the deployment and inflation sequence of a stratospheric balloon (31 km altitude, ~ Mars condition) of a Goddard/Wallops prototype Mars pumpkin balloon in 2006.

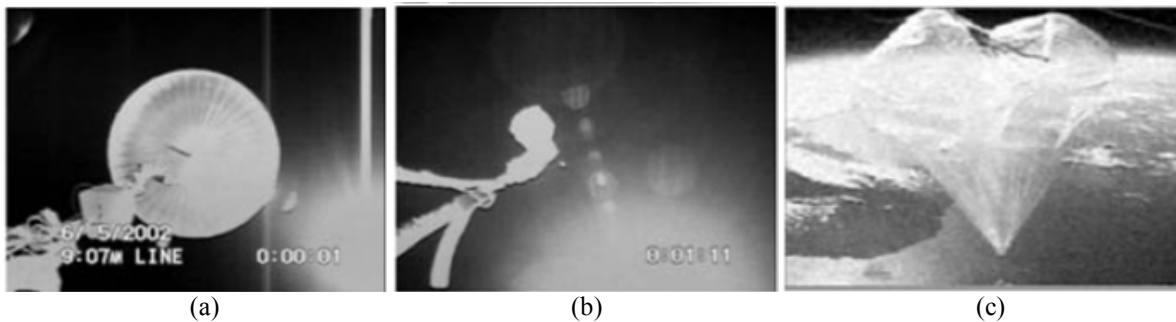


Figure 1-2: Deployment and inflation of Goddard/Wallops prototype Mars pumpkin balloon: (a) upward view of carrier balloon just prior to deployment; (b) upward view of prototype balloon just after deployment; (c) side view of Mars prototype during descent

A spherical balloon was also tested that same year. Previously, a Tropospheric deployment and inflation test of a 3-meter Mylar balloon was executed in 1998 (NASA/JPL). The test validated the technology involved in deployment and inflation of a thin film balloon in “dense” atmospheres (~ Venus, Titan, and Jupiter). Additional tests have also been carried out jointly by GSFC and JPL.

Of interest, especially insofar as deployment of balloons in rarified atmospheres, coupled to atmospheric entry at relatively high speeds, is the German Mars Society “Archimedes” (Aerial robot carrying high resolution imaging magnetometer experiment and direct environmental sensors) experiment. Archimedes is a balloon vehicle planned to be used for in-situ Mars atmospheric observation, and constitutes a private effort of a number of organizations agglutinated through the German Mars Society. This experimental vehicle has had two suborbital flight tests where the balloon is intended for deployment off a sounding rocket (REGINA and MIRIAM), both with mixed results. REGINA successfully deployed the balloon, but it did not fully inflate. MIRIAM suffered a launch vehicle separation system failure (delayed deployment) that also prevented its full inflation. A third test is planned for 2013 ⁶.

1.2.5 *Autonomy – mission enabling technology*

This is required given the large distances, communication blackouts due to Titan rotation and orbit, lack of terrain data, and non-deterministic balloon flight path that precludes precise a priori planning of science data measurements. Operational altitudes for autonomous operation would follow recommendations from the joint TSSM study report:

- For altitudes <6 km there is increased risk of precipitation, potentially causing changes in balloon mass, and adding complexity due to contamination and draining. Also, winds are close to zero for altitudes below ~5 km, which would limit balloon motion to survey varying surface features.
- The atmospheric density is smaller for high altitudes, which would require a larger balloon envelope to support a given payload mass.
- A nominal altitude of 10 km was assumed, with a possible range from 6 – 12 km.

1.2.6 Extreme Environments – mission enabling technology

Titan is shrouded by a dense, cold atmosphere, comprised primarily of nitrogen (98.4%) and methane (1.6%) with traces of argon and hydrocarbons. The organic (carbon-based) compounds are formed as the methane is destroyed by sunlight. At a nominal altitude of 10 km, the balloon operating conditions include temperatures down to -189°C (84K), pressure of 884 mbar, and wind speed of 4 km/hr (from Descent Imager / Spectral Radiometer, DISR movie data on Huygens ⁷). In particular, low temperatures impact chemical, electronic, and mechanical components, sensors and actuators, and balloon materials. Although some components can be shielded from the extreme environment, some must be exposed due to operational and measurement needs (thermal, pressure and wind sensors, for instance). The ability to operate a balloon and its instruments in such environment require mission enabling technologies mature enough for operational flight. Figure 1-3 illustrates Titan’s atmospheric structure and major chemical components (figure adapted from several NASA sources).

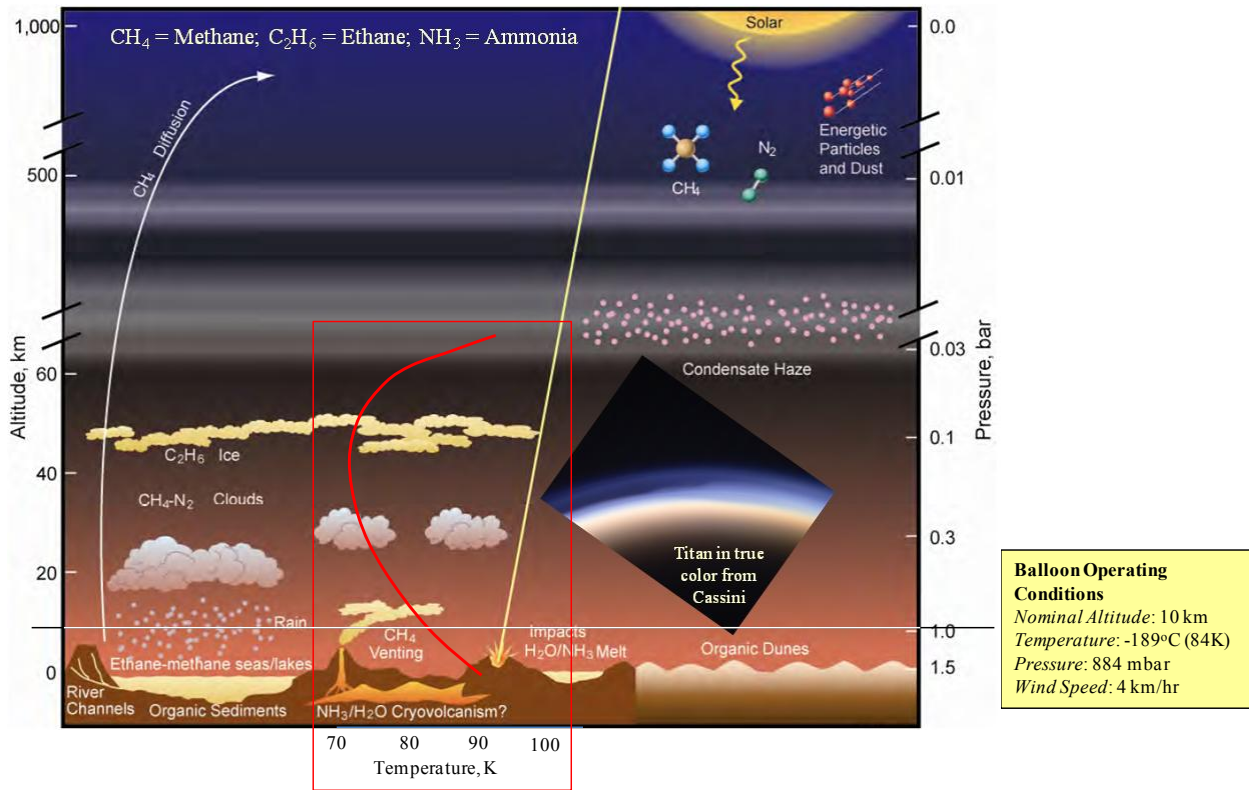


Figure 1-3: Titan’s atmospheric structure and TABS balloon operating conditions (NASA)

1.2.6 *Entry Systems – mission enhancing and enabling technology*

Insofar as materials already exist that can handle extreme environments, improvements can be certainly enhancing. There are certain materials however that either need additional qualification, or that currently do not exist in a manner that allows repeatable manufacturing. Such is the case for instance with high entry speeds thermal ablaters. Availability of these materials then become enabling for certain outer planetary (and Earth return) entry missions at hyperbolic speeds.

Entry systems for extreme environments include miniaturized and low power integrated sensors, transmitters, and avionics, thermal materials, power management systems, and on-board processing systems. Among key areas:

- Components and instrument systems that can withstand the high temperature/pressure environment during entry
- Strong, lightweight materials that can provide improved payload mass fraction.
- Thermal protection and control materials necessary to maintain probe interior at moderate temperatures for long-duration missions (Enabling for TABS)

Thermal Protection Systems (TPS) for high heat flux and pressures during direct atmospheric entry. Fast flight times can lead to relatively large entry velocities.

- A minimum energy direct transfer results in about 4 km/s entry speed, as a lower boundary. Huygens entered at about 6 km/sec.
- TABS trajectory estimates for a 4 to 5 year flight time results in ~10.4 km/s hyperbolic inertial entry speed.

1.2.7 *In situ sensing of surface and atmospheres / Components and miniaturization – mission enabling technologies*

In situ instruments that facilitate atmospheric and surface measurements will have to tolerate a low temperature extreme environment of about 84K (if they cannot be thermally isolated). Key technologies for such instrument systems include:

- Cryogenic sample acquisition from atmospheres and surfaces (if balloon “touches” surface)
- Sample distribution/interrogation front ends and sample transfer staging technologies
- Actuators
- Instrument electronic devices
- Battery technology (to supplement RPS or to take advantage of deployed systems, such as TABS tank platform)

Reducing the volume, mass and power requirements of instrument systems is essential to maximize the science return. Key geophysical instruments, e.g. magnetometers and analytic instruments systems, e.g. high resolution/sensitivity gas chromatography/mass spectrometers must be developed and used for TABS. In addition, a Titan mission would be strongly enhanced by development of miniature long-lived, low power cryogenic electronics.

1.2.8 *Remote Sensing – mission enhancing technology*

Here it suffices to quote a paragraph from the OPAG document: “Instruments have to be low in mass and require low power. For Titan, the instruments must have the capability to see through the atmosphere to the surface as well as analyze the atmosphere and measure its gravitational field. They also have to be capable of high spatial (and in the case of spectrometers, high spectral) resolution and high sensitivity to answer the scientific questions that have emerged from Cassini.”

1.3 Dissertation Methodology/Outline

This dissertation follows a traditional systems engineering approach. To that end, the science and measurement objectives are used to define instrument requirements, which within the frame of an operational context serve to define the mission. As this dissertation *concentrates on the entry probe itself*, there are a few *key elements* of the mission that constrain the entry system, *in particular as it concerns to volume and mass*. The volume requirements of the instruments input into the size of the gondola. However, instrument volume alone does not fully define the system size. The buoyant tanks and the communications system (antenna) are also major variables in determining the overall gondola and by extension aeroshell and entry probe size (and mass). From a technology perspective, the thermal protection system required to ensure survival of the vehicle during the intense entry heating is within the facility and expertise availability at the University of Stuttgart. Therefore research into development of a new carbon/Phenolic ablator is also included as an enabler to the mission. Obviously, all the subsystems of a space mission are necessary for its success. The on-board avionics for instance is equally essential. However, this subsystem can be implemented within the bounds of the overall preliminary size/mass constraints presented here, and was not described beyond allocating for its mass and power needs (i.e., it is not a major buoyant system constraining subsystem). The same applies for all other subsystems not specifically covered herein. Again, the scope of this research is to tackle major select components that directly enter into the *sizing* of the entry probe / buoyant system, and also to place this system into the *context* of an overall design. It is not the intent however, to provide a complete discourse in mission design. Figure 1-4 shows a graphic “map” of the dissertation structure and areas of emphasis. Figure 1-4 (a) shows the overall mission design flow, and Figure 1-4 (b) shows the parameters influencing the entry probe volume/mass constraints and the ensuing carrier/delivery system and choice of launch vehicle.

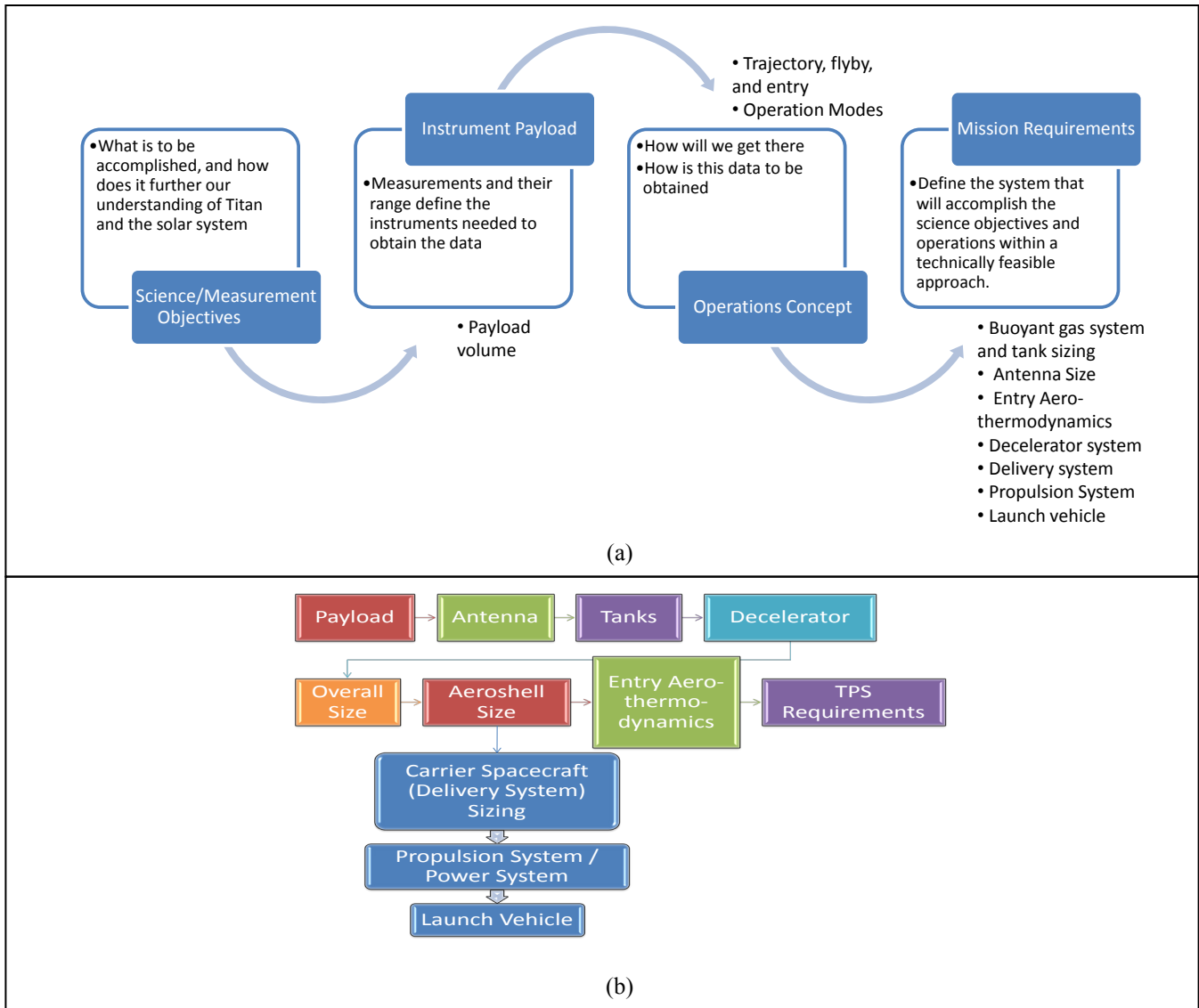


Figure 1-4: Dissertation structure and areas of emphasis; (a) overall mission design flow; (b) volume/mass constraints

2.0 Scientific Objectives and Science Instruments

The emphasis of this dissertation is not to develop a case for visiting Titan. That justification has been amply provided and exists in open literature. Rather, this dissertation concentrates on key engineering and technology areas that would provide alternatives to consensus designs and available (or unavailable) systems. Hence, TABS will follow the recommendation for a payload suite as defined in the TSSM Study Report for the balloon system component⁵. Definition of this payload only serves to constrain the engineering implementation, but there will be no attempt at developing this capability through work contained here. Furthermore, individual instrument sizes were only shown in allocation volumes. Hence, TABS allocated a space within its instrument deck that comprises the total volume shown in Reference 5. Additional requirements not provided in the reference document, such as data sampling rates and volumes were inferred from existing or planned instruments. Table 2-1 provides a summary of measurement requirements, and the instrument suite needed to satisfy them. It will also serve to size the communications system, and define the operational modes of the mission.

3.0 Mission Design

3.1 Design Approach

A direct trajectory and Titan entry approach was motivated by the need to constrain costs by concentrating on the in-situ element. Insofar as costs may be spread across multiple organizations, this design also lends itself to international collaboration, as certain elements may be added to enhance the science return. For instance, the carrier spacecraft may be converted into an orbiter for Titan and Enceladus exploration, or a Lander added to TABS deployed components, such as the tank carrier structure or even the heat shield, as proposed elsewhere. The final objective of course, is to achieve a design that can be flown sooner rather than later.

3.2 Trajectory Design

The TABS trajectory design follows a similar approach used in Reference 3. The trajectory design for a mission to Saturn and its moons is inexorably attached to the propulsion technology proposed. The great distance to Saturn dictates the use of either gravity assist maneuvers, advanced propulsion options such as Electric Propulsion (EP), chemical propulsion, or a combination of all of them. The current TABS baseline trajectory design uses all the options above, in what is known as a Solar Electric Earth Gravity Assist (SEEGA) trajectory. Here, Solar Electric Propulsion (SEP) is used until the Earth swing-by at which time the spacecraft accumulates enough energy to reach Saturn in a hyperbolic trajectory. Once the SEP module is jettisoned after EGA, minor trajectory adjustments en route are performed by the chemical propulsion system. It will be shown that the need for a SEP stage is only valid for a requirement to use the least expensive launch vehicle possible.

A rough idea for the magnitude of the problem may be obtained by looking at the classic minimum-energy, co-planar, direct-transfer trajectory (Hohman Transfer). Detailed calculations for the actual SEEGA trajectory will be shown later, but for the simple direct transfer case it suffices to say that it would take about 6.1 years, and require an energy C_3 equal to $106.1 \text{ km}^2/\text{s}^2$, assuming Earth departure from a 185 km circular orbit. In this case, TABS would enter Titan's atmosphere at an inertial speed of about 4 km/s. Although this represents a reasonable flight time and benign entry speed, the launch energy is excessive and unachievable by current launch vehicles. This issue is addressed by the SEEGA trajectory, which yields a fast transfer time, reduced launch energy, but at the price of increased entry speeds (about 10.4 km/s).

The advantage of a SEP system increases for small delivered mass, high transfer energies, and high arrival hyperbolic excess velocities. The baseline trajectory used here uses a SEP low-thrust trajectory in the inner solar system, and a chemical mission for the remainder of the voyage. The trajectory calls for using SEP within a distance of 1.8 AU from the Sun, combined with a two-year Earth gravity assist (SEEGA). After the Earth swing-by, the SEP propulsion stage is dropped together with the solar arrays, and the spacecraft then continues with the chemical (CHEM) system to Saturn using power from TABS own thermoelectric source. At Saturn, the carrier spacecraft maneuvers to drop TABS into an intersect trajectory with Titan, and continues to relay entry data back to Earth. Figure 3-1 illustrates the baseline trajectory and summarizes the major flight dynamics data from launch to Titan entry.

Table 2-1: TABS science objectives define instruments and mission requirements

<i>Measurement Objectives</i>	<i>Measurement Range</i>	<i>Science Instrument</i>	Mass CBE (kg)	Peak Power CBE (W)	Data Sample Rate (kbps)	Image/ Data Sample Size (kb)	On-Board Data Acquisition Time (s)	Reduced Image/ Data Sample Size (kb)	On-Board Reduced Data Sample Acquisition Time (s)	Carrier Spacecraft Downlink Data Sample Size (kb)	Notes
Stereo surface characterization and atmospheric phenomena.	0.4 μm to 0.7 μm.	Visible Imaging System Balloon. Three wide angle and one narrow angle cameras.	1.7	4.2	1638	4915	3	4915	3	1228.8	320x240 pixels/frame at 1 fps and 16bit/pixel (1/3 rate) - 4 det ranges. Carrier s/c only 1 det ranges (non-stereo)
Composition and temperature mapping of surface at regional and local scale. Composition and optical properties of haze and clouds.	1 μm to 5.6 μm, spectral sampling 10.5 nm.	Balloon Imaging Spectrometer. Imaging diffraction grating spectrometer.	2.5	8.3	11213	538214	48				320x240 pixels/frame at 1 fps and 16bit/pixel (1/48 rate) - 438 det ranges (to achieve spectral sampling)
Methane/ethane mole fraction, noble gas concentration at 10s of ppb. Characterises molecules in atmosphere above ppm levels. Chemical composition of aerosols.	Mass range 10 to 600 Da	Titan Montgolfière Chemical Analyser. Ion trap mass spectrometer.	5.0	6.7	2.4	1.2	0.5	1.2	0.5	1.2	Data based on 1000 amu scan, requiring 8000 points (8 points per amu x 1000 amu). 12 bits = 8192 points, co-add 100 times to reduce S/N (Ref: http://www.adronsystem.com/faqs.htm#rate)
Temperature profile, atmospheric density and pressure measurements during entry and throughout the whole mission.	± 50 Gs; 80 to 4000K; 0 to 1.6 bar	Atmospheric Structure Instrument / Meteorological Package. Accelerometers, temperature sensors, capacitive sensors	0.8	4.2	48	120	2.5	40	8.33E-01	40	Data based on SMART
Lightning detection	+ 20 KV/m	Titan Electric Environment Package Balloon	0.8	0.8	9.6	0.008	8.33E-04	0.008	8.33E-04	0.008	Data based on Boltek EFM-100 Electric Field Monitor
Magnetic field characterization	+ 2 Gauss, 67 uGaus Resol.	Magnetometer	0.4	1.3	1.2	0.048	0.04	0.048	0.04	0.048	Data based on Honeywell HMR2300r with 25 sps at 16 bits*3 per sample
Sound for ice underneath the crust	10 - 30 MHz	Titan Radar Sounder	6.7	12.5	176	0.012	6.82E-05	0.012	6.82E-05	0.012	Data based on SELENE Radar Sounder
Space plasma and radio physics		Montgolfière Radio Science Transmitter	0.0								Uses existing radio transmitter package
Totals			17.88	37.92		543250.87	54	4956.47	4	1270.07	No data compression included
Total Downlink Data Rate*											
<i>Full Data Set Rate (kbps)</i>	10052.6	Mode 1 downlink									
<i>Reduced Data Set Rate (kbps)</i>	1133.1	Mode 2 downlink									
<i>Carrier Spacecraft Data Store Time (s)</i>	60										
<i>Carrier Spacecraft Data Set Rate (kbps)**</i>	21.17	Mode 3 (entry and early ops) downlink									

* The downlink data rate is an "effective rate", and not the arithmetic sum of each instrument dissimilar sampling rates.

** Carrier spacecraft acts in a "store and forward" mode, downlinking a full set of entry mode data every 60 seconds.

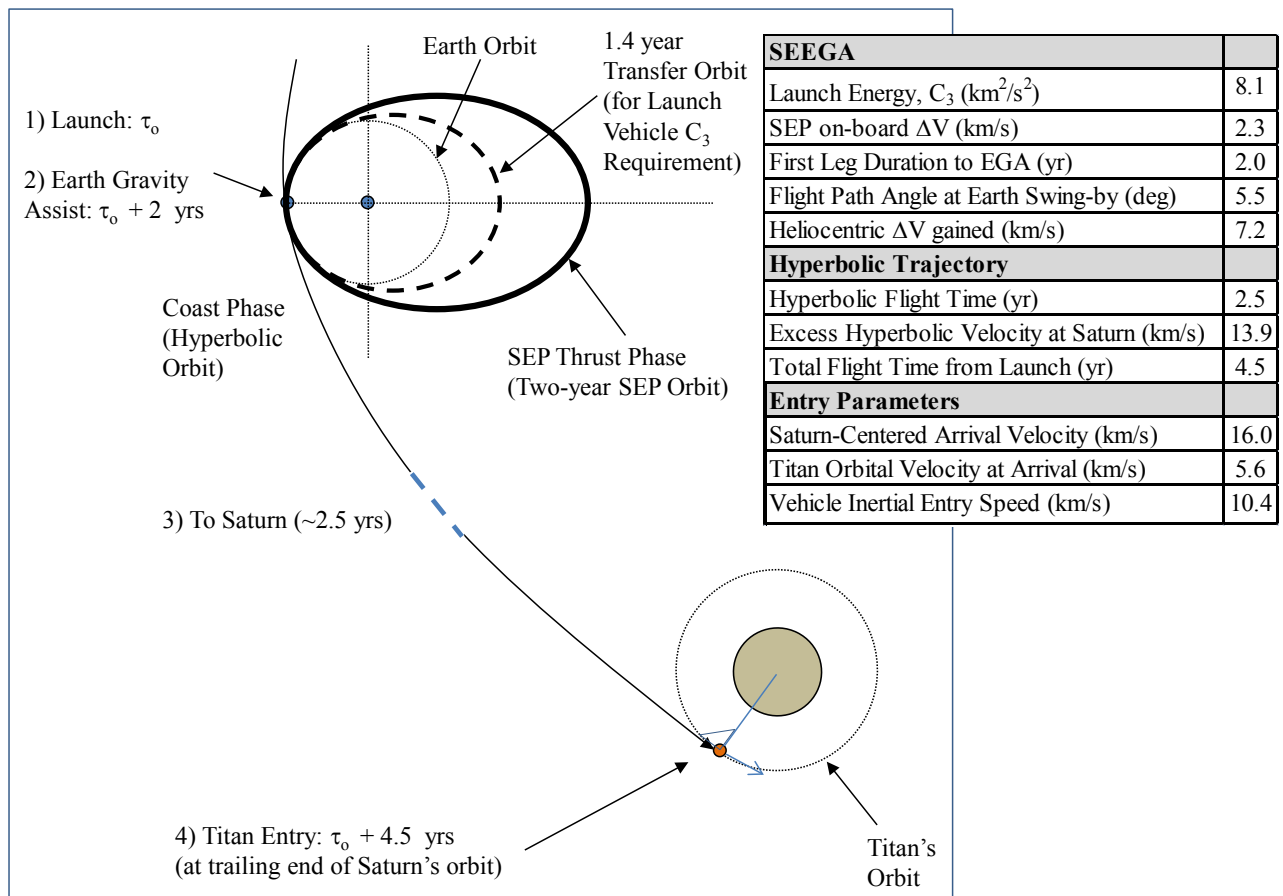


Figure 3-1: TABS SEE GA trajectory to Titan

3.3 Trajectory Computation

The complete trajectory was calculated using a unique analytical approximation method developed without the need to resource to numerical integration or calculus of variations³. Although this technique is only good for conceptual design, it is capable of highlighting the main mission design drivers and showing implementation feasibility. Following are the steps followed and the assumptions made.

- 1) The spacecraft is injected into a 1.4 year Hohman Transfer orbit by the launch vehicle.
- 2) The SEP system provides a spacecraft ΔV such that the energy at Earth swing-by is equivalent to that of a 2 year keplerian orbit. Note that the choice of orbits in steps 1 and 2 is given by the desired arrival speed at Titan, and the launch vehicle energy (not to be excessive).
- 3) The approach velocity (V_∞) is equivalent to that of a Hohman transfer for the two-year's trajectory.
- 4) The flight-path angle is adjusted to allow for energy gain after the Earth flyby.
- 5) The SEP module is ejected after the SEE GA is complete, after which the spacecraft is in a hyperbolic (coast) trajectory to Saturn.
- 6) A ballistic-entry analysis⁸ is performed at Titan, where the inertial entry speed is given by the difference of the spacecraft arrival velocity and Titan's orbital velocity. Titan's rotation is not included, as it only adds a relatively small contribution at this level of analysis.
- 7) The entry flight path angle is adjusted to find a balance of G-loading, and heat loading. Also, to ensure TABS does neither "skip", nor crashes into the surface.
- 8) Aero-thermodynamic loads are computed, and the heat shield thickness chosen based on material properties for TABS heat shield.

Detailed computations for steps 1 through 5 are shown next. Steps 6 to 8 will be shown once the probe system is defined, since vehicle mass and aeroshell configuration are needed in entry computations. However, it is noted that this was an iterative process, where the entry probe mass and Aeroshell geometry were initially estimated and refined as unique TPS material properties were developed experimentally, and the probe subsystems better understood.

Step 1: The spacecraft is injected into a ~1.4 year Hohman Transfer orbit by the launch vehicle (*the smaller size orbit*). The C_3 for this orbit will define the Earth *departure* energy (ELV) requirements.

Variable Definition	Earth	Saturn	Sun
Mean Distance From the Sun	$r_e := 149500000\text{km}$	$r_n := 1433264000\text{km}$	
Equatorial Radius	$R_e := 6378.14\text{km}$	$R_n := 60268\text{km}$	
Reduced Mass	$\mu_e := 398600.4 \frac{\text{km}^3}{\text{s}^2}$	$\mu_n := 37939519.7 \frac{\text{km}^3}{\text{s}^2}$	$\mu_s := 1.327 \cdot 10^{11} \frac{\text{km}^3}{\text{s}^2}$
Hohman Target Position	$r_{t1} := 1.5 \cdot r_e$	target position for a 1.4-year Hohman transfer orbit	
Heliocentric Orbital Speeds	$V_{eh} := \sqrt{\frac{\mu_s}{r_e}} = 29.793 \cdot \frac{\text{km}}{\text{s}}$		at periapsis
	$V_{nh} := \sqrt{\frac{\mu_s}{r_n}} = 9.622 \cdot \frac{\text{km}}{\text{s}}$		at apoapsis

Launch Vehicle departure orbit (choose a circular orbit in this case)

Altitude at Periapsis of Departure Orbit from Earth $h_{dp} := 185\text{km}$ (input)

Apoapsis Altitude of Departure Orbit $h_{da} := 185\text{km}$ (input)

Semimajor Axis of Departure Orbit

$$a_d := \frac{(h_{dp} + h_{da} + 2 \cdot R_e)}{2} = 6.563 \times 10^3 \cdot \text{km}$$

Heliocentric Segment (Transfer Orbit, TO)

Outer Target Transfer

Semi-Major Axis

$$a_{to1} := \frac{(r_e + r_{t1})}{2} = 1.869 \times 10^8 \cdot \text{km}$$

Transfer Orbit Period

$$P_{to1} := 2 \cdot \pi \cdot \sqrt{\frac{a_{to1}^3}{\mu_s}} = 1.396 \cdot \text{yr} \quad \text{which is the desired orbital period}$$

Earth Departure

Velocity at Periapsis of TO

$$V_{pto1} := \sqrt{\mu_s \cdot \left(\frac{2}{r_e} - \frac{1}{a_{to1}} \right)} = 32.637 \cdot \frac{\text{km}}{\text{s}}$$

Excess Hyperbolic Velocity (V_∞)

$$V_{\infty 1} := V_{pto1} - V_{eh} = 2.844 \cdot \frac{\text{km}}{\text{s}}$$

C_3 - This is the launch vehicle energy required for the mission, and hence the choice for the size of this orbit.

$$C_{3a} := V_{\infty 1}^2 = 8.086 \cdot \frac{\text{km}^2}{\text{s}^2}$$

Geocentric Departure Hyperbola

Earth departure radius (parking orbit periapsis radius)

$$r_{spe} := R_e + h_{dp} = 6.563 \times 10^3 \cdot \text{km}$$

Orbital velocity at departure (assume departure at periapsis of elliptical "transfer" orbit)

$$V_{spe} := \sqrt{\mu_e \cdot \left(\frac{2}{r_{spe}} - \frac{1}{a_d} \right)} = 7.793 \cdot \frac{\text{km}}{\text{s}}$$

Spacecraft velocity at parking orbit (needed to reach V_∞ departure, or geocentric escape velocity)

$$V_{sd} := \sqrt{V_{\infty 1}^2 + 2 \cdot \frac{\mu_e}{r_{spe}}} = 11.382 \cdot \frac{\text{km}}{\text{s}}$$

Departure ΔV (*this is the launch vehicle upper stage requirement*)

$$\Delta V_D := V_{sd} - V_{spe} = 3.589 \cdot \frac{\text{km}}{\text{s}}$$

Step 2: ΔV Computations for a Saturn SEP Trajectory using an Earth Gravity Assist. Assume a ~ 2 year Hohman Transfer Orbit (*the larger-size orbit*). This will define the Earth flyby heliocentric parameters, and the subsequent hyperbolic direct trajectory to Saturn/Titan. The target position for this larger size orbit must result in a period that is a multiple of an Earth's year (or very close to), in order to facilitate Earth re-encounter and gravity assist. This is also the period of time available to the SEP system to bring the spacecraft back to Earth.

Hohman target position $r_t := 2.2109r_e$ (Input such as period is $\sim 2\text{yr}$)

Heliocentric Segment (Transfer Orbit, TO)

Semi-Major Axis

$$a_{to2} := \frac{(r_e + r_t)}{2} = 2.4 \times 10^8 \cdot \text{km}$$

Transfer Orbit Period

$$P_{to2} := 2 \cdot \pi \cdot \sqrt{\frac{a_{to2}^3}{\mu_s}} = 2.032 \cdot \text{yr}$$

Transfer orbit Eccentricity

$$e_{to2} := \frac{(r_t - r_e)}{(r_t + r_e)} = 0.377$$

Earth Departure

Velocity at Periapsis of transfer orbit

$$V_{pto2} := \sqrt{\mu_s \cdot \left(\frac{2}{r_e} - \frac{1}{a_{to2}} \right)} = 34.962 \cdot \frac{\text{km}}{\text{s}}$$

Excess Hyperbolic Velocity

$$V_{\infty 2} := V_{pto2} - V_{eh} = 5.169 \cdot \frac{\text{km}}{\text{s}}$$

Launch energy

$$C_{3b} := V_{\infty 2}^2 = 26.722 \cdot \frac{\text{km}^2}{\text{s}^2}$$

This is the *effective "launch" energy* required should it not be for the SEP system (that makes-up the additional energy from the 1.4-year to the 2-year Hohman transfer). The **Spacecraft Heliocentric ΔV** is the difference between the V_{∞} at Earth Departure (smaller-size orbit Hohman Transfer) and V_{∞} at Earth arrival (or departure after gravity assist). Hence the **SEP system must provide**

$$V_{\infty 2} - V_{\infty 1} = 2.326 \cdot \frac{\text{km}}{\text{s}}$$

or

$$\Delta V_{1SEP} := V_{pto2} - V_{pto1} = 2.326 \cdot \frac{\text{km}}{\text{s}}$$

This is equivalent to saying that the spacecraft on-board ΔV (in Heliocentric frame) is equal to the *difference* between the Earth *departure velocity* (in heliocentric frame it is the velocity at the periapsis of the Hohman transfer orbit) *and the arrival velocity* (velocity at periapsis of second "Hohman" orbit, prior to gravity assist).

Steps 3-5: After the larger (2 year) size orbit, the spacecraft swings by the Earth, and is injected into a direct hyperbolic trajectory to Saturn. Here, the Earth gravity assist parameters are computed from this transfer orbit.

Heliocentric Segment

Spacecraft arrival velocity

$$V_{SA} := V_{pto2} = 34.962 \cdot \frac{\text{km}}{\text{s}}$$

Hyperbolic excess velocity

$$V_{\infty} := V_{\infty 2} = 5.169 \cdot \frac{\text{km}}{\text{s}} \quad C_{3b} = 26.722 \cdot \frac{\text{km}^2}{\text{s}^2}$$

Hyperbolic trajectory parameters (Earth Centered)

Periapsis radius

$$r_p := h_{dp} + R_e = 6.563 \times 10^3 \cdot \text{km}$$

Eccentricity

$$e_h := 1 + \frac{r_p \cdot V_\infty^2}{\mu_e} = 1.44 \quad (e_h > 1 \Rightarrow \text{Hyperbolic Orbit})$$

Turning Angle of Passage

$$\Psi := 2 \cdot \arcsin\left(\frac{1}{e_h}\right) \quad \text{rad} \quad \Psi = 87.967 \cdot \text{deg}$$

Heliocentric Velocity Change due to turning angle of passage

$$\Delta V_{ga} := 2 \cdot \frac{V_\infty}{e_h} = 7.18 \cdot \frac{\text{km}}{\text{s}} \quad \text{or} \quad 2 \cdot V_\infty \cdot \sin\left(\frac{\Psi}{2}\right) = 7.18 \cdot \frac{\text{km}}{\text{s}}$$

Although Hohman transfers have been used as a convenient way to estimate spacecraft energies (velocities), the actual trajectory deviates from it because of on-board (SEP) propulsion use. The gravity-assist flyby must occur between the Earth and the Sun, in order to achieve energy gain. This gain is also maximized when the angle between the vectors \mathbf{V}_{SA} and $\Delta \mathbf{V}_{ga}$, ν , is maximum (180 deg). To this effect, the flight path angle of arrival is adjusted accordingly.

Flight path angle of s/c arrival velocity $\gamma_{SA} := 0.0962$ radians $\gamma_{SA} = 5.512 \cdot \text{deg}$ (input)

$$\phi_A := \pi - \arcsin\left(\frac{V_{SA}}{V_\infty} \cdot \sin(\gamma_{SA})\right) = 2.434 \quad \phi_A = 139.486 \cdot \text{deg}$$

$$\nu := \frac{3 \cdot \pi}{2} + \frac{\Psi}{2} - \phi_A + \gamma_{SA} = 3.142 \quad \nu = 180.009 \cdot \text{deg}$$

The heliocentric spacecraft departure velocity is hence

$$V_{SD} := \sqrt{V_{SA}^2 + \Delta V_{ga}^2 - 2 \cdot V_{SA} \cdot \Delta V_{ga} \cdot \cos(\nu)} = 42.142 \cdot \frac{\text{km}}{\text{s}}$$

Note: Spacecraft arrival flight path angle has been chosen to maximize the energy gain for this situation. The hyperbolic orbit semi-major axis is,

$$a_h := \frac{r_p}{(e_h - 1)} = 1.492 \times 10^4 \cdot \text{km}$$

Now, determine the **(Heliocentric) elements of new orbit** after Earth flyby.

The flight path angle of the new spacecraft velocity (heliocentric) after the gravity assist is given by

$$\gamma_{SD} := \gamma_{SA} + \arcsin\left(\frac{\Delta V_{ga}}{V_{SD}} \cdot \sin(\nu)\right) = 0.096 \quad \gamma_{SD} = 5.51 \cdot \text{deg}$$

We now have position and velocity information. Then use the vis-viva equation and solve for the semimajor axis to get

$$a_o := \frac{r_e \cdot \mu_s}{2 \cdot \mu_s - r_e \cdot V_{SD}^2} = -1.888 \times 10^{11} \cdot \text{km}$$

Since the semimajor axis is negative, the **new orbit is hyperbolic**.

The eccentricity of the new orbit is

$$e_o := \sqrt{\left[\left(\frac{r_e \cdot V_{SD}^2}{\mu_s} - 1 \right)^2 - 1 \right] \cdot (\cos(\gamma_{SD}))^2 + 1} = 1.001$$

The true anomaly immediately after the flyby is found from

$$\theta_{o1} := \frac{\frac{r_e \cdot V_{SD}^2}{\mu_s} \cdot \sin(\gamma_{SD}) \cdot \cos(\gamma_{SD})}{\left(\frac{r_e \cdot V_{SD}^2}{\mu_s} \right) \cdot (\cos(\gamma_{SD}))^2 - 1} \quad \theta_{o1} = 11.154 \cdot \text{deg}$$

The heliocentric position immediately after the flyby is now to be determined. First, the *parameter* is given by

$$p := a_o \cdot (1 - e_o^2) = 2.964 \times 10^8 \cdot \text{km}$$

and the heliocentric position after the flyby is

$$r_{o1} := \frac{p}{(1 + e_o \cdot \cos(\theta_{o1}))} = 1.495 \times 10^8 \cdot \text{km}$$

The hyperbolic anomaly is then

$$F_{o1} := \operatorname{acosh} \left[\frac{1}{e_o} \cdot \left(1 - \frac{r_{o1}}{a_o} \right) \right] = 3.867 \times 10^{-3}$$

Check this with the equivalent formula (dependent on theta alone)

$$\operatorname{acosh} \left(\frac{e_o + \cos(\theta_{o1})}{1 + e_o \cdot \cos(\theta_{o1})} \right) = 3.867 \times 10^{-3}$$

The mean motion

$$n_o := \sqrt{\frac{\mu_s}{(-a_o)^3}} = 4.44 \times 10^{-12} \cdot \text{s}^{-1}$$

The time since periapsis passage when the EGA occurs, assuming $t=0$ at periapsis is then

$$t_{01} := \frac{1}{n_0} \cdot (e_0 \cdot \sinh(F_{01}) - F_{01}) = 7.933 \cdot \text{day}$$

The true anomaly at Saturn encounter is given by (computed for orbit visualization only)

$$\theta_{02} := \arccos \left[\frac{1}{e_0} \cdot \left(\frac{p}{r_n} - 1 \right) \right] = 2.486 \quad \theta_{02} = 142.43 \cdot \text{deg}$$

The hyperbolic anomaly at Saturn's encounter is

$$F_{02} := \operatorname{acosh} \left[\frac{1}{e_0} \cdot \left(1 - \frac{r_n}{a_0} \right) \right]$$

Hence

$$t_{02} := \frac{1}{n_0} \cdot (e_0 \cdot \sinh(F_{02}) - F_{02}) = 2.539 \cdot \text{yr}$$

The **flight time from Earth gravity assist to Saturn encounter** is then

$$\tau_f := t_{02} - t_{01} = 2.517 \cdot \text{yr}$$

The **total flight time from launch** is

$$T_f := P_{t02} + \tau_f = 4.55 \cdot \text{yr}$$

Saturn arrival parameters

The heliocentric radial velocity at encounter is found from

$$V_r := \frac{n_0 \cdot a_0^2}{r_n} \cdot e_0 \cdot \sinh(F_{02}) = 12.912 \cdot \frac{\text{km}}{\text{s}}$$

The heliocentric tangential velocity at encounter is

$$V_\theta := \frac{\sqrt{\mu_s \cdot p}}{r_n} = 4.375 \cdot \frac{\text{km}}{\text{s}}$$

The heliocentric Flight Path angle at encounter is

$$\gamma_{\text{sh}} := \operatorname{atan} \left[\frac{e_0 \cdot \sin(\theta_{02})}{(1 + e_0 \cdot \cos(\theta_{02}))} \right] = 1.244 \quad \text{rad} \quad \gamma_{\text{sh}} = 71.281 \cdot \text{deg}$$

The spacecraft heliocentric velocity magnitude at encounter is then computed from either radial or tangential components, and the flight path angle:

$$V_s := \frac{V_r}{\cos\left(\frac{\pi}{2} - \gamma_{\text{sh}}\right)} = 13.634 \cdot \frac{\text{km}}{\text{s}}$$

which is very close to the radial component, as expected.

The **heliocentric ΔV at Saturn** is given by

$$V_{\infty n} := \sqrt{V_{nh}^2 + V_s^2 - 2 \cdot V_{nh} \cdot V_s \cdot \cos(\gamma_{sh})} = 13.938 \cdot \frac{\text{km}}{\text{s}}$$

Saturn-Centered Encounter Hyperbola

Once at Saturn, the assumption is made that the spacecraft velocity vector is parallel to Titan's orbital velocity (Figure 3-1). To compute the entry speed, one must then determine the spacecraft's excess velocity compared to Titan's orbital velocity. This " ΔV " is in fact, the inertial entry speed into Titan's atmosphere.

Altitude (with respect to Saturn) of Arrival at Target - Assume at Titan's orbit.

$$h_{na} := 1221830\text{km} - R_n \quad (\text{input})$$

Saturn Arrival "Orbit" Semi-major axis (in Saturn Radii), or Titan Semi-major axis

$$a_{nar} := 20.273 \quad (\text{input})$$

Saturn Arrival Orbit Semi-major axis (km)

$$a_{na} := a_{nar} \cdot R_n = 1.222 \times 10^6 \cdot \text{km}$$

Saturn Arrival Orbit Period (days) - This is Titan's orbital period

$$P_{an} := 2\pi \cdot \sqrt{\frac{a_{na}^3}{\mu_n}} = 15.945 \cdot \text{day}$$

Saturn Arrival Radius (At Periapsis of Arrival Orbit)

$$r_{spn} := R_n + h_{na} = 1.222 \times 10^6 \cdot \text{km}$$

Assume we encounter Titan at its periapsis. Given the small eccentricity (~ 0.03) however, we could just as well assume intersection at a different position in its orbit without any significant change in entry speed,

$$V_{spn} := \sqrt{\mu_n \cdot \left(\frac{2}{r_{spn}} - \frac{1}{a_{na}} \right)} = 5.572 \cdot \frac{\text{km}}{\text{s}}$$

S/C Velocity at Arrival (Needed to reach V_{∞} Arrival, or Saturn Escape Velocity)

$$V_{sa} := \sqrt{V_{\infty n}^2 + 2 \cdot \frac{\mu_n}{r_{spn}}} = 16.011 \cdot \frac{\text{km}}{\text{s}}$$

Arrival ΔV - or entry velocity into Titan's atmosphere

$$\Delta V_A := V_{spn} - V_{sa} = -10.439 \cdot \frac{\text{km}}{\text{s}}$$

where the negative sign convention is used to imply that the velocity change occurs opposite the velocity vector. This is the relative velocity of the spacecraft with respect to Titan (its orbital speed), and hence represents **the entry velocity into Titan's atmosphere**. Further, this can be considered the **inertial entry speed**, since Titan's rotation is not being considered.

It is important to note that this analysis does not take into consideration launch dates, so the results are meant to provide an idea of the orbital energies that could be achieved given the combination of assumptions used in the derivation. It is reasonable to assume that there exists a given launch date that fits these energies, and hence constrain the travel time, SEP requirements, and entry velocity. To check the validity of this assumption, a literature search was carried out. The work presented in Reference 9 in particular, shows that for SEEGA trajectories, as travel time decreases the entry speeds increase (not surprisingly).

The important point is that a solution may be obtained that compares to the results of this analytical analysis. Figure 3-2 shows a digitized copy of the curve corresponding to an EGA with the Delta 4450 ELV (Figure 9, Ref. 9). The curve fit yields an inertial entry speed of about 10.99 km/s for a flight time of 4.55 years, a result closely matching the one obtained through this analysis.

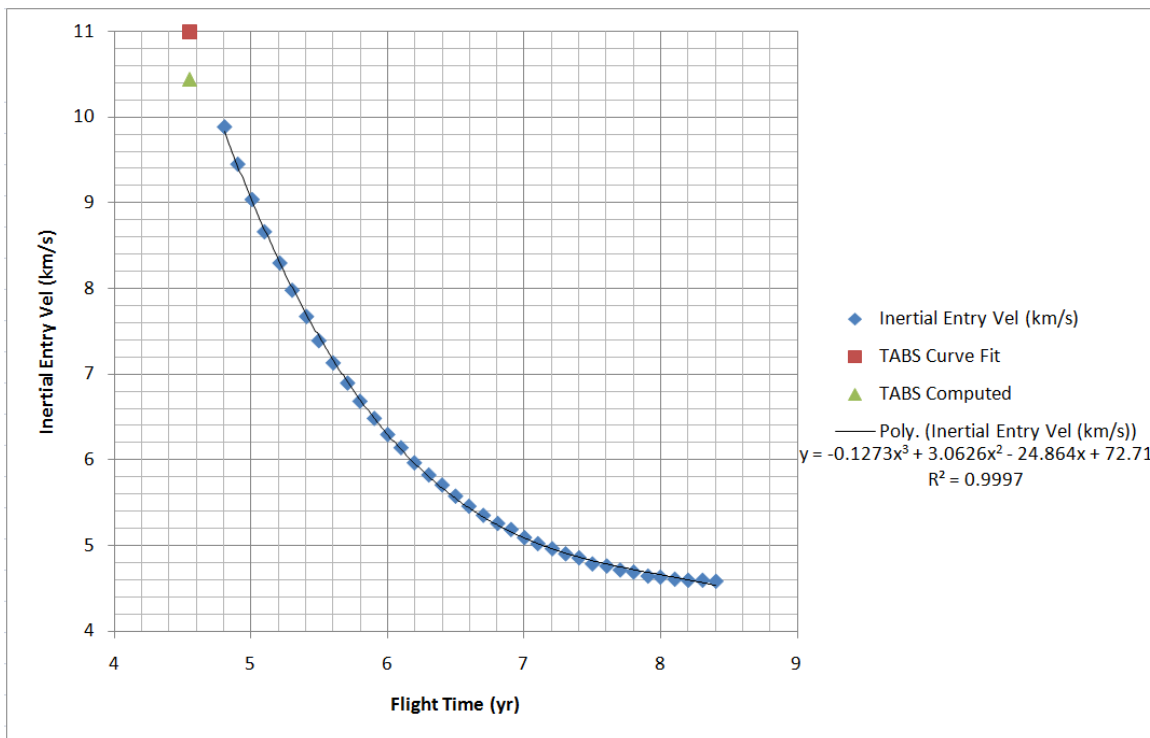


Figure 3-2: Titan inertial entry velocities at 1000 km altitude as a function of flight time from Ref. 9. The analytical result obtained here is marked with the (green) triangle, whereas the curve fit yields the (red) square.

From a perspective of entry velocities, and as a mean of comparison, the entry velocity for previous atmospheric entry probes are ¹⁰: Venera: 11.2 km/s; Pioneer Venus Large and Small Probes: 11.7 km/s; Galileo Probe: 48 km/s (relative), 60 km/s (inertial); Huygens: 6 km/s.

3.4 Trajectory Correction Maneuvers (TCM)

A detailed quantitative analysis of cruise and flyby flight dynamics is beyond the scope of this dissertation. Hence trajectory correction and approach maneuvers will not be analyzed directly. However, sizing of the chemical propulsion system requires a rough knowledge of the total trajectory correction ΔV required after EGA, including maneuvers leading to TABS entry.

The SEP module is jettisoned after EGA, and the vehicle continues with its chemical propulsion system. The ΔV that must be accommodated by this system is inferred from Cassini's TCM data²⁵. It is understood that these numbers are specific to Cassini's configuration, including moments of inertia, center of mass, and thruster locations. Nonetheless, to a first-order approximation they may also be applied to TABS with an appropriate margin (30%). Cassini flew by Mars, and targeted Phoebe for observation. Since TABS does not use the chemical propulsion system during the first part of the trajectory, both the Earth approach maneuvers and the Phoebe targeting maneuvers used in Cassini may reasonably represent the situation of cruise and Titan targeting for TABS. Table 3-1 shows the maneuvers in question, and the total requirement inferred for TABS after the margin is applied.

Table 3-1: Cassini's TCM flight data (extracted from Reference 25)

TCM/ Date/ Type*/	Burn Duration (s)	Delta V (m/s)		Notes
TCM-09 7/6/99 ME 459.576		43.54	Earth collision avoidance	
TCM-10 7/19/99 ME 54.711		5.13		Used to minimize any risk of Earth impact in case of S/C failure
TCM-11 8/2/99 ME 391.572		36.3		
TCM-12 8/11/99 ME 133.518		12.26		Earth Flyby
TCM-13 8/31/99 ME 72.35		6.7	Outer Cruise and Saturn approach phases	
TCM-14 6/14/00 ME 6.159		0.5546		
TCM-17 2/28/01 ME 5.436		0.4905		
TCM-18 4/3/02 ME 9.845		0.8907		
TCM-19 5/1/03 ME 17.532		1.595		
TCM-19A 9/10/03 RCS 197.875		0.12		
TCM-19B 10/1/03 ME 21.843		2		
TCM-20 5/27/04 ME 362.146		34.7228		Targeted Cassini to a 2000 km flyby of Phoebe
TCM-21 6/16/04 ME 38.385		3.6956		Targeted the spacecraft trajectory to a precise corridor between the F and G rings of Saturn
TOTAL		148		
30% Margin		192		Used for CHEM propulsion system sizing

* ME=main Engine; RCS=Reaction Control System

3.5 Entry Flight Path Angle

The entry flight path angle needs to be defined in order to ensure TABS neither skips-off the atmosphere, nor it crashes onto the surface. It will be estimated first from a purely geometric account, and iterated as aerothermodynamic parameters are computed so as to provide a reasonable balance between deceleration and heat load inputs. If a 1000 km entry interface is chosen, then a flight path angle of at least $\sim 44^\circ$ would ensure geometric contact of the trajectory with the ground at 2480 km downrange, for a straight undisturbed flight path. It will be shown that a flight path angle of 50° proves adequate for TABS. This angle is consistent with previous planetary entry probes to Venus and Titan. Figure 3-3 illustrates the flight path geometry and simple computations.

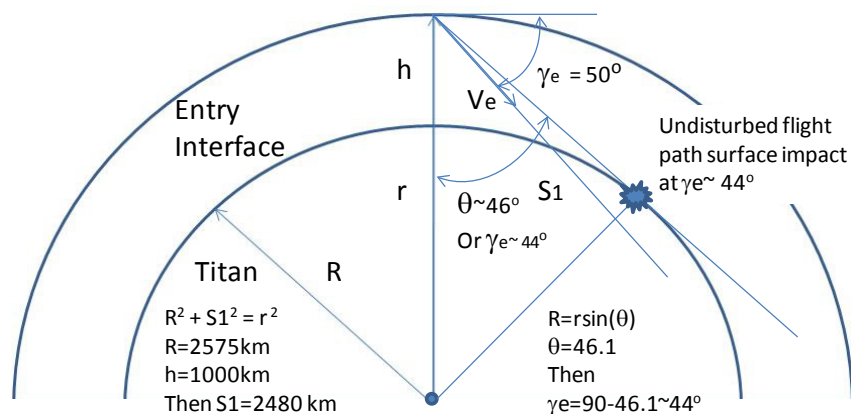


Figure 3-3: Flight path angle assessment for 1000 km altitude entry interface

4.0 Communications

Early entry operations including carrier spacecraft communication relay requirements must be understood in order to size its downlink and the low-gain antenna requirements on-board the entry probe. Relay operations will also define the back-up battery power required to operate the carrier spacecraft during the flyby for a determined period of time. In addition, science operations will require a certain amount of Direct-to-Earth (DTE) communications from the probe High Gain Antenna (HGA).

There are three operating modes that affect the communications rate from the Carrier Spacecraft (CS) to Earth and directly from TABS to Earth. These are defined in Table 2-1.

The Mode 1 (M1) downlink corresponds to the full data set rate for DTE communications from the gondola. It is basically the full science operating mode. A link analysis is necessary to determine a reasonable size antenna, and the data that may be downlink in “real time”, versus data stored for later downlink. Given the large distances and the amount of data to be down-linked, TABS must have intelligent software on board to sift through “interesting” events, as the downlink rates impose important constraints. Alternatively, ground command may instruct TABS to collect full data for some period of time for later analysis on the ground. Again, such full-date collection events must be pre-defined. The Mode 2 (M2) downlink corresponds to a reduced set of data for DTE communication, containing most of the instrument input, except for the spectrometer. Finally, Mode 3 (M3) downlink corresponds to the data to be sent back to Earth during entry and early operations, and represents the design reference requirements for the CS relay communications.

The key element in the Radio Frequency (RF) communications link budget analysis is to ascertain that the antenna and receiver will be able to pick up and recognize successfully the signal being transmitted. It is then necessary to compute the power arriving at the antenna, as well as the signal-to-noise ratio of the signal being received. This analysis applies both for the on-board spacecraft receiver, as well as the receiving antenna. A quantitative derivation of link parameters for TABS DTE communications will be provided next. It will also serve to size the on-board antenna.

4.1 Link Analysis and TABS Antenna Sizing

We assume a parabolic High Gain Antenna (HGA) on the spacecraft, and size it based on reasonable results for the link (or power) budget at distances out to Saturn. Assuming a 55W DC power communications system with a ~50% efficiency²⁶, the RF out can then be reasonably estimated. Assuming that 45 W are allocated to the transmit portion, the following ESA assumption is adopted for the RF output⁵.

$P_t := 25$ watts is the maximum Spacecraft RF Output Power (From Reference 5)

The probe parabolic dish antenna diameter is actually iterated until a reasonable solution is found. Such solution is shown below.

$D_t := 1.0$ meters

$\eta_t := 0.6$ Typical satellite directional-antenna efficiency value

$D_r := 70$ meters DSN (receiving) antenna aperture used

$\eta_r := 0.5$ DSN antenna efficiency

DSN receiver bandwidth is,

$B_r := 4000$ Hz wide around the downlink frequency

Note: The bandwidth is actually the initial data rate, which may be increased with encoding techniques to reach a higher number. The maximum data rate, or channel capacity, is proportional to the bandwidth and is given by the Shannon "error-free" limit. The bottom line is that by increasing the bandwidth the link (receiver) noise will also increase, but so will the maximum data rate capability. The trick is to find the correct balance to obtain the desired results. See additional discussion below, when selecting the actual data rate.

The downlink frequency is

$f_t := 35$ GHz in the Ka-band

The DSN receiver components are cooled to

$T_r := 28.5$ Kelvin

The sky temperature is a function of several factors including elevation angle of the antenna, atmospheric conditions, and receiving frequency. For our case a reasonable number to use is ⁸,

$$T_{\text{sky}} := 40 \quad \text{Kelvin}$$

Total effective noise temperature is then

$$T_{\text{eq}} := T_r + T_{\text{sky}} = 68.5 \quad \text{K}$$

The communications slant range (distance between antennae) is taken (worst case) as the sum of distances of Saturn and the Earth to the Sun (Saturn at Conjunction)

$$r_e := 149500000 \quad \text{km} \quad \text{Mean distance from the Sun to the Earth}$$

$$r_n := 1433264000 \quad \text{km} \quad \text{Mean distance from the Sun to Saturn}$$

$$R_{\text{slant}} := r_n + r_e \quad R_{\text{slant}} = 1.583 \times 10^9 \quad \text{km} \quad (\text{worst case})$$

Incidental downlink losses (due to atmosphere, ionosphere, electromagnetic interference, etc.), assumes contacts occur at elevations above ~ 20 degrees. This is a reasonable assumption for planetary missions:

$$L_{\text{id}} := 1.0 \quad \text{dB} \quad \text{or} \quad L_i := 10 \frac{L_{\text{id}}}{10}$$

The effective transmitter antenna area is given by

$$A_{\text{et}} := \eta_t \cdot \pi \cdot \frac{D_t^2}{4} = 0.471 \quad \text{m}^2$$

$$\text{or} \quad A_{\text{etd}} := 10 \cdot \log(A_{\text{et}}) = -3.268 \quad \text{dB}$$

The effective receiver antenna area is

$$A_{\text{er}} := \eta_r \cdot \pi \cdot \frac{D_r^2}{4} = 1.924 \times 10^3 \quad \text{m}^2$$

$$\text{or} \quad A_{\text{erd}} := 10 \cdot \log(A_{\text{er}}) = 32.843 \quad \text{dB}$$

The transmitter antenna gain is

$$c := 2.998 \cdot 10^8 \quad \frac{\text{m}}{\text{sec}} \quad \text{speed of light in vacuum}$$

$$G_t := \frac{4 \cdot \pi \cdot (f_t \cdot 10^9)^2 \cdot A_{\text{et}}}{c^2} = 8.071 \times 10^4$$

$$\text{or} \quad G_{\text{td}} := 10 \cdot \log(G_t) = 49.069 \quad \text{dB}$$

$$\ln(10) = 2.303$$

$$\log(10) = 1$$

where the frequency is expressed in Hertz. The receiver antenna gain is similarly

$$G_r := \frac{4 \cdot \pi \cdot (f_r \cdot 10^9)^2 \cdot A_{\text{er}}}{c^2} = 3.296 \times 10^8$$

$$\text{or} \quad G_{rd} := 10 \cdot \log(G_r) = 85.179 \quad \text{dB}$$

The free space (or path) loss represents losses of the transmitted signal as the wavefront expands between transmitter and receiver. It is given by

$$L_s := \left[\frac{4 \cdot \pi \cdot R_{\text{slant}} \cdot 10^3}{\left(\frac{c}{f_t \cdot 10^9} \right)} \right]^2 = 5.392 \times 10^{30}$$

$$\text{or} \quad L_{sd} := 10 \cdot \log(L_s) = 307.317 \quad \text{dB}$$

where the slant distance is given in meters, and the frequency in Hertz.

The power received by the DSN antenna is given as

$$P_r := \frac{P_t \cdot G_t \cdot G_r}{L_s \cdot L_i} = 0 \quad \text{watts}$$

$$\text{or} \quad P_{rd} := 10 \cdot \log(P_r) = -160.089 \quad \text{dBW}$$

Assuming a White Gaussian Noise (WGN), the DSN receiver noise is computed as

$$k := 1.38 \cdot 10^{-23} \frac{\text{watts}}{\text{K} \cdot \text{Hz}} \quad \text{is the Stefan- Boltzmann Constant}$$

$$N_{or} := k \cdot T_{\text{eq}} \cdot B_r \quad \text{watts}$$

$$N_{ord} := 10 \cdot \log(N_{or}) = -174.224 \quad \text{dBW}$$

The *signal-to-noise ratio of the receiver* is then

$$\text{SNR}_r := \frac{P_r}{N_{or}} = 25.909$$

$$\text{or} \quad \text{SNR}_{rd} := 10 \cdot \log(\text{SNR}_r) = 14.134 \quad \text{dB}$$

Which proves adequate for TABS chosen antenna size and RF output power. The "*error free*" data rate (or channel capacity) of the link is proportional to the SNR, and is given by Shannon's limit:

$$x_2 := 1 + \text{SNR}_r \quad \log_2(n, x_2) := \frac{\ln(x_2)}{\ln(2)} \quad (\text{Defines the logarithm to base 2})$$

$$C_{\text{rate}} := B_r \cdot \log_2(2, x_2) \quad C_{\text{rate}} = 1.9 \times 10^4 \quad \text{bps} \quad (\text{Shannon error-free limit})$$

Using error detection algorithms (e.g. Reed-Solomon code), it is possible to safely increase the starting bit rate (bandwidth) for successful communications to a point up to, but not above the channel capacity given in Shannon's theorem. We will assume here that we can get a bit rate *equal* to Shannon's limit, with the caveat that the encoding technique must be very efficient. Hence,

$$C_{\text{rate.n}} := 1 \cdot C_{\text{rate}} = 1.9 \times 10^4 \quad \text{bps}$$

As the worst case, downlink rate (Saturn in conjunction)

For comparison, the TandEM mission proposal with similar science payload had a buoyant station (s) to orbiter uplink rate of 20 kbps²⁷. The TSSM study also showed a Direct-to-Earth (DTE) transmission rate from the balloon of about 0.111 kbps (Ref. 5, Table 17: *Link characteristics for Montgolfière DTE data transmission*). The expected DTE rate of 19 kbps for TABS proves then a reasonable result. Since the nominal science payload is estimated to acquire and downlink data at a rate of about 10 Mbps (Table 2-1) it becomes necessary to compress and store data for transmission.

Note that if we were to use an "average" slant range distance to Saturn,

$$R_{\text{slant2}} := \sqrt{r_e^2 + r_n^2} = 1.441 \times 10^9 \quad \text{km}$$

the data rate is not much changed (to ~20 kbps). Using the distance at opposition (closest to Earth) will not change things much either, achieving a rate of ~ 21 kbps.

4.2 Onboard Storage, Downlink Duty Cycle, and Total Data

It was shown that with the current communications capability, all TABS data must first be stored, then compressed and transmitted back to Earth. It now becomes necessary to allocate for an on-board recorder. The time and duty cycle required to downlink this stored data is now computed. TABS will need to include smart software to recognize notable changes of scientific interest, and record-to-transmit only important information during times when a DTE link is available.

The nominal instrument acquisition rate (Table 2-1) is,

$$SR_{\text{cam}} := 10052.6 \quad \text{kbps}$$

The science data acquisition storage time allocated to acquire 100 complete set of science images / data samples at 54 secs/data sample (again, Table 2-1) is

$$\tau_{\text{sci.acq}} := \frac{54}{3600} \cdot 100 = 1.5 \quad \text{hr}$$

The number of data sets chosen (100) is somewhat arbitrary, except that it results in reasonable time as seen. The total "raw" science data to be stored (and transmitted) per acquisition time is then

$$D_{\text{science.r}} := [\tau_{\text{sci.acq}} \cdot 3600 \cdot (SR_{\text{cam}})] \cdot \frac{1}{1000} = 5.428 \times 10^4 \quad \text{Mbits}$$

Assuming a 6-to-1 lossless compression ratio, the actual stored data that needs to be transmitted is

$$D_{\text{science}} := \frac{D_{\text{science.r}}}{6} = 9.047 \times 10^3 \quad \text{Mbits}$$

With the data rate used above, the time required to downlink the stored data is then

$$\tau_{\text{dump}} := \frac{D_{\text{science}} \cdot 10^6}{C_{\text{rate.n}}} \cdot \frac{1}{3600} \cdot \frac{1}{23.93} = 5.527 \quad \text{days}$$

This means that high-rate instruments must be cycled, and information only targeted for areas of interest. Low-rate meteorological information on the other hand, can be acquired more frequently. Assuming the DSN can support 1 such data dumps per two weeks, its duty cycle (time allocated to TABS) bi-weekly would be

$$DSN_{\text{dc}} := \frac{1}{14} \tau_{\text{dump}} = 0.395 \quad \text{out of 1 (or 39.5\%)}$$

The number of complete data sets downlinked per month assuming a 39.5% DSN coverage is then

$$N_{\text{spectral}} := 200$$

Assuming a 6-month baseline mission life, the total number of bits and images received would amount to

$$\text{life} := 6 \quad \text{months}$$

$$2D_{\text{science.r}} \cdot \text{life} = 6.514 \times 10^5 \quad \text{Mbits of science data}$$

$$N_{\text{spectral}} \cdot \text{life} = 1.2 \times 10^3 \quad \text{Complete image / data samples}$$

For a reduced set of data (mode 2 downlink), containing most of the instrument input, except for the spectrometer, the data acquisition volume is improved by at least an order of magnitude. The reduced TABS instrument acquisition rate is (Table 2-1)

$$SR_{\text{cam2}} := 1133.1 \quad \text{kbps}$$

Science data acquisition storage time allocated to acquire 1000 complete set of science images / data samples at 4 secs/data sample

$$\tau_{\text{sci.acq2}} := \frac{4}{3600} \cdot 1000 = 1.111 \quad \text{hr}$$

The total "raw" science data to be stored (and transmitted) per acquisition time is then

$$D_{\text{science.r2}} := \left[\tau_{\text{sci.acq2}} \cdot 3600 \cdot (SR_{\text{cam2}}) \right] \cdot \frac{1}{1000} = 4.532 \times 10^3 \quad \text{Mbits}$$

Assuming a 6-to-1 lossless compression ratio, the actual stored data that needs to be transmitted is

$$D_{\text{science2}} := \frac{D_{\text{science.r2}}}{6} = 755.4 \quad \text{Mbits}$$

With the data rate used above, the time required to downlink the stored data is then

$$\tau_{\text{dump2}} := \frac{D_{\text{science2}} \cdot 10^6}{C_{\text{rate.n}} \cdot 3600 \cdot 23.93} = 0.462 \quad \text{days}$$

a much smaller time than the full data set. Still, the imager may be cycled, and information only targeted for areas of interest. Assuming the DSN can support 1 such data dumps per two weeks (for comparison purposes), its duty cycle (time allocated to TABS) bi-weekly would be

$$DSN_{\text{dc2}} := \frac{1}{14} \tau_{\text{dump2}} = 0.033 \quad \text{out of 1 (or 3.3\%)}$$

A much reduced duty cycle. The number of complete data downlinked per month assuming a 3.3% DSN coverage is then 2000 (no spectral data).

$$N_{\text{spectral2}} := 2000$$

Assuming a 6-month baseline mission life, the total number of bits and images received would amount to

$$2D_{\text{science.r2}} \cdot \text{life} = 5.439 \times 10^4 \quad \text{Mbits of science data}$$

$$N_{\text{spectral2}} \cdot \text{life} = 1.2 \times 10^4 \quad \text{Complete image / data samples or an order of magnitude larger}$$

In order to accommodate ground station schedules, and DTE capability during real operational scenarios, the actual instrument data acquisition scheme may be varied accordingly. From this analysis however, it can be seen that significant scientific data can be acquired in any given scenario, for a DTE link approach.

4.3 Carrier Spacecraft Flyby and Relay Communications

Based on the cruise spacecraft flyby time for communications with TABS, we estimate the maximum slant range for communications during the entry phase. If the closest approach is chosen at 1,300 km and the communications time set to 4 hrs, then

$t_{\text{com}} := 4\text{hr}$ communications time

$V_e := 10.44 \frac{\text{km}}{\text{s}}$ Titan-relative inertial vehicle velocity at flyby (same as TABS entry speed)

$r_{\text{close}} := 1300\text{km}$ carrier spacecraft closest approach to Titan

The distance traveled by the carrier spacecraft during communications is

$$R_{\text{flight}} := V_e \cdot t_{\text{com}} = 1.503 \times 10^5 \cdot \text{km}$$

The communications slant range is then

$$R_{\text{scom}} := \sqrt{r_{\text{close}}^2 + \left(\frac{R_{\text{flight}}}{2}\right)^2} = 7.518 \times 10^4 \cdot \text{km}$$

Figure 4-1 shows the corresponding geometry during flyby.

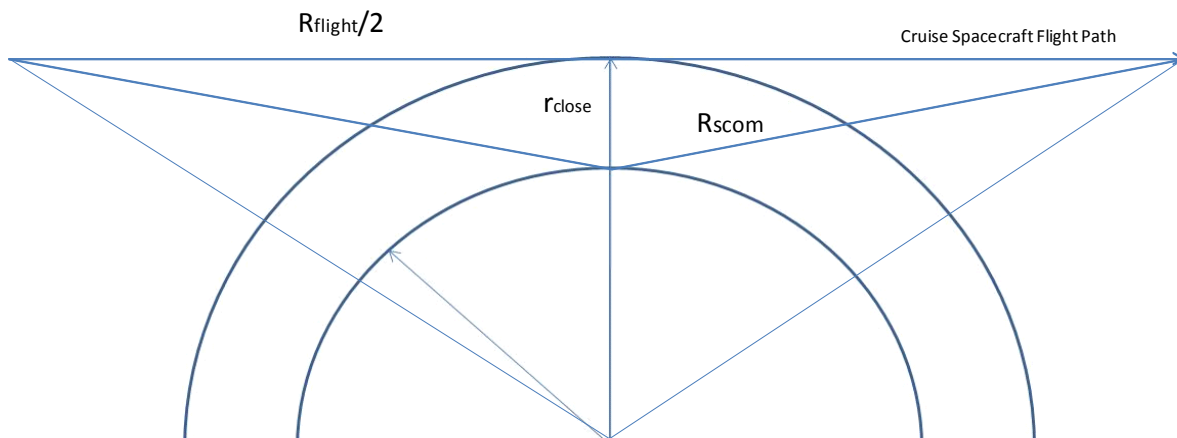


Figure 4-1: Carrier spacecraft relay geometry

4.4 Communications Summary

Table 4-1 provides a summary of the mission communication modes and link parameters. As can be seen, the system as designed is capable of satisfying the data communication requirements during critical mission operations (flyby and early entry), and provides up to 892 Mbits of DTE science data per day.

Table 4-1: Mission Communications Characteristics

	TABS		Carrier Spacecraft
	DTE Downlink	TABS-to-CS Uplink	DTE Downlink
Transmit System			
Antenna Type	Parabolic Reflector	Halfwave Dipole	Parabolic Reflector
Frequency (GHz) / Band	35 / Ka	2 / S	35 / Ka
Antenna Diam / Length (cm)	100	7	100
RF Output Power (W)	25	25	100
Antenna Efficiency	0.6	0.6	0.6
Effective Antenna Area (m2)	0.471	2.93E-03	0.471
Antenna Gain (dB)	49.1	2.15	49.1
Receive System			
Antenna Type	DSN	Parabolic Reflector	DSN
Antenna Dia. (m)	70	1	70
Antenna Efficiency	0.5	0.6	0.5
Effective Antenna Area (m2)	1924	0.471	1924
Receiver Bandwidth (Hz)	4000	10000	4000
Total Effective Receiver Noise Temp (K)	68.5	210	68.5
Antenna Gain (dB)	85.2	24.2	85.2
Link Characteristics			
Slant Range (km)	1.583E+09	7.517E+04	1.583E+09
Incidental Losses (dB)	1	1	1
Free Space Loss (dB)	307.3	196	307.3
Receiver Signal-to-Noise Ratio (dB)	14.1	8.7	20.2
Link Rate (kbps)	19	30.8	26.8
Required Mode 3 - Entry and Early Ops (kbps)			
Link Rate Margin (%)	n/a	21.2	21.2
Normalized Downlink Data Volume (per day)*			
Mode 1 (Mbits) - Full Science	892		
Mode 2 (Mbits) - Reduced Science	75		

* DSN Bi-weekly dump duty cycle (39.5% for M1 and 3.3% for M2)

5.0 TABS Buoyant Gas System

Huygens was the first probe to enter Titan's atmosphere. Its design however, only included provisions for a parachute deployment and landing, did not have a buoyant envelope, and did not require extended operations. On the other hand, proposals for a buoyant probe at Titan have generally followed the consensus that a Montgolfier must be used primarily on the basis of system longevity ⁵. It will be shown that a lighter-than-air design is not only a viable alternative to the consensus approach, but that system complexity may be reduced especially during the initial deployment sequence. Of course, complexity is a relative term, and TABS exchanges deployment simplicity at the expense of added tank and entry probe mass, which in turn complicates packaging. Nonetheless, buoyant gas tank technology is well established, and long duration balloons have already flown, from simple weather crafts to ultra-long duration “pumpkin” balloons.

Of the different types of balloons available, super-pressure balloons have seen the greatest operational lifetimes, with some balloon flights lasting for several years ¹⁰. It is this design that is chosen as an alternative to the hot-air case and will be sized next. A trade analysis of different balloon types including Montgolfier and buoyant gas at different pressures (zero and super-pressure) will be presented. First however, the baseline balloon is sized and the payload capacity (gondola) defined.

5.1 Hydrogen Balloon (baseline)

First, one must select the most benign environment for deployment and operations of the balloon at Titan. That means choosing the best combination of pressure, temperature, and atmospheric conditions, in particular wind speeds and shear. From wind data obtained by Huygens, the regions below 5 km has winds below 1 m/s, reaching close to zero at the surface. However, for regions below ~6 km precipitation is more likely, and can complicate the system design. Higher altitudes require a larger balloon for a given payload mass. Hence, the recommendations from the TSSM study are followed, and a nominal height of 10 km is baseline in this work.

Based on this and Huygens data ⁷, we define the initial conditions for balloon deployment, where the subscript "a" refers to "ambient" conditions,

Operational altitude,	$h_0 := 10\text{km}$	
Temperature at altitude,	$T_a := 84\text{K}$	
Pressure at altitude	$P_a := 0.884\text{bar}$	$P_a = 8.84 \times 10^4 \text{ Pa}$

For a super-pressure balloon, the pressure of the buoyant gas (H in this case) is greater than the ambient pressure ($\Delta P > 0$). As a first approximation we use the ideal gas law, since the operating pressure is assumed to be at about 1 atmosphere.

The molecular weight of H is $\mu_g := 0.001 \frac{\text{kg}}{\text{mol}}$

The Universal gas constant $R_c := 8.314 \frac{\text{J}}{\text{K} \cdot \text{mol}}$

We first start sizing the balloon by constraining its volume, and examining its lift capacity. A desired size is obtained iteratively. Hence, a balloon diameter, D_b is chosen. D_b is the single parameter that will later determine the payload mass. Use a spherical balloon and estimate the gas volume,

$$D_b := 4.6\text{m} \quad (\text{Input}) \quad V_b := \frac{4}{3} \cdot \pi \cdot \left(\frac{D_b}{2}\right)^3 \quad V_g := V_b \quad V_g = 50.965 \cdot \text{m}^3$$

Compute the density of Hydrogen at the operating conditions in Titan of temperature (gas temp=ambient temp), but assuming greater pressure (superpressure) using the ideal gas law.

To calculate the superpressure, we assume a material similar to the one developed by Lamart, Inc. and JPL ¹¹,

$$\tau_s := 16400 \frac{\text{N}}{\text{m}} \quad \text{Tensile strength of Mylar/Polyester balloon material at 77K (close to operating condition)}$$

$$\Delta P_{\text{burst}} := \frac{\tau_s}{\frac{D_b}{2}} = 7.13 \times 10^3 \text{ Pa} \quad \text{or} \quad \Delta P_{\text{burst}} = 0.071 \cdot \text{bar}$$

We define the *superpressure*, ΔP to be a fraction of this burst pressure.

$$\Delta P := \frac{\Delta P_{\text{burst}}}{4} \quad \Delta P = 1.783 \times 10^3 \text{ Pa} \quad \text{or} \quad \Delta P = 0.018 \cdot \text{bar}$$

The density of Hydrogen inside the balloon can then be calculated.

$$\rho_g := \frac{\mu_g \cdot (P_a + \Delta P)}{R_c \cdot T_a} \quad \rho_g = 0.129 \frac{\text{kg}}{\text{m}^3} \quad \text{Density of H at Titan}$$

Note: If $\Delta P=0$, then the density of the gas may be written as the ambient density times the ratio of molecular weights (do not have to use the universal gas constant):

Given that $P_a/(R_c T_a) = \rho_a/\mu_a$ (ideal gas law), then $\rho_g = \rho_a(\mu_g/\mu_a)$

The *mass of buoyant gas* is then

$$M_g := \rho_g \cdot V_g = 6.581 \text{ kg}$$

If we assume a leak rate through the balloon material to be 72gm/week¹¹, then the gas mass loss over a 6 month operational lifetime is

$$L_r := \frac{72 \text{ gm}}{7 \text{ day}} \quad m_{\text{gaux}} := L_r \cdot \frac{365}{2} \text{ day} = 1.877 \text{ kg}$$

This is the amount of *Hydrogen gas that must be carried by an auxiliary gas tank*. This will be added to the gondola mass, and is computed later. For a balloon with this volume, assuming an aerial density of the balloon material $A_d=98.0 \text{ gm/m}^2$ ¹², and a supporting structure mass of 10% in addition, *the mass of the balloon is then*,

$$A_d := 1.1 \cdot 0.098 \frac{\text{kg}}{\text{m}^2} \quad A_d = 107.8 \cdot \frac{\text{gm}}{\text{m}^2} \quad \text{Input (note: TandEM assumed } \sim 48 \text{ gm/m}^2)$$

$$\text{Mass of the balloon,} \quad M_b := 4\pi \cdot \left(\frac{D_b}{2}\right)^2 \cdot A_d = 7.166 \text{ kg}$$

Note: Typical values for A_d are 0.02 to 0.3 kg/m²¹³. We use $\sim 0.11 \text{ kg/m}^2$ as a "conservative" value.

The mean molecular weight of the ambient atmosphere at the surface from Voyager 1 IR data¹⁴ is,

$$\mu_a := 0.02875 \frac{\text{kg}}{\text{mol}}$$

The atmospheric density is then

$$\rho_a := \frac{\mu_a \cdot P_a}{R_c \cdot T_a} = 3.639 \frac{\text{kg}}{\text{m}^3}$$

The payload mass that can be lifted by this balloon, at equilibrium, is then derived (includes instruments, structure, avionics, power, i.e, the Gondola). Note: H_2 tanks stay behind once inflation is complete, and do not form part of the Gondola. Auxiliary tank and gas however, are part of the gondola.

Setting the gas temperature equal to the ambient temperature $T_g := T_a$ then

$$M_p := \rho_a \cdot V_b \cdot \left[1 - \left(1 + \frac{\Delta P}{P_a} \right) \cdot \frac{\mu_g \cdot T_a}{\mu_a \cdot T_g} \right] - M_b = 171.722 \text{ kg}$$

The possible total *floating* mass is then (note the tank mass is not included since it is jettisoned)

$$M_T := M_b + M_g + M_p = 185.47 \text{ kg}$$

5.2 Montgolfier Balloon

A Montgolfier balloon is now sized to compare its lifting capacity and inflation time with that of an equivalent H_2 balloon. As before, we fix the volume by choosing a balloon diameter, D_{bm} . As a means of comparison, we set the volume and balloon material (aerial density) equal to the H_2 balloon case, and choose a spherical geometry. Hence, the balloon mass remains equal. Choosing a temperature differential (superheat temperature) with the environment compatible with an MMRTG heat source ($\sim 2\text{KW}$), the payload mass that can be lifted by this balloon, at equilibrium, is

$$\Delta P_m := 0$$

$$\mu_{gm} := \mu_a$$

$$\Delta T := 31\text{K} \quad \text{temperature difference achievable by MMRTG for given envelope}$$

$$T_{gm} := T_a + \Delta T$$

$$M_{pm} := \rho_a \cdot V_b \cdot \left[1 - \left(1 + \frac{\Delta P_m}{P_a} \right) \cdot \frac{\mu_{gm} \cdot T_a}{\mu_a \cdot T_{gm}} \right] - M_b = 42.83 \text{ kg}$$

Or about 129 kg less payload than an equivalent size H_2 balloon (a low superheat value of 20K would make the difference even more striking, at 143 kg less capacity). The possible total floating mass is then

$$M_{Tm} := M_b + M_{pm} = 49.996 \text{ kg}$$

Now we compute the *required heat input to raise the given volume of gas by the given ΔT* . This should be approximately equal to the heat output capacity of the MMRTG. The specific heat capacity, often referred as specific heat, is the measure of the heat energy required to increase the temperature of a unit quantity of a substance by a unit of temperature. The specific heat of Nitrogen and Hydrogen (at 298K) and Methane (at 275K) at constant pressure is ²¹,

$$C_{pN2} := 1.040 \frac{\text{J}}{\text{gm}\cdot\text{K}} \quad C_{pCH4} := 2.191 \frac{\text{J}}{\text{gm}\cdot\text{K}} \quad C_{pH2} := 14.30 \frac{\text{J}}{\text{gm}\cdot\text{K}}$$

The specific heat of the atmosphere is approximated from the relative abundance of Titan's atmospheric components (Ref. 22, Table 3 at 981 Km) as,

$$C_{pg} := 0.984 \cdot C_{pN2} + 0.0131 \cdot C_{pCH4} + 0.0033 \cdot C_{pH2} = 1.099 \cdot \frac{\text{J}}{\text{gm}\cdot\text{K}}$$

The mean Volumetric Heat Capacity (VHC) of Titan's atmosphere is then approximately,

$$\text{VHC} := C_{pg} \cdot \rho_a = 4 \times 10^3 \cdot \frac{\text{J}}{\text{m}^3 \cdot \text{K}}$$

The equation relating heat energy to VHC, where the unit quantity is in terms of volume is then:

$$Q_g := V_g \cdot \text{VHC} \cdot \Delta T = 6.32 \times 10^6 \text{ J}$$

This is the heat input required to raise the temperature of the given volume of gas the specified temperature interval.

If the energy source outputs a given wattage (heat), then it would take some determinate amount of time for the volume to heat-up. This power source must be computed for the steady state condition, where the heat input is balanced by the heat loss due to free and forced convection at the balloon walls. Radiative loss is not considered given the low temperatures found at Titan, and the dominance of convective heat transfer at the (outer) balloon wall. Using "typical" values for low superheat (ΔT) temperatures ($\sim 20\text{K}$ ¹³, so 31K used here is within acceptable range) we get

$$h_c := 1 \frac{\text{W}}{\text{m}^2 \cdot \text{K}} \quad \text{convection heat transfer coefficient}$$

$$P_s := \pi \cdot D_b^2 \cdot h_c \cdot (\Delta T) = 2.061 \times 10^3 \text{ W} \quad (\text{consistent with the analysis above})$$

$$t_{\text{heat}} := \frac{Q_g}{P_s} = 0.852 \cdot \text{hr}$$

So it would take ~ 2 KW and ~ 1 hr to heat the balloon volume to provide a payload capacity about 129 kg lower than the hydrogen-base balloon. As we will see later in this Section, a H_2 balloon can take less than half the time to inflate.

5.3 Comparison of Different Balloon Types

The performance of the baseline design is now compared against that of several alternatives, including the consensus Montgolfier design option. It is important to note that one specific application may be better suited than other based on operational and technical assumptions, just as much as on the comparisons to be highlighted (i.e., what is important to the designer). For a Titan balloon mission, it is believed that the buoyant gas alternative has been pitched against unfavorable design guidelines or assumptions. The flip-side will be presented to ensure a balance of engineering, risk, and technology.

5.3.1 Super Pressure Hydrogen versus Montgolfier Balloons

Figure 5-1 shows a comparison of Super-Pressure (SP) Hydrogen (700 bar) and Montgolfier balloons at different superheat temperatures. As can be seen, the SP H_2 balloon comes ahead in payload carrying capability for a given envelope. At the 31K superheat temperature, the Montgolfier volume would have to be about 4 times larger ($\sim 193 \text{ m}^3$) than the H_2 balloon for an equivalent payload capacity. This clear advantage is not to be under-estimated: a larger balloon envelope is considerably more likely to encounter deployment problems (tears, partial inflation, etc.), and is more likely to suffer adverse aerodynamic loading during its lifetime than a smaller balloon. In addition, the superheat required to achieve buoyancy at a larger envelope is not insignificant, and may represent a challenge in the maintenance of a sustained operational capability (avoid thermal losses, leaks, etc.).

Figure 5-2 compares the time required to inflate the balloon to its payload-carrying capacity. The SP H₂ balloon is ahead by at least half an hour. Again, this advantage should not be under-estimated, as the longer time to inflate, the longer the loose material will be exposed to aerodynamic loading and possible tear. A more detailed discussion will be given later in this respect.

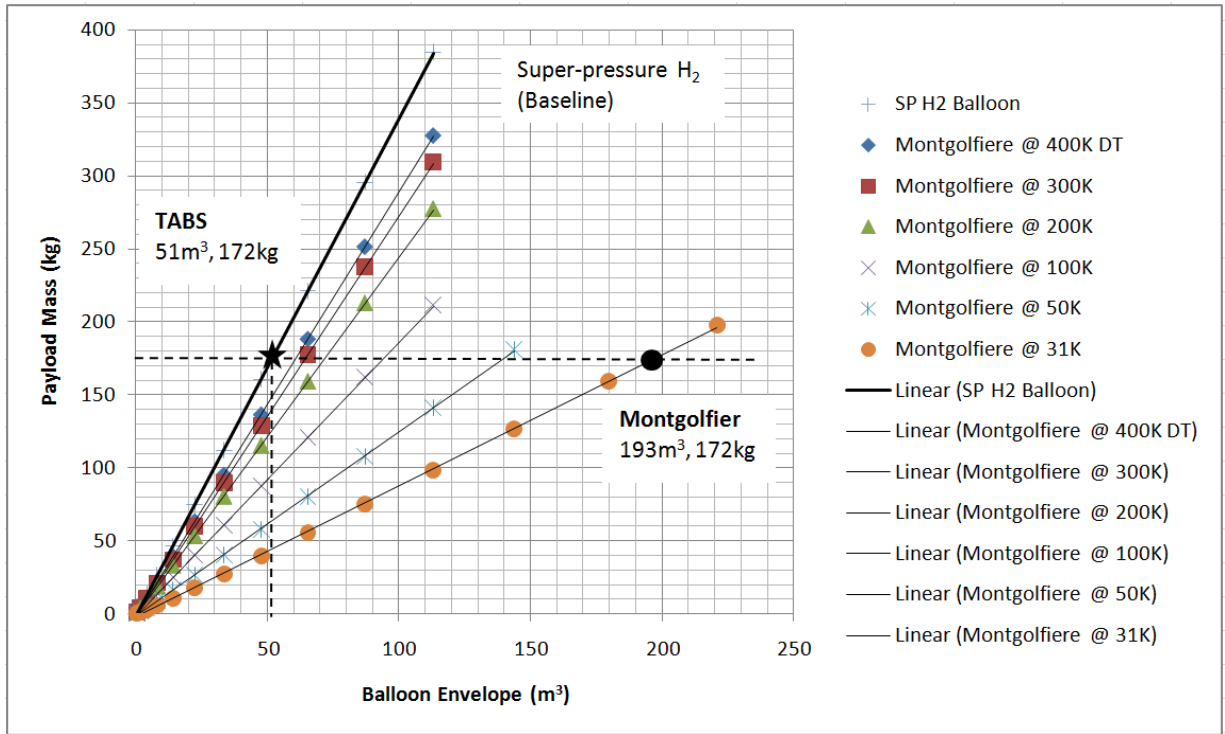


Figure 5-1: Comparison of TABS balloon design baseline and Montgolfier at several superheat temperatures show a clear advantage in payload carrying capacity for a given balloon envelope

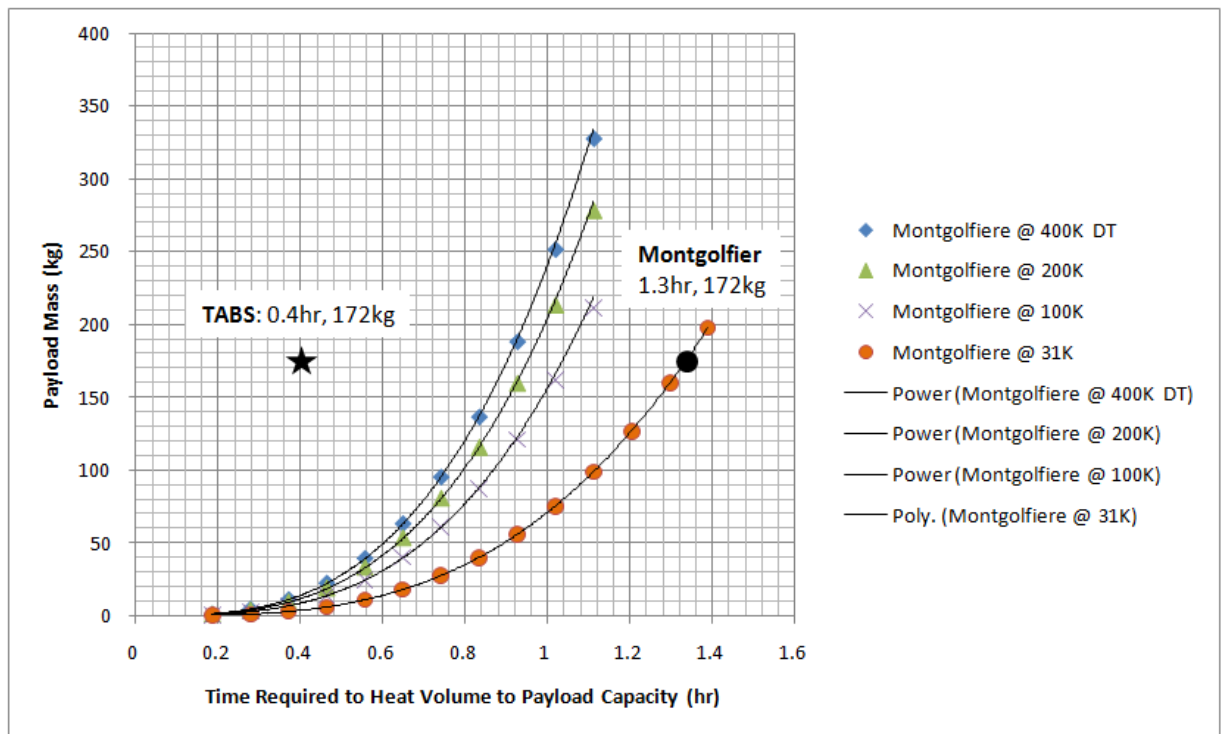


Figure 5-2: Comparison of time required to inflate balloon envelope to payload-carrying capacity, about 1.3 hrs for 31K superheat

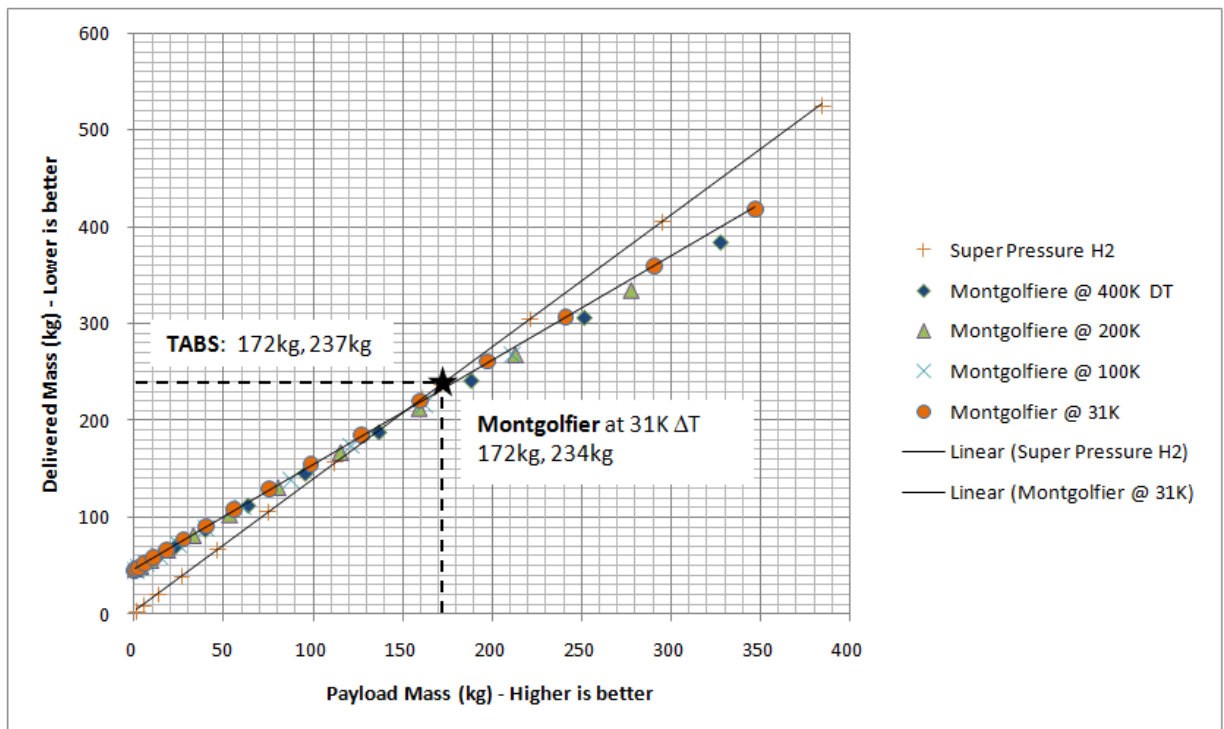


Figure 5-3: SP H₂ mass efficiency is about the same as a Montgolfier @ 31K ΔT

Figure 5-3 compares the delivered mass versus the payload mass for the different balloon choices. The most efficient system would maximize the payload mass, and minimize the delivered mass to the floating altitude. For the SP H₂ gas case, the delivered mass includes the mass of the gas, balloon, tank, and payload. For the Montgolfier case, the delivered mass includes the mass of the balloon, MMRTG, and payload. As can be seen, superheat Montgolfier balloons at 100K or above prove slightly more efficient (by 15kg) for the desired payload mass. However, for a Montgolfier at 31K the difference is insignificant (3kg). The small increase in efficiency at this payload level does not justify the relatively large balloon envelopes required. Nor it justifies the rather complex and risk-prone deployment sequence, where an MMRTG must be inserted into the balloon envelope through a complicated scheme of line ties and cables.

The advantage of Montgolfiers becomes more noticeable for relatively large payload masses, where the difference in delivered mass is larger (Figure 5-3). Another advantage often cited, is that there is no need to carry buoyant gas, and in principle such a balloon could operate indefinitely at Titan. Nonetheless, a system-level look at the overall mission, which must take into consideration not only longevity, but also the likelihood of mission success, begins to put into question whether a Montgolfier is the best approach for TABS. Smaller balloon envelopes, shorter inflation times, well understood technology with clear deployment and operational approaches, and adequate payload mass delivery, all coalesce into favoring a SP H₂ approach. The rest of this dissertation will be dedicated to establishing feasibility of a H₂-based balloon mission to Titan. And along the way, new capabilities will be demonstrated. But first, a comparison of Hydrogen versus Helium balloons is in order.

5.3.2 Super Pressure Hydrogen versus Helium Balloons

The advantages of a Hydrogen versus a Helium (He) balloon are shown in Figures 5-4 and 5-5. Super pressure (700 bar) and operating conditions at Titan are identical in both cases. Figure 5-4 shows that there is about a 20 kg payload advantage for a 51m³ H₂ balloon over an equivalent He balloon. Figure 5-5 shows about a 30 kg delivered mass advantage for H₂ over He. On both counts, the efficiency of H₂ translates into important advantages for a given payload carrying capacity, in particular for tank mass (~6.5kg), and gas mass (~23.1kg).

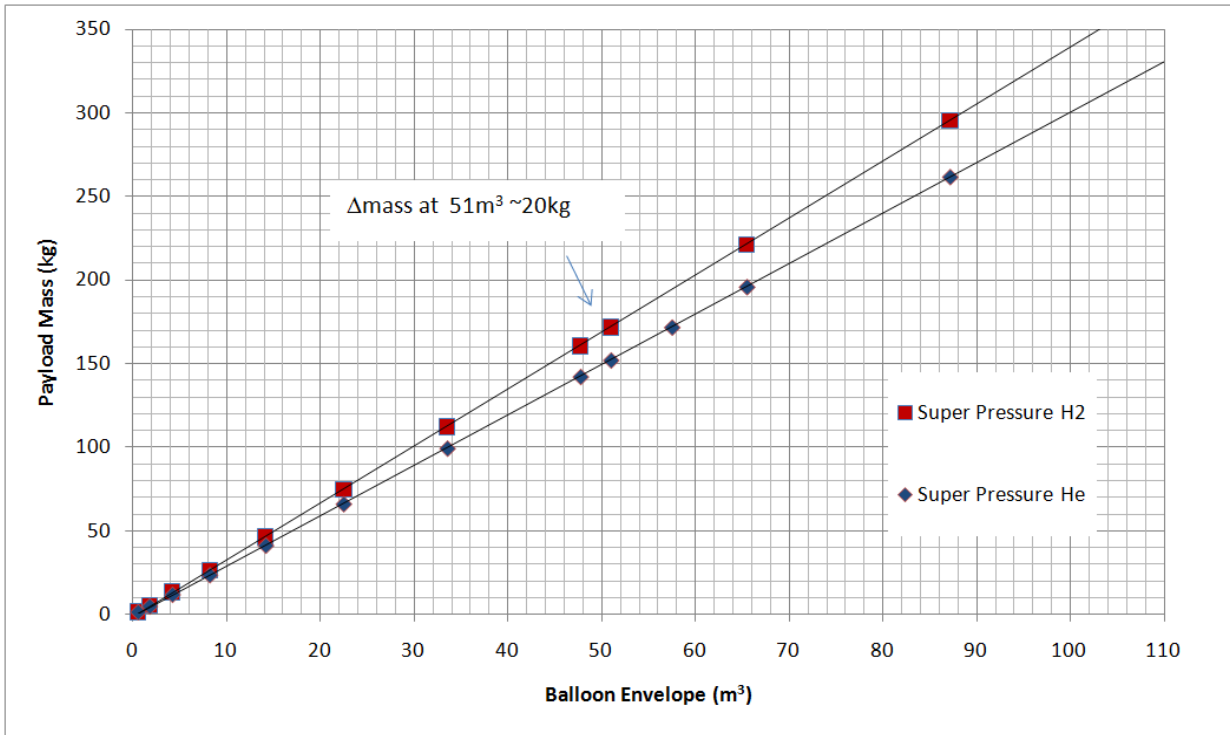


Figure 5-4: Comparison of payload carrying capacity versus balloon envelope for H₂ and He balloons.

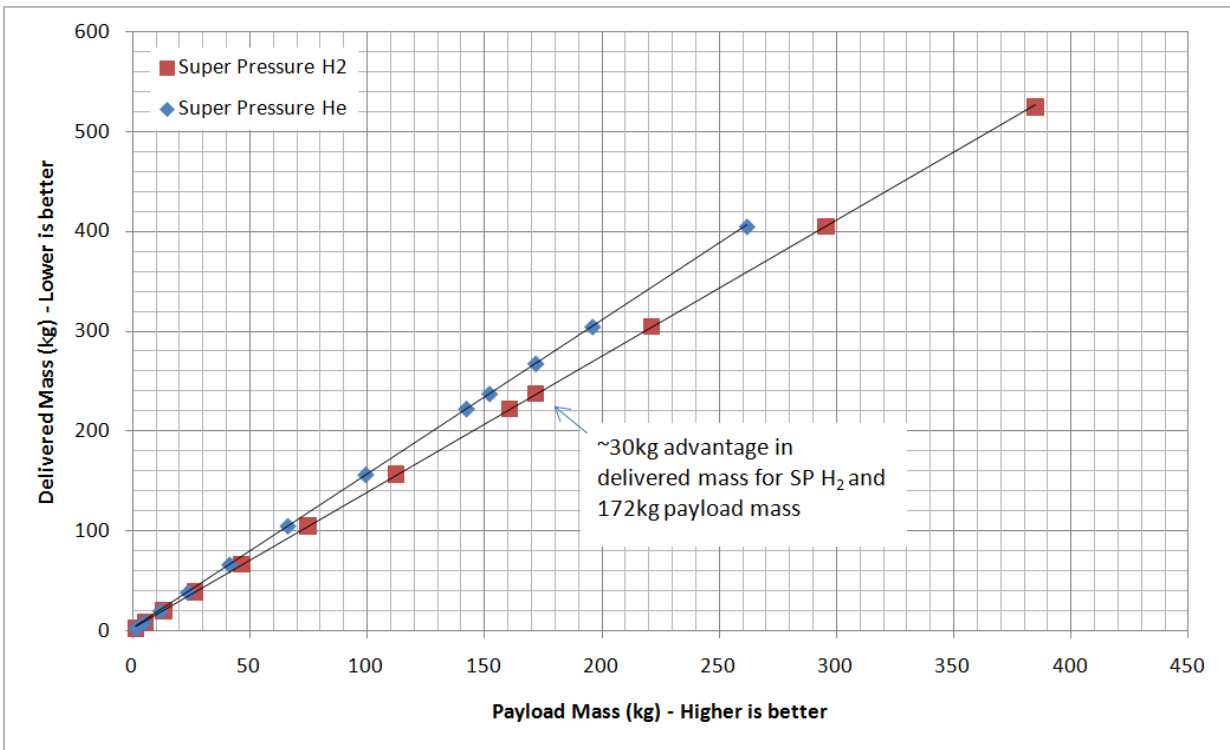


Figure 5-5: SP H₂ mass efficiency over He proves enabling for TABS

These differences proved to be enabling from a tank and spacecraft packaging perspective. Literally, the overall entry vehicle dimension and mass scale largely with the volume required to hold buoyant gas in both primary and auxiliary tanks (Section 5.2). Safety measures resulting from the use of the reactive H₂ as opposed to the inert He gas are not reason enough to preclude its use. In addition, vapor barriers and leakage concerns can be effectively managed, and again do not preclude the use of the more efficient buoyant solution for TABS. The tank mass and flow rates used to inflate the chosen balloon are shown next.

5.4 TABS H₂ Tank Sizing

We must now size the primary and auxiliary tanks required to hold the given amount of Hydrogen ¹⁵. Tank mass is one of the single most challenging factors in executing a balloon mission to Titan in this manner. Although Hydrogen gas could be manufactured in-situ through decomposition of CH₄ (Methane) ¹², such technology is currently at low readiness levels. In addition, initial balloon deployment is not possible unless gas is carried within tanks, as Hydrogen production would be better suited for replenishment, rather than inflation. Spherical and toroidal tanks were examined. A toroidal tank resulted in a most efficient use of space within the entry probe, and hence is used as the baseline.

5.4.1 Primary Spherical Tank Sizing

The tank pressure is chosen based on recent work done through the US Department of Energy in the manufacturing and test of low-cost, high-efficiency, high-pressure Hydrogen storage systems for automobiles ¹⁶. From the combined gas law, we can compute the volume of Hydrogen under pressure inside of a storage tank. Since $P_1 V_1 / T_1 = P_2 V_2 / T_2$, then

Gas temperature, pressure, and volume at operational altitude in Titan

$$P_1 := P_a + \Delta P$$

$$V_1 := V_g$$

$$T_1 := T_a$$

Temperature and pressure within the H₂ tank.

$$T_2 := 293\text{K}$$

$$P_2 := 700\text{bar}$$

Required H₂ tank volume

$$V_2 := \frac{P_1 \cdot V_1}{T_1} \cdot \frac{T_2}{P_2} = 229.026\text{L}$$

First, we assume the tank is made entirely of Ti-5Al-2.5Sn, a Titanium alloy suitable for low-temperature applications ¹⁷. Material properties are

$$F_{tu} := 847962000\text{Pa} \quad \text{ultimate strength of the material, or allowable strength}$$

$$\rho_{mat} := 4484.16 \frac{\text{kg}}{\text{m}^3} \quad \text{density}$$

The structure design burst pressure (p_b) is the Maximum Expected Operating Pressure (MEOP) times a factor of safety (2.0 typical for pressure vessels). Hence, for a 700 bar MEOP,

$$p_b := 2 \cdot P_2 = 1.4 \times 10^3 \cdot \text{bar}$$

The **radius of a spherical tank** is computed from the gas volume at the MEOP, P_2 .

$$r_s := \sqrt[3]{\frac{3}{4 \cdot \pi} \cdot V_2} \quad r_s = 0.38\text{m} \quad \text{inner tank radius}$$

Hence the wall thickness is

$$t_s := \frac{p_b \cdot r_s}{2 \cdot F_{tu}} = 0.031\text{m}$$

And the tank mass is

$$m_s := 4 \cdot \pi \cdot r_s^2 \cdot t_s \cdot \rho_{\text{mat}} = 254.337 \text{ kg}$$

The resulting tank mass fraction is then

$$\frac{m_s}{M_g} = 38.646$$

As can be seen from this analysis, a high-strength material like Ti is not mass-efficient for this application. In order to provide a better solution, the structural material is changed from Titanium to Graphite. In particular, we use Epoxy/Graphite HM (high modulus), with UD (Uni-directional) tape properties (Ref: 18, p. 3-6).

The ultimate strength and density of such material are (the subscript letter "g" is added to the variable name subscripts above to indicate "graphite" as the structural material)

$$F_{\text{tug}} := 1585620000 \text{ Pa} \quad \rho_{\text{matg}} := 1577.76 \frac{\text{kg}}{\text{m}^3} \quad (\text{or } 230 \text{ ksi, and } 0.057 \text{ lb/in}^3)$$

The resulting thickness is

$$t_{\text{sg}} := \frac{p_b \cdot r_s}{2 \cdot F_{\text{tug}}} = 0.017 \text{ m}$$

And tank mass

$$m_{\text{sg}} := 4 \cdot \pi \cdot r_s^2 \cdot t_{\text{sg}} \cdot \rho_{\text{matg}} = 47.857 \text{ kg}$$

A much more mass-efficient result. Now if we use a composite overwrapped pressure vessel (COPV), an use titanium as the liner, and graphite as the overwrap, then the mass would be somewhat higher. The titanium liner is now non-structural, and is used as a vapor/pressure barrier. We compute the mass by assuming a Titanium liner of 0.051 cm¹⁹, and volume V2.

$$t_l := 0.051 \text{ cm} \quad \text{defined thickness of Titanium liner}$$

$$m_l := 4 \cdot \pi \cdot r_s^2 \cdot t_l \cdot \rho_{\text{mat}} = 4.14 \text{ kg} \quad \text{mass of liner tank}$$

Hence,

$$M_{\text{COPV}} := m_l + m_{\text{sg}} = 51.997 \text{ kg}$$

Is the result of a spherical COPV tank. The thickness of the (structural) graphite overwrap is

$$t_{\text{sg}} = 1.676 \cdot \text{cm}$$

The outer tank radius is then,

$$r_s + t_l + t_{\text{sg}} = 0.397 \text{ m}$$

Tankage mass fraction is

$$\frac{M_{\text{COPV}}}{M_g} = 7.901$$

If we were to use three spherical tanks instead rather than one, then each tank would have to hold 1/3 the volume at MEOP, and the resulting mass of each tank would be 17.9 kg, the outer radius 0.275 m, and the tankage mass fraction for each tank about 8.2. The combined tank mass would be 53.8 kg. Due to packaging constraints and the need to fit all components, including the tanks, within a reasonably sized aeroshell, other alternatives for tank geometry had to be explored. In fact, the spacecraft size resulting from the use of three spherical tanks was ~ 3m diameter x 2m high, and this was deemed too large for the application. The result using cylindrical rather than spherical tanks was no better. Assuming that both ends of each of three cylindrical tanks were hemispherical, the tank end radius was 0.19 m (0.38 m thick), and the overall tank length was 0.8 m.

5.4.2 Primary Toroidal Tank Sizing

The concurrent TABS structure and aeroshell design indicated that reduction in tank size along the axial direction was critical in overall system mass. To accomplish this reduction, multiple spherical and cylindrical tank geometries were explored. Nonetheless, the most effective way of reducing this axial dimension was by using a toroidal tank design instead. To illustrate this point, Table 5-1 compares this dimension for spherical versus toroidal tanks. Even when the the sphere volume is split by four, the toroidal tank axial dimension still comes ahead. The slightly larger toroid diameter is by far outweighed by the axial height advantage (the tank size design evolution is shown later in Figure 11-1, whereas the baseline is detailed in Figure 6-5).

Table 5-1: Axial height comparison for spherical versus toroidal tanks

	R (m)	r (m)	V (m ³)	A (m ²)	Diameter (m)	Axial Height (m)
Toroid	0.413	0.168	0.23009	2.739171	1.162	0.336
Sphere	0.38		0.229847	1.814584	0.760	0.76
Sphere/3	0.263		0.076616		0.527	0.527
Sphere/4	0.239		0.057462		0.479	0.479

Since the axial size is fixed by the toroid radius, r, we set a convenient number that fits within the TABS entry probe layout, and size the toroidal tank from it.

$R_{tor} := 0.413m$ define input for overall toroid dimension. R_{tor} is the toroid characteristic radius.

$$r_{tor} := \sqrt{\frac{V_2}{2 \cdot \pi^2 \cdot R_{tor}}} = 0.168m \quad \text{where } V_2 \text{ is the volume at MEOP, and } r_{tor} \text{ is the toroid cross-section radius. This determines the vertical size}$$

The Titanium tank mass is then

$$m_{t3} := 4 \cdot \pi^2 \cdot R_{tor} \cdot r_{tor} \cdot t_t \cdot \rho_{mat} = 6.25 \text{ kg}$$

The Graphite tank is

$$t_{sg3} := \frac{P_b \cdot r_{tor}}{F_{tug}} = 0.015m \quad \text{is the thickness of the (structural) graphite overwrap}$$

$$m_{sg3} := 4 \cdot \pi^2 \cdot R_{tor} \cdot r_{tor} \cdot t_{sg3} \cdot \rho_{matg} = 63.809 \text{ kg} \quad \text{is the overwrap tank mass}$$

The total mass of the COPV toroidal tank is then

$$M_{COPV3} := m_{t3} + m_{sg3} = 70.059 \text{ kg}$$

and the tankage mass fraction

$$\frac{M_{\text{COPV3}}}{M_g} = 10.645$$

The tank Outer Radius and axial height are

$$\text{OR3} := r_{\text{tor}} + t_1 + t_{\text{sg3}} = 0.183 \text{ m}$$

$$2 \cdot \text{OR3} = 0.366 \text{ m}$$

Although this particular design results in about 20 kg of additional tank mass, the axial size is reduced by about 19 cm, a desirable result from a flight dynamic and packaging perspective. Effectively, the probe center of mass moves closer to the front, and the overall aeroshell (and vehicle) size is reduced, with the ensuing mass benefit. This is TABS baseline choice.

5.4.3 Auxiliary Toroidal Tank Sizing

The same analysis that yielded the best geometry for the primary tank also resulted in a toroidal auxiliary tank. This tank is sized next. Although a H₂ generation system is clearly an option for providing gas replenishment, an auxiliary tank proves a near-term (albeit non-exclusive) solution.

The required tank volume for a given gas mass at room temperature and compressed pressure is again obtained from the ideal gas law,

$$V_{\text{taux}} := \frac{m_{\text{gaux}}}{\mu_g} \cdot \frac{R_c \cdot T_2}{P_2} = 0.065 \cdot \text{m}^3 \quad T_2 = 293 \text{ K} \quad P_2 = 700 \cdot \text{bar}$$

The auxiliary tank dimension is obtained from the concurrent structure design, and is chosen to fit the available TABS volume. Hence,

$$R_{\text{tora}} := 0.63 \text{ m} \quad \text{define } \mathbf{input} \text{ from TABS envelope sizing.}$$

$$r_{\text{tora}} := \sqrt{\frac{V_{\text{taux}}}{2 \cdot \pi^2 \cdot R_{\text{tora}}}} = 0.072 \text{ m} \quad \text{where } V_{\text{taux}} \text{ is the volume at MEOP, and } R_{\text{tora}} \text{ is the toroid characteristic radius.}$$

The Titanium tank mass is

$$m_{\text{l4}} := 4 \cdot \pi^2 \cdot R_{\text{tora}} \cdot r_{\text{tora}} \cdot t_1 \cdot \rho_{\text{mat}} = 4.122 \text{ kg}$$

The Graphite tank is

$$t_{\text{sg4}} := \frac{P_b \cdot r_{\text{tora}}}{2F_{\text{tug}}} = 3.2 \times 10^{-3} \text{ m} \quad \text{is the thickness of the (structural) graphite overwrap}$$

$$m_{\text{sg4}} := 4 \cdot \pi^2 \cdot R_{\text{tora}} \cdot r_{\text{tora}} \cdot t_{\text{sg4}} \cdot \rho_{\text{matg}} = 9.1 \text{ kg} \quad \text{graphite tank mass}$$

The mass of the composite overwrapped auxiliary pressure vessel is then

$$M_{\text{COPV4}} := m_{\text{l4}} + m_{\text{sg4}} = 13.223 \text{ kg}$$

and the tankage mass fraction

$$\frac{M_{\text{COPV4}}}{m_{\text{gaux}}} = 7.044$$

The tank Outer Radius and diameter are

$$OR4 := r_{\text{tora}} + t_1 + t_{\text{sg}4} = 0.076 \text{ m}$$

$$2 \cdot OR4 = 0.152 \text{ m}$$

These numbers are used in the structure layout and system mass budget.

5.5 Tank Gas Flow Rate and Balloon Inflation Time

A key parameter in the estimation of balloon inflation time is obviously the rate of gas flow from the tanks. The choice of this variable depends on a number of factors. First, as the balloon inflates, its material will be re-arranged and expanded to fit-in the flowing gas. The gas should enter the envelope slowly to allow for this material expansion to occur in an orderly fashion, and prevent creases from acting as localized stress knots that can damage the balloon wall material. This flow rate in turn is controlled by the size of the pipe through which the gas flows. Since the gas is to flow out of the tank only once at a set initial velocity, there is no need to provide for gas "throttling", i.e., a "control valve" is not required. Hence, the pipe sizing itself will determine the valve size. The valve's job is simply to fully open and close. In fact, this is expected to happen at least twice: once during fill, and last during drain. Nonetheless, testing will require multiple fill/drain cycles prior to launch.

If nothing is done to force the gas from the tank to the balloon envelope, the flow rate will start at some nominal value and decrease to zero once equilibrium is reached at some ambient pressure. At equilibrium, the H_2 gas pressure in the balloon is equal to that in the tank. If full inflation occurs at an altitude greater than the nominal 10km, then the residual gas in the tanks will be small enough that no active pumping or bladder will be required. The remaining gas in the tanks will be treated as "ullage". To prevent gas from re-entering the tanks at lower altitudes (higher atmospheric pressure), the tanks will need to be outfitted with one-directional valves. Since the balloon is super-pressure at its operating altitude, to be safe we require inflation to occur by an altitude equivalent to $1/2P_a$, or ~23km.

$$\frac{1}{2} \cdot P_a = 4.42 \times 10^4 \text{ Pa} \quad @ \sim 23 \text{ km altitude}$$

Since,

$$V_2 = 229.026 \text{ L} \quad \text{Tank Volume, and} \quad V_g = 5.097 \times 10^4 \text{ L} \quad \text{is the balloon volume at operating pressure and temperature (10km)}$$

The remaining total *ullage* is at most

$$\frac{V_2}{V_g} = 0.449\%$$

of the balloon envelope, a small enough value that can be ignored in preliminary sizing of the tank.

The mass flow rate through a pipe can be estimated from the Bernoulli equation using mass conservation, compressible fluid, zero viscosity, and assuming circular pipe geometry²⁰. First from the ideal gas law we obtain the density of Hydrogen at the initial tank pressure, and assume the pressure at the balloon envelope to be the final desired pressure of $P_a + \Delta P$.

$$P_0 := P_2 \quad \text{initial pressure} \quad P_f := P_a + \Delta P \quad \text{final total pressure}$$

$$\rho_i := \frac{P_0}{R_c \cdot T_a} \cdot \mu_g = 100.233 \frac{\text{kg}}{\text{m}^3} \quad H_2 \text{ density inside tank}$$

$$\rho_f := \frac{P_f}{R_c \cdot T_a} \cdot \mu_g = 0.129 \frac{\text{kg}}{\text{m}^3} \quad H_2 \text{ density in balloon envelope}$$

$$D_i := 2 \cdot r_{\text{tor}} = 0.335 \text{ m} \quad \text{is the tank's inner diameter}$$

The pipe's diameter is iterated to obtain the desired mass flow rate and inflation time. Hence,

$$d_p := 0.15 \text{ cm} \quad \text{It is the pipe's diameter (input).}$$

An initial estimate of the mass flow rate is then,

$$Q_{m0} := \sqrt{\frac{1}{\frac{\rho_i}{\rho_f} - \frac{d_p}{D_i}} \cdot \frac{\pi}{4} \cdot d_p^2 \cdot \sqrt{2 \cdot (P_0 - P_f)} \cdot \rho_i} = 7.509 \times 10^{-3} \frac{\text{kg}}{\text{s}}$$

The *time to inflate* is given by

$$t_{\text{full}} := \frac{M_g}{Q_{m0}} = 14.608 \cdot \text{min}$$

So the tank will "bleed" gas through a very small hole. The total time can be better estimated by a series of decremental pressure steps, from initial pressure to final pressure.

$$P_0 = 700 \cdot \text{bar} \quad P_f = 0.902 \cdot \text{bar} \quad \text{Incr} := 1 \text{ bar}$$

$$N_t := \frac{P_0 - P_f}{\text{Incr}} \quad N_t = 699.098 \quad i := 0..N_t$$

$$P(i) := P_0 - i \cdot \text{Incr} \quad P(0) = 700 \cdot \text{bar} \quad P(N_t) = 0.902 \cdot \text{bar}$$

$$\rho(i) := \frac{P(i)}{R_c \cdot T_a} \cdot \mu_g$$

$$Q_m(i) := \sqrt{\frac{1}{\frac{\rho(i)}{\rho(i+1)} - \frac{d_p}{D_i}} \cdot \frac{\pi}{4} \cdot d_p^2 \cdot \sqrt{2 \cdot (P(i) - P(i+1))} \cdot \rho(i)}$$

Where the last vector needs to be ignored, since it corresponds to an out-of-bound P_f , i.e., $P(N_t+1)$ is undefined.

The *first 1/3* flow rate is (close to Q_{m0} , since the initial flow is dominant as the pressure gradient is greatest)

$$Q_0 := \sum_{i=0}^{232} \frac{Q_m(i)}{232} = 7.256 \times 10^{-3} \frac{\text{kg}}{\text{s}}$$

The *middle 1/3* flow rate (close to the mean) is

$$Q_1 := \sum_{i=232}^{464} \frac{Q_m(i)}{232} = 5.613 \times 10^{-3} \frac{\text{kg}}{\text{s}}$$

As comparison, the mean flow rate is

$$\sum_{i=0}^{698} \frac{Q_m(i)}{698} = 5.296 \times 10^{-3} \frac{\text{kg}}{\text{s}}$$

The *final 1/3* flow rate is

$$Q_f := \sum_{i=464}^{696} \frac{Q_m(i)}{232} = 3.109 \times 10^{-3} \frac{\text{kg}}{\text{s}}$$

The total time to inflation computed in this manner can then range from

$$t_{0t} := \frac{M_g}{3} = 5.039 \cdot \text{min} \quad t_{1t} := \frac{M_g}{Q_1} = 6.514 \cdot \text{min} \quad t_{ft} := \frac{M_g}{Q_f} = 11.76 \cdot \text{min}$$

where we use 1/3 of total mass for each flow rate, even if this is not to be the case: the mass remaining in the tank would decrease faster first, and slow down with lower flow rates. Assuming the final inflation time to be equal to the sum of these values, we get

$$t_{bi} := t_{0t} + t_{1t} + t_{ft} = 23.312 \cdot \text{min}$$

The lower the differential pressure and flow rate, the longer it takes for the remaining gas to flow. This is an obvious result. What is not obvious is that in the limit, this time can be exceedingly large if active pumping is not used, either through a bladder or mechanical pump, in spite of the previous reasoning. A pump and bladder system will then be used for redundancy, and must be accommodated in the tank mass estimates. A second alternative is to use a fairly large pipe, but then inflation control and dynamic issues as described above can be encountered. Yet a third approach is to actually have a control valve, that starts the flow of hydrogen through a narrow opening as given above, but then opens to a large enough opening to provide better gas evacuation at lower differential pressure.

This last approach could also eliminate the need for a bladder or pump, but adds a control valve system. Redundancy would still be required to ensure all the gas is injected into the envelope in a reasonable amount of time. A combination of bladder, pump, and control valve would result in a triple-redundant system. Either dual-redundant system would be acceptable, and the simplest combination may be a bladder plus control valve. Figure 5-6 shows the progression of flow rate with differential pressure changes, without assisted evacuation. The flow rate decreases asymptotically as the pressure approaches zero.

Since the formula used provides only a theoretical estimate of fluid flow and does not take into consideration turbulent flow or thermo-dynamical energy conservation, it should be used with caution, and only to bound a possible flow rate. What we see is that the flow opening needs to be small first. We also see that the time required to inflate the balloon can be conservatively constrained to be within half an hour or so, if some means of extracting the final bit of gas is used. *If we size the main parachute to allow for about t_{bi} minutes of flotation time prior to balloon inflation at 23 km or above, then the system will be reasonably designed.*

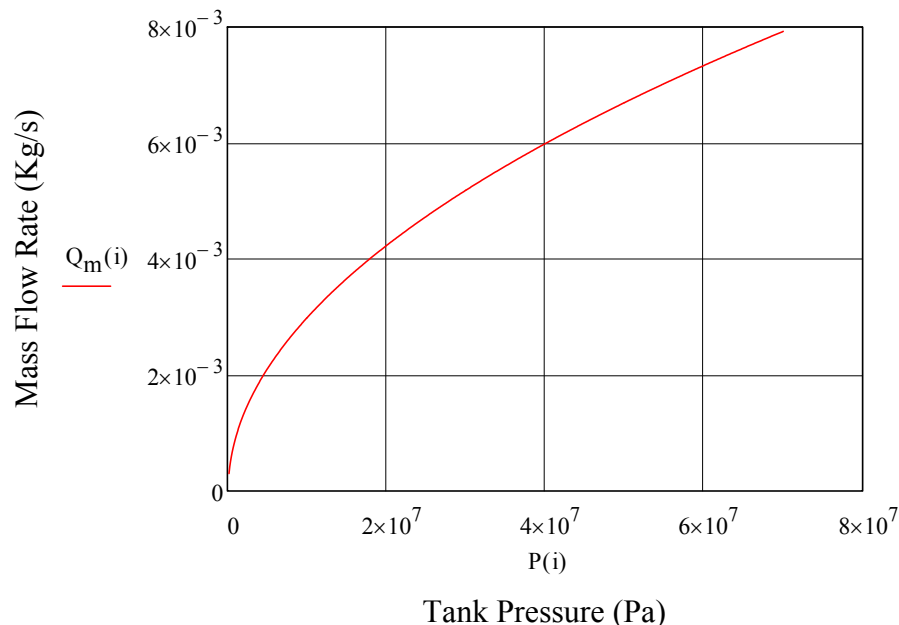


Figure 5-6: Mass flow rate decreases asymptotically as differential pressure approaches zero

6.0 Entry Probe

The entry probe conceptual layout is one of the most important and challenging elements of the mission design. It includes instrument volume accommodation, as well as packaging of buoyant system elements (tanks, balloon, support subsystems, etc.). At this stage of mission formulation, it is only sufficient however to demonstrate feasibility, i.e., the ability to fit all major elements within a reasonably sized vehicle. A detailed analysis of the structure and its dynamics is beyond the scope of this work. Nonetheless, the design considers mass balance, aerodynamic center of pressure, and center of mass as basic inputs from the outset. Symmetry is an over-arching objective, and the structure and probe layout as given provide a good starting point for more detailed analysis. Several layouts were tried out. Ultimately, the configuration that was selected presents the best measure in mass, size, and aerodynamic form. Some of these properties are shown numerically, others are inferred qualitatively.

In order to properly size the structure, the properties of a few major elements have to be determined. These include the science instrument volume, tank volume, and high-gain antenna size. These major components ultimately determine the overall size and exact geometry of the aeroshell (iteratively with aerothermodynamic computation results). In the following sections, properties of these major elements are estimated. The tank size was already defined in Section 5.

6.1 Instrument Platform

The basic TABS size was derived from the volume and instrument footprint area allocations given in Reference 5 for the TSSM in-situ probe instrument suite. No attempt was made to select any other science payload allocations, as it is believed that much thought had been given in the lengthy ESA study. Figure 6-1 defines the design envelope in question for both the TSSM in-situ probe and TABS. Although the TABS payload envelope is slightly smaller (due to a sharper-angled aeroshell), its footprint is correspondingly larger. In fact, instrument footprint was the initial design target for TABS sizing. The instrument volume is defined as the space within the payload thermal shield below the mounting plate (shown in pink/dark shading for both cases in Figure 6-1). Additional instrumentation would also be located above the mounting plate, some of it exposed to the environment by necessity (e.g., temperature, wind speed, magnetometer, antennae), some locally shielded from the extreme cold (e.g., antenna electronics).

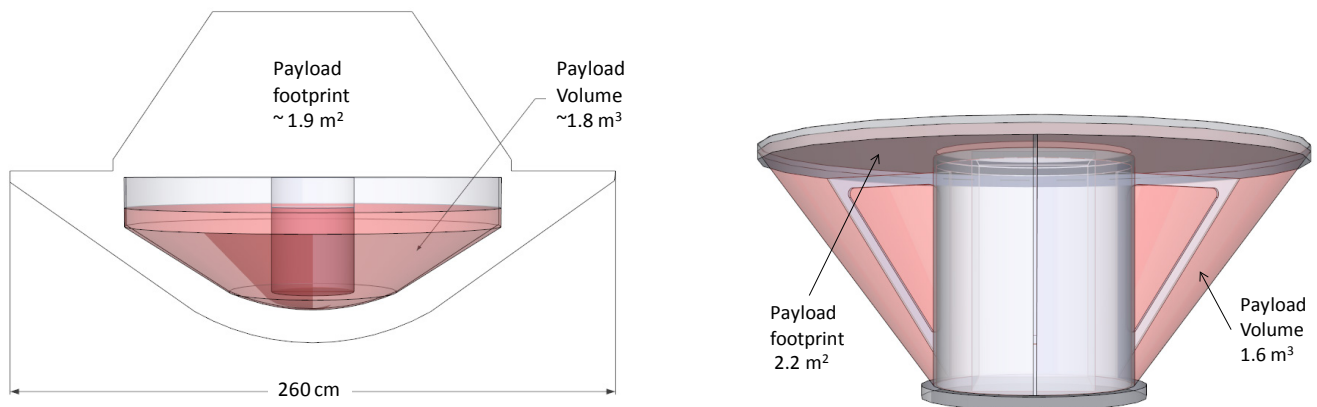


Figure 6-1: The TSSM in-situ probe instrument area and volume allocations (left), and the corresponding allocations in TABS (right). Pictures are not scaled equal.

6.2 High Gain Antenna

The High Gain Antenna (HGA) needs to provide enough downlink capability to return a sufficient amount of science data. The link analysis in Section 4 has shown that a 1-meter parabolic dish is sufficient to cover the science data needs. What remains is consideration of the antenna operating environment and mechanical concept design. Given that the HGA will be operated in an exposed area, it is important to ensure there is a minimum of deploying mechanisms, which points to an antenna of monolithic construction. In addition, composite material is used in order to minimize mass and reduce heat losses, as the antenna must interface mechanically (and electrically) to the thermally insulated structure and area of the gondola.

As the antenna faces back within the entry vehicle, and is located in the rear-half of the entry probe “below” the packaged balloon and decelerator systems, the larger its dimension along the vehicle’s longitudinal axis, the further the center of mass is shifted aft. The desire to shift the center of mass forward however, necessitates the use of a focal point deployment mechanism. In this arrangement the antenna focal point structure is pre-loaded and held against the top rim of the dish by the (main) gas tank base plate, compressing the antenna axial size and hence reducing the overall longitudinal dimension of the aft section of the probe (the rear-half of the probe is shown later in Figure 6-5).

A steerable antenna is also a requirement to ensure the most favorable link margin during DTE downlink periods. Therefore an alt-azimuth mechanism is thermally protected and covered by Multi-Layer Insulation (MLI). The 1-meter antenna and key parameters are shown in Figure 6-2, in deployed and stowed configurations. Since the focal point distance is inversely proportional to the dish depth, it is desirable to minimize the shell material (smallest depth), while maintaining a reasonable focal point distance. The combination of parameters yields a depth of 17cm, and a focal point distance of 36.8cm.

Parabolic Dish: Diameter = 100cm; Focal Point = 36.8cm; Depth = 17cm



Figure 6-2: 1-meter parabolic dish in deployed and stowed configurations

6.3 Aeroshell Geometry and Size

Once the payload volume, antenna size, and tank volume had been established, and a reasonable solution found, the overall aeroshell shape and dimensions needed to be defined. A search for past high-speed, ballistic-entry aeroshell designs was carried out, and several options explored. Ultimately, a sphere-cone was deemed the most appropriate design option, having been used in entry vehicles such as Galileo, Pioneer Venus, Stardust, Viking, Mars Pathfinder, and Huygens²³. These designs offer enough experimental data on performance, and lend themselves to analytical tools to estimate aero-thermodynamic properties. The actual sphere radius and cone angles were henceforth iteratively derived based on results from the aerothermodynamic computations: a balance of entry deceleration and heat loads. Such computations will be shown later on. Figure 6-3 shows TABS front shield geometry in comparison with Galileo’s²⁴. It features a medium semi-apex angle of 34.4°, and a spherical nose radius of 0.58m. With a diameter of 2.06m, the *bluntness ratio* (nose radius / diameter) is 0.28, similar to Galileo (0.176) and Mars Pathfinder (0.25). In fact, the front shield overall design geometry is similar to Galileo’s, which had a semi-apex angle of 44.85° (although TABS is about 1.6 times wider).

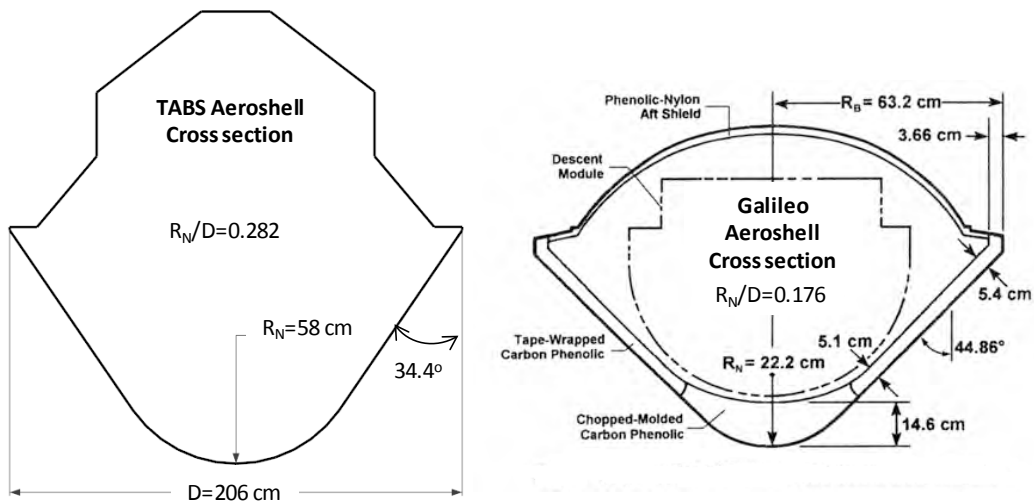


Figure 6-3: TABS and Galileo aeroshell cross-sections.

6.4 Payload Thermal Control

The ASRG is located centrally within the gondola. It provides not only electrical power to subsystems and instruments, but also the required heat to ensure components operate within their design envelope. Silica Aerogel may be used as an effective, extremely low-density insulating material. At least 20-layer MLI may also be used, with larger density and mass. With an assumed Silica Aerogel thermal conductivity of 0.03 W/mK²⁸, a heat source of about 554 W (ASRG and subsystems), an outside temperature of 84K, a surface area of 3.7 m², and an Aerogel thickness of about 4 cm, the inside of the gondola reaches thermal equilibrium at about 11.5°C. This result assumes the inside and outside wall temperatures are equal to the ambient temperatures, or “zero” convective resistance (obviously a simplification). Figure 6-4 shows the ASRG location within TABS central thrust cylinder and the “internal” temperatures for given insulation thickness.

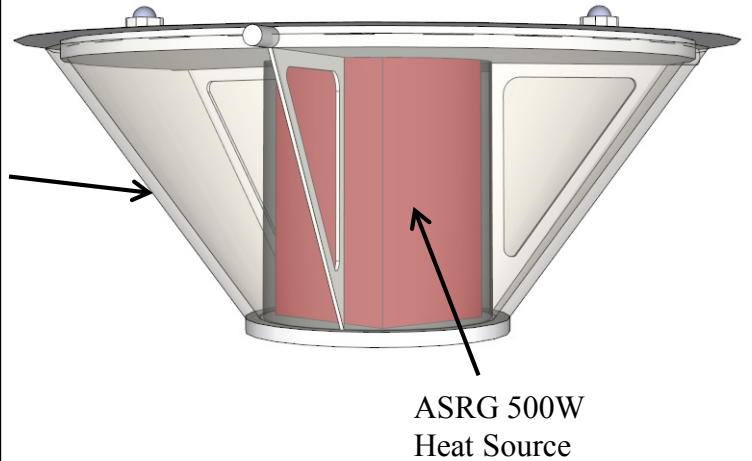
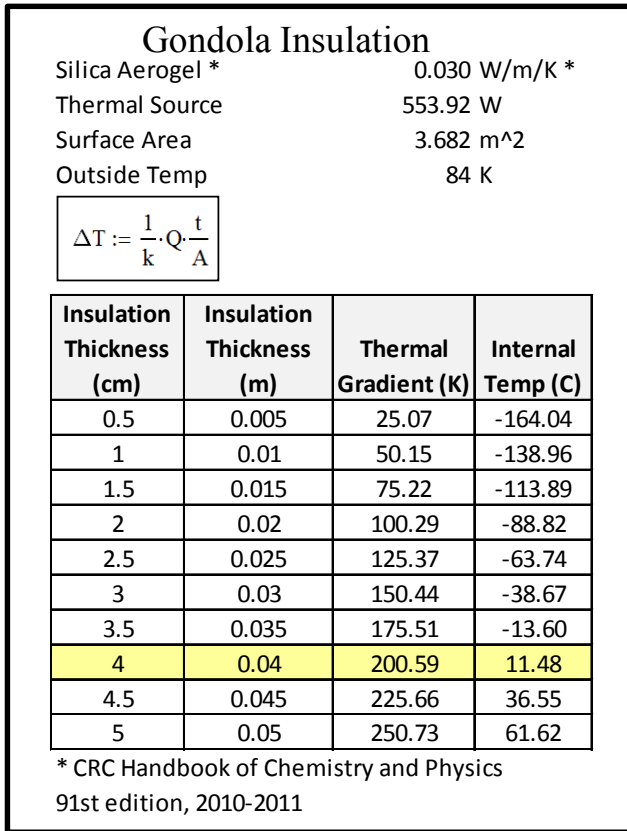


Figure 6-4: The ASRG provides enough heat to safely operate components

6.5 Aft Component Accommodation

The forward end of the TABS probe accommodates the gondola instruments and the power source. The aft end of the probe accommodates the H₂ tanks, antenna, balloon, and parachutes. They must be protected by the aft shell during entry. Accommodation of these components was not an easy task, and the ultimate design of the H₂ tanks was driven by the need to constrain the probe’s vertical size, and hence the overall aeroshell (Section 5). Figure 6-5 illustrates the aft shell and volume allocations for the several components. The structure surrounding the antenna is necessary to ensure the balloon material does not grab any part of the antenna either during launch/cruise or during deployment. The mesh is assumed to be made of RF transparent material, as it will remain with the gondola during normal operations. Allocations for the packaging of parachutes (computed later) will be compared against the volumes resulting from this layout.

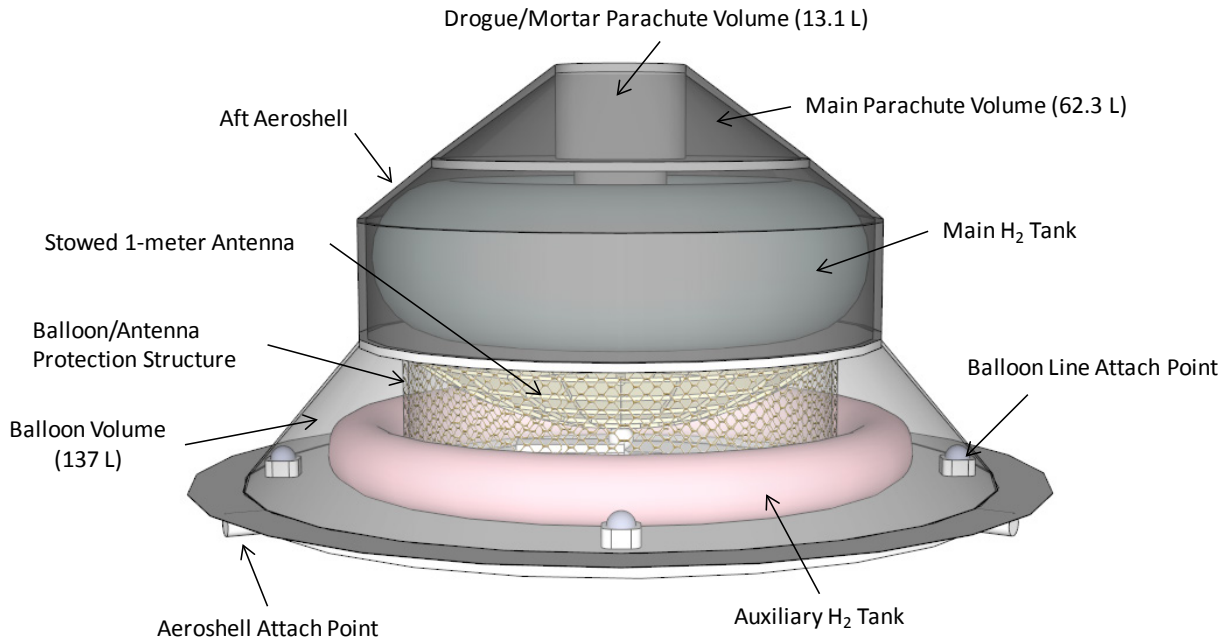


Figure 6-5: Aft Component Identification and Accommodation

6.6 Probe Layout and Overall Dimension

All the major components needed to constrain the size of the entry probe have been defined. The resulting probe configuration is shown in Figure 6-6. The aeroshell is composed of the front shell (FS), and aft shell (AS). The FS TPS material will be discussed at length later, as it is made of a newly developed carbon/Phenolic composite. The AS TPS material is made of heritage SLA-561 construction.

6.7 Vehicle Aerodynamic Stability Considerations

The entry vehicle is designed to have axial symmetry. As it spins on entry, it is also important to ensure spin-balanced component location. A detailed computational fluid dynamics analysis was beyond the scope of this work, and was also considered unnecessary at this stage of design. Rather, a simple determination of the Center of Pressure (CP) in relation to the Center of Gravity (CG) was undertaken. Given axial symmetry, it is only necessary to ensure the CP is as far aft of the CG as possible. The CP was derived from a determination of the geometric centroid. The CG is computed from the axis-symmetric distribution of TABS component masses. Figure 6-7 shows the CP and CG locations, as well as the location of the CG for the forward and aft mass distribution. The “stations” (STA) are defined such that STA=0 is located at the tip of the FS nose, and STA=2049 is located at the end of the AS (measured in millimeters). The important result is that the CG is located 366mm forward of the CP. Forward ballast was required to achieve this result. These 40.5 kg can either be “dead weight”, or effectively used to outfit the FS with scientific instruments and used as a “Lander”. Table 6-1 shows the mass distribution used in the CG estimation.

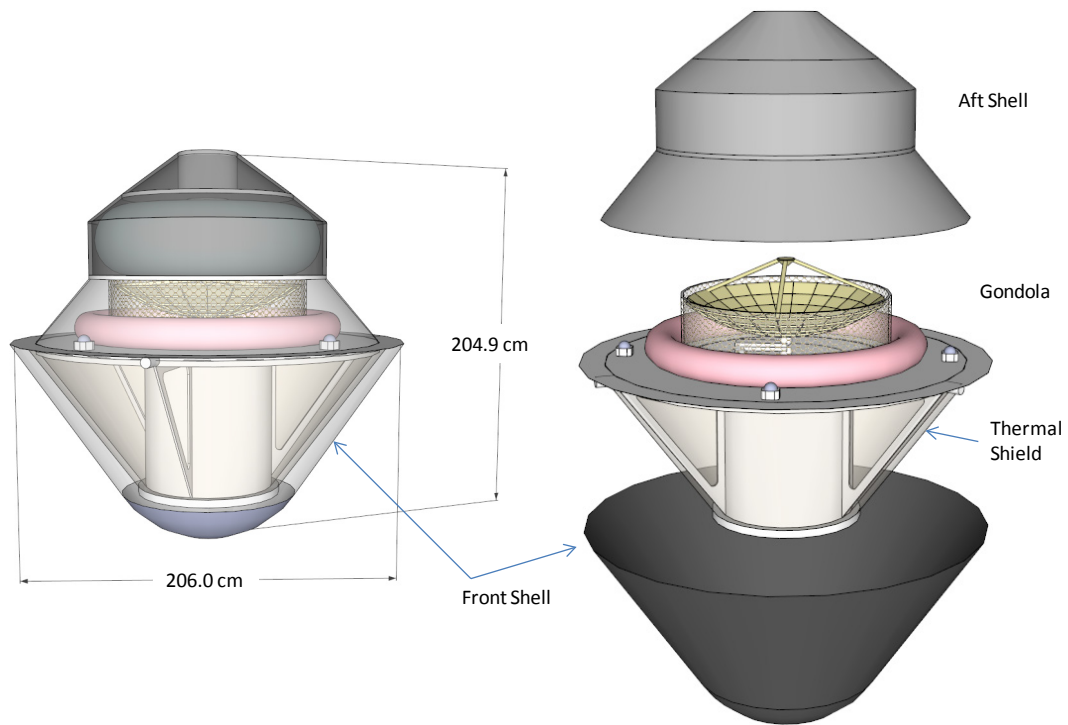


Figure 6-6: TABS entry probe, aeroshell, and gondola

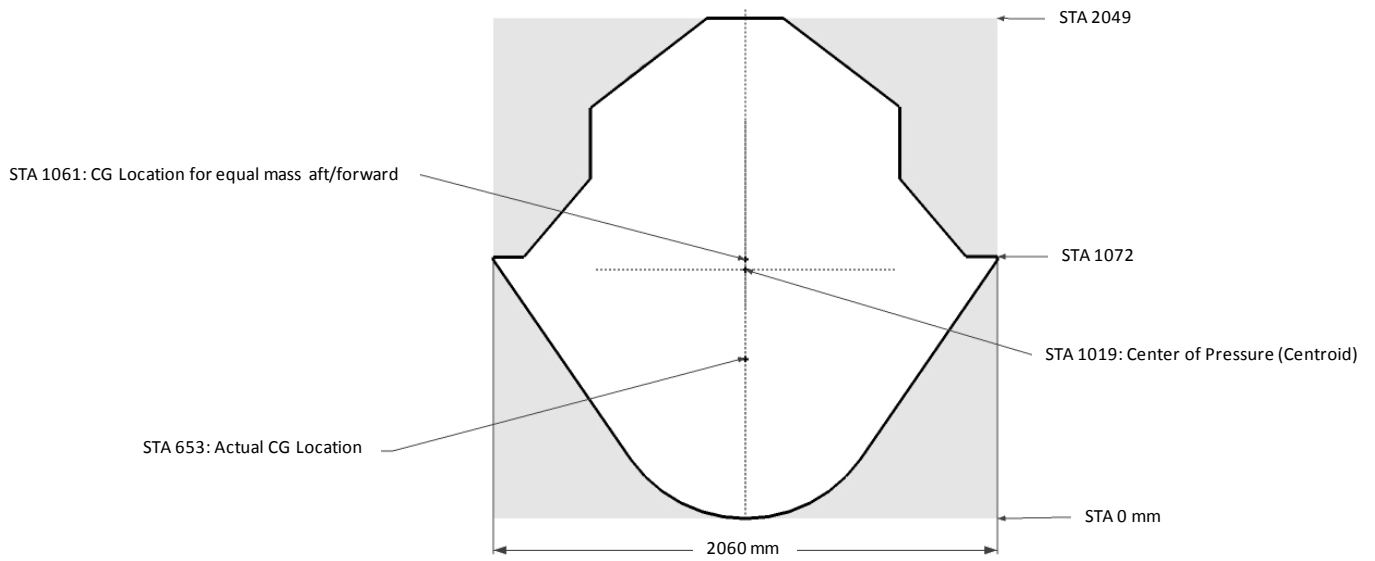


Figure 6-7: TABS aerodynamic stability consideration

Table 6-1: Mass distribution used in CG estimation (kg)

Center of mass/pressure estimation	STA 0-1072	STA 1072-2049	Totals
Centroid STA	646	1476	
	Forward	Aft	
Forward Ballast	40.52		40.52
Aeroshell	152.37	48.52	200.89
Gondola	35.89	0.85	36.74
Main Tank Support Structure		9.85	9.85
Drogue and Parachute Container		4.13	4.13
Buoyant Gas System		99.00	99.00
Science Instruments	17.88		17.88
Bus Components	52.45		52.45
Parachute System		21.68	21.68
Totals	299.11	184.03	483.14
Center of Pressure Location (centroid)	STA		1019
Center of Mass Location	STA	for Mass Aft = Mass Forward	1061
Actual CG	STA		652.80

Note: STA=mm from nose tip

6.8 Deployment Scheme and Operational Configuration

TABS enters Titan’s atmosphere at 10.44 km/s. Figure 6-8 shows the sequence of events from entry interface at 1000 km altitude to balloon inflation about 50 minutes later, at 14 km altitude. First, the vehicle decelerates for 136 seconds after entry to Mach 1.2, at which point the drogue decelerator can be safely deployed. The main is deployed 15 seconds later when the vehicle is traveling at 126 m/s. Balloon inflation begins when the terminal velocity stabilizes at 9.9 m/s, 28 km above the surface. The FS is kept during inflation to ensure there is enough mass to facilitate the vehicle’s descent even after the balloon has been fully inflated. This prevents parachute-line slack, and entanglement. After the balloon is fully inflated, the AS is released, then the FS is released, and the antenna and instruments deployed for normal science operations. A quantitative description of the vehicle descent through the atmosphere is given in the aerothermodynamic entry analysis section (Section 7), including sizing of the parachute decelerators.

The probe configuration changes during descent are shown in more detail in Figure 6-9, starting with the entry configuration (1) through the final operational configuration (11).

The balloon deployment is a challenging aspect of the mission. In order to ensure the deployment loads are not unduly carried by the fabric, reinforced material is used to connect the balloon lines during initial drop-off and opening. Inflation will then occur after the system is fully extended. This load path is illustrated in Figure 6-10. This is however, a relatively “simple” enough rigging job, which does not involved insertion of extraneous material into the fabric.

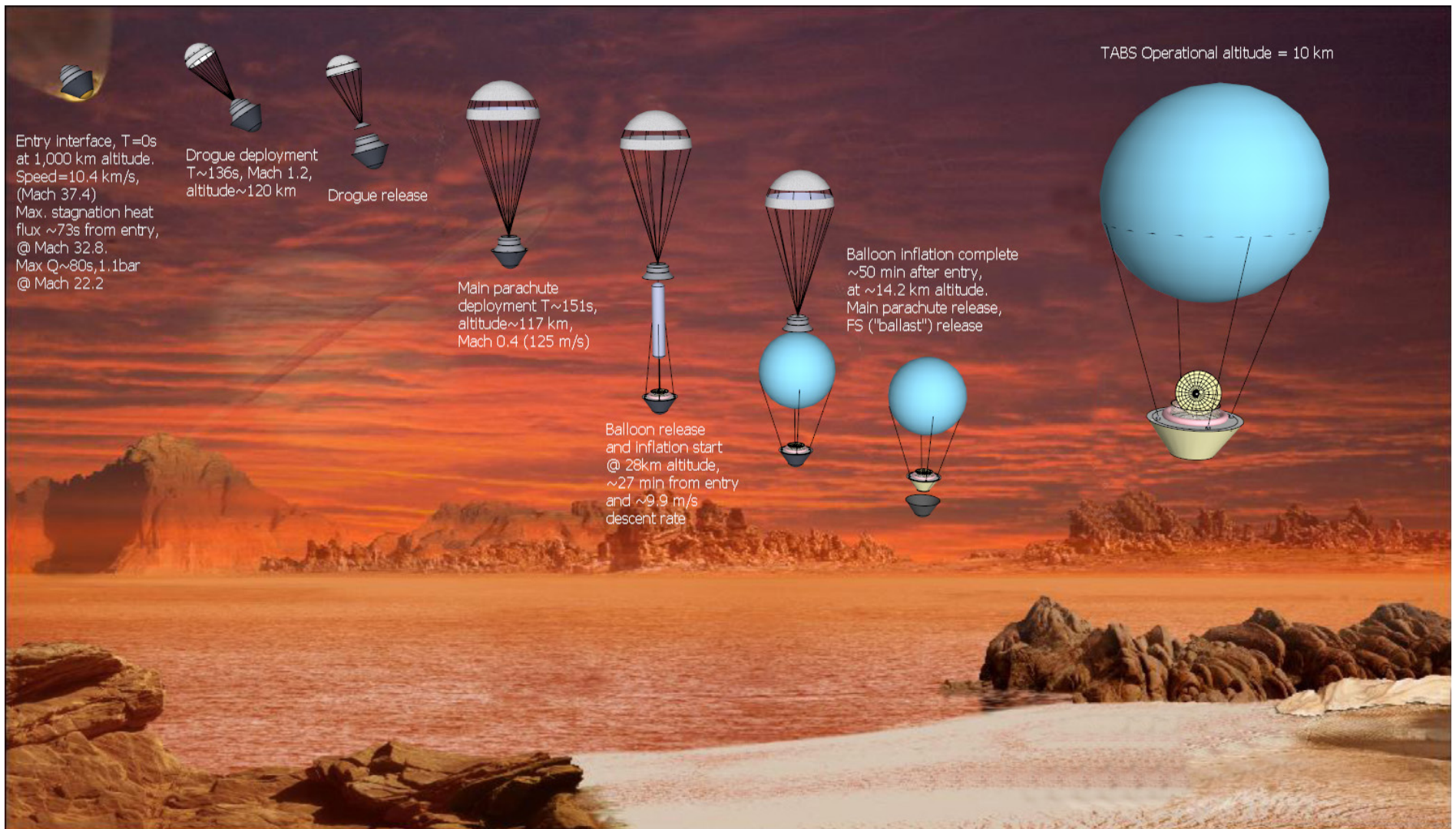


Figure 6-8: TABS entry and deployment sequence

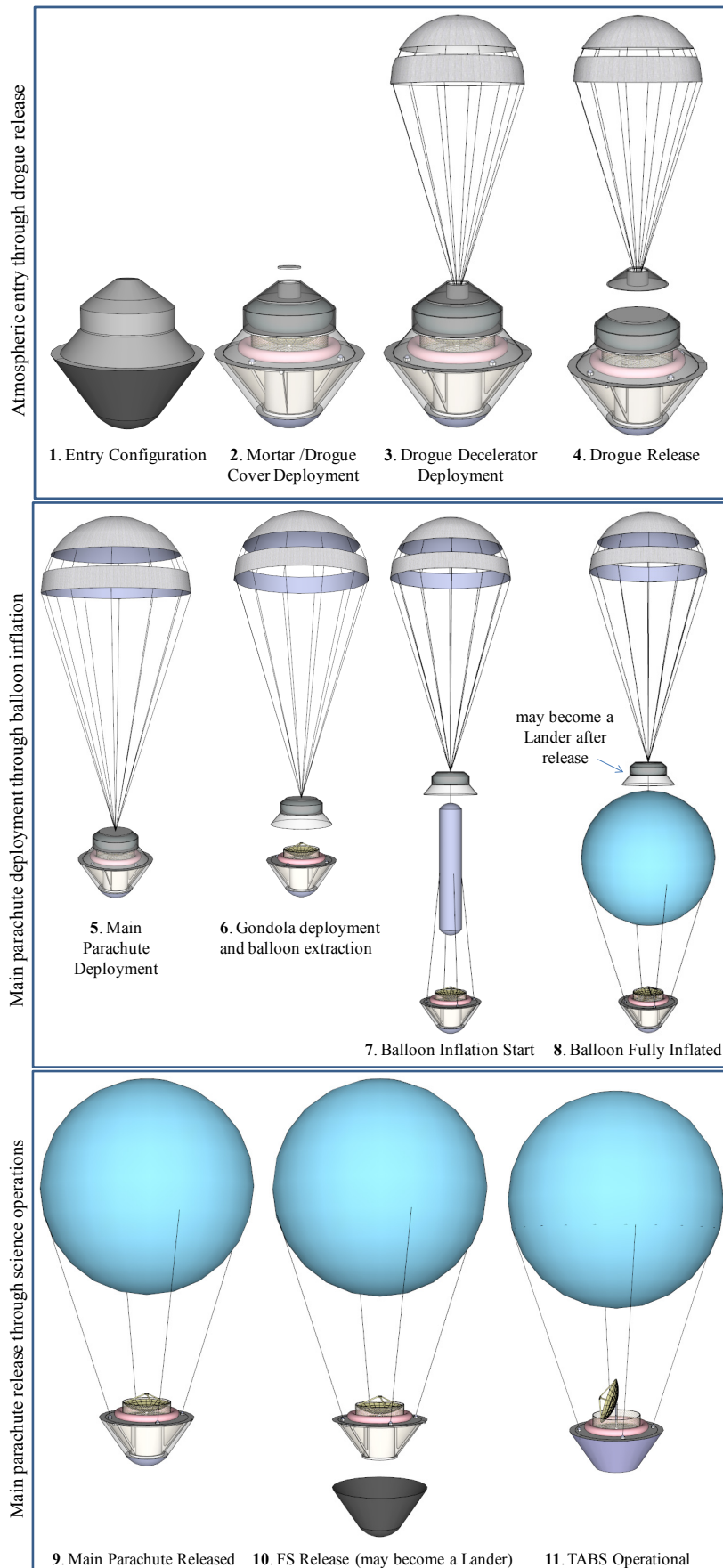


Figure 6-9: TABS configuration changes during descent

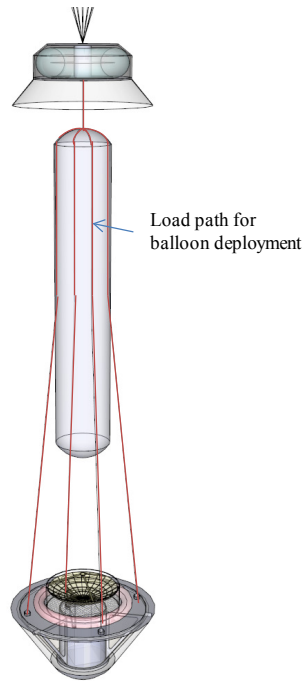


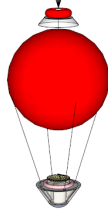
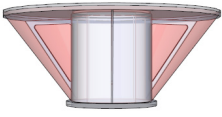
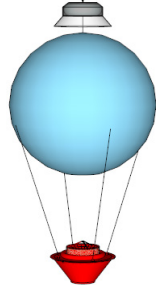
Figure 6-10: Load path lanyard for balloon deployment ensures fabric will not be unduly stressed.

6.9 Entry Probe Equipment List

The equipment list for the buoyant system, including the mass of the primary H₂ tank is shown in Table 6-2. Note that this is not the mass of the entry vehicle, but the mass of the portion of the vehicle that “hangs” from the balloon, with the exception of the primary tank which is released after inflation. The total gondola mass (instruments and bus) with 30% contingency is 157.7 kg. There is an additional 8.2% mass margin left, which is the difference between the gondola mass plus contingency, and the maximum lift capability of the buoyant system. These numbers are appropriate for this level of system development. The power margin after a 30% contingency is applied is 24.5%, assuming the ASRG outputs 110 W.

Table 6-3 shows the equipment list for the complete entry system, and identifies the materials used in the analysis. The Current Best Estimate (CBE) is 483 kg, and 628 kg including 30% contingency. This latter number will be input in the aerothermodynamic computations. This number together with the aeroshell geometry fully specifies the system input parameters needed to estimate the entry aerodynamic and the thermal loads.

Table 6-2: TABS Floating System Mass and Power Budgets

Component	Mass CBE* (kg)	Peak Power CBE (W)		
Bouyant Gas System (BGS) 4.6-meter Dia. H2 @ 10-km				
Balloon material (~0.11 kg/m ²)	7.2			
Mass of H2 gas	6.6			
H2-Tank Single Toroid	70.1			
Total Bouyant Gas System	83.90			
Gondola (Payload)			 <p style="text-align: center;">Instrument Volume</p>	
Science Instruments				
Visible Imaging System Balloon (VISTA-B)	1.7	4.2		
Balloon Imaging Spectrometer (BIS)	2.5	8.3		
Titan Montgolfière Chemical Analyser (TMCA)	5.0	6.7		
Atmospheric Structure Instrument / Meteorological Package (ASI/MET)	0.8	4.2		
Titan Electric Environment Package Balloon (TEEP-B)	0.8	0.8		
Magnetometer (MAG)	0.4	1.3		
Titan Radar Sounder (TRS)	6.7	12.5		
Montgolfière Radio Science Transmitter (MRST)	0.0			
Total Instruments	17.88	37.92		
Bus				
Structure	35.87			
Thermal	4.58			
Avionics	1.7	16		
Communications	8.00	10		
Power (SRG) - Avail power ~110We (2x55We). Heat power ~500W	38.17			
Auxiliary H-Tank	13.20			
Auxiliary H-gas	1.90			
Total Bus	103.419	26		
Total Gondola	121.29	63.92		
Total Gondola + 30% Contingency	157.68	83.09		
Total Delivered System with contingency (incl. Main H2 tank which is later jettisoned)	241.58	83.09		
Margins				
BGS Gondola Lift Capacity/ Power System Capacity	171.7	110		
Total Gondola w/Cont.	157.68	83.09		
Lift capacity/power margin	14.02	26.91		
Lift capacity/power margin	8.16%	24.46%		

*CBE = Current Best Estimate

Table 6-3: Entry System Mass Budget Estimation

Station	Component	Quantity	Material	Size (cm)			Mass Composite Honeycomb (kg)			Mass Comp.	Select Mass
				Thickness	Area	Material Volume	Composite (0.2 or 2x0.1 cm)	Al Core	SubTotal	(kg)	(kg)
	Forward Ballast	1	TBD								40.52
0	Aeroshell										
0	Front Shield										
	Spherical Dome TPS *	1	Carbon/Phenolic	1.62	8687.30	14082.11				19.71	
	Spherical Dome Structure	1	Composite/Al Honeycomb	2.20	8687.30		2.74	1.42	4.16		
	FS Frustum TPS *	1	Carbon/Phenolic	1.62	46522.90	75413.62				105.58	
	FS Frustum Structure	1	Composite/Al Honeycomb	2.20	46522.90		14.68	7.58	22.26		
	Rear Front Shield Exposed Annulus *	1	SLA-561	0.34	7555.90	2553.89				0.65	
1072	Aft Shield										
	BS 1st Frustum TPS *	1	SLA-561	0.34	20489.90	6925.59				1.78	
	BS 1st Frustum Structure	1	Epoxy/Graphite HM	1.00	20489.90	20489.90				32.33	
	BS Tank Enclosure Cylinder TPS *	1	SLA-561	0.34	10721.10	3623.73				0.93	
	BS Tank Enclosure Cylinder Structure	1	Composite/Al Honeycomb	2.20	10721.10		3.38	1.75	5.13		
	BS 2nd+3rd Frustum TPS *	1	SLA-561	0.34	14666.00	4957.11				1.27	
	BS 2nd+3rd Frustum Structure	1	Composite/Al Honeycomb	2.20	14666.00		4.63	2.39	7.02		
	Droge Enclosure Top Cover TPS *	1	SLA-561	0.34	742.30	250.90				0.06	
	Structure Mount Pegs	3	Epoxy/Graphite HM	9.40	19.63	184.57				0.87	
	Subtotal										201.76
	<i>* Spacecraft surface Area for Radiation</i>				109385.40						
245	Gondola										
	Thermal Enclosure	1	Silica Aerogel Insulation	4.00	39188.40	156753.60				3.61	
	Thrust Cylinder	1	Composite/Al Honeycomb	1.20	16189.40	19427.28	5.11	1.32	6.43		
	Thrust Cylinder bottom cap	1	Composite/Al Honeycomb	4.00	4484.80	17939.20	1.42	1.39	2.80		
	3A-Truss (x3)	3	Epoxy/Graphite HM	1.00	808.50	808.50				3.83	
	Main Instrument Shelf	1	Composite/Al Honeycomb	5.00	25437.50	127187.50	8.03	9.95	17.98		
	Thermal Seal	1	Prosil 2000	0.10	7555.90	755.59				0.38	
	RF Transparent Mesh	1/10	Epoxy/Graphite HM	0.50	10759.60	5379.80				0.85	
	Subtotal										35.87
1392	Main Tank Support Structure										
	Thrust Cylinder (inside Toroid)	1	Epoxy/Graphite HM	1.00	2728.40	2728.40				4.30	
	Tank Base Plate	1	Composite/Al Honeycomb	2.20	11592.90	25504.38	3.66	1.89	5.55		
	Subtotal										9.85
1808	Droge and Parachute Container										
	Droge Enclosure Cylinder (sans cover)	1	Composite/Al Honeycomb	1.20	1937.20	2324.64	0.61	0.16	0.77		
	Droge Enclosure Top Cover	1	Composite/Al Honeycomb	2.20	742.30	1633.06	0.23	0.12	0.36		
	Droge and Main Base Plate	1	Composite/Al Honeycomb	2.20	6289.30	13836.46	1.98	1.03	3.01		
	Subtotal										4.13
	Total Structure and Entry System										292.13
	Buoyant Gas System										99.00
	Science Instruments										17.88
	Bus Components										52.45
	Parachute System										21.68
	Droge decelerator									4.91	
	Main Parachute									16.77	
	Total Entry System CBE										483.14
	Contingency	30%									144.94
	Total Entry System										628.08

Aluminum Properties (Ref. 18):

The four most common aluminium grades available as sheet metal are 1100-H14, 3003-H14, 5052-H32, and 6061-T6. Grade 6061-T6 is a common heat treatable structural aluminium alloy. Low cost, formable, weldable.
 Density 0.098 lb/in³
 0.00271264 kg/cm³
 2712.64 kg/m³
 Ftu (ksi) 42

Composite Properties:

Al Honeycomb Core 81.5 kg/m³ 8.150E-05 kg/cm
 Epoxy/Graphite HM 1577.76 kg/m³ 1.578E-03 kg/cm
 Back Shield Density 500 kg/m³ 5.000E-04 kg/cm
 20 layer MLI 0.75 kg/m² 7.500E-05 kg/cm
 Outer Cover Density 0.17 kg/m² 1.700E-05 kg/cm
 Carbon/Phenolic 1.400E-03 kg/cm
 SLA-561 2.563E-04 kg/cm
 CRPAA/CR11, 5056 Al; Hexcel™
 ESA-SRE(2008)4, p.103
 OC=Outer Cover (Ref. 59)
 Galileo and others
 Viking, MPPF, MER, Phoenix

7.0 Aerothermodynamic Entry Analysis

Atmospheric entry computations will follow a first-order ballistic entry analysis, with the following assumptions ⁸:

- Zero-g, flat-earth solution
- Zero lift: Small asymmetries taken out by slowly rolling the vehicle during entry, at ~15 deg/s (Mercury spacecraft)
- Flight path angle remains constant at the entry value (entry at a reasonably steep angle, $-\gamma_e > 5$ deg)
- Planar Trajectory
- Non-rotating planet
- Non-thrusting entry
- Entry Interface Conditions: r_e (function of ρ_e), V_e , γ_e , where r_e is vehicle position, V_e its entry velocity, and γ_e the entry flight path angle.
- Entry density, $\rho_e = 0$
- Model for atmospheric density $\rho(h)$ is an exponential function of altitude (h)
- Vehicle control parameter: C_D (coefficient of Drag)
- Constant Scale Height given by, $1/\beta$
- Constant ballistic coefficient (m/SC_D), where m =vehicle mass, S =vehicle reference area for lift and drag

The entry flight path angle was first derived geometrically. It is iterated and adjusted to strike a balance between aerodynamic loads and thermal loads. It also must be chosen such that there is no possibility of skip-out. If a 1000 km entry interface is chosen, then a flight path angle of ~44 degrees would ensure geometric contact of the trajectory with the ground for a straight undisturbed flight path (grazing). Hence, 50-degrees is finally chosen. This angle is consistent with previous planetary entry probes to Venus and Titan.

$$\gamma_e := -50.0\text{deg} \quad \text{entry flight path angle}$$

The inertial entry velocity was earlier computed, and is

$$V_e := 10.439 \frac{\text{km}}{\text{s}}$$

The front shield semi-apex angle was defined to be

$$\delta_{ha} := 34.4\text{deg}$$

The coefficient of drag for this geometry can then be estimated from

$$C_D := 2 \cdot \sin(\delta_{ha})^2 = 0.638$$

Also the vehicle reference area for drag is its cross-sectional area in the direction of motion, or

$$A_s := 3.33\text{m}^2$$

which is the projected area of the 2.06-meter diameter front shield.

The entry probe mass is given in Table 6-3, $m_{sn} := 628.08\text{kg}$

Hence, the probe ballistic coefficient C_B is

$$C_B := \frac{m_{sn}}{A_s \cdot C_D} = 295.457 \cdot \frac{\text{kg}}{\text{m}^2}$$

Note that m_{sn} is the probe mass at Titan entry, including contingency. Hence the calculations here have an intrinsic conservatism built-in.

7.1 Titan's Atmospheric Model

7.1.1 Atmospheric Scale Height

Titan's normalized atmospheric composition for major elements (mixing ratios), at 981 km is obtained from Reference 22:

$$H_2 := 0.0033 \quad N_2 := 0.984 \quad CH_4 := 0.0131$$

The corresponding molecular weights are

$$H_{2m} := 2.016 \frac{\text{gm}}{\text{mol}} \quad N_{2m} := 28.013 \frac{\text{gm}}{\text{mol}} \quad CH_{4m} := 12.011 \frac{\text{gm}}{\text{mol}} + 4.03 \frac{\text{gm}}{\text{mol}}$$

Hence, the molecular mass of Titan's atmospheric gas at 981 km is (approximately: note the use of molecular weight multipliers instead of divisors of mass fractions)

$$\mu := H_2 \cdot H_{2m} + N_2 \cdot N_{2m} + CH_4 \cdot CH_{4m} = 0.028 \text{ mol}^{-1} \cdot \text{kg}$$

Given the universal gas constant

$$R_u := 8.31441 \frac{\text{J}}{\text{mol} \cdot \text{K}}$$

The atmospheric gas constant is

$$R_{\text{gas}} := \frac{R_u}{\mu} = 299.278 \cdot \frac{\text{J}}{\text{kg} \cdot \text{K}}$$

We must now determine the temperature gradient at about ~1,000 to ~200 kilometers (~ main ballistic entry corridor), and use data in Reference 29 to this effect. There, it can be seen that the atmosphere remains rather isothermal, with wide fluctuations about a median. We then take the gradient to be zero for this altitude interval.

$$T_{\text{grad}} := 0 \frac{\text{K}}{\text{km}}$$

The reference temperature is further chosen to lie within the range of temperatures at entry and deceleration altitudes, from about ~1000 to 200 km. Figure 7-1 shows the altitude versus temperature changes as obtained from Huygens DISR data ⁷. A reference temperature of 181K gives the best approximation for an exponential atmospheric model, and will be the reference temperature for this study.

$$T_{\text{ref}} := 181\text{K}$$

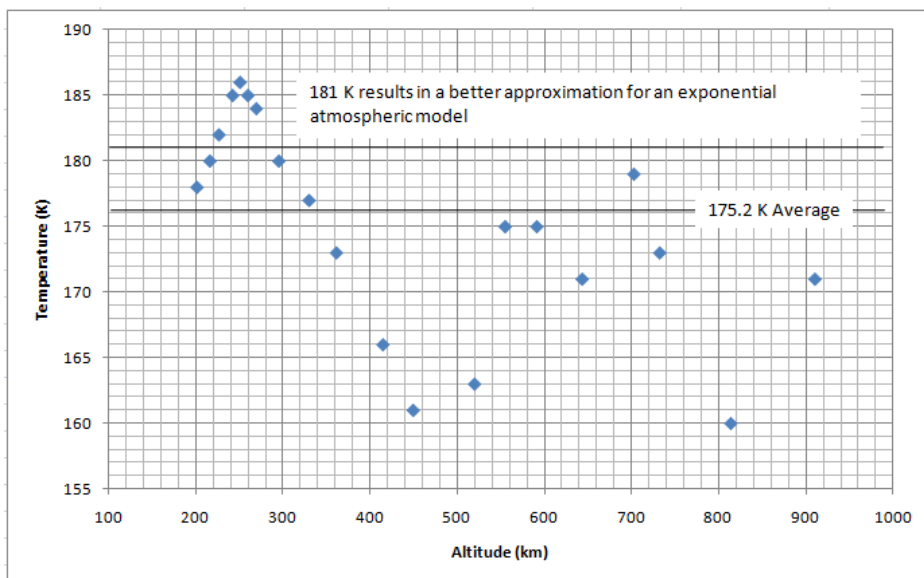


Figure 7-1: Estimation of atmospheric temperature for ballistic corridor

The atmospheric scale height for the high-altitude region of interest is then computed:

$$g_n := 1.354 \frac{\text{m}}{\text{s}^2} \quad \text{Titan's surface gravity (Ref. 29)}$$

$$\beta := \frac{\frac{g_n}{R_{\text{gas}}} + T_{\text{grad}}}{T_{\text{ref}}} = 2.5 \times 10^{-5} \text{ m}^{-1}$$

The atmospheric scale height is then

$$\frac{1}{\beta} = 40.007 \cdot \text{km}$$

The scale height here is optimized for relevant ballistic entry altitudes, and is consistent with the value calculated prior to Huygens³⁰.

7.1.2 Exponential Atmospheric Model

Titan's atmospheric density and pressure models are derived from DISR and HASI (Huygens Atmospheric Structure Instrument) data. For altitudes between 1000 km down to about 300 km, HASI density data is used directly²⁹. DISR pressure data⁷ together with the perfect gas law is used to derive the density for altitudes below 300 km. The combined data so obtained is then fit by an exponential function. Two such exponential curve fits are derived, one for altitudes from 1000 down to 0 km (or the "high-altitude" model), and one for altitudes below 120 km down to the surface ("low-altitude" model). The high-altitude atmospheric density model is shown in Figure 7-2. The curve fit given from this model tends to predict slightly larger densities from about 50 to 400 km, and hence result in a conservative estimate of aerodynamic G-loading, and a slightly lower total integrated heat load. These values are considered appropriate for this level of mission design however, and a "tighter" model was not used. In fact, atmospheric bulk properties are expected to fluctuate at any given time anyway, with corresponding changes in model estimation. The reference density for this exponential curve fit

$$\rho_0 := 0.7763 \frac{\text{kg}}{\text{m}^3}$$

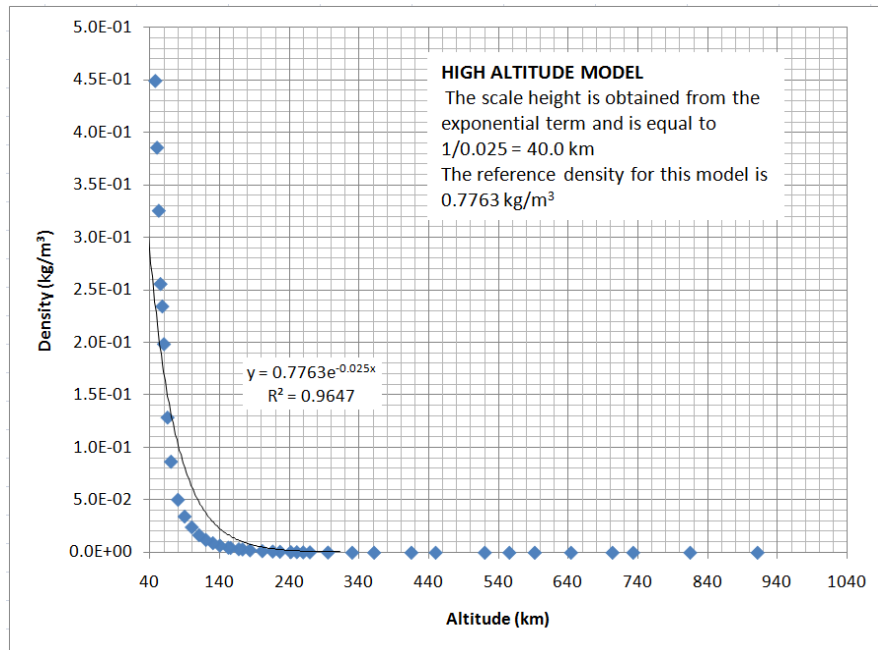


Figure 7-2: Titan exponential atmospheric model for high altitudes (>~40 km)

and would correspond to the density at the "surface". Obviously this is not the case, and this model is only good down to an altitude of about 40 km, or one scale height. Note that the scale height from the curve fit is consistent with the value computed from Titan's atmospheric composition and temperature. The Exponential atmospheric model for Titan at altitudes > ~40 km is hence

$$\rho_{\text{mod}}(h) := \rho_0 \cdot e^{-\beta \cdot h} \quad h := 40\text{km}, 60\text{km}.. 1000\text{km}$$

The altitude can then be estimated as a function of density,

$$h(\rho) := \frac{-1}{\beta} \cdot \ln\left(\frac{\rho}{\rho_0}\right) \quad (\text{high-altitude relation})$$

As stated, this model is good for ballistic entry calculations, but should not be used for altitudes below 40 km. In fact, it will be shown that the drogue parachute can be deployed at an altitude of about 120 km. Hence, it becomes necessary to develop a model that fits the data below this height. Hence, for altitudes below 120 km a second exponential curve fit is derived and shown in Figure 7-3. In this case,

$$\beta_{120} := \frac{0.055}{\text{km}} = 5.5 \times 10^{-5} \text{ m}^{-1} \quad \rho_{120} := 5.8867 \frac{\text{kg}}{\text{m}^3} \quad \text{density at the surface}$$

closer to the value obtained from DISR at the surface, or 5.3 kg/m³. The atmospheric scale height applicable in this region is

$$\frac{1}{\beta_{120}} = 18.182 \cdot \text{km}$$

The exponential atmospheric model for Titan at altitudes < ~120 km is then

$$\rho_{\text{m120}}(h_{120}) := \rho_{120} \cdot e^{-\beta_{120} \cdot h_{120}} \quad h_{120} := 0\text{km}, 10\text{km}.. 120\text{km}$$

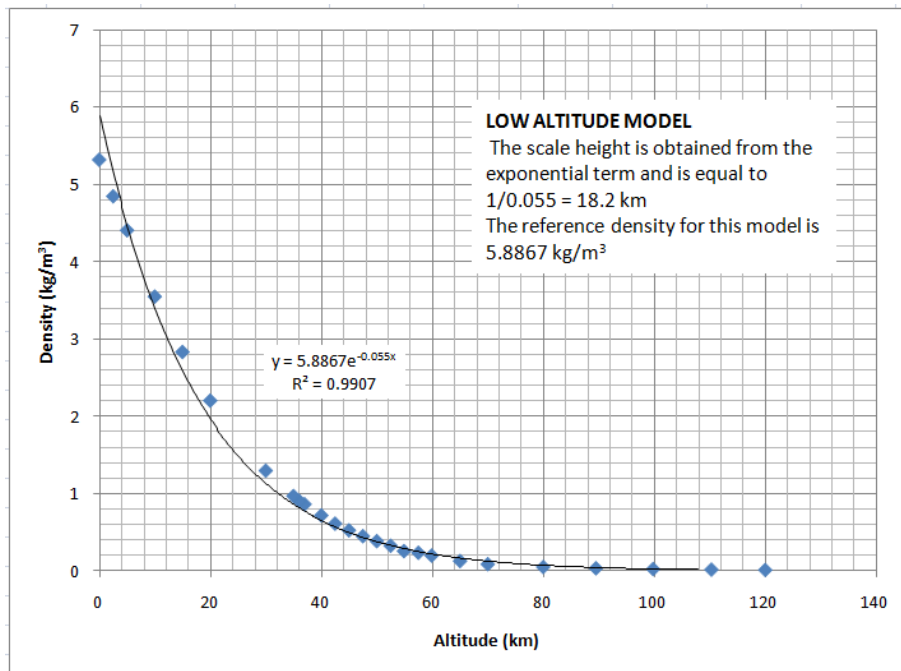


Figure 7-3: Titan exponential atmospheric model for low altitudes (<~120 km)

Once again, the altitude can be estimated as a function of density, which in this region is

$$h_0(\rho) := \frac{-1}{\beta_{120}} \cdot \ln\left(\frac{\rho}{\rho_{120}}\right) \quad (\text{low-altitude relation})$$

It is useful for low altitudes to explicitly derive the atmospheric pressure model. Since the ballistic entry atmospheric model is only good to approximately 40km, and since this model is not appropriate after drogue deployment (at ~120 km), we develop an approximate correlation based on a curve-fit to DISR data for (static) atmospheric pressures between 120 and 0 km altitude. This is shown in Figure 7-4. Hence,

$$P_{120}(h_{120}) := 115000 \text{Pa} \cdot e^{-0.049 \cdot \frac{h_{120}}{\text{km}}}$$

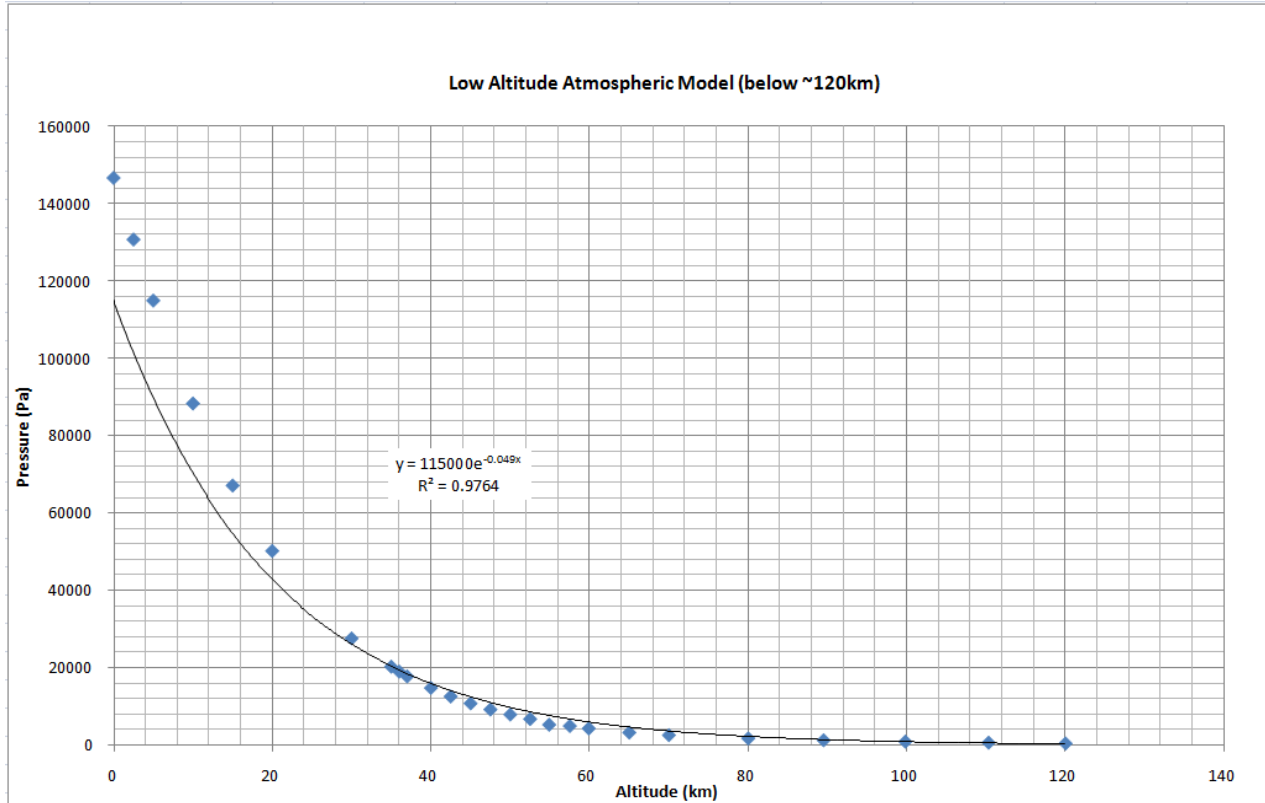


Figure 7-4: Titan exponential pressure-altitude model for low altitudes (<~120 km)

7.1.3 Atmospheric Model Comparison

Since the exponential atmospheric (high-altitude) model used for the ballistic entry analysis in this work was derived from two separate sources as described, it is important to compare it with at least two known references. These are the Global Reference Atmospheric Model (GRAM) for Titan (or Titan-GRAM 2004) ^{32,33}, and Huygens HASI data ²⁹. Figure 7-5 presents such a comparison. The "Esper Model" (EM) data and the corresponding exponential curve fit are shown against the Titan-GRAM and HASI data. As can be seen, all data sets track fairly well. On the other hand, the Titan-GRAM and HASI exponential fits are fairly close, resulting in scale heights of 47.6 and 45.5 km, respectively. The Jaime Esper exponential fit yields a lower atmospheric scale height (40 km), with the end-result of over-estimating the density at altitudes between 50 and 400 km, and under-estimating it at altitudes above. As mentioned before, the outcome is a more conservative estimation of aerodynamic G-loading, and slight under-estimation of the integrated heat load. Nonetheless, the differences are not large enough to significantly affect the results from this study. Furthermore, a scale height of 40 km is consistent with the value computed from basic aero-chemical properties, and as mentioned, the one used prior to Huygens arrival.

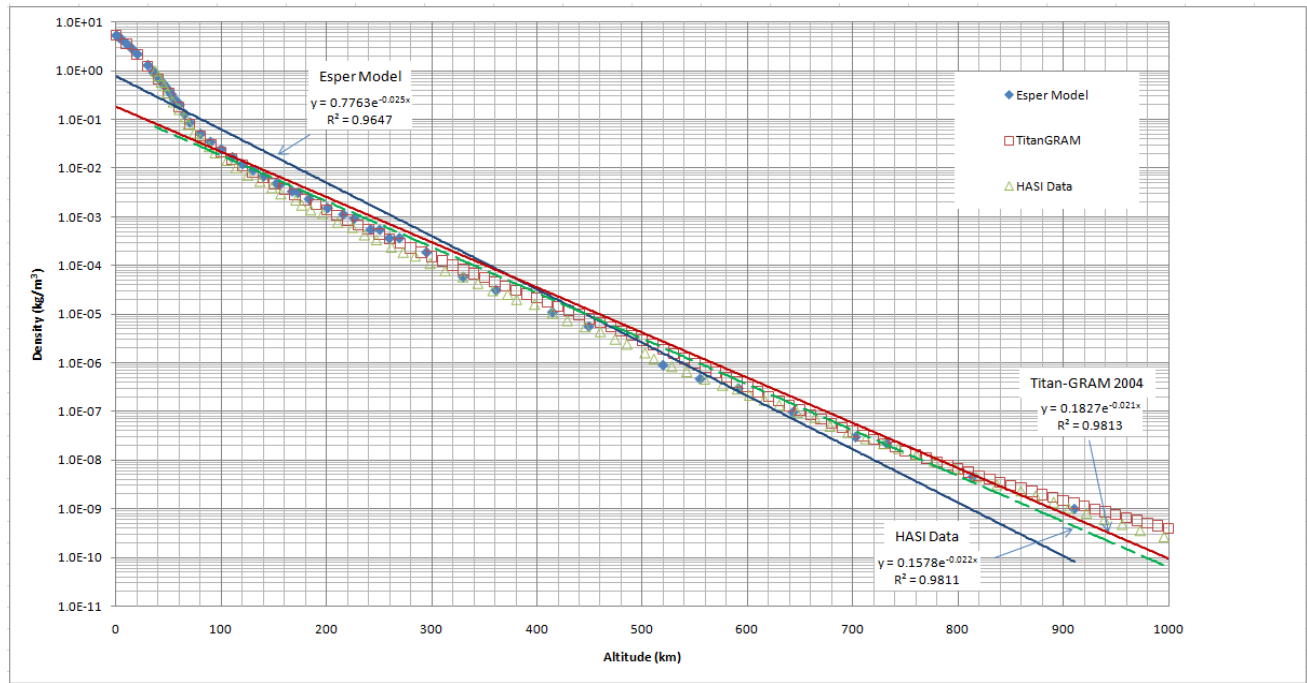


Figure 7-5: Comparison of different exponential atmospheric models

7.1.4 Flow Regime Estimation

A qualitative characterization of the flow regime for this case may be obtained from the mean free path between collisions of atmospheric gas particles³³. Whether it is continuum, continuum flow with slip effects, disturbed free molecular flow, or free molecular flow. This in turn will help to assess the relevance of the analytical techniques used in estimating the thermodynamic heat loads into the vehicle. To determine this, we compute the Knudsen number.

The viscosity of Nitrogen at 1 atmosphere as a function of temperature T_{N_2} is given by the empirical correlation³⁴:

$$\mu_{vN_2}(T_{N_2}) := \frac{0.1 \cdot 5.58114 \cdot 10^{-4} \cdot T_{N_2}^{1.04322}}{T_{N_2} + 900.67} \frac{\text{kg}}{\text{m} \cdot \text{s}}$$

where T_{N_2} is input in units of Kelvin. The mean free path is then obtained from:

$$\lambda_p := \frac{16}{5} \frac{\mu_{vN_2}(172.7)}{\rho_0} \cdot \frac{1}{\sqrt{2 \cdot \pi \cdot R_{\text{gas}} \cdot 172.7\text{K}}} = 8.115 \times 10^{-8} \text{ m}$$

Where the temperature (and resulting viscosity) is the average for the ballistic entry corridor from 1000km altitude to 120 km, or 172.7 Kelvin. If the characteristic length is taken as the axial length of the entry probe (204.9cm), then the Knudsen number is

$$L_s := 204.9\text{cm} \quad \text{TABS axial length}$$

$$K_n := \frac{\lambda_p}{L_s} = 3.961 \times 10^{-8}$$

Hence continuum flow analysis is applicable. It is noted that the Newton theory for hypersonic flow may be used as an (inviscid) computational tool in the continuum regime down to Mach~ 2.

7.2 Aerodynamics

7.2.1 Aerodynamic Loading and Velocity Evolution

The Deceleration peak value (max g-load) is obtained from the scale height and the entry velocity. First, the maximum deceleration is

$$a_{\max} := \frac{-\beta \cdot V_e^2}{2 \cdot e} \cdot \sin(\gamma_e) = 383.807 \text{ m} \cdot \text{s}^{-2}$$

Since Earth's gravitational acceleration is

$$g_e := 9.807 \text{ m} \cdot \text{s}^{-2}$$

Then

$$g_{\text{load}} := \frac{a_{\max}}{g_e} = 39.136 \quad \text{Gs}$$

an acceptable result. By comparison: the Galileo Jupiter atmospheric probe experienced a $g_{\text{load}} = 230\text{g}$; Veneras 400-500g; Pioneer Venus Small probe 280g; Pioneer Venus Large probe 223-458g.

The *critical altitude* at which the maximum acceleration occurs is given by

$$h_{\text{crit}} := \frac{1}{\beta} \cdot \ln\left(\frac{-1}{\beta} \cdot \frac{1}{C_B} \cdot \frac{\rho_0}{\sin(\gamma_e)}\right) = 196.897 \cdot \text{km}$$

where ρ_0 is the reference density at the bottom of the specified layer for an exponential atmospheric model. The following ("sufficiently light") test is meant to demonstrate the vehicle will not impact the ground, as the selection of flight path angle must yield an argument of the logarithm greater than one:

$$0 < -\sin(\gamma_e) = 0.766 < \frac{1}{C_B} \cdot \frac{\rho_0}{\beta} = 105.116 \quad (\text{True})$$

The velocity evolution as a function of altitude (or density) and flight path angle may be obtained from the first-order ballistic analysis⁸ and is given by

$$V_{\text{sc}}(x) := V_e \cdot \exp\left[\left(\frac{1}{2 \cdot \beta} \cdot \frac{\rho_0}{\sin(\gamma_e)} \cdot \frac{A_s \cdot C_D}{m_{\text{sn}}}\right) \cdot \exp(-\beta \cdot x)\right] \quad x := 50\text{km}, 75\text{km}.. 1000\text{km}$$

The *Mach Number* over the trajectory is expressed as

$$\gamma_{\text{N}_2} := 1.437 \quad \text{Average ratio of specific heats of N}_2 \text{ from +15 to -181 } ^\circ\text{C}$$

$$c_s := \sqrt{\frac{\gamma_{\text{N}_2} \cdot R_u \cdot T_{\text{ref}}}{\mu}} = 0.279 \cdot \frac{\text{km}}{\text{s}} \quad \text{The average speed of sound at relevant altitudes in Titan}$$

$$M_a(x) := \frac{V_{\text{sc}}(x)}{c_s} \quad \text{Mach Number}$$

Figure 7-6 shows the velocity and Mach number of the trajectory from the 1000 km entry interface down to 40 km altitude. Normally, drogue decelerators are deployed at supersonic speeds between Mach 1 and 2. At 120 km the vehicle speed is about Mach 1.2, and is hence selected as the drogue deployment altitude.

$$M_a(120\text{km}) = 1.227$$

Drogue deployment Mach number (and altitude)

The velocity at which maximum deceleration occurs is then

$$V_{sc}(h_{crit}) = 6.332 \cdot \frac{\text{km}}{\text{s}}$$

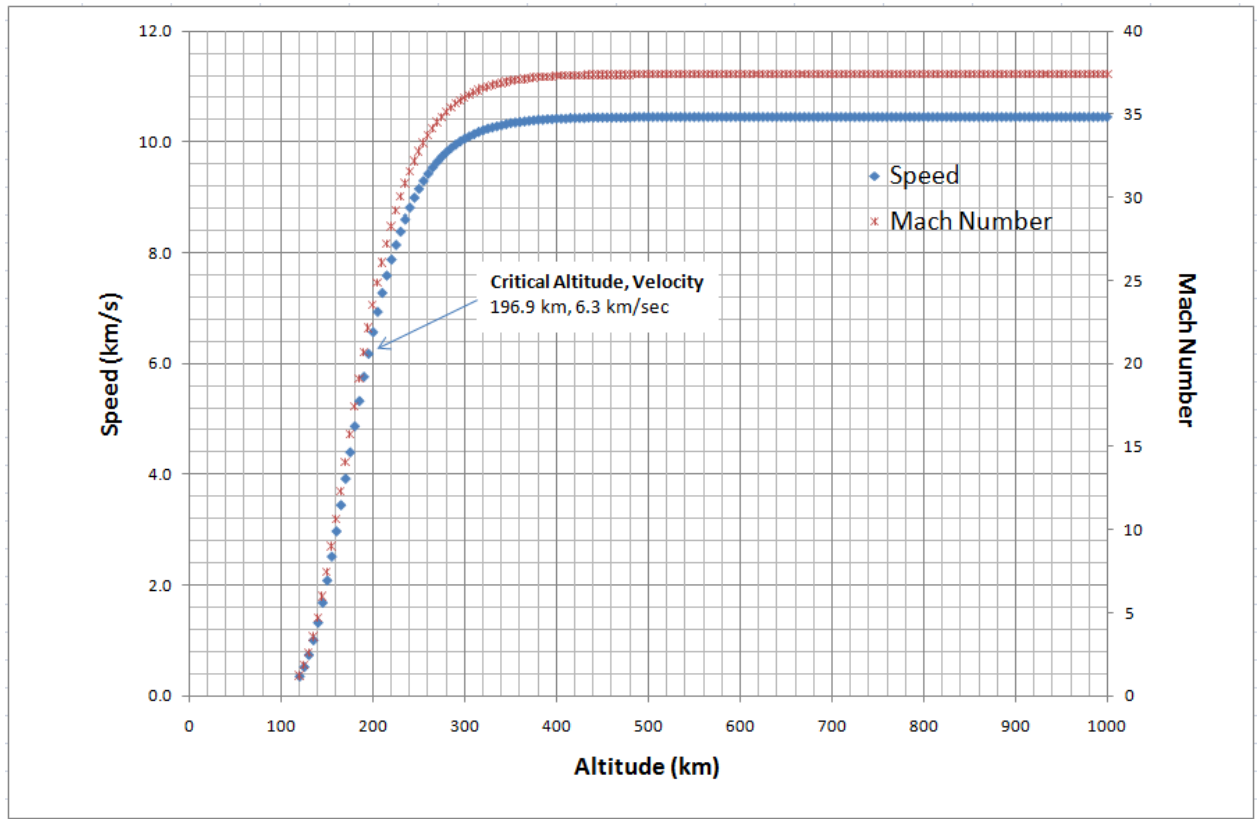


Figure 7-6: Velocity evolution over the ballistic trajectory with the critical locus of maximum deceleration

7.2.2 Dynamic Pressure

In order to estimate the dynamic forces applied on the entry heat shield, and hence aid in the selection and test of its mechanical and material properties, a few parameters are derived. These include the stagnation pressure, and the drag force. The *stagnation pressure* is equal to the sum of the free-stream dynamic pressure and static pressures. At high speeds the dynamic pressure is \gg static (or free-stream) pressure, and hence the latter term can be zero out. Therefore the stagnation pressure is nearly equal to the *dynamic pressure*, and for an incompressible flow approximation this is given (as a function of altitude) by,

$$P_{sp}(x) := \frac{1}{2} \cdot \rho_{mod}(x) \cdot (V_{sc}(x))^2$$

The maximum stagnation point (or *~maximum dynamic*) pressure, corresponds to the critical altitude (maximum deceleration) and is then

$$P_{sp}(h_{crit}) = 1.134 \times 10^5 \cdot \text{Pa}$$

$$P_{sp}(h_{crit}) = 1.134 \cdot \text{bar}$$

$$P_{sp}(h_{crit}) = 1.119 \cdot \text{atm}$$

where $h_{crit} = 196.897 \cdot \text{km}$

In fluid dynamics the *drag force* is related to the dynamic pressure by

$$F_D(x) := P_{sp}(x) \cdot C_D \cdot A_s$$

As expected from physical consideration, the maximum drag force occurs also at the point of maximum deceleration

$$t_{\text{bef}} := \sum_{i=0}^{176} tx_i = 135.904 \text{ s} \quad \text{Ballistic entry flight time}$$

It takes approximately 136 seconds, or 2.3 minutes from entry interface at 1000 km altitude to drogue deployment. Figure 7-8 shows this correlation in graphic form.

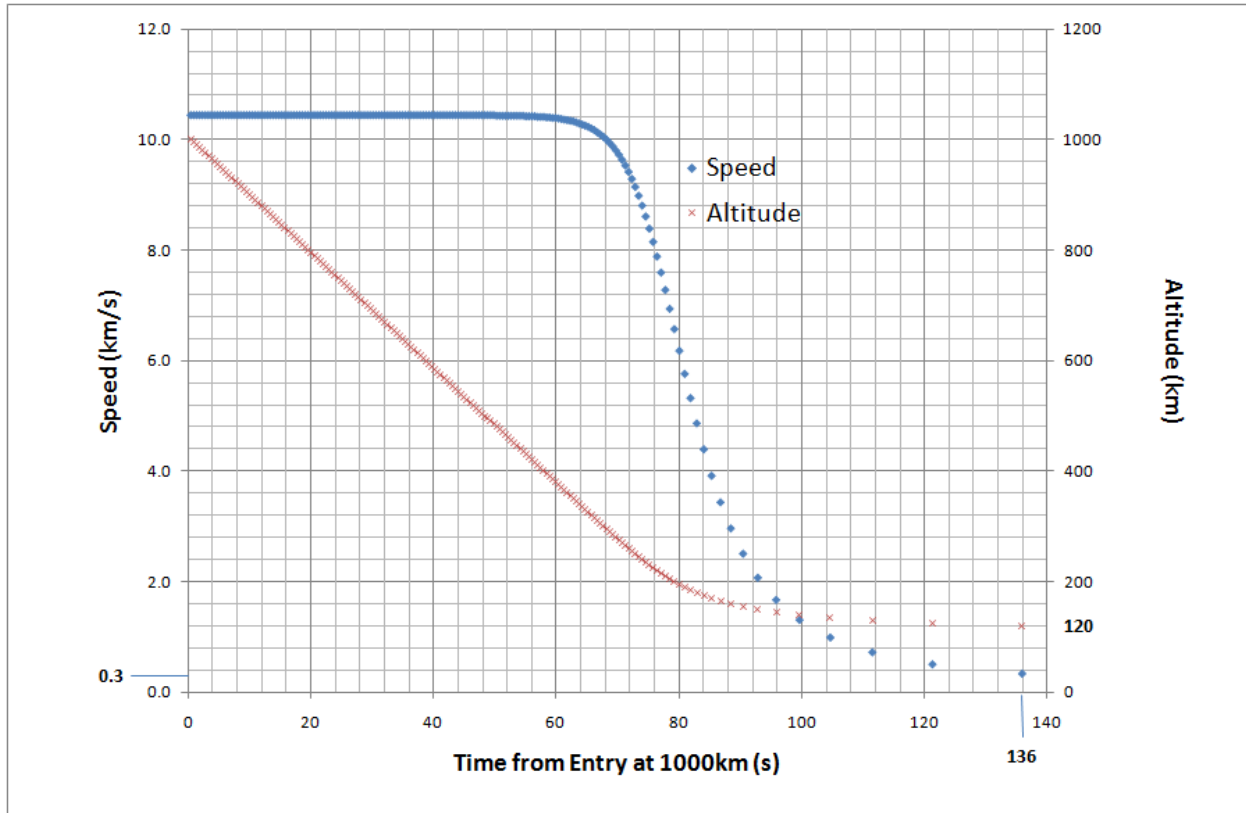


Figure 7-8: Time evolution of the entry trajectory

7.3 Aerothermodynamics

The thermal loads on the entry vehicle significantly affect its design, including the selection of an appropriate TPS. The *total heat load* will result in an overall increase in the vehicle temperature. The *instantaneous heating rate*, being local or body average, affects the thermal gradients across the vehicle, and hence can significantly result in differential expansion and mechanical stresses of the structural components. The maximum local heating rate occurs at the leading edge of a blunt body, or at the *stagnation point*. Whereas a shallow, larger trajectory will increase the total heat input, or overall vehicle temperature (longer flight time), a steep trajectory (shorter flight time, greater deceleration and friction) will increase the local heating rate, particularly at the stagnation point. A balance is achieved by adjusting the flight path angle, which in combination with the vehicle geometry and mass, yield a determinate heat input. The parameters chosen for TABS are the result of numerous iterations designed to reach reasonable mechanical and thermal loads. The deceleration load was computed before. In the following sections, the different thermal loads are estimated. But first, a general characterization of the total energy (or enthalpy) of the vehicle on entry is given.

The *total enthalpy* is conserved across the shock wave, and is proportional to the vehicle kinetic energy on approach, and the enthalpy of the undisturbed atmosphere. At hypersonic speeds the kinetic energy contribution is dominant, and hence the total enthalpy may be approximated by

$$H_{\text{oc}} := \frac{V_e^2}{2} = 5.449 \times 10^7 \cdot \frac{\text{J}}{\text{kg}}$$

This is also called the "recovery enthalpy" in some references³⁵. The recovery enthalpy will be useful later-on to compare with the results obtained from the aerothermodynamic computations.

7.3.1 Total Convective Heat Load and Body Average Heating Rate

The total entry heat load as well as the body average entry heating rate is now computed. The analytical approximation uses the approach followed by Allen and Eggers³⁶, and summarized in Reference 8. This *assumes that the primary source of energy input is convective heating from laminar boundary-layer flow over the entire vehicle*. This is of course an order of magnitude approximation, since radiation is an important source of heating, particularly at high altitudes and velocities (about greater than 10 km/s). In addition, real-gas (vibrational and chemical excitation) effects are ignored. From a perspective of feasibility assessment however, the approach selected suffices.

First, compute the body-averaged skin friction coefficient C_F using flat-plate theory. The Reynolds number is obtained from

$$V_{ef} := V_{sc}(120\text{km}) = 342.295 \text{ m}\cdot\text{s}^{-1} \quad \text{Velocity at which Drogue parachute is deployed, or effectively the "final" velocity to be considered for aeroheating.}$$

$$V_{ave} := 9.6 \frac{\text{km}}{\text{s}} \quad \text{Average velocity through the atmospheric flight from entry interface to drogue deployment}$$

$$T_{N2a} := 500 \quad \text{Boundary layer temperature for estimating viscosity (in Kelvin)}$$

$$\rho_{max} := \rho_{mod}(120\text{km}) = 0.039 \text{ m}^{-3}\cdot\text{kg} \quad \text{Maximum atmospheric density reached by spacecraft during ballistic flight}$$

$$Re_L := \frac{\rho_{max}\cdot V_{ave}\cdot L_s}{\mu_{vN2}(T_{N2a})} = 2.919 \times 10^7 \quad \text{Reynolds number, dimensionless}$$

$$\frac{Re_L}{L_s} = 1.424 \times 10^7 \text{ m}^{-1}$$

The skin friction coefficient is then

$$C_F := \frac{1.328}{\sqrt{Re_L}} = 2.458 \times 10^{-4} \quad \text{(dimensionless)}$$

where the low speed (incompressible flow) result was used to calculate C_F , as it yields a more conservative value from the perspective of entry heating. From this and the spacecraft body "wall" area exposed to entry heating, or "total aeroshell wetted area", S_w , the *total (convective) heat load* (E_L) is

$$S_w := 109385.4\text{cm}^2 = 10.939 \text{ m}^2$$

$$E_L := \frac{1}{4} \cdot m_{sn} \cdot (V_e^2 - V_{ef}^2) \cdot \frac{S_w \cdot C_F}{A_s \cdot C_D} = 2.162 \times 10^7 \cdot \text{J}$$

This equation is valid for an entry profile where the spacecraft slows-down sufficiently enough ("light" vehicle). A light vehicle criterion obtained from ballistic entry analysis and is given by:

$$0 < -\sin(\gamma_e) = 0.766 < \frac{1}{C_B} \cdot \frac{\rho_{max}}{\beta} = 5.236 \quad \text{(true)}$$

Now estimate the maximum body average heating rate, and the density (altitude) and velocity at which it occurs. Using the formulas applicable for ballistic entry⁸:

$$q_{\text{avmax}} := \frac{C_F}{6 \cdot e} \cdot \frac{m_{\text{sn}}}{A_S \cdot C_D} \cdot \beta \cdot V_e^3 \cdot \sin(\gamma_e) = -9.7 \cdot \frac{\text{W}}{\text{cm}^2} \quad q_{\text{avmax}} = -9.7 \times 10^4 \cdot \frac{\text{W}}{\text{m}^2} \quad \text{or} \quad \frac{\text{Joule}}{\text{s} \cdot \text{m}^2}$$

The critical density at which the peak heating rate occurs is found from

$$\rho_{\text{crit}} := \frac{-2}{3} \cdot \frac{m_{\text{sn}}}{A_S \cdot C_D} \cdot \beta \cdot \sin(\gamma_e) = 3.772 \times 10^{-3} \cdot \frac{\text{kg}}{\text{m}^3}$$

and the corresponding altitude is

$$h(\rho_{\text{crit}}) = 213.118 \cdot \text{km}$$

Note that this is slightly before peak deceleration (at ~197 km), and so the result is consistent with expectation. The critical velocity is

$$V_{\text{crit2}} := \frac{V_e}{\sqrt[3]{e}} = 7.48 \cdot \frac{\text{km}}{\text{s}}$$

From the velocity function as a function of altitude

$$V_{\text{sc}}(h(\rho_{\text{crit}})) = 7.48 \cdot \frac{\text{km}}{\text{s}}$$

a result which shows 100% internal consistency of the model.

7.3.2 Stagnation Point Heating - Convective

Now, we compute the *Stagnation Point Heat Flux* for both convection and radiation following a similarity analysis to Earth entry computations as given by Detra and Hidalgo³⁷, as an approximation of the relation given by Fay and Riddell³⁸, and summarized in Reference 33. Start with the "convective" or gas-to-wall stagnation heating.

$$R_{\text{nose}} := 0.58\text{m} \quad \text{Front shield spherical nose radius of curvature}$$

$$\rho_{\text{fs}} := 0.0019 \frac{\text{kg}}{\text{m}^3} \quad \text{Average "free stream" atmospheric density for ballistic corridor altitudes between 120 to 1000 km, from EM data (Fig. 7-5).}$$

$$q_{\text{gws}} := 11030 \cdot \frac{\text{W}}{\text{cm}^2} \cdot \sqrt{\frac{1\text{m}}{R_{\text{nose}}}} \cdot \left(\frac{\rho_{\text{fs}}}{\rho_0}\right)^{0.5} \cdot \left(\frac{V_e}{7950 \frac{\text{m}}{\text{s}}}\right)^{3.15}$$

$$q_{\text{gws}} = 1.69 \times 10^3 \cdot \frac{\text{W}}{\text{cm}^2} \quad \text{or} \quad q_{\text{gws}} = 1.69 \times 10^7 \cdot \frac{\text{W}}{\text{m}^2}$$

This local convective heat flux is about 174 times larger than the total body average convective heating rate computed before.

A plot of the stagnation point heat flux versus altitude gives insight into the sensitivity of this equation to free stream density and velocity (Figure 7-9). Since we use the corresponding free stream density for a given free stream (or probe) speed, the function provides a profile of the maximum stagnation (convective) heat flux.

$$q_{gwsf}(x) := 11030 \cdot \frac{W}{cm^2} \cdot \sqrt{\frac{1m}{R_{nose}}} \cdot \left(\frac{\rho_{mod}(x)}{\rho_0} \right)^{0.5} \cdot \left(\frac{V_{sc}(x)}{7950 \frac{m}{s}} \right)^{3.15}$$

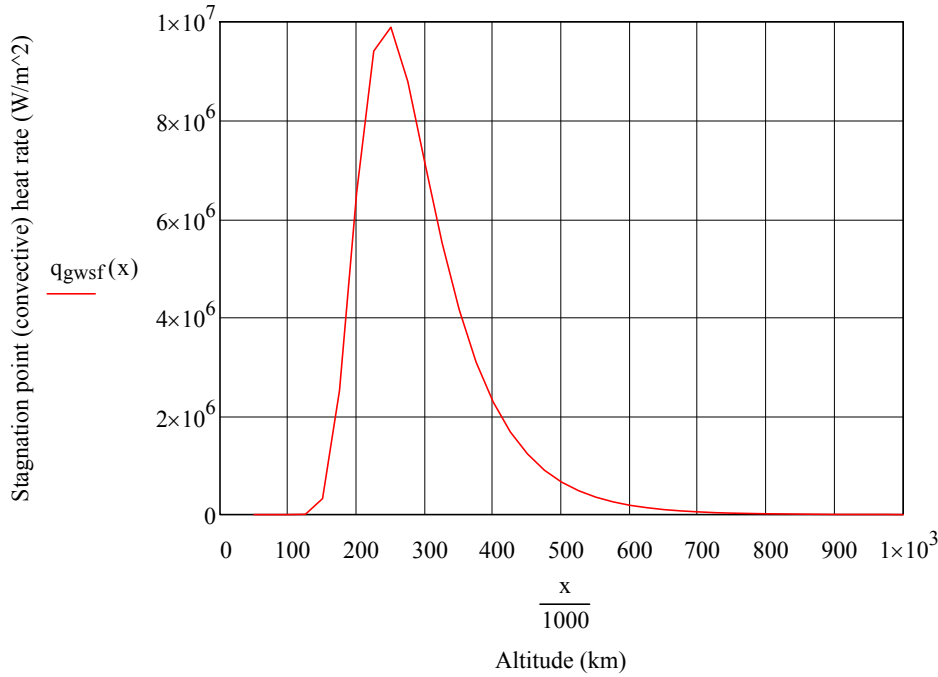


Figure 7-9: Convective stagnation point heat flux versus altitude and corresponding free-stream density and speed

The maximum value is then found at about 245km, and is

$$Q_{scmax} := q_{gwsf}(245km) = 9.957 \times 10^6 \cdot \frac{W}{m^2}$$

maximum (convective)
stagnation heat rate.

$$\text{or } Q_{scmax} = 995.745 \cdot \frac{W}{cm^2}$$

The body average heating rate computed before occurred at about 213 km, so a stagnation peak heat rate at 245 km is indeed consistent with the earlier results. *We use this as the maximum (convective) stagnation heat rate for this work.*

As a means of checking the result, we now calculate the convective heating rate at the stagnation point by using a different formula. Reference 39 provides an equation for estimating the maximum heating rate (in air) without making use of the atmospheric density directly. Rather, the flight path angle and ballistic coefficient are used to obtain

$$q_{gwsmax2} := 7.011 \frac{W}{cm^2} \cdot \left(\frac{\beta \cdot C_B \cdot \sin(-\gamma_e)}{R_{nose}} \cdot \frac{m^4}{kg} \right)^{0.5} \cdot \left(\frac{V_e}{1000 \frac{m}{s}} \right)^3 = 787.68 \cdot \frac{W}{cm^2}$$

This is consistent with the results obtained above. The integrated convective heat flux at the stagnation point during the flight is also given as ³⁹:

$$Q_{scmax2} := 0.0353 \cdot \frac{J}{cm^2} \cdot \left(\frac{C_B}{R_{nose} \cdot \beta \cdot \sin(-\gamma_e)} \cdot \frac{m^2}{kg} \right)^{0.5} \cdot \left(\frac{V_e}{1000 \frac{m}{s}} \right)^2 = 1.984 \times 10^4 \cdot \frac{J}{cm^2}$$

This may also be estimated from the total flight time corresponding to the main input in the convective stagnation point heating, corresponding to the time between ~400km to 180km in Figure 7-9. Hence

$t_{\text{heat}} := 25\text{s}$ flight time where majority of heat input occurs

$$Q_{\text{scmax}2t} := q_{\text{gwsmax}2} \cdot t_{\text{heat}} = 1.969 \times 10^4 \cdot \frac{\text{J}}{\text{cm}^2}$$

Since the heat input is rather sharp (delta function), the use of a ~FWHM heating time results in a reasonable estimate of the integrated heat flux, as seen by comparison with the equation above. Another estimate may be obtained by direct integration between the relevant altitudes,

$$Q_{\text{Cint}} := \int_{120\text{km}}^{1000\text{km}} \frac{q_{\text{gwsf}}(x)}{V_{\text{sc}}(x)} dx = 1.91 \times 10^4 \cdot \frac{\text{J}}{\text{cm}^2}$$

The result is *used in this work as the integrated convective heat flux for the stagnation point during the flight*. To summarize, the convective heating rate at the stagnation point is 996 W/cm², and the integrated heat flux is ~19 KJ/cm².

7.3.3 Stagnation Point Heating - Radiative

An estimate of the radiative heat flux from the shock layer to the wall surface for flight speeds above about 6 km/s at the stagnation point is given by³³:

$$q_{\text{rs}} := 7.9 \cdot 10^7 \frac{\text{W}}{\text{cm}^2} \cdot \frac{R_{\text{nose}}}{1\text{m}} \cdot \left(\frac{\rho_{\text{fs}}}{\rho_0} \right)^{1.5} \cdot \left(\frac{V_e}{10^4 \frac{\text{m}}{\text{s}}} \right)^{12.5}$$

$$q_{\text{rs}} = 9.492 \times 10^7 \cdot \frac{\text{W}}{\text{m}^2} \qquad q_{\text{rs}} = 9.492 \times 10^3 \cdot \frac{\text{W}}{\text{cm}^2}$$

or about 5.6 times larger than the equivalently computed convective heating rate (1.7 KW/cm²). Again we use the corresponding free stream density for a given free stream (or probe) speed to get a profile of the maximum stagnation (radiative) heat flux from this equation (Figure 7-10).

$$q_{\text{rsf}}(x) := 7.9 \cdot 10^7 \frac{\text{W}}{\text{cm}^2} \cdot \frac{R_{\text{nose}}}{1\text{m}} \cdot \left(\frac{\rho_{\text{mod}}(x)}{\rho_0} \right)^{1.5} \cdot \left(\frac{V_{\text{sc}}(x)}{10^4 \frac{\text{m}}{\text{s}}} \right)^{12.5}$$

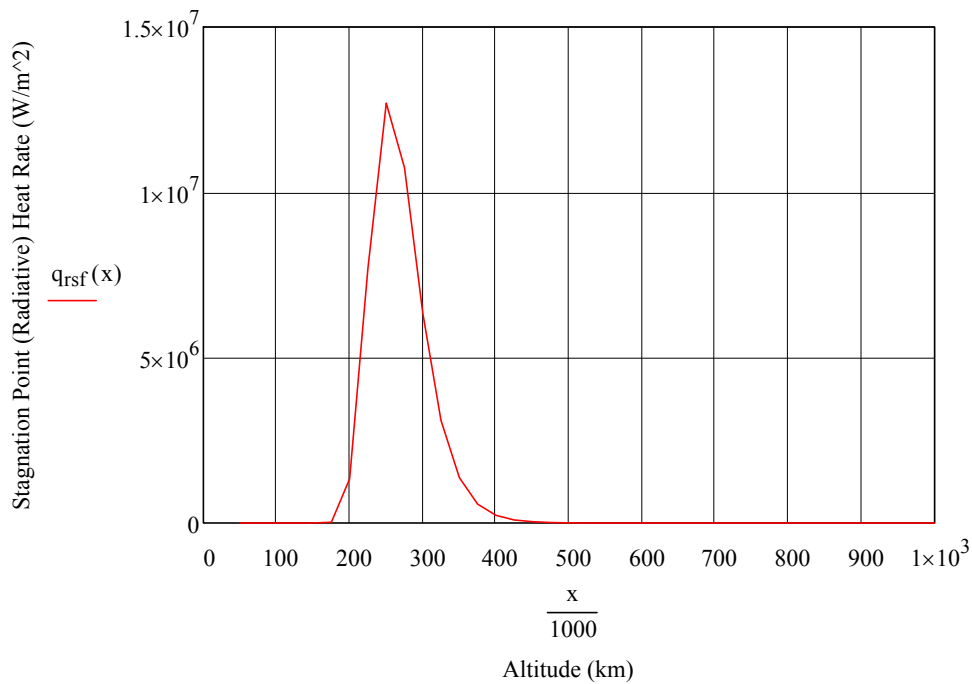


Figure 7-10: Radiative stagnation point heat flux versus altitude and corresponding free-stream density and speed

The maximum value so obtained is about

$$q_{rsf}(255\text{km}) = 1.279 \times 10^7 \cdot \frac{\text{W}}{\text{m}^2}$$

or

$$q_{rsf}(255\text{km}) = 1.279 \times 10^3 \cdot \frac{\text{W}}{\text{cm}^2}$$

This input is about 1.3 times the equivalent convective heating rate obtained before (996 W/cm^2), and hence radiation cannot be ignored at these entry speeds.

Again, it is necessary to check this result. The equilibrium and non-equilibrium radiation from the shock layer in air is given by Reference 39 as:

$$q_{rs2} := 10^{-\left[-0.6458 + 0.546 \frac{\text{s}}{\text{km}} \cdot V_e + (0.306 + 0.66) \cdot \log\left(\rho_{fs} \cdot R_{nose} \cdot \frac{\text{m}^2}{\text{kg}}\right)\right]} \frac{\text{W}}{\text{cm}^2} = 157.268 \cdot \frac{\text{W}}{\text{cm}^2}$$

This is about 8 times smaller number than the 1.3 KW/cm^2 given before.

Not surprisingly, we find that the radiative heating rate is rather difficult to estimate consistently. To attack this problem, a hypothesis is developed concerning the radiative heat flux from the shock layer into the wall as follows. From references (e.g., 40), we can reasonably assume that the radiative input is at least as large as the convective input for speeds between ~10 to 20 km/s. We also know that the gas will be heated to a significant level in the lower part of the trajectory, up to the point where dissociation and recombination occurs. Also, the Hirschel equation used here (Ref. 33) assumes a calorically and thermally perfect gas (with constant heat capacity), which is not true for high speeds. The heat capacity of the gas actually increases as available thermal energy is used to dissociate and ionize the gas molecules. The gas temperature will be smaller than expected, and radiation will also be smaller. What would be a reasonable number to use must be derived from more detailed work on the subject. In particular, we *derive a correlation of radiative heat flux versus convective heat flux for various missions* using Reference 41. The data is shown in Figure 7-11, and the correlation takes the form of a power curve as follows:

$$q_{rsf2}(x) := 10.063 \frac{W}{cm^2} \cdot \left(q_{gwsf}(x) \cdot \frac{cm^2}{W} \right)^{0.7594}$$

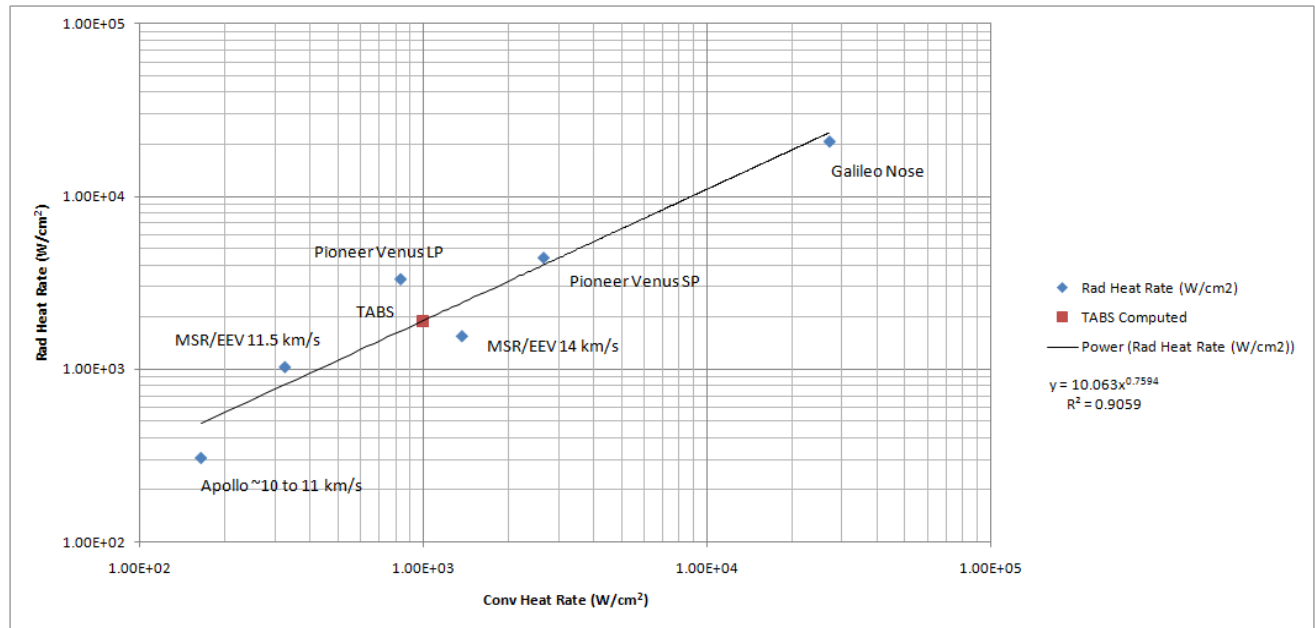


Figure 7-11: Developing a correlation between convective and radiative heating rate at the stagnation point based on results for different atmospheric entry missions

This correlation is then used to obtain an estimate of the peak heating rate at the stagnation point. To that end, the altitude for peak convection is used (245 km), yielding

$$q_{rsf2}(245km) = 1.903 \times 10^3 \cdot \frac{W}{cm^2}$$

for the corresponding convective heating rate of

$$q_{gwsf}(245km) = 995.745 \cdot \frac{W}{cm^2}$$

This data pair is shown in Figure 7-11 as the "TABS Computed" point in the plot.

We see that this is consistent with the result obtained at the peak of the profile of heating rate versus altitude given in Figure 7-10 (~1.3 KW/cm²), and gives confidence to the results for this particular speed. Nonetheless, the radiative input may very well range between these two numbers. We then *use the following value as the maximum radiative stagnation heating rate for this work*:

$$Q_{s\text{rmax}} := q_{\text{rsf}2}(245\text{km}) = 1.903 \times 10^3 \cdot \frac{\text{W}}{\text{cm}^2}$$

Figure 7-12 shows the radiative heating rate profile versus altitude for the correlation derived. The peak corresponds to $Q_{s\text{rmax}}$.

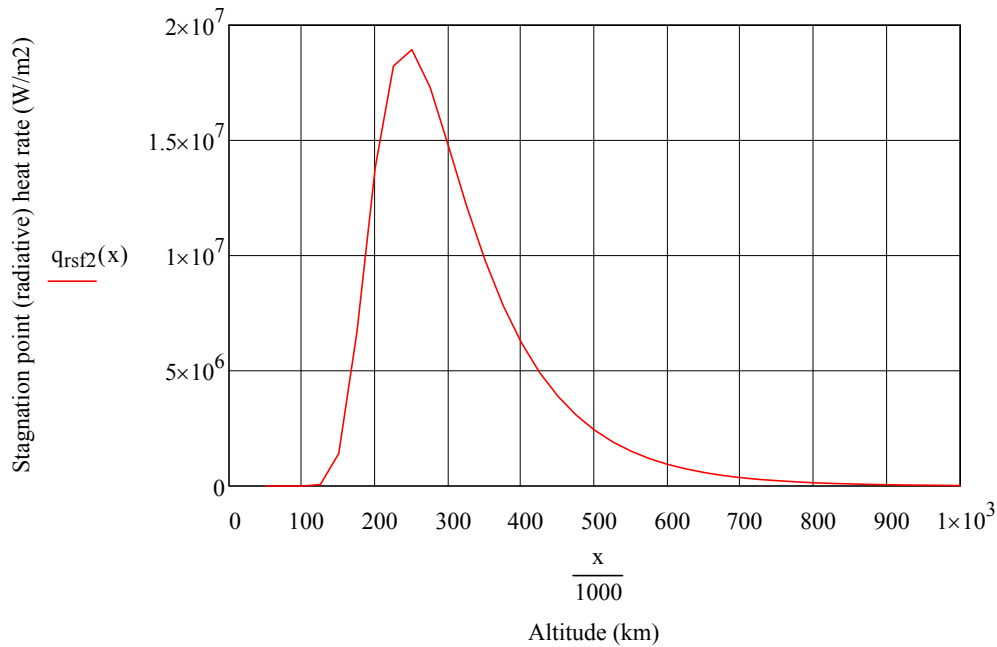


Figure 7-12: Stagnation point heating rate versus altitude derived from power curve correlation

An estimate for the integrated radiative heat rate input at the stagnation point is obtained for the maximum function derived above.

$$Q_{\text{RintMax}} := \int_{120\text{km}}^{1000\text{km}} \frac{q_{\text{rsf}2}(x)}{V_{\text{sc}}(x)} dx = 4.422 \times 10^4 \cdot \frac{\text{J}}{\text{cm}^2}$$

This is the *integrated radiative heating rate at the stagnation point to be used in this work*. Note that a similar result is obtained if we use the peak heating time as before

$$q_{\text{rsf}2}(245\text{km}) \cdot t_{\text{heat}} = 4.758 \times 10^4 \cdot \frac{\text{J}}{\text{cm}^2}$$

7.3.4 Total Heat Input at the Stagnation Point

The *total heating rate at the stagnation point* is then the sum of convective and radiative inputs, or $\sim 2.9 \text{ KW/cm}^2$:

$$Q_{\text{scmax}} = 995.745 \cdot \frac{\text{W}}{\text{cm}^2} \quad Q_{\text{srmx}} = 1.903 \times 10^3 \cdot \frac{\text{W}}{\text{cm}^2}$$

$$Q_{\text{Wt}} := Q_{\text{scmax}} + Q_{\text{srmx}} = 2.899 \times 10^7 \cdot \frac{\text{W}}{\text{m}^2} \quad \text{or} \quad Q_{\text{Wt}} = 2.899 \times 10^3 \cdot \frac{\text{W}}{\text{cm}^2}$$

Correspondingly, the *total integrated convective and radiative heat flux* at the stagnation point during the flight is $\sim 63 \text{ KJ/cm}^2$:

$$Q_{Tsp} := Q_{Cint} + Q_{RintMax} = 6.332 \times 10^4 \cdot \frac{\text{J}}{\text{cm}^2}$$

This is the number used at the plasma wind tunnel for testing the new TPS material developed through this dissertation.

This heat input necessitates an ablative heat shield design, and carbon-phenolic (or equivalent) is chosen (Ref. 42, Table 3). For comparison, the total maximum stagnation point heating (convection + radiation) for the Galileo probe was $\sim 35 \text{ KW/cm}^2$ at $\sim 60 \text{ km/s}$ inertial speed. The combined heating rates for the Pioneer Venus probes entering at $\sim 11.54 \text{ km/s}$ were ~ 5.2 to 10.6 KW/cm^2 , and the total integrated load from 12-14 KJ/cm^2 ⁴¹. The higher load result for TABS is consistent with its mass being ~ 2 times the entry mass of the Pioneer Venus large probe (about 317 kg versus 628 kg).

We now provide a rough check of our results given conservation of energy principles. We have estimated the total recovery enthalpy of the system per unit mass, as a function of the vehicle's kinetic energy on arrival.

$$H_{oe} = 5.449 \times 10^7 \cdot \frac{\text{J}}{\text{kg}}$$

Given the results from the aerothermodynamic analysis, the specific heat input (enthalpy) of the vehicle during its atmospheric deceleration is (using the stagnation point values as opposed to the body average results which do not include radiation),

$$Q_{Wt} \cdot \frac{S_w}{m_{sn}} \cdot t_{\text{heat}} = 1.262 \times 10^7 \cdot \frac{\text{J}}{\text{kg}} \quad (\text{using } t_{\text{heat}})$$

or

$$Q_{Tsp} \cdot \frac{S_w}{m_{sn}} = 1.103 \times 10^7 \cdot \frac{\text{J}}{\text{kg}} \quad (\text{using the integrals})$$

This value is within an order of magnitude of the recovery enthalpy. The fact that it is smaller indicates that not all the energy transported toward the vehicle results in heating of the vehicle surface. Thankfully, much of it is dissipated in the atmosphere during entry, especially one considers that the stagnation point heating is the worst case scenario for the whole vehicle. Hence, from conservation of energy, some of the kinetic energy converted into heat enters the vehicle, some does not. What does not, is dissipated through convection (and ablation for our case), and radiated away into the surrounding atmosphere.

7.3.5 Thermal Protection System (TPS) Requirements

The TPS material choice must be such that the total heat into the vehicle is dissipated effectively in order to avoid structural failure. Since this is a single point failure, there must be confidence in the results. Testing and ample safety margins can be applied. Optimization of the material choice for a given application must also be exercised however, if the system is not to be "over-designed". To that effect, we look at the most efficient material choices for TABS. Since the heat inputs are relatively large, it was already established that an ablator is necessary, as they are capable of accommodating high heat loads and rates through phase change and mass loss. Exactly which type is in question.

Typically an ablator is characterized by its density. The higher the density, the greatest its strength but also its thermal conductivity. A balance must be achieved such that strength does not compromise the TPS' ability to effectively remove heat. Since thermal conductivity increases with density, so does the likelihood of Char "spallation". Spallation is to be avoided, as it consumes material with inefficient removal of heat. In order to ascertain the density requirements of the TPS material, Figure 7-13 shows the "optimal" performance regime of a TPS material based on the pressure/thermal environment ⁴¹. As can be seen, a high-density material is most appropriate for TABS. The high-density heritage Carbon/Phenolic materials are about 1.45 gm/cm^3 . This value is used in determining the TPS mass requirements. Also, this is the target for the new TPS material to be developed in the laboratory (Appendix A).

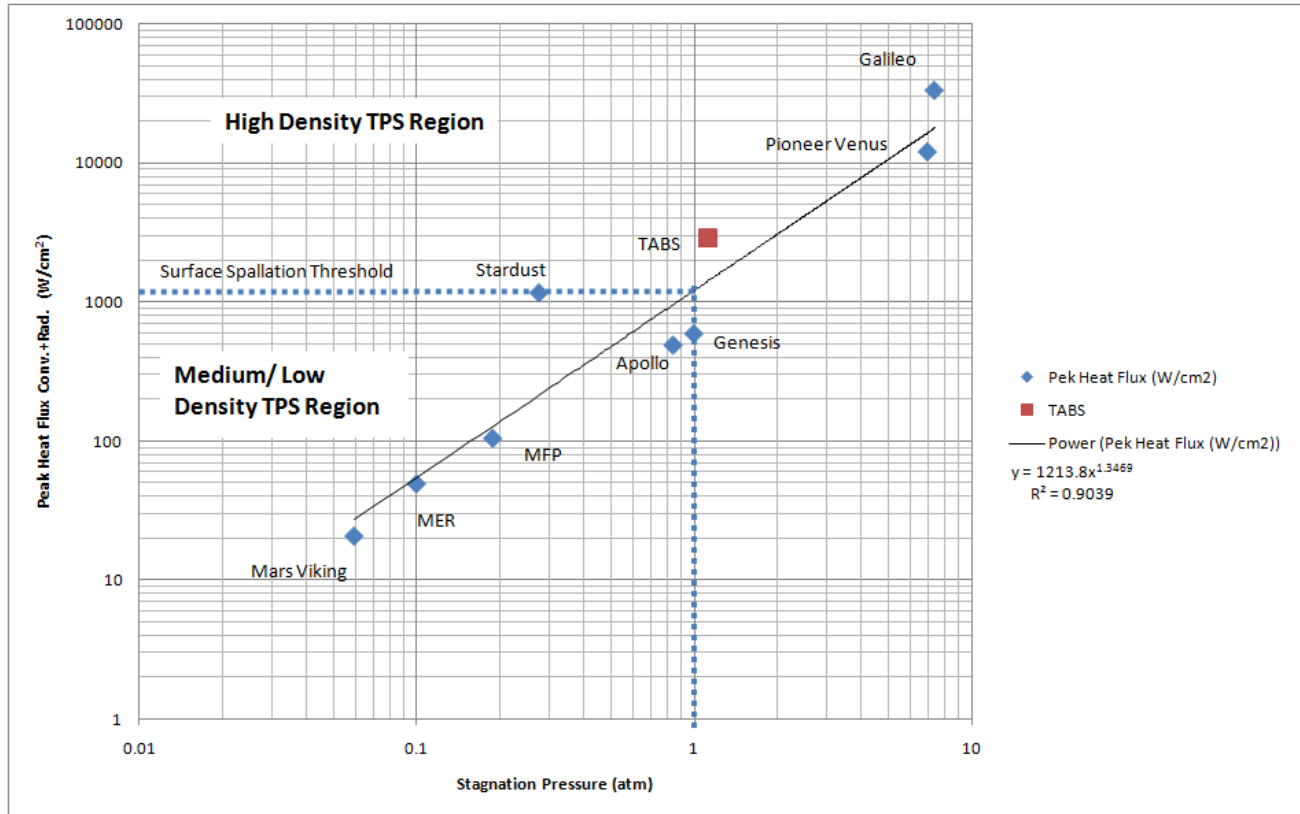


Figure 7-13: Ablative TPS material density requirement based on pressure and peak heat flux environment

We now estimate the thermal protection requirements. As illustrated in Figure 7-13, of particular relevance is heritage high-density Carbon/Phenolic or equivalent^{41,42}, the material choice for TABS' heat shield. A few material properties are summarized.

$$h_v := 26.5 \cdot 10^6 \frac{\text{J}}{\text{kg}}$$

Heat of ablation for (non-pure) Carbon is 29.7 MJ/kg¹⁰. Nylon Phenolic is 23.3 MJ/kg³⁹. Use the average. (Note: enthalpy of vaporization for pure carbon is 59.2 x 10⁶ J/kg)

$$\rho_{hs} := 1.45 \frac{\text{gm}}{\text{cm}^3}$$

Heat shield density (average TABS TPS measured density, Appendix A)

$$t_{hs} := \frac{Q_{Tsp}}{h_v \cdot \rho_{hs}} = 1.648 \cdot \text{cm}$$

The forebody heat shield thickness. Since this value had to be iterated, 1.62 cm was adopted for TABS heat shield sizing (Table 6-3). Results shown in Appendix A will update this requirement based on actual data.

This is a reasonable estimate, consistent with data shown in Reference 35 for charring ablator recession (~0.8 cm), given an equivalent recovery enthalpy as that found in TAB's entry. The extra thickness hence provides a ~2x safety factor, appropriate for the current analysis. As a means of comparison with previous missions, the Galileo probe burned through ~ 4.6 cm of Carbon/Phenolic heat shield material⁴¹, entering at an inertial speed about 6 times faster than TABS.

The temperature at the wall of the front shield is now estimated. If the entry vehicle surface is radiation cooled, and the heat flux into the wall has reached a state of nearly zero, then the wall temperature is in equilibrium and is equal to the radiation adiabatic temperature (a surface is called an "adiabatic surface" when no exchange of heat takes place). This "radiation adiabatic wall" has the following heat flux properties: $q_w \sim 0$; $q_{rad} = q_{conv}$ (where $q_{conv} = q_{gw}$ - the heat flux of the gas at the wall); $T_w = T_{ra}$ (wall temperature is the radiation adiabatic temperature). The actual emissivity of a material will vary depending on temperature and surface finish. For carbon (as well as black paint), the average emissivity under varying conditions is about 0.85⁸. Since carbon is the main constituent of the TABS TPS heat shield, the emissivity can be reasonably set to ~0.85, and the flux balance ($q_{rad} = q_{conv}$) yields

$$\epsilon_s := 0.85 \quad \text{TPS material emissivity}$$

$$\sigma := 5.670400 \cdot 10^{-8} \frac{\text{W}}{\text{m}^2 \cdot \text{K}^4} \quad \text{Stefan- Boltzmann constant}$$

$$T_w := \sqrt[4]{\frac{Q_{scmax}}{\sigma \cdot \epsilon_s}} = 3.791 \times 10^3 \text{ K} \quad \text{or} \quad T_w = 3.518 \times 10^3 \cdot ^\circ\text{C}$$

This provides an order of magnitude estimate of the *maximum temperature at the stagnation point, for a radiatively cooled surface*. Since TABS is ablatively cooled, the maximum surface temperature is expected to be significantly lower. This temperature depends sharply on the TPS material properties, and hence will be measured from plasma wind tunnel tests of candidate TABS TPS samples (Appendix A).

For a radiatively cooled surface, the stagnation point surface temperature evolution during the flight path can be represented by

$$T_{wx}(x) := \sqrt[4]{\frac{q_{gwsf}(x)}{\sigma \cdot \epsilon_s}}$$

This is shown in Figure 7-14.

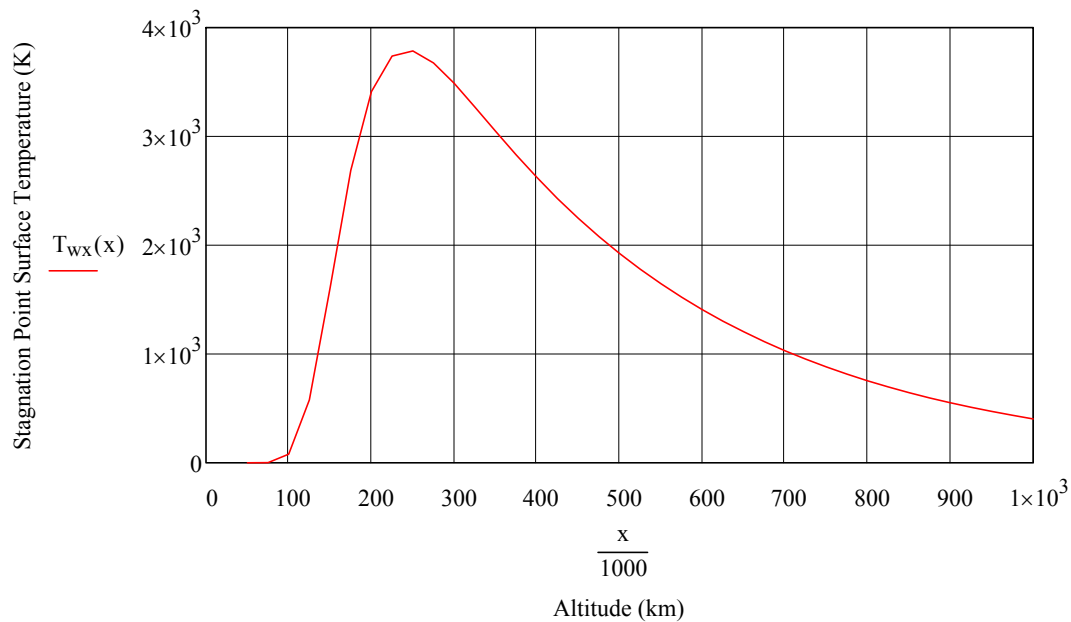


Figure 7-14: Front Shield maximum surface temperature assuming radiation cooling alone

We now estimate the heat shield requirements for the afterbody, based on the stagnation point heating rates. Not much data has been collected on afterbody heating, but data shown in Reference 43 from Fire-II at comparable entry speeds in Earth's atmosphere indicates that this heating is only a fraction of the stagnation point value. Furthermore, it shows that radiation heating of the afterbody is expected to be negligible. We consider here the 1.5% of the total stagnation heating as the value to use for aft shield sizing, and include the radiative heating as well due to the presence of methane in Titan, which contributes to a significant higher radiation value compared to Earth:

$$Q_{Wta} := 0.015 \cdot Q_{Wt} = 43.487 \cdot \frac{\text{W}}{\text{cm}^2}$$

$$Q_{Ta} := 0.015 \cdot Q_{Tsp} = 949.764 \cdot \frac{\text{J}}{\text{cm}^2}$$

A light-weight material is chosen. From Ref. 42, Table 4, SLA 561 (Super Lightweight Ablator) is a good candidate for the heat loads at hand. With this, we compute the shield thickness:

$$h_{va} := 12.1 \cdot 10^6 \frac{\text{J}}{\text{kg}} \quad \text{Heat of ablation for SLA 561 (Ref. 39, pg. 181)}$$

$$\rho_{hsa} := 0.256 \frac{\text{gm}}{\text{cm}^3} \quad \text{Heat shield density (SLA 561)}$$

$$t_{hsa} := \frac{Q_{Ta}}{h_{va} \cdot \rho_{hsa}} = 0.307 \cdot \text{cm} \quad \text{The afterbody heat shield thickness to be used for mass sizing. The iterative result used in Table 6-3 (0.338 cm) is hence appropriate.}$$

The radiation adiabatic maximum surface temperature of the aft shell is estimated the same way as for the front shell. Assuming the same emissivity, and entering the corresponding values we obtain

$$T_{wb} := \sqrt[4]{\frac{0.015 Q_{scmax}}{\sigma \cdot \epsilon_s}} = 1.327 \times 10^3 \text{ K} \quad \text{or} \quad T_{wb} = 1.054 \times 10^3 \cdot ^\circ\text{C}$$

7.4 Aerothermodynamic Model Validation Based on Huygens Results

Although the results obtained so far have been found reasonable by comparison with references throughout, it may be useful to run a complete analysis of Huygens atmospheric entry parameters through the same assumptions and formulas used in this work, and compare the results with those obtained by numerical methods. This section will run through this exercise, and summarize the results of both TABS and Huygens based on the engineering model at hand.

7.4.1 Entry Aerodynamics

Figure 7-15 shows the basic geometry and dimensions of the Huygens probe. Combined with entry parameters, the following variables are defined ^{44,45}:

$$\gamma_e := -65.1 \text{deg}$$

$$V_e := 6.022 \frac{\text{km}}{\text{s}}$$

$$\delta_{\text{ha}} := 60.0 \text{deg} \quad \text{Front shell cone half angle}$$

$$C_D := 2 \cdot \sin(\delta_{\text{ha}})^2 = 1.5 \quad \text{Coefficient of drag}$$

The vehicle reference area for drag is ⁴⁵,

$$A_s := \pi \cdot (1.35 \text{m})^2 = 5.726 \text{m}^2 \quad \text{Design cross-sectional area}$$

which is the projected area of the 2.70-meter diameter front shield. The spacecraft ballistic coefficient C_B is given by ⁴⁶:

$$m_{\text{sn}} := 320 \text{kg}$$

Hence

$$C_B := \frac{m_{\text{sn}}}{A_s \cdot C_D} = 37.26 \cdot \frac{\text{kg}}{\text{m}^2}$$

where m_{sn} is again the probe mass at Titan entry.

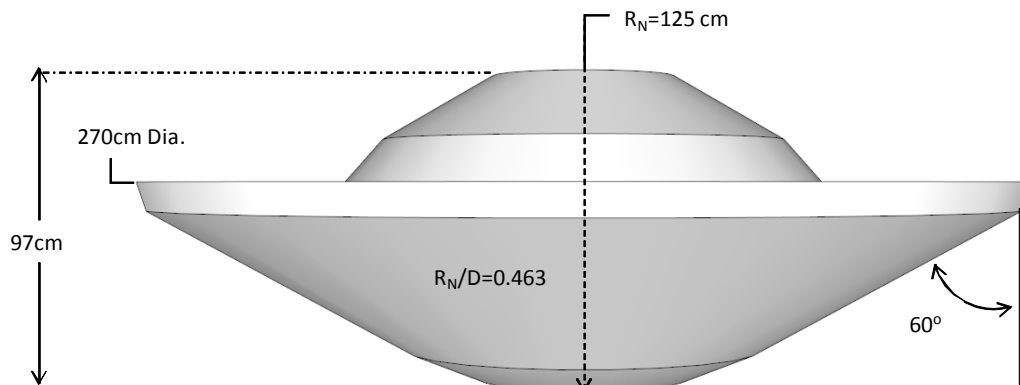


Figure 7-15: Huygens Probe Aeroshell geometry and dimensions

Since $\beta := 2.5 \cdot 10^{-5} \text{m}^{-1}$ and $g_e := 0.009807 \frac{\text{km}}{\text{s}^2}$

the maximum deceleration and G-load are then

$$a_{\max} := \frac{-\beta \cdot V_e^2}{2 \cdot e} \cdot \sin(\gamma_e) = 151.26 \text{ m} \cdot \text{s}^{-2}$$

$$g_{\text{load}} := \frac{a_{\max}}{g_e} = 15.424 \quad \text{Gs}$$

The accelerometer measurements from Huygen's were clipped at 10 Gs. However, from Ref. 44, Fig 3 it can be seen that ~15 G is a likely result. Furthermore, Reference 47, Figures 2b and 5, show an estimated maximum deceleration of ~120 m/s² with a ~ 2m/s² residual peak-to-peak. Hence the estimated G-load for Huygens is

$$\frac{120 \text{ m} \cdot \text{s}^{-2}}{g_e} = 12.236 \quad \pm \quad \frac{2 \text{ m} \cdot \text{s}^{-2}}{g_e} = 0.204 \quad \text{Gs}$$

This is also consistent with the predictions of Reference 48, Fig 1. of ~ 12 Gs.

It is hence concluded that *the current model provides an acceptable estimate of peak deceleration loads*. As expected from the density model chosen however, the predicted deceleration load is more conservative since the model density is somewhat larger than the data shows.

The critical altitude at which the maximum deceleration occurs is given by

$$\rho_0 := 0.7763 \frac{\text{kg}}{\text{m}^3} \quad h_{\text{crit}} := \frac{1}{\beta} \cdot \ln \left(\frac{-1}{\beta} \cdot \frac{1}{C_B} \cdot \frac{\rho_0}{\sin(\gamma_e)} \right) = 272.923 \cdot \text{km}$$

From Ref 47 and DISR data, the estimated altitude of peak deceleration is about 246 km, somewhat lower than predicted here. Again, this is expected based on a higher density model.

The velocity evolution as a function of altitude (or density) and flight path angle is given by

$$V_{\text{sc}}(x) := V_e \cdot \exp \left[\left(\frac{1}{2 \cdot \beta} \cdot \frac{\rho_0}{\sin(\gamma_e)} \cdot \frac{A_s \cdot C_D}{m_{\text{sn}}} \right) \cdot \exp(-\beta \cdot x) \right] \quad x := 50 \text{ km}, 75 \text{ km} \dots 1000 \text{ km}$$

From this, the critical speed at which maximum deceleration occurs is

$$V_{\text{sc}}(h_{\text{crit}}) = 3.653 \cdot \frac{\text{km}}{\text{s}}$$

From DISR data the corresponding velocity at the critical altitude of 272.9 km is about 12,712 km/hr, or 3.53 km/s, in good agreement with the model here.

For a desired drogue deployment speed between Mach 1 and 2, the flight time from the 1000 km entry interface and the corresponding velocity at the time of deployment is estimated. From the velocity evolution, the flight time through the atmosphere is

$$x_0 := 50 \text{ km} \quad x_1 := 1000 \text{ km} \quad \text{incr} := 5 \text{ km}$$

$$N_{\text{et}} := \text{ceil} \left(\frac{x_1 - x_0}{\text{incr}} \right) \quad N_{\text{et}} = 190 \quad i := 0 \dots N_{\text{et}}$$

$$t_{x_i} := \left(\frac{\text{incr}}{V_{\text{sc}}(x_1 - i \cdot \text{incr})} \right) \quad \text{the flight time evolution per 10km interval, from 1000km down to 50 km.}$$

The Mach number over the trajectory is expressed as

$$c_s := 0.279 \frac{\text{km}}{\text{s}} \quad \text{The speed of sound at relevant altitudes in Titan}$$

$$M_a(x) := \frac{V_{sc}(x)}{c_s}$$

The desired drogue opening Mach number occurs then at

$$M_a(x_1 - 159\text{incr}) = 1.405$$

which corresponds to an altitude of 205 km

$$M_a(205\text{km}) = 1.405 \quad \text{drogue deployment}$$

The vehicle velocity at time of deployment is

$$V_{sc}(205\text{km}) = 392.089 \text{ m} \cdot \text{s}^{-1}$$

The total ballistic entry flight time to drogue deployment is hence

$$t_{\text{bef}} := \sum_{i=0}^{159} t_{x_i} = 183.702 \text{ s}$$

From DISR data, the drogue deployed at a speed of about 382 m/s (Ref. 44 shows 310 m/s), at an altitude of about 153 km, and some 203 seconds from an altitude of 925 km. Clearly, the results here are reasonable. Again, the higher density model used for the ballistic corridor results in a higher deployment altitude and shorter flight time for a given speed, although not significantly different to loose confidence on this first-order approximation.

The dynamic pressure, at the stagnation point given our exponential atmospheric model is

$$\rho_{\text{mod}}(h) := \rho_0 \cdot e^{-\beta \cdot h}$$

$$P_{\text{sp}}(x) := \frac{1}{2} \cdot \rho_{\text{mod}}(x) \cdot (V_{sc}(x))^2$$

The maximum dynamic pressure corresponds to the critical altitude (maximum deceleration) and is then

$$P_{\text{sp}}(h_{\text{crit}}) = 5.636 \times 10^3 \cdot \text{Pa} \quad P_{\text{sp}}(h_{\text{crit}}) = 0.056 \cdot \text{bar} \quad P_{\text{sp}}(h_{\text{crit}}) = 0.056 \cdot \text{atm}$$

where $h_{\text{crit}} = 272.923 \cdot \text{km}$

This value is in agreement with the 0.1 atm found in the references ⁴⁶.

The drag force is

$$F_D(x) := P_{\text{sp}}(x) \cdot C_D \cdot A_s$$

The maximum drag force is then

$$F_D(h_{\text{crit}}) = 4.84 \times 10^4 \cdot \text{N}$$

The dynamic pressure at the time of drogue deployment for this case is

$$P_{\text{sp}}(205\text{km}) = 354.822 \cdot \text{Pa}$$

$$M_a(205\text{km}) = 1.405$$

The Mach number and corresponding pressure agrees with data in Reference 10, Table 4.2 for deployment of the Huygens pilot (M~1.5, P_{sp}~400 Pa).

7.4.2 Entry Aerothermodynamics

The *entry heating* parameters for Huygens are now also estimated based on the same formulas and assumptions used for TABS.

$$V_{ef} := V_{sc}(205\text{km}) = 392.089 \text{ m}\cdot\text{s}^{-1}$$

$$L_s := 0.97\text{m} \quad \text{Huygens body axial length}^{46}$$

$$V_{ave} := 5.54 \frac{\text{km}}{\text{s}} \quad \text{Weighted average velocity through the atmospheric flight}$$

$$\mu_{vN2}(T_{N2}) := \frac{0.1 \cdot 5.58114 \cdot 10^{-4} \cdot T_{N2}^{1.04322}}{T_{N2} + 900.67} \frac{\text{kg}}{\text{m}\cdot\text{s}} \quad \text{Viscosity of Nitrogen at 1 atm and temperature } T_{N2}$$

$$T_{N2a} := 500 \quad \text{Boundary layer estimated temperature for viscosity - Kelvin}$$

$$\rho_{max} := \rho_{mod}(205\text{km}) = 4.616 \times 10^{-3} \text{ m}^{-3} \cdot \text{kg} \quad \text{Maximum atmospheric density reached by spacecraft during ballistic flight}$$

$$Re_L := \frac{\rho_{max} \cdot V_{ave} \cdot L_s}{\mu_{vN2}(T_{N2a})} = 9.518 \times 10^5 \quad \text{Reynolds number, dimensionless}$$

$$C_F := \frac{1.328}{\sqrt{Re_L}} \quad C_F = 1.361 \times 10^{-3} \quad \text{Skin friction coefficient, dimensionless}$$

The *total (convective) heat load* (E_L) into the spacecraft is obtained from

$$S_w := 193803.2\text{cm}^2 = 19.38\text{m}^2 \quad \text{spacecraft body "wall" area exposed to entry heating, or "total aeroshell wetted area" - From Huygens CAD, Fig. 7-15}$$

$$E_L := \frac{1}{4} \cdot m_{sn} \cdot (V_e^2 - V_{ef}^2) \cdot \frac{S_w \cdot C_F}{A_s \cdot C_D} = 8.874 \times 10^6 \cdot \text{J}$$

This equation is valid for an entry profile where the spacecraft slows-down sufficiently enough ("light" vehicle). A light vehicle criterion is obtained from ballistic entry analysis and is given by:

$$0 < -\sin(\gamma_e) = 0.907 < \frac{1}{C_B} \cdot \frac{\rho_{max}}{\beta} = 4.956 \quad (\text{true})$$

The *maximum body average (convective) heating rate*, and the density (altitude) and velocity at which it occurs.

$$q_{avmax} := \frac{C_F}{6 \cdot e} \cdot \frac{m_{sn}}{A_s \cdot C_D} \cdot \beta \cdot V_e^3 \cdot \sin(\gamma_e) = -1.54 \cdot \frac{\text{W}}{\text{cm}^2} \quad \text{or} \quad q_{avmax} = -1.54 \times 10^4 \cdot \frac{\text{W}}{\text{m}^2}$$

The critical density at which the peak heat rate occurs is found from

$$\rho_{crit} := \frac{-2}{3} \cdot \frac{m_{sn}}{A_s \cdot C_D} \cdot \beta \cdot \sin(\gamma_e) = 5.633 \times 10^{-4} \cdot \frac{\text{kg}}{\text{m}^3}$$

Since

$$h(\rho) := \frac{-1}{\beta} \cdot \ln\left(\frac{\rho}{\rho_0}\right)$$

The corresponding altitude is

$$h(\rho_{\text{crit}}) = 289.141 \cdot \text{km}$$

Note that this is about the same altitude of peak deceleration, and so the result is consistent with expectation.

The critical velocity is

$$V_{\text{crit2}} := \frac{V_e}{\sqrt[3]{e}} = 4.315 \cdot \frac{\text{km}}{\text{s}}$$

Now, compute the *Stagnation Point Heat Flux* for both convection and radiation following a similarity analysis to Earth entry computations, as given by Fay and Riddell and others (Hirschel p. 34). Start with the *convective* or gas-to-wall stagnation heating.

$$R_{\text{nose}} := 1.25\text{m} \quad \text{Front shield spherical nose radius of curvature}^{45}$$

$$\rho_{\text{fs}} := 0.00028 \frac{\text{kg}}{\text{m}^3} \quad \text{Average "free stream" atmospheric density for ballistic corridor altitudes between 205 to 1000 km, from EM data (Fig. 7-5).}$$

$$q_{\text{gws}} := 11030 \cdot \frac{\text{W}}{\text{cm}^2} \cdot \sqrt{\frac{1\text{m}}{R_{\text{nose}}}} \cdot \left(\frac{\rho_{\text{fs}}}{\rho_0}\right)^{0.5} \cdot \left(\frac{V_e}{7950 \frac{\text{m}}{\text{s}}}\right)^{3.15}$$

$$q_{\text{gws}} = 78.111 \cdot \frac{\text{W}}{\text{cm}^2} \quad \text{or} \quad q_{\text{gws}} = 7.811 \times 10^5 \cdot \frac{\text{W}}{\text{m}^2}$$

Where the free stream density is taken at the critical altitude. This heat flux is about 51 times larger than the total body average heating rate.

A plot of the stagnation point heat flux versus altitude is shown in Figure 7-16, and the function is

$$q_{\text{gwsf}}(x) := 11030 \cdot \frac{\text{W}}{\text{cm}^2} \cdot \sqrt{\frac{1\text{m}}{R_{\text{nose}}}} \cdot \left(\frac{\rho_{\text{mod}}(x)}{\rho_0}\right)^{0.5} \cdot \left(\frac{V_{\text{sc}}(x)}{7950 \frac{\text{m}}{\text{s}}}\right)^{3.15}$$

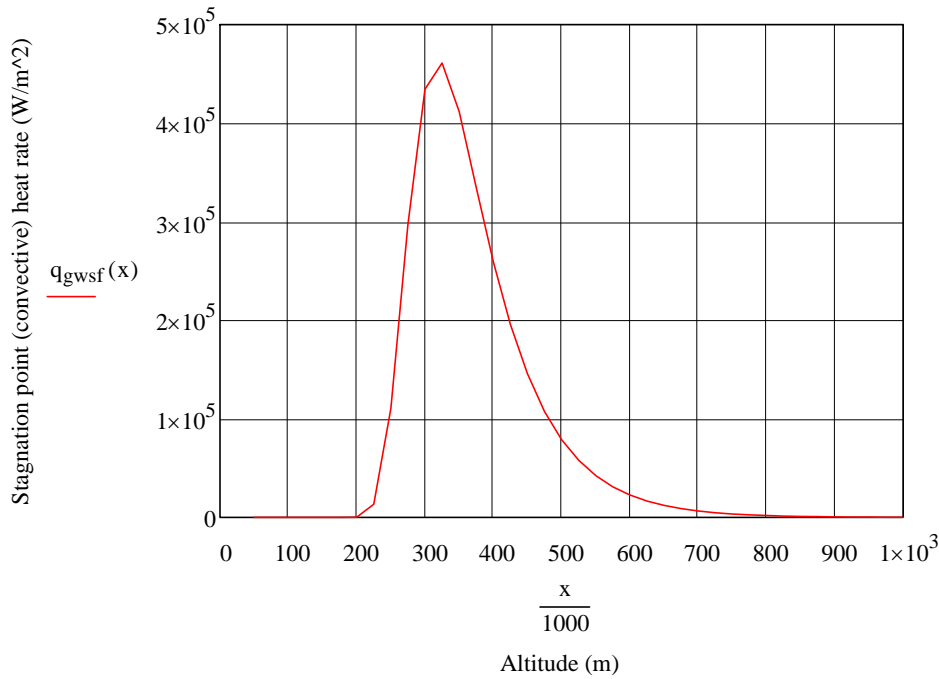


Figure 7-16: Predicted Huygens stagnation point (convective) heating rate

The maximum value is then about 320 km altitude, consistent with ballistic entry analysis.

$$Q_{scmax} := q_{gwsf}(320\text{km}) = 4.636 \times 10^5 \cdot \frac{\text{W}}{\text{m}^2} \quad \text{or} \quad Q_{scmax} = 46.36 \cdot \frac{\text{W}}{\text{cm}^2}$$

This value is remarkably close to the more sophisticated predictive result with a maximum $\sim 46 \text{ W/cm}^2$ at the stagnation point ⁴⁹.

The integrated convective heating for the stagnation point during the flight is

$$Q_{Cint} := \int_{205\text{km}}^{1000\text{km}} \frac{q_{gwsf}(x)}{V_{sc}(x)} dx = 1.54 \times 10^3 \cdot \frac{\text{J}}{\text{cm}^2}$$

Another way to estimate this is

$$Q_{scmax2} := 0.0353 \cdot \frac{\text{J}}{\text{cm}^2} \cdot \left(\frac{C_B}{R_{nose} \cdot \beta \cdot \sin(-\gamma_e)} \cdot \frac{\text{m}^2}{\text{kg}} \right)^{0.5} \cdot \left(\frac{V_e}{1000 \frac{\text{m}}{\text{s}}} \right)^2 = 1.468 \times 10^3 \cdot \frac{\text{J}}{\text{cm}^2}$$

Finally, this may also be estimated from the total flight time corresponding to the peak in either the convective or radiated stagnation point heating. That corresponds to the time between $\sim 400\text{km}$ to 250km .

$$t_{heat} := 32.9\text{s} \quad \text{flight time where majority of heat input occurs}$$

$$Q_{scmax2t} := Q_{scmax} \cdot t_{heat} = 1.525 \times 10^3 \cdot \frac{\text{J}}{\text{cm}^2}$$

All results in reasonable agreement.

An estimate of the *radiative heating rate* from the shock layer to the wall surface for flight speeds near and above about 6 km/s at the stagnation point is given by

$$q_{rs} := 7.9 \cdot 10^7 \frac{W}{cm^2} \cdot \frac{R_{nose}}{1m} \cdot \left(\frac{\rho_{fs}}{\rho_0} \right)^{1.5} \cdot \left(\frac{V_e}{10^4 \frac{m}{s}} \right)^{12.5}$$

$$q_{rs} = 1.194 \times 10^4 \cdot \frac{W}{m^2} \quad \text{or} \quad q_{rs} = 1.194 \cdot \frac{W}{cm^2}$$

Using the corresponding free stream density for a given free stream (or probe) speed gives (Figure 7-17)

$$q_{rsf}(x) := 7.9 \cdot 10^7 \frac{W}{cm^2} \cdot \frac{R_{nose}}{1m} \cdot \left(\frac{\rho_{mod}(x)}{\rho_0} \right)^{1.5} \cdot \left(\frac{V_{sc}(x)}{10^4 \frac{m}{s}} \right)^{12.5}$$

The maximum value is about

$$q_{rsf}(330km) = 1.642 \times 10^3 \cdot \frac{W}{m^2} \quad \text{or} \quad q_{rsf}(330km) = 0.164 \cdot \frac{W}{cm^2}$$

A relatively small value compared with the convective heating rate.

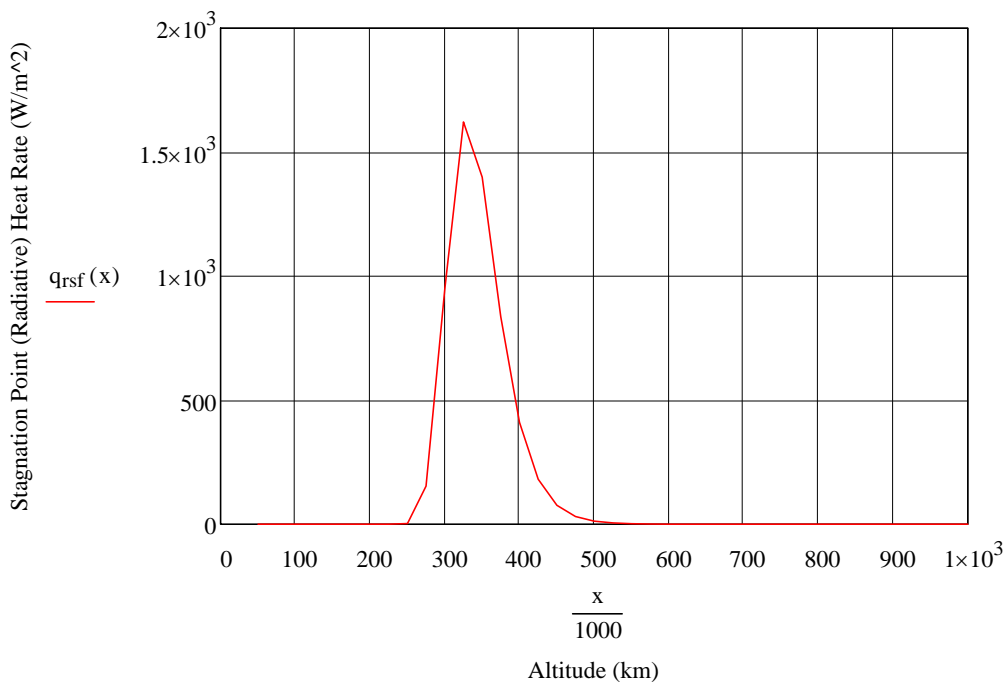


Figure 7-17: Radiative stagnation point heat flux versus altitude and corresponding free-stream density and speed

The power curve correlation on the other hand gives

$$q_{rsf2}(x) := 10.063 \frac{W}{cm^2} \cdot \left(q_{gwsf}(x) \cdot \frac{cm^2}{W} \right)^{0.7594}$$

with a peak at about 320 km, or

$$q_{rsf2}(320\text{km}) = 185.351 \cdot \frac{W}{\text{cm}^2}$$

All possible results for the radiative heating rate at the stagnation point are given below

$$q_{rsf2}(320\text{km}) = 185.351 \cdot \frac{W}{\text{cm}^2} \quad \text{using peak of power curve correlation baseline for TABS}$$

$$q_{rsf2}(h_{\text{crit}}) = 126.688 \cdot \frac{W}{\text{cm}^2} \quad \text{using power curve correlation but at the critical altitude}$$

$$q_{rsf}(330\text{km}) = 0.164 \cdot \frac{W}{\text{cm}^2} \quad \text{using formula in Ref. 33 with corresponding free stream density and velocity}$$

$$q_{rs} = 1.194 \cdot \frac{W}{\text{cm}^2} \quad \text{using formula in Ref. 33 with average free stream density for ballistic corridor and entry speed.}$$

The range of radiative heating rates are shown in Figure 7-18, together with the convective heating rate.

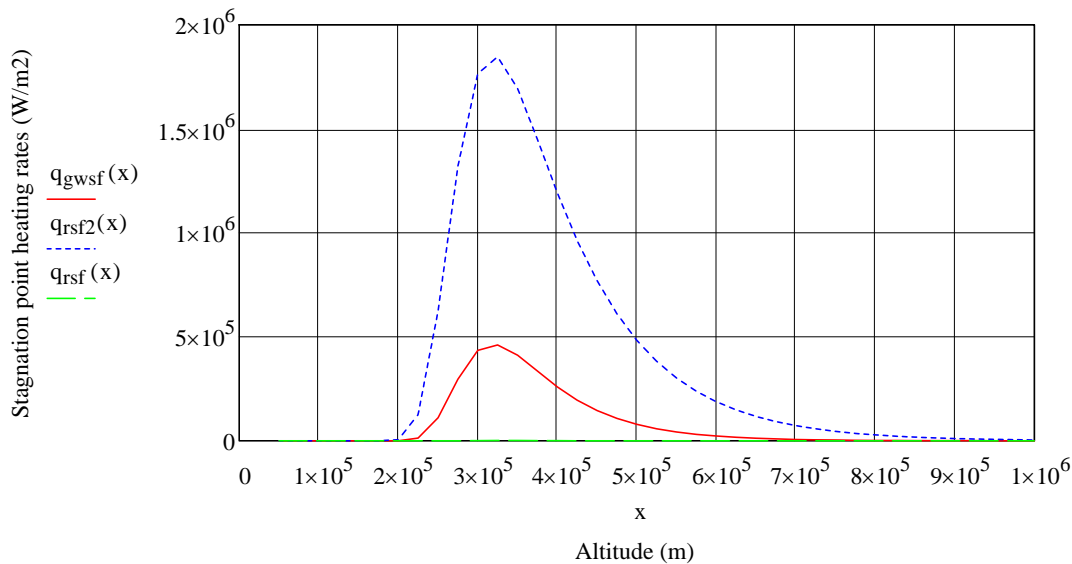


Figure 7-18: Convective heating rate and range of radiative heating rates for Huygens based on EM assumptions

The result obtained using the peak of the power curve correlation baseline for TABS ($\sim 185 \text{ W/cm}^2$) is larger, but not out of family with the maximum results from sophisticated analysis ($\sim 150 \text{ W/cm}^2$) at the stagnation point (Reference 49, Fig. 10). In fact the radiative heat flux increases for Huygens shield away from the stagnation point, reaching a predicted maximum of 180 W/cm^2 at the edge. It should be pointed out however, that the power fit equation here was derived for speeds greater than $\sim 10 \text{ km/s}$, so it may not be the best model to use in this case. Nonetheless, even with sophisticated analysis, radiation is difficult to predict. For instance, Reference 50 shows large variations in the radiative heating rates at the stagnation point, varying from $\sim 4 \text{ W/cm}^2$ to $\sim 70 \text{ W/cm}^2$, in line with the results obtained here. The lower value is consistent with Ref. 33, if we use the free stream average density. The power equation over-estimates the heat rate, but this may be a conservative number to use at this stage in the TABS design process. In particular, reference 51, Fig. 8, shows a total and 1D maximum radiative heat flux from 120 to $\sim 160 \text{ W/cm}^2$ for a -65 deg flight path without absorption, depending on the model used. This highlights the difficulty in accurately estimating the radiative heating rate, and brings the current analysis closer to the more sophisticated analyses. Indeed, the functions q_{rsf} and q_{rsf2} in their "simplicity", are good enough to bound the radiation problem for a preliminary design.

We then use as the maximum radiative stagnation heat flux as

$$Q_{srmax} := q_{rsf2}(320km) = 185.351 \cdot \frac{W}{cm^2}$$

The integrated radiative heat rate input at the stagnation point is then

$$Q_{RintMax} := \int_{205km}^{1000km} \frac{q_{rsf2}(x)}{V_{sc}(x)} dx = 7.438 \times 10^3 \cdot \frac{J}{cm^2}$$

Or using t_{heat}

$$Q_{srmax} \cdot t_{heat} = 6.098 \times 10^3 \cdot \frac{J}{cm^2}$$

The *total heating rate at the stagnation point* is then the sum of convective and radiative inputs.

$$Q_{scmax} = 46.36 \cdot \frac{W}{cm^2} \quad Q_{srmax} = 185.351 \cdot \frac{W}{cm^2}$$

$$Q_{Wt} := Q_{scmax} + Q_{srmax} = 2.317 \times 10^6 \cdot \frac{W}{m^2} \quad \text{or} \quad Q_{Wt} = 231.711 \cdot \frac{W}{cm^2}$$

The *total integrated convective and radiative heat flux* for the stagnation point during the flight is then,

$$Q_{Tsp} := Q_{Cint} + Q_{RintMax} = 8.978 \times 10^3 \cdot \frac{J}{cm^2}$$

Using t_{heat} this would be

$$(Q_{scmax} + Q_{srmax}) \cdot t_{heat} = 7.623 \times 10^3 \cdot \frac{J}{cm^2}$$

Reference 50 shows a range from 2.1 to 4.2 KJ/cm² depending on the model. Hence the results here are conservative, but within an order of magnitude appropriate for this design level.

We now estimate the thermal protection requirements for Huygens, based on the AQ60/I material used. Since a NASA thermochemical model ⁵² attributes the ablation of AQ60 to the vaporization of silica (the predominant component in AQ60), we will then use the heat of vaporization of glass (~12.5 kJ/gm) as the assumed value for this material.

$$h_v := 12.5 \cdot 10^6 \frac{J}{kg} \quad \text{Assumed heat shield ablation for AQ60/I}$$

$$\rho_{hs} := 280 \frac{kg}{m^3} \quad \text{Heat shield density (AQ60/I, Ref. 46)}$$

$$t_{hs} := \frac{Q_{Tsp}}{h_v \cdot \rho_{hs}} = 2.565 \cdot cm \quad \text{The forebody heat shield thickness}$$

The front shield thickness of Huygens was 1.74 to 1.82 cm⁴⁶, so the result here is appropriately conservative. A heat of ablation of roughly 17 MJ/kg instead of 12.5 MJ/kg would result in the same thickness as that chosen for Huygens.

We now estimate the heat shield requirements for the afterbody, based on the stagnation point heating rates.

$$Q_{Wta} := 0.015 \cdot Q_{Wt} = 3.476 \cdot \frac{W}{cm^2} \quad \text{or} \quad Q_{Wta} = 3.476 \times 10^4 \cdot \frac{W}{m^2}$$

$$Q_{Ta} := 0.015 \cdot Q_{Tsp} = 134.666 \cdot \frac{J}{cm^2} \quad \text{or} \quad Q_{Ta} = 1.347 \times 10^6 \cdot \frac{J}{m^2}$$

Huygens used PROSIAL as the aft shield material, a silicone elastomere with an average density of about 0.57 gm/cm³. Although this material is not intended for use as an ablator, we estimate its required thickness based on that assumption nonetheless, to maintain consistency with the TABS model. Furthermore, we assume a heat of ablation similar to glass, or that of SLA 561. With this, we compute the shield thickness:

$$h_{va} := 12.1 \cdot 10^6 \frac{J}{kg} \quad \text{Heat of ablation for SLA 561 assumed}$$

$$\rho_{hsa} := 0.57 \frac{gm}{cm^3} \quad \text{Average density of PROSIAL }^{46}$$

$$t_{hsa} := \frac{Q_{Ta}}{h_{va} \cdot \rho_{hsa}} = 0.195 \cdot mm \quad \text{The afterbody heat shield thickness}$$

The thickness of the PROSIAL shield on Huygens ranged from 0.3 mm to 3.1 mm⁴⁶. The result here, even though it assumes an ablator, is certainly within an order of magnitude. For higher speeds such as the one for TABS, this assumption becomes more valid.

7.4.3 Summary Results and Comparison

Table 7-1 provides a summary of TABS aerothermodynamic entry parameters based on the basic engineering model developed. It also summarizes the comparison of the model applied to Huygens, versus the results of more detailed analyses. TPS requirements, in particular those of the front shield are summarized as well. It should be noted that the aft shield design was not particularly emphasized in this dissertation, and only a rough order of magnitude sizing was required. The analysis carried out to derive the complete aeroshell requirements proves sufficient for this level of design.

In conclusion, the model derived for TABS aerothermodynamic calculations based on simple engineering formulas is good enough to at least an order of magnitude, and agrees quite well in some cases with results obtained using more complex numerical computations. This was proven both for the flight regime expected in TABS, as well as the flight regime encountered during Huygens entry into Titan.

Table 7-1: Summary of Aerothermodynamic entry calculations and comparison of model with Huygens values

BALLISTIC ENTRY AEROTHERMODYNAMIC ANALYSIS	EM Model / TABS	EM Model / Huygens	Huygens	Reference No.
Exponential Atmospheric Model				
Composition	98.4% N ₂ , 1.31% CH ₄ , 0.33% H ₂ (at 981 km)		77% N ₂ , 3% CH ₄ , 20% Ar ("worst Atmosphere")	22, 46
Molecular mass (kg/mol)	0.028			
Reference Temperature for Ballistic Corridor (K)	181			
Scale Height (km)	40			
Flow Regime	Continuous			
Entry Characteristics				
Entry Interface Altitude (km)	1000		1200	
Inertial Entry Velocity (km/s)	10.44	6.02		44,45
Flight Path Angle (deg)	-50	-65.1		44,45
Entry Vehicle / Aeroshell Specification				
Maximum Diameter (cm)	206	270		46
Axial Length (cm)	204.9	97		46
FS Half Cone Angle (deg)	34.4	60.0		44,45
Nose Radius (cm)	58	125.0		45
Entry Vehicle Mass (kg)	628.1	320		46
Ballistic Coefficient (kg/m ²)	295.5	37.3		
Aerodynamics				
Maximum Deceleration (m/s ²)	384	151		
Max. Deceleration G-Load	39	15.4	12.4	47
Velocity at Max G (km/s)	6.3	3.7	3.5	DISR
Critical Altitude (km)	197	273	246	47
Maximum Stagnation Point Dynamic Pressure (atm)	1.12	0.1	0.1	46
Drogue Deployment Mach No.	1.23	1.4	1.4	DISR
Flight Time From Entry Interface to Drogue Deployment (s)	136	184	203	DISR
Aerothermodynamics				
Total Convective Heat Load and Body Average Heating Rate				
Total Enthalpy (J/kg)	5.4E+07			
Total Convective Heat Load (J)	2.2E+07	8.9E+06		
Max. Body Average Heating Rate (W/cm ²)	9.7	1.5		
Critical Altitude (km)	213	289		
Velocity at Peak Heating Rate (km/s)	7.5	4.3		
Stagnation Point Heating - Convective				
Max. Stagnation Point Heating Rate (W/cm ²)	996	46	46	49
Critical Altitude (km)	245	320		
Approximate Heat Pulse Duration (s)	25	32.9		
Integrated Convective Heat Flux (J/cm ²)	1.9E+04	1468		
Stagnation Point Heating - Radiative				
Max. Stagnation Point Heating Rate (W/cm ²)	1.3E+03 to 1.9E+03	185	150	49
Critical Altitude (km)	245	330		
Approximate Heat Pulse Duration (s)	25	32.9		
Integrated Convective Heat Flux (J/cm ²)	4.4E+04	7438		
Peak Heat Loads at the Stagnation Point (Conv. + Rad.)				
Maximum Heating Rate (W/cm ²)	2.90E+03	232	196	49
Maximum Integrated Heat Flux (J/cm ²)	6.33E+04	8.9E+03	4.20E+03	50
Estimated Peak Heat Loads Aft Shell (Conv. + Rad.)				
Maximum Heating Rate (W/cm ²)	43.5			
Maximum Integrated Heat Flux (J/cm ²)	950			
TPS Characteristics				
Front Shell				
Material	Carbon/Phenolic Ablator	AQ60/I		46
Emmissivity	0.85			
Radiation Adiabatic Max. Surface Temperature (°C)	3518			
Density (gm/cm ³)	1.45	280		46
Thickness (cm)	1.65	2.6	1.8	46
Aft Shell				
Material	SLA 561	PROSIAL		
Emmissivity	0.85			
Radiation Adiabatic Max. Surface Temperature (°C)	1054			
Density (gm/cm ³)	0.256	0.57		
Thickness (mm)	3.1	0.2	0.3 to 3.1	46

8.0 Decelerator System Sizing and Balloon Inflation

The following four requirements must be factored in the design of the decelerator system (both drogue and main parachutes):

1. *Strength*: The decelerator must survive deployment forces without damage
2. *Drag*: The *drogue* parachute drag shall be adjusted to allow for safe deployment at the given speed and dynamic pressures, while minimizing mass. The *main parachute* must reduce the descent speed to allow sufficient time for the balloon to inflate. Descent rate must also be slow enough to minimize the relative vertical wind speed (dynamic forces) to acceptable levels for material deployment and inflation
3. *Volume*: The decelerator system must strive to occupy the minimum volume possible, or fit within the volume constraints imposed by the vehicle design
4. *Stability*: The drogue and main parachutes must be stable enough to reduce oscillations that can either affect main deployment after drogue release, or balloon inflation under main parachute.

A *Disk-Gap-Band* (DGB) is chosen for both the drogue and main parachutes, following the rationale employed in the selection of Huygens parachutes⁵³. The following variables affect the performance parameters as given below in the proportionality indicated (direct or inverse):

1. *Diameter* affects *drag* (direct) and packing *volume* (direct).
2. *Band Width* affects *stability* (direct), *drag* (inverse), *volume* (direct).
3. *Material Thickness* affects *strength* (direct) and pack *volume* (direct).

First, we concentrate on sizing of the Drogue decelerator while developing the concept and formulas which will be used to size the main parachute as well. The requirements listed here, together with the interdependency of the major factors will be kept in mind throughout the following discussion.

8.1 Drogue Decelerator Sizing

A key parameter determining the strength of the drogue parachute is the vehicle dynamic pressure (a function of speed, as shown above) at deployment. If we constrain the speed alone to be between Mach 1 and 2, then from the information presented here the dynamic pressure and altitude of deployment are:

$$P_{dd} := P_{sp}(h_d) = 2.265 \times 10^3 \cdot \text{Pa} \quad \text{dynamic pressure at deployment}$$
$$h_d = 120 \cdot \text{km} \quad \text{deployment altitude}$$

The maximum parachute structural loads generally occur during inflation, so this point defines its required strength. The sudden change in the coefficient of drag (C_d) during the drogue deployment creates an almost instantaneous shock impulse of deceleration. This translates to some G-value. The *parachute opening shock* is computed based on drogue characteristics. These characteristics are iterated to reach a reasonable loading. The simplest way of estimating parachute opening shock load is to modify the steady drag equation by some factor. In particular, "finite mass" opening shock factors can be used to provide rapid estimates of parachute opening loads, and will be used here⁵⁴.

The parachute drag coefficient depends on material porosity, surface area, vehicle speed, gas properties, etc. The value chosen below is a starting point based on reference data (e.g., 55 and 56). Larger drag coefficients appear to be rare in aerospace decelerator applications, since C_d decreases for high dynamic pressures or high deployment speeds (Ref. 57, Figure 3, pg. 3). For a DGB drogue, drag coefficients can range between 0.52 to 0.58 (Ref. 58, Table 2.2, pg. 76). Hence we choose as a starting point,

$$C_{Dd} := 0.55 \quad \text{Rough estimate of drag coefficient of drogue parachute}$$

$$R_d := 0.9\text{m} \quad \text{Drogue radius (iterative result)}$$

$$S_d := 2\pi \cdot R_d^2 = 5.089\text{m}^2 \quad \text{Drogue nominal area (assume hemispherical/round). This is the total surface area of the fabric used to build the parachute (including holes), not the projected area.}$$

The drogue radius is obtained after an iterative process whereby acceptable deceleration is achieved. This will be shown later on. The *nominal diameter* for this type of parachute is computed from (this is *not* the geometric diameter of the sphere),

$$D_o := 2 \cdot \sqrt{\frac{S_d}{\pi}} = 2.546 \text{ m}$$

The finite mass opening shock factor is based on a mass ratio defined by the characteristic fluid mass/system mass. For practical purposes, the system mass is the same as the probe mass (with an initial estimate of parachute mass). Finite mass implies significant deceleration during inflation. During inflation, a large fluid mass (relative to probe mass) is *accelerated*, resulting in probe *deceleration* due to momentum transfer. The mass ratio is given by

$$R_m := \frac{\rho_{\text{mod}}(h_d) \cdot (C_{Dd} \cdot S_d)^{1.5}}{m_{\text{sn}}} = 2.883 \times 10^{-4}$$

From Ref. 54, the corresponding opening force factor for an unreefed parachute (or inflation to 1st reefed stage), for the given mass ratio is ~ 1.4, and from 1st reefed stage to opening is about the same. Hence,

$$C_k := 1.4 \quad \text{opening force factor}$$

The *drogue opening shock* is then

$$F_{dd} := C_k \cdot C_{Dd} \cdot S_d \cdot P_{dd} = 8.878 \times 10^3 \cdot \text{N} \quad \text{or} \quad F_{dd} = 1.996 \times 10^3 \cdot \text{lbf}$$

The probe deceleration is then

$$a_{dd} := \frac{F_{dd}}{m_{\text{sn}}} = 14.135 \frac{\text{m}}{\text{s}^2} \quad \text{or} \quad \frac{a_{dd}}{g} = 1.441 \quad \text{Gs}$$

As a comparison, the probe drag force at the exact location just prior to drogue release is

$$F_D(h_d) = 4.816 \times 10^3 \cdot \text{N}$$

This value must be smaller than the shock force of drogue deployment (or its drag force) if the drogue is to successfully trail behind the probe. One-half is a reasonable estimate ($F_{dd} \sim 1.8F_D$). The deployment of the drogue provides an additive effect on the vehicle deceleration, above the value normally experienced in its ballistic trajectory. The resulting opening loads for the drogue parachute with the chosen parameters are reasonable, and hence this design will be used for preliminary system sizing.

For a DGB drogue with the parameters given above, the initial disk, gap, and band areas are chosen to be similar to the Viking percentages (Ref. 58, pg.100), or 53%, 12%, and 35 % respectively of the total (nominal) area, S_d (or reference area). Hence,

$$\text{Disk}_{Ad} := 0.53 \cdot S_d = 2.697 \times 10^4 \cdot \text{cm}^2$$

$$\text{Gap}_{Ad} := 0.12 \cdot S_d = 6.107 \times 10^3 \cdot \text{cm}^2$$

$$\text{Band}_{Ad} := 0.35 \cdot S_d = 1.781 \times 10^4 \cdot \text{cm}^2$$

For the Gore layout, the geometric parameters are

$$N_{gd} := 12 \quad \text{Number of gores (Huygens Pilot)}$$

$$h_{1Dd} := \left(\frac{S_d}{1.887 \cdot N_{gd} \cdot \tan\left(\frac{180\text{deg}}{N_{gd}}\right)} \right)^{0.5} = 0.916 \text{ m} \quad \text{length of disk gore laid out flat}$$

$$h_{2Gd} := 0.113 \cdot h_{1Dd} = 0.103 \text{ m} \quad \text{gap length}$$

$$h_{3Bd} := 0.33 \cdot h_{1Dd} = 0.302 \text{ m} \quad \text{length of band gore laid out flat}$$

And the parachute line length is

$$l_{ed} := 1.69 \cdot (2 \cdot R_d) = 3.042 \text{ m}$$

Figure 8-1 illustrates the DGB gore layout with parameters h_1 , h_2 , h_3 (additional subscripts omitted). The parachute line length l_e and approximate dimensions are also shown.

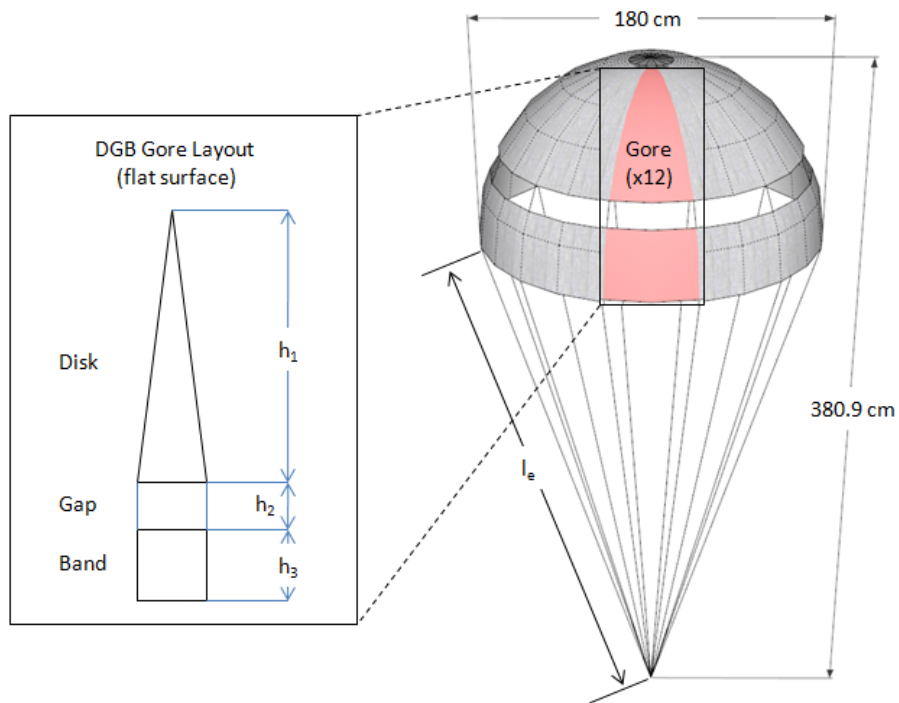


Figure 8-1: Droge gore layout and approximate dimensions

A correlation for the mass of the complete parachute decelerator system can be obtained from Ref. 58. The correlation for a Conical Ribbon Classes V-VIII parachute weight versus diameter is given in Figure 8-2. A power curve fitting to this graph yields results that are about 3 times larger than the results of Huygens. This may be reasonable if we consider the higher dynamic loads on the TABS drogue, as opposed to the Huygens case. Leaving this higher value as margin, we obtain:

$$m_{dr} := 0.4126 \text{ lb} \cdot \left(D_o \cdot \frac{3.281}{\text{m}} \right)^{1.539} = 4.907 \text{ kg} \quad \text{mass of TABS drogue decelerator system}$$

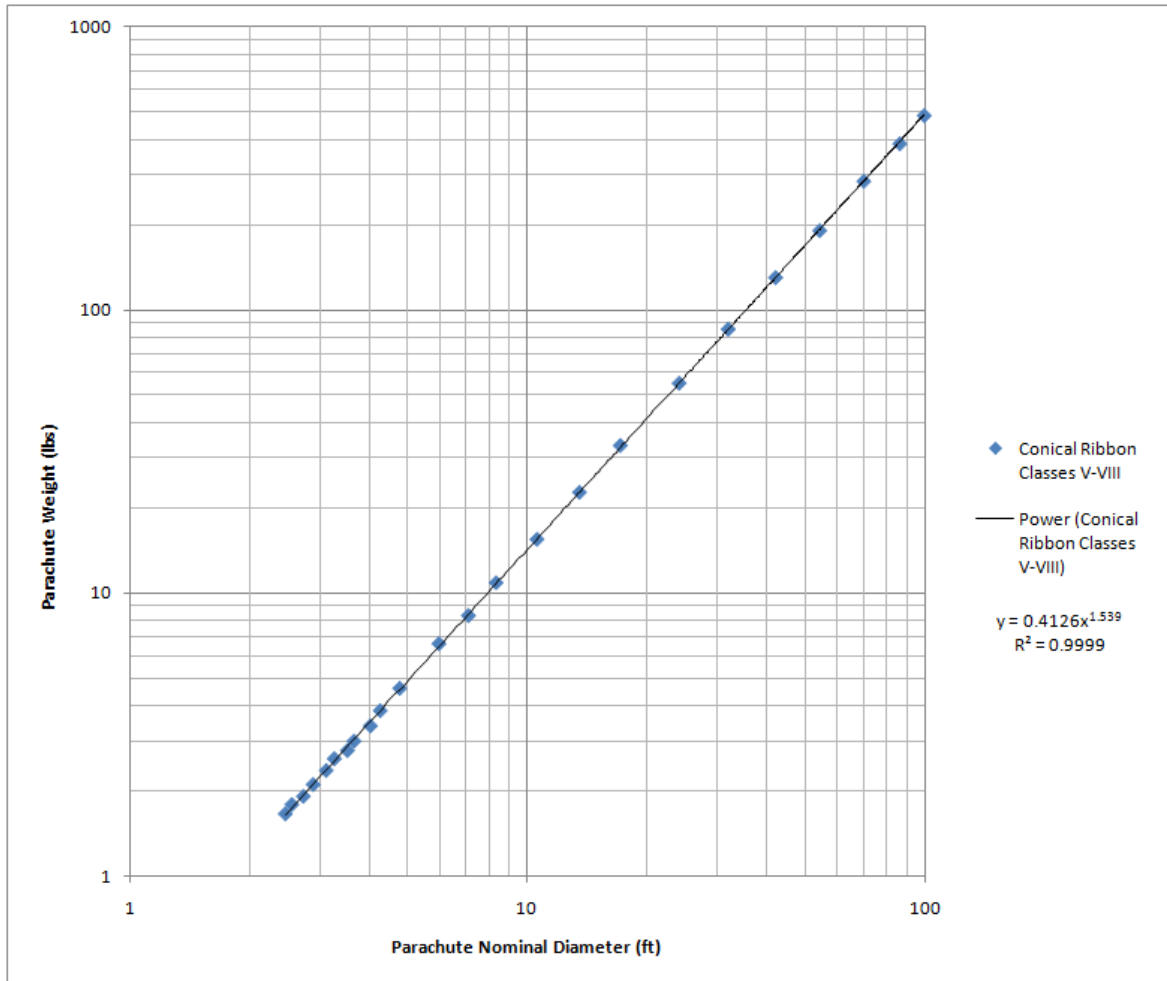


Figure 8-2: Correlation of parachute system mass with nominal diameter ⁵⁸

Again, using Ref. 58 (weight and volume discussion, pg. 432 Table 8.11), with constants for a high-strength (4.75 Oz) nylon decelerator, the estimated drogue system mass would be as follows:

$$m_{dp} := 0.09\text{lb} \cdot \left(2 \cdot \frac{3.281}{\text{m}} \cdot R_d\right)^2 + 0.6\text{lb} \cdot \left(2 \cdot \frac{3.281}{\text{m}} \cdot R_d\right) = 3.031 \text{ kg}$$

or about the same result we obtained before. We keep the more conservative estimate.

If we use an air-press packing method, the pack density is (Ref. 58, Table 8.12),

$$d_{hp} := 35 \frac{\text{lb}}{\text{ft}^3} = 560.646 \cdot \frac{\text{kg}}{\text{m}^3}$$

Although this is a higher pack density than Huygens' 300 kg/m³ ⁵³, it is nonetheless a reasonable number to use considering that this pack density was being obtained back in 1978. The drogue container volume is then

$$V_d := \frac{m_{dr}}{d_{hp}} = 8.753 \times 10^3 \cdot \text{cm}^3 \quad \text{or} \quad V_d = 8.753 \text{ L}$$

The baseline TABS preliminary design has an allocation of 13.1L (Fig. 6-5). Indeed, this proves more than adequate to fit the parachute and mortar system, with a 50% volume contingency left over.

8.2 Main Parachute Sizing and Balloon Inflation

The main parachute sizing is inexorably attached to the balloon inflation in that its size must support the orderly and safe deployment of the balloon by a predefined altitude. Unlike Huygens, the main parachute in TABS will be released *after* crossing-over through Mach 1. The reason is the need to maintain the back cover to protect the Hydrogen tanks and lines through the transonic phase. This has the added advantage of reducing the deployment load on the main, making it lighter and providing for a better inflation environment. The disadvantage is that a larger parachute provides better stabilization through the transonic phase. Nonetheless, stabilization can be addressed if needed via a larger drogue. We now size the main parachute.

The *terminal velocity* (where the drag force equals the vehicle weight) after drogue deployment can be estimated from

$$V_t := \sqrt{\frac{2 \cdot m_{sn} \cdot g_n}{C_{Dd} \cdot \rho_{mod}(h_d) \cdot S_d}} = 125.353 \frac{m}{s}$$

where the atmospheric density at time of drogue deployment is used. To recap,

$$\rho_{mod}(h_d) = 0.039 \cdot \frac{kg}{m^3} \quad S_d = 5.089 m^2 \quad C_{Dd} = 0.55$$

The time lapse from drogue deployment to terminal velocity may be roughly estimated if we assume that the drag force remains constant during this period of time. Since $F = m \, dV/dt$,

$$dV_t := V_{sc}(h_d) - V_t = 216.943 \frac{m}{s}$$

$$t_t := \frac{m_{sn} \cdot dV_t}{F_{dd}} = 15.348 \, s$$

The distance traveled from drogue deployment to terminal velocity is then,

$$h_{tv} := \int_0^{t_t} dV_t \, dt = 3.33 \cdot km$$

The *main parachute deployment altitude* can then be estimated to correspond to the time when terminal velocity has been reached under the drogue, and is hence,

$$h_m := h_d - h_{tv} = 116.67 \cdot km$$

To properly size the main parachute, its descent rate must be such that complete balloon inflation is achieved by its desired operational altitude, or 10km, starting from ~117 km. More importantly, it must provide a decent rate that minimizes dynamic loads on the balloon material as it inflates. We take that descent rate to be in the neighborhood of 5 to 10 m/s (TandEM assumed 5 m/s at the start of Montgolfier inflation⁵).

The time required to inflate the balloon is estimated from the flow rate of H₂ gas. From Section 5.5, the balloon should be inflated by ~23 km altitude to provide some level of inflation redundancy (differential pressure between gas tank and balloon), as this is half the pressure at operating altitude (10 km). The inflation time is also calculated to be ~23 minutes.

The *inflation start altitude* is chosen at a point where the atmospheric density supports a slow-enough descent rate. As mentioned, this is chosen to be between 5 to 10 m/s. The inflation start time is estimated below, based on main parachute parameters. This is an iterative process.

$C_{Dp} := 0.55$ Rough estimate of drag coefficient of main DGB parachute

$R_p := 2.0\text{m}$ Iterative result for main parachute radius: further radius increase will not significantly reduce the descent rate.

$S_p := 2\pi \cdot R_p^2 = 25.133\text{m}^2$ Main nominal area (assume hemispherical/round). Again, this is the *total* surface area of the fabric used to build the parachute (including holes), not the projected area.

The *nominal diameter* for this type of parachute is computed from

$$D_p := 2 \cdot \sqrt{\frac{S_p}{\pi}} = 5.657\text{m} \qquad D_p = 18.559\text{ft}$$

We validate this choice of parameters by analyzing the resulting terminal velocity at different altitudes (i.e., its dependence on atmospheric density). We also keep in mind the requirements enumerated above, namely descent rate between 5 to 10 m/s, balloon inflation time of ~23 min., and inflation by ~23 km (if possible). The terminal velocity (or descent rate) under the main can be estimated versus altitude as,

$$h_t := 10\text{km}, 11\text{km}.. h_m$$

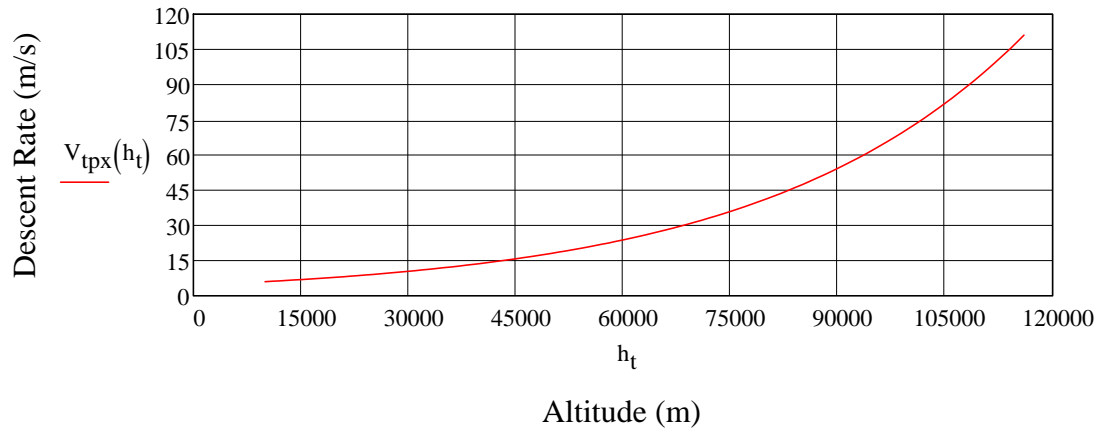
$$V_{\text{tpx}}(h_t) := \sqrt{\frac{2 \cdot m_{\text{sn}} \cdot g_n}{C_{Dp} \cdot \rho_{m120}(h_t) \cdot S_p}} \qquad \text{Main parachute descent rate}$$

Note that for these calculations the *low-altitude atmospheric model must be used*, or the results will be excessively inaccurate. The resulting plots give an insight into the "optimal" location where balloon inflation should occur (Figure 8-3 *a* and *b*). This is at (or below) the point in the curve where the descent rate becomes somewhat insensitive to altitude variations, providing for a more dynamically stable environment. This should also be below the desired maximum 10 m/s descent rate.

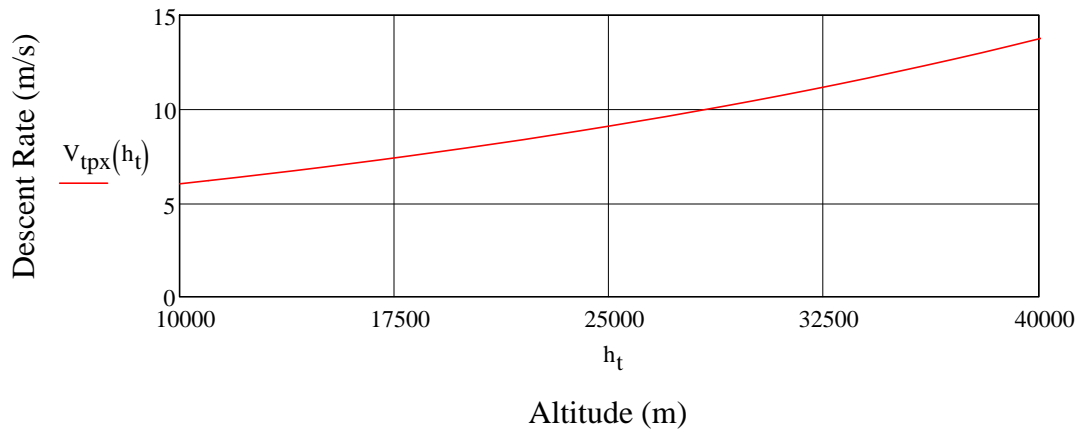
As can be seen, the descent rate (curve slope) below ~37 km is nearly constant (Fig. 8-3a). Also, at ~28 km the rate drops below 10 m/s (Fig. 8-3b). We choose this as the balloon inflation start altitude.

$$h_b := 28\text{km} \qquad \text{Inflation start altitude}$$

$$V_{\text{tpx}}(28\text{km}) = 9.874 \frac{\text{m}}{\text{s}} \qquad \text{Main parachute descent rate at and below 28 km}$$



(a)



(b)

Figure 8-3: Main parachute descent rate versus altitude (a), and detail below 40 km (b)

The parachute nominal area must also support complete balloon inflation near the recommended ~23km. The mass ratio for the parameters chosen is

$$R_{mp} := \frac{\rho_{m120}(h_m) \cdot (C_{Dp} \cdot S_p)^{1.5}}{m_{sn}} = 7.87 \times 10^{-4}$$

Note that we used the atmospheric density model for altitudes below ~120 km. Again, the opening force factor is ⁵⁴,

$$C_{kp} := 1.4 \quad \text{opening force factor}$$

The dynamic pressure under main control is equal to the sum of the free-stream dynamic pressure and static pressures. At low speeds the dynamic pressure and static (or free-stream) pressures are comparable. The vehicle velocity is equal to the terminal velocity, plus a small addition due to the deployment lag from drogue release to main deployment. If deployment occurs 20 meters after drogue release, then

$$x_{drop} := 20\text{m}$$

$$\sqrt{V_t^2 + 2 \cdot g_n \cdot x_{drop}} = 125.568 \frac{\text{m}}{\text{s}}$$

is the final velocity which can be safely ignored since $V_t = 125.353 \frac{m}{s}$

Therefore the *total (dynamic + static) pressure on the vehicle at main parachute opening* (valid between 0 and 120km) is given by Bernoulli's equation,

$$P_d(h_{120}) := \frac{1}{2} \cdot \rho_{m120}(h_{120}) \cdot V_t^2 + P_{120}(h_{120})$$

Hence

$$P_{d0} := P_d(h_m) = 453.92 \cdot \text{Pa} \quad \text{or} \quad P_{d0} = 9.48 \cdot \text{psf}$$

where $h_m = 116.67 \cdot \text{km}$ is the altitude at which TABS's main parachute deployment occurs.

The *main parachute opening shock* (or drag force) is then

$$F_{pp} := C_{kp} \cdot C_{Dp} \cdot S_p \cdot P_{d0} = 8.784 \times 10^3 \cdot \text{N} \quad F_{pp} = 1.975 \times 10^3 \cdot \text{lbf}$$

The probe deceleration is then

$$a_{pp} := \frac{F_{pp}}{m_{sn}} = 13.986 \frac{m}{s^2} \quad \text{or} \quad \frac{a_{pp}}{g} = 1.426 \quad \text{Gs}$$

comparable to the deceleration load after drogue deployment (1.44G). The probe drag force at the location just prior to main parachute deployment is

$$F_{Dp}(h_{120}) := P_d(h_{120}) \cdot C_D \cdot A_s$$

$$F_{Dp}(h_m) = 964.94 \cdot \text{N}$$

As before, *this value must be smaller than the shock force of drogue deployment (or its drag force)* if the main is to successfully trail behind the probe. Here, we find about a factor of nine, more than enough ($F_{pp} \sim 9F_{Dp}$). The resulting opening loads for the main parachute with the chosen parameters are reasonable, and hence this design will be used for preliminary system sizing.

For a DGB drogue with parameters given above, the initial disk, gap and band areas are chosen to be similar to the drogue values, or 53%, 12%, and 35 % respectively of the total (nominal) area, S_d (or reference area). Hence,

$$\text{Disk}_{Ap} := 0.53 \cdot S_p = 1.332 \times 10^5 \cdot \text{cm}^2$$

$$\text{Gap}_{Ap} := 0.12 \cdot S_p = 3.016 \times 10^4 \cdot \text{cm}^2$$

$$\text{Band}_{Ap} := 0.35 \cdot S_p = 8.796 \times 10^4 \cdot \text{cm}^2$$

For the Gore layout, the geometric parameters are

$$N_{gp} := 12 \quad \text{Number of gores}$$

$$h_{1Dp} := \left(\frac{S_d}{1.887 \cdot N_{gd} \cdot \tan\left(\frac{180\text{deg}}{N_{gd}}\right)} \right)^{0.5} = 0.916 \text{m}$$

$$h_{2Gp} := 0.113 \cdot h_{1Dd} = 0.103 \text{ m}$$

$$h_{3Bp} := 0.33 \cdot h_{1Dp} = 0.302 \text{ m}$$

The line length is

$$l_{ep} := 1.69 \cdot (2 \cdot R_p) = 6.76 \text{ m}$$

Figure 8-4 shows the main parachute approximate size, next to the drogue (to scale).

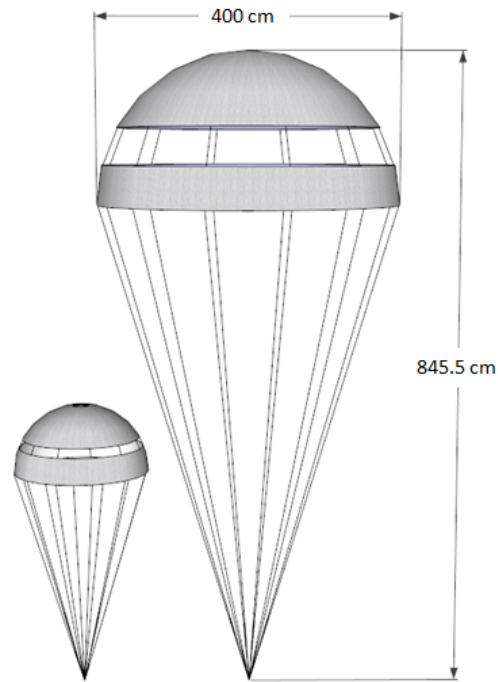


Figure 8-4: Main parachute approximate size next to Drogue (drawn to scale)

The mass of the main is calculated as before,

$$m_{drp} := 0.4126 \text{ lb} \cdot \left(D_p \cdot \frac{3.281}{\text{m}} \right)^{1.539} = 16.77 \text{ kg} \quad \text{mass of TABS main parachute system}$$

As before, we check this mass again using reference 58:

$$m_{dpp} := 0.09 \text{ lb} \cdot \left(2 \cdot \frac{3.281}{\text{m}} \cdot R_p \right)^2 + 0.6 \text{ lb} \cdot \left(2 \cdot \frac{3.281}{\text{m}} \cdot R_p \right) = 10.603 \text{ kg}$$

or within the same order of magnitude as obtained before (although the more conservative value is adopted for TABS sizing, this provides a useful mass range).

As a means of comparison, the TSSM in-situ Montgolfier probe had an 18.2 kg mass allocation for the decelerator system without contingency, for an entry mass allocation of 600 kg including margin⁵. From the results here, TABS allocates 22 kg for the decelerator system without contingency, with an entry mass allocation of 628 kg including margin. Although TABS enters at a higher speed, parachute deployments occur at equivalent speeds in either case. Hence the mass allocations for TABS decelerator system are quite reasonable given the preliminary calculations made.

If we use an air-press packing method, the pack density is as before⁵⁸, hence the main parachute system volume is

$$V_p := \frac{m_{\text{drp}}}{d_{\text{hp}}} = 2.991 \times 10^4 \cdot \text{cm}^3 \quad \text{or} \quad V_p = 29.912 \text{L}$$

The main parachute container has a volume allocation of 62.3L (Fig. 6-5), or 2.1 times the required value. This hence proves adequate to fit the parachute and mortar system.

The terminal velocity right after main deployment is given by

$$V_{\text{tp}} := \sqrt{\frac{2 \cdot m_{\text{sn}} \cdot g_{\text{n}}}{C_{\text{Dp}} \cdot \rho_{\text{m120}}(h_{\text{m}}) \cdot S_{\text{p}}} = 113.11 \frac{\text{m}}{\text{s}}$$

where the atmospheric density at time of main deployment is used.

$$\rho_{\text{m120}}(h_{\text{m}}) = 9.618 \times 10^{-3} \cdot \frac{\text{kg}}{\text{m}^3} \quad S_{\text{p}} = 25.133 \text{m}^2 \quad C_{\text{Dp}} = 0.55$$

The time lapse from main parachute deployment to terminal velocity is

$$dV_{\text{tp}} := V_{\text{t}} - V_{\text{tp}} = 12.243 \frac{\text{m}}{\text{s}}$$

$$t_{\text{tp}} := \frac{m_{\text{sn}} \cdot dV_{\text{tp}}}{F_{\text{pp}}} = 0.875 \text{s}$$

The distance traveled from main parachute deployment to terminal velocity (at that altitude) is then,

$$h_{\text{tp}} := \int_0^{t_{\text{tp}}} dV_{\text{tp}} dt = 0.011 \cdot \text{km}$$

The balloon inflation start altitude was derived before, and is

$$h_{\text{b}} = 28 \cdot \text{km}$$

The balloon inflation time is (Section 5-5):

$$t_{\text{bi}} := 23.3 \text{min}$$

The altitude at which the balloon is fully inflated is then

$$h_{\text{full}} := h_{\text{b}} - V_{\text{tpx}}(h_{\text{b}}) \cdot t_{\text{bi}} = 14.196 \cdot \text{km}$$

Although this is below the 23 km target, the pressure at this altitude (~70KPa) is about 26% smaller than the pressure at the operating altitude of 10 km (P_{a}), and hence proves sufficient for the current design.

As the balloon inflates, its buoyancy increases, and the main parachute with everything under it will therefore descend at a smaller rate than shown here. This effect is being ignored in this preliminary analysis, so the results are "worst case" for descend rates and balloon inflation altitudes. As long as ballast is kept to always ensure the balloon is being loaded more than its buoyancy gas can support, then positive descent is assured, and the main parachute will continue to be "loaded", albeit not at its initial full capacity. To this effect, the front heat shield with its additional mass will be retained as "ballast" until the balloon is fully inflated, at which time it will be released.

9.0 Carrier Spacecraft

The carrier spacecraft must physically accommodate the probe during the flight to Saturn. It must provide the support systems for safe house-keeping and the propulsion system for delivery of TABS to Titan. The mission design and communications sections gave a description of how this would be accomplished. Now it is necessary to develop the relevant details of the delivery system. Only those subsystems germane to this particular example will be defined. There will be no attempt at doing a full carrier spacecraft system design beyond those critical systems.

9.1 Interface Structure and TABS Accommodation

The interface frame structure must be robust enough to withstand the launch loads, while providing an interface between TABS and the carrier spacecraft. It must also not interfere with TABS itself. The carrier spacecraft bus structure interfaces with the interface frame structure, and the SEP propulsion module. The interface and bus structures are shown in Figure 9-1. Table 9-1 summarizes the major mass components. The mass for the tank and instruments shown in Figure 9-1 is allocated later.

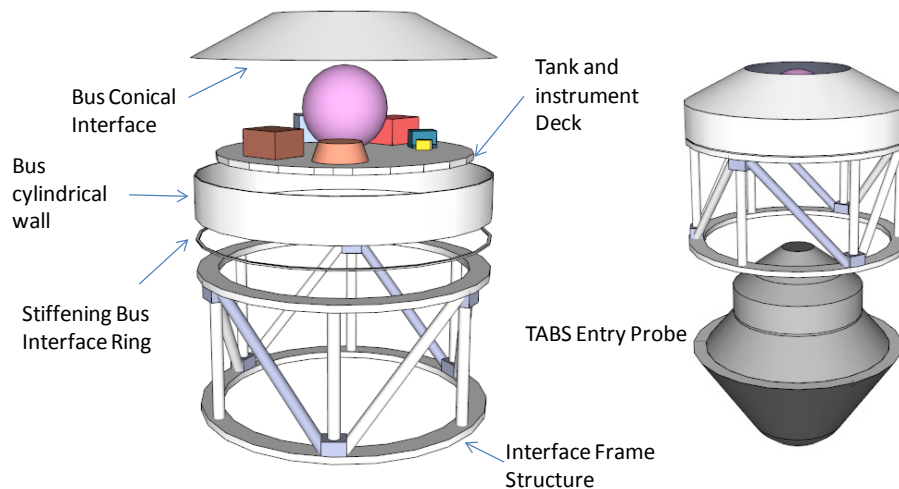


Figure 9-1: TABS interface and carrier spacecraft structures

Table 9-1: Mass allocations for TABS interface and carrier spacecraft structures

Component	Quantity	Material	Size (cm)			Mass Al (kg) SubTotal	Mass Composite Honeycomb (kg)			Mass Comp. (kg) SubTotal	Select Mass (kg) Totals
			Thickness	Area	Material Volume		Composite (1.0 or 2x0.5 cm)	Al Core	SubTotal		
Interface Frame Structure											
Top/Bottom Interface Rings	2	Composite/Al Honeycomb	5	8714.20	43571.00		13.75	2.84	16.59		33.18
Longitudinal Support Rods	6	Epoxy/Graphite HM	1	9.42	1199.77					1.89	11.36
Axial Support Rods	6	Epoxy/Graphite HM	1	9.42	848.23					1.34	8.03
Frame Joints	6	Grade 6061-T6 Aluminum			1180.00	3.20					19.21
Cruise Spacecraft Bus Structure											
Stiffening Bus Interface Ring	1	Grade 6061-T6 Aluminum	1	1279.60	1279.60	3.47					3.47
Bus cylindrical wall	1	Epoxy/Graphite HM	1	19547.60	19547.60					30.84	30.84
Bus Conical Interface	1	Epoxy/Graphite HM	0.5	29785.50	14892.75					23.50	23.50
Tank and instrument Deck	1		0.7	24878.50	17414.95		7.85	1.01	8.86		8.86
Total Structure											138.45

9.2 Carrier Spacecraft (CS) Sizing

The carrier spacecraft must include the chemical propulsion system (CHEM) used for trajectory corrections en-route, attitude control, and final targeting to Titan. The structure mass allocation was given in Table 9-1. Specifying the remaining subsystem masses is necessary to size the CHEM system. These masses are shown in Table 9-2, which include TABS' as it is part of the CHEM system payload. Again, no attempt is made to develop the subsystem details beyond establishing a preliminary boundary on the masses that can be used for sizing the rest of the system. In addition, power requirements are established to understand the need to allocate for power generation sources. Initially, it was thought that the bus could draw its power only from the TABS ASRG during cruise, and then operate on batteries during the flyby. However, relying on batteries alone during this critical phase is a risky proposition. Therefore, an identical power source as in TABS is used to feed the CS and trickle charge its batteries. Using the same type of ASRG

also simplifies the implementation. Table 9-2 also shows the three power operating modes that define the power boundary condition: *Cruise* and flyby *receive* and *transmit* modes. All power modes are bounded within these three scenarios.

Table 9-2: Mass and power allocations for CS sizing

SUBSYSTEM	MASS (kg)	Peak POWER (Watt)	Cruise POWER (Watt)	Flyby POWER (Watt) - rcv4 hrs	Flyby POWER (Watt) - xmt 1.3 hr
Payload (TABS Entry Probe)	483.1	16.0			
Structure and Mechanisms	138.4				
Command & Data Handling	20.0	48.0	26.4	48.0	48.0
Communication	21.1	200.0	20.0	20.0	200.0
High-Gain Antenna (parabolic)	7.1				
Spacecraft Transceiver	9.0				
Low-Gain Antennae (2)	1.0				
Amplifiers (2)	4.0				
Power Systems	73.6	14.0	4.2	14.0	14.0
ASRG	38.2				
Power Control Electronics	17.0				
Battery	18.4				
Thermal Control	13.8	10.0	10.0	10.0	10.0
Harness / Fasteners	20.8				
ACS Sensors and Actuators	27.0	30.0	30.0	30.0	30.0
RWA / IMU	17.0				
Star Trackers (2) / Sun Sensors (8)	10.0				
Chemical Thrusters Power (mass below)		6.0			
Total Carrier Spacecraft Power Requirements(w/o SEP Module)		318.0	90.6	122.0	302.0
Spacecraft Dry Mass (w/o CHEM and SEP Module)	797.9				
Add 30% contingency for mass and 20% contingency for power	1037.3	381.6	108.7	146.4	362.4

As can be seen from Table 9-2, the CS ASRG is capable of supplying the spacecraft load during the cruise phase. However, it falls short during the flyby. In order to supplement the ASRG power, batteries are carried on-board. These batteries are conservatively sized to fully supply the loads without use of the ASRG. A Li-Ion technology is chosen because of this battery's large energy density.

The Loads during flyby receive and transmit modes (including 20% contingency) are

$$P_{Lr} := 146.4W \quad \text{load during flyby receive mode}$$

$$P_{Lt} := 362.4W \quad \text{load during flyby transmit mode}$$

The following input variables are defined

$$\text{Bus Voltage,} \quad V_b := 28V$$

$$\text{Load Duration,} \quad L_r := 4hr$$

$$\quad \quad \quad L_t := 1.3hr$$

Battery Energy Density,	$E_d := 115 \text{ W} \cdot \frac{\text{hr}}{\text{kg}}$	for 100% discharge
Average cell voltage,	$V_c := 4.2 \text{ V}$	
Maximum DOD,	$\text{DOD} := 50\%$	

Given these inputs, the results are

Number of cells,	$N_c := \text{round}\left(\frac{V_b}{V_c}\right) = 7$
Battery Voltage,	$V_{ba} := N_c \cdot V_c = 29.4 \text{ V}$
Total battery capacity,	$C_b := \frac{P_{Lr} \cdot L_r + P_{Lt} \cdot L_t}{\text{DOD} \cdot V_{ba}} = 71.886 \cdot \text{A} \cdot \text{hr}$
Battery Stored Energy,	$E_s := C_b \cdot V_{ba} = 2.113 \times 10^3 \text{ W} \cdot \text{hr}$
Battery Mass,	$m_b := \frac{E_s}{E_d} = 18.378 \text{ kg}$

An estimate of the thermal requirements that influence the mass shown in Table 9-2 is given next. A rough analysis of the thermal balance characteristics of the CS and all its components (including TABS) was performed in order to size the radiators. During the flight to Saturn, TABS will be spending a little more than about half its time within 1 to 2 AU from the sun. Hence it is important to size the radiators so as to prevent subsystems from overheating while in the inner solar system. The problem is essentially a steady-state, radiation balance formulation. More importantly, the thermal balance will depend on chosen emissivity, and on the internal heat available. Of course, the first basic assumption is that the spacecraft can achieve thermal balance. Figure 9-2 shows the relevant geometry used in estimating this balance. Shown is the total cross-sectional area, which includes the SEP module. Since the SEP module is not defined until later, this is obviously an iterative result.

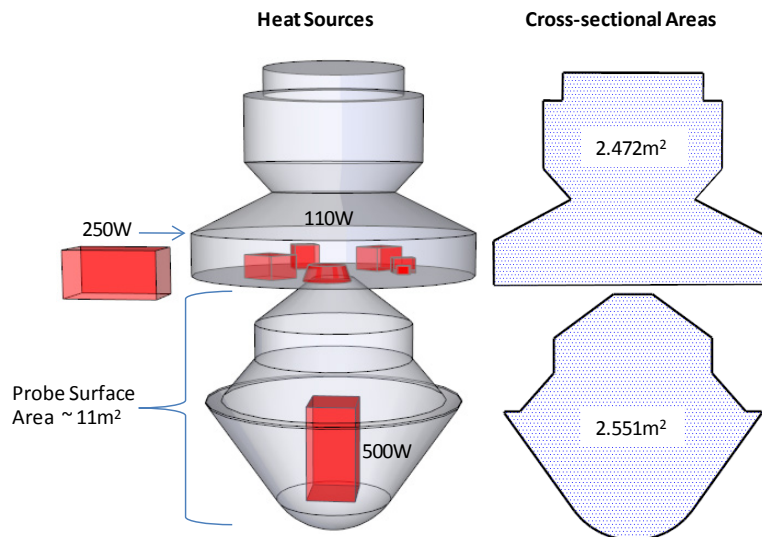


Figure 9-2: Geometry used in thermal energy balance estimation

First, define the operating conditions:

$$r_{\text{ops}} := 1 \quad \text{AU}$$

$$I_{\text{sun}} := \frac{1350 \text{ W} \cdot \text{m}^{-2}}{r_{\text{ops}}^2} = 1.35 \times 10^3 \cdot \frac{\text{W}}{\text{m}^2} \quad \text{Solar irradiance at operating distance}$$

$$\epsilon_s := 0.85 \quad \text{Spacecraft surface emissivity. Value for carbon is 0.8 (~ aeroshell).}$$

$$\alpha_s := 0.85 \quad \text{Spacecraft surface absorptivity. For a black body, this would be the same as the emissivity. Value for carbon is 0.8 (~ aeroshell).}$$

$$\sigma := 5.67 \cdot 10^{-8} \frac{\text{W}}{\text{m}^2 \cdot \text{K}^4} \quad \text{Stefan - Boltzman constant}$$

The internally generated heat (ASRG + electronic components) is $Q_{\text{ip}} = 860 \text{ W}$. Assume the spacecraft faces its full, largest cross-sectional area (A_{cs}) to the Sun. Hence the area normal to the Sun is the area of the entry probe (25513.7 cm^2) plus the area of the bus and SEP module (24721 cm^2), or

$$A_{\text{cs}} := 25513.7 \text{ cm}^2 + 24721 \text{ cm}^2 = 5.023 \text{ m}^2$$

The solar input to the spacecraft is then

$$Q_{\text{sun}} := \alpha_s \cdot A_{\text{cs}} \cdot I_{\text{sun}} = 5.764 \times 10^3 \cdot \text{W}$$

The total surface area for radiation is assumed to be the area of the TABS entry probe alone (worst case), or $A_s = 11.029 \text{ m}^2$. Hence, the average thermal equilibrium temperature of the spacecraft is (assume $T_{\text{space}} \sim 0 \text{ K}$)

$$T_{\text{sc,peak}} := \sqrt[4]{\frac{(Q_{\text{sun}} + Q_{\text{ip}})}{\epsilon_s \cdot \sigma A_s}} = 334.117 \text{ K} \quad \text{or} \quad T_{\text{sc,peak}} = 60.967 \cdot ^\circ\text{C}$$

This temperature is acceptable for most electronic components. However, since this is a rough preliminary estimate, it is wise at this stage of design to allocate for thermal radiators. How large these should be based on the current analysis is a matter of engineering judgment. We target about 10 degrees lower. If an additional radiator area is added that is not directly facing the sun, then the spacecraft would cool accordingly. For an $A_{\text{rad}} = 1.381 \text{ m}^2$, the new equilibrium temperature would be

$$T_{\text{sc,cool}} := \sqrt[4]{\frac{(Q_{\text{sun}} + Q_{\text{ip}})}{\epsilon_s \cdot \sigma (A_s + A_{\text{rad}})}} = 324.407 \text{ K} \quad \text{or} \quad T_{\text{sc,cool}} = 51.257 \cdot ^\circ\text{C}$$

Figure 9-3 shows the thermal balance for distances from 1 AU to Saturn's. As can be seen, the spacecraft equilibrium temperature at $\sim 9.6 \text{ AU}$ is about $-75 \text{ }^\circ\text{C}$. Naturally, heat is not uniformly distributed, and some components can tolerate cold better than others. The actual thermal design will incorporate these requirements, and allocated available heat as needed.

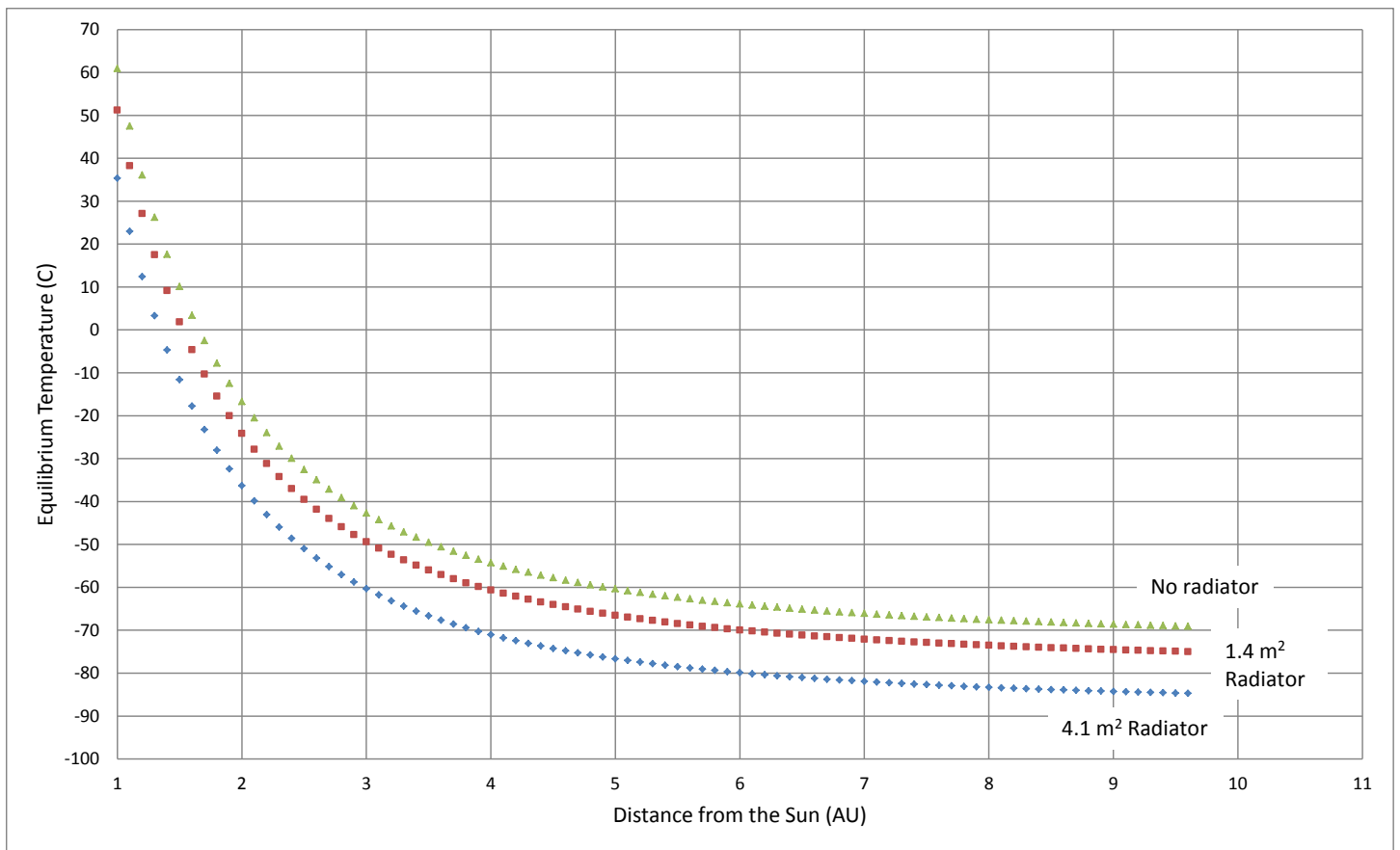


Figure 9-3: Spacecraft equilibrium temperature at different distances in its trajectory to Saturn

Finally, the communications system incorporates the requirements established in Section 4. The resulting CS configuration is shown in Figure 9-4, and this now becomes the complete “payload” that must be carried by the CHEM module.

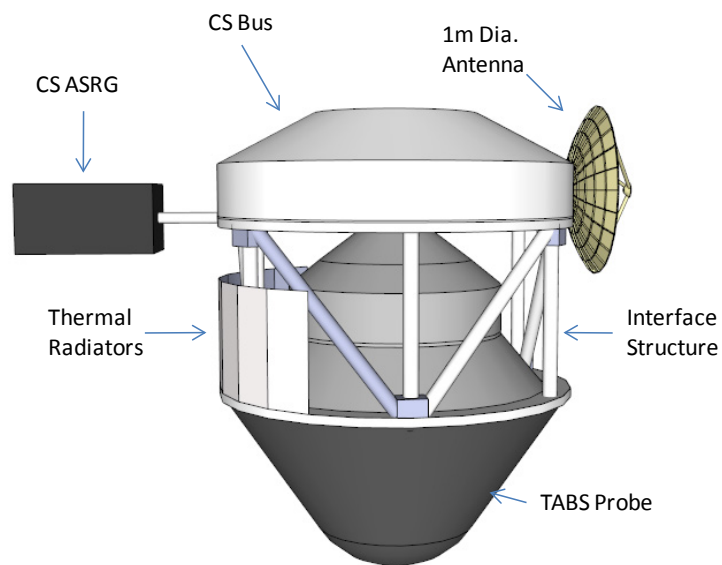


Figure 9-4: CHEM propulsion system payload, with TABS probe and CS

9.3 Chemical Propulsion System (CHEM)

There is now enough information to size the CHEM system, as we have the ΔV it must provide and the mass it must carry. The chemical propulsion system will be used for trajectory corrections en-route to Saturn after the Earth gravity assist (SEP is the operating system prior to this time), and for final maneuvering during flyby. A simple Hydrazine-based blow-down monopropellant system will be used. Current Hydrazine-based systems require that the catalyst bed be heated to facilitate hydrazine ignition. For a Hydrazine Mono-Propellant Thruster, the specific impulse is

$$I_{sp,CHEM} := 246s \quad \text{Specific Impulse}$$

Furthermore, the CHEM system will be utilized to provide attitude control authority, with capability to provide continuous and pulsed operation.

The initial vehicle mass is

$$m_{oc} = m_{pc} + m_{tc} + m_{ec} + m_{Lc}$$

where

- m_{oc} = Initial Vehicle Mass (without SEP module)
- m_{pc} = Propellant Mass
- m_{tc} = Propellant Tank Mass
- m_{ec} = Engine Mass (includes thruster structure, feed system, valves)
- m_{Lc} = Payload Mass (Spacecraft minus the chemical propulsion system)

Assuming complete propellant depletion (no ullage), the vehicle's final mass, m_{fc} is:

$$m_{fc} = m_{tc} + m_{ec} + m_{Lc}$$

The following parameters are known or specified by the monopropellant thruster system:

$m_{Lc} := 1037.3\text{kg}$ Payload mass (spacecraft dry mass plus 30% *except* CHEM propulsion system)

$f_{tc} := 0.2$ Tankage Structure Factor = m_{tc} / m_{pc}

$m_{ec} := 6\text{kg}$ Engine mass (estimate)

The ΔV used is based on the assumption that only trajectory corrections are required. Furthermore, it is assumed that a Cassini-style RCS system is sufficient to account for ΔV s less than 5 m/s⁶⁰. The TCM delta V depends on launch date, and gravity assist approach among other factors. However, a reasonable first-order approximation to size the chemical propulsion system is to use Cassini's TCM maneuvers, and extract those that may be applicable to TABS. From Table 3-1,

$$\Delta V_{CHEM} := 192 \frac{\text{m}}{\text{s}}$$

The gaseous exhaust velocity (in this study it is assumed that in the first approximation this is the same as the effective exhaust velocity) is

$$v_{e,CHEM} := g \cdot I_{sp,CHEM} = 2.412 \times 10^3 \text{ m} \cdot \text{s}^{-1}$$

The vehicle initial mass (without the SEP module) is

$$m_{oc} := \frac{m_{Lc} + m_{ec}}{(1 + f_{tc}) \cdot \exp\left(\frac{-\Delta V_{CHEM}}{v_{e,CHEM}}\right) - f_{tc}} = 1.149 \times 10^3 \text{ kg}$$

The propellant mass is obtained from

$$m_{pc} := m_{oc} \cdot \left(1 - \exp\left(\frac{-\Delta V_{CHEM}}{v_{e,CHEM}}\right) \right) = 87.883 \text{ kg}$$

The tank mass is obtained directly from the tankage structure factor

$$m_{tc} := f_{tc} \cdot m_{pc} = 17.577 \text{ kg}$$

The spacecraft final mass at end-of-life (assuming all the propellant is consumed, i.e., *no* ullage), is

$$m_{fc} := m_{tc} + m_{ec} + m_{Lc} = 1.061 \times 10^3 \text{ kg}$$

The propellant volume is obtained from the Hydrazine density,

$$\rho_{HZ} := 1.01 \frac{\text{gm}}{\text{cm}^3}$$

hence the propellant tank volume is

$$V_{tc0} := \frac{m_{pc}}{\rho_{HZ}} = 0.087 \text{ m}^3$$

Allowing for a 3% ullage (personal experience), the total tank volume is

$$V_{tc} := V_{tc0} \cdot 1.03 = 0.09 \text{ m}^3$$

Assuming a spherical tank, the tank radius is then

$$r_{tc} := \sqrt[3]{\frac{3}{4 \cdot \pi} \cdot V_{tc}} = 0.278 \text{ m}$$

The surface area of the spherical tank is

$$A_{tc} := 4 \cdot \pi \cdot r_{tc}^2 = 0.968 \text{ m}^2$$

If a composite Graphite fiber tank is used, with a density = 1.550 gm/cm³, the the wall thickness is

$$t_{tc} := \frac{m_{tc}}{A_{tc} \cdot 1.550 \text{ gm} \cdot \text{cm}^{-3}} = 0.012 \text{ m}$$

The inner (ID) and outer (OD) tank diameters are then

$$ID_t := 2 \cdot r_{tc} = 0.555 \text{ m} \quad OD_t := ID_t + 2 \cdot t_{tc} = 0.579 \text{ m}$$

We have thus sized the chemical propulsion system, and estimated the dimensions of the propellant tank shown in Figure 9-1.

9.4 Solar Electric Propulsion (SEP) Module

The requirements for the SEP module were defined in Sections 3.3 (ΔV) and 9.3 (payload mass). The initial requirements of the SEP system are then given by the variables:

$$m_{\text{pay}} := m_{\text{oc}} + 52\text{kg} = 1.201 \times 10^3 \text{ kg}$$

which is the payload mass that must be carried along by the SEP system (including contingency). Also, 52kg have been added to account for the SEP system *structure, solar array boom and deployment mechanism, and array drive* (including 30% contingency), which is also considered payload to be carried by the SEP system. Table 9-3 define these components and respective mass allocations. Both aluminum honeycomb with composite facesheets, and carbon composite materials are used. It should be pointed out that these are the result of an iterative process, and that the structure is meant to accommodate three ion thrusters, as will be seen later.

Table 9-3: SEP System structure mass allocations

	Quantity	Material	Size (cm)			Mass Composite Honeycomb (kg)			Mass Comp. (kg)	Select Mass (kg)
			Thickness	Area	Material Volume	Composite (1.0 or 2x0.5 cm)	Al Core	SubTotal	SubTotal	Totals
Cylindrical body	1	Ribbed, Epoxy/Graphite HM	0.5	21621.4	10810.7				17.06	17.06
Thruster Base Plate	1	Composite/Al Honeycomb	2.2	14720.8	32385.76	4.65	2.40	7.04		7.04
Cone Interface	1	Ribbed, Epoxy/Graphite HM	0.5	11721.5	5860.75				9.25	9.25
Array boom and deployment mechanism and array drive	1									6.67
Subtotal SEP Structure										40.02
Total with contingency	30%									52.02

The total ΔV required is

$$\Delta V_{\text{ISEP}} := 2.326 \frac{\text{km}}{\text{s}}$$

Want to find the SEP system optimum payload mass fraction. Assume the propulsion system performance is based on the NASA NSTAR Ion Propulsion System (IPS) flight validated through the New Millennium DS-1 mission (and DAWN). Performance data (at 2.5 kw source power level) is given by ⁶¹:

$$\tau_{\text{SEP}} := 8000\text{hr} \quad \text{Total allowable thrust time (Conservative Max design time)}$$

$$\beta_{\text{ppu}} := 5 \frac{\text{kg}}{\text{kW}} \quad \text{Power Processing Unit Specific Mass}$$

$$\eta_{\text{ppu}} := 0.92 \quad \text{Power Processing Unit efficiency (power conditioning for the thruster)}$$

$$\eta_{\text{th}} := 0.64 \quad \text{Thruster Efficiency: Efficiency of converting electric power to thrust power}$$

$$\beta_{\text{th}} := 2.8 \frac{\text{kg}}{\text{kW}} \quad \text{Thruster mass fraction}$$

$$\beta_{\text{s}} := 10.7 \frac{\text{kg}}{\text{kW}} \quad \text{Power source specific mass EOL. Although applicable to a solar concentrator array with mini-dome panel and multi-junction solar cells, it is a good enough approximation for TABS}$$

$$\eta_{\text{s}} := 1.0 \quad \text{Efficiency of converting raw power into electric power. For photovoltaic arrays, the output power is already in the form of electricity, so the efficiency = 1.0}$$

$$\beta_{\text{H}} := 0.4 \frac{\text{kg}}{\text{kW}} \quad \text{Typical radiator specific mass}$$

$$K_{\text{h}} := 0.1 \quad \text{Fraction of power lost in the thruster that needs to be handled by the radiator (estimate).}$$

$$f_{\text{tk}} := 0.15 \quad \text{Tankage structure factor (mass of tank/mass of propellant). Assume the mass of the feed system is also included with the tankage structure factor (obviously an approximation).}$$

Hence, the total propulsion system efficiency, source power to jet (or thrust) power is

$$\eta_T := \eta_{th} \cdot \eta_{ppu} \cdot \eta_s = 0.589$$

The jet specific mass, or the propulsion system mass per unit of jet power, is then

$$\beta_J := (\beta_{ppu} + \beta_{th} \cdot \eta_{ppu}) \cdot \eta_s + \beta_s + \frac{\beta_H \cdot [K_h \cdot (1 - \eta_{th}) \cdot \eta_{ppu} \cdot \eta_s]}{\eta_{th} \cdot \eta_{ppu} \cdot \eta_s} = 18.299 \frac{\text{kg}}{\text{kW}}$$

The specific mass of the entire propulsion system is then

$$\beta_T := \beta_J \cdot \eta_T = 10.774 \frac{\text{kg}}{\text{kW}}$$

Now we have all the elements needed to find the optimal payload mass fraction by adjusting the exhaust speed (and hence the Isp).

$$I_{sp} := 0\text{s}, 100\text{s}.. 10000\text{s} \quad \frac{1}{\beta_T} = 0.093 \frac{\text{kW}}{\text{kg}}$$

$$m_{fp}(I_{sp}) := \exp\left(\frac{-\Delta V_{1SEP}}{g \cdot I_{sp}}\right) - \left(1 - \exp\left(\frac{-\Delta V_{1SEP}}{g \cdot I_{sp}}\right)\right) \cdot \frac{\beta_T \cdot (g \cdot I_{sp})^2}{2 \cdot \eta_T \cdot \tau_{SEP}}$$

This equation is plotted and shown in Figure 9-5.

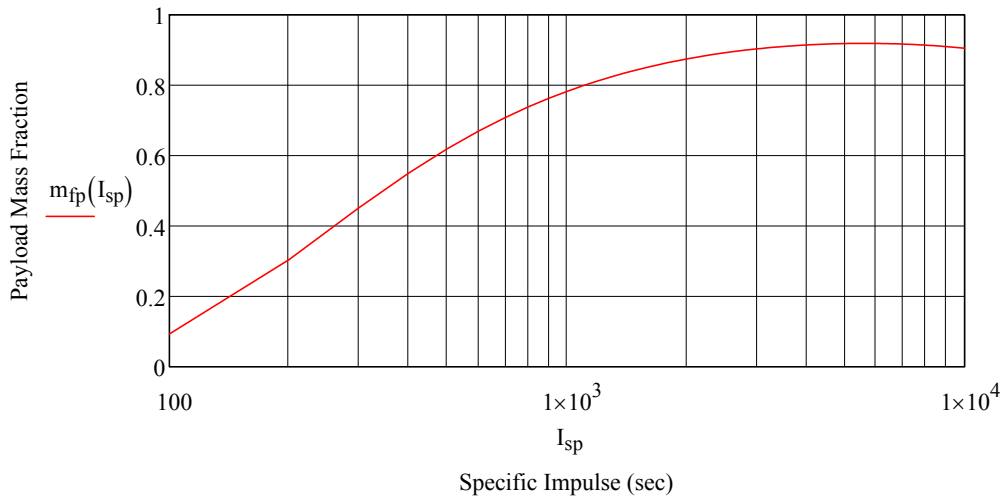


Figure 9-5: Finding the optimum specific impulse

An ion thruster efficiency is optimized at Isp's greater than 3000 seconds⁶². Given the large range of "optimal" exhaust velocities shown in the payload mass fraction optimization curve, it is quite reasonable to set the Isp at 3,100 seconds (NSTAR). This results in an exhaust speed equal to

$$I_{sp,SEP} := 3100\text{s}$$

$$v_{e,SEP} := g \cdot I_{sp,SEP} = 3.04 \times 10^4 \text{ m} \cdot \text{s}^{-1}$$

Since the I_{sp} selected is within the range of optimal payload mass fractions, as shown in Figure 9-5, the SEP system as defined can be optimized. In reality (as shown elsewhere), its use may not be entirely justified, as a chemical propulsion system may just as well provide the required performance to accomplish this mission. The key still relies on the payload mass fraction / launch vehicle combination. If the launch vehicle performance is such that the payload mass fraction is brought within values close to 1, the SEP system becomes the clear choice. This means that for the first time, the launch vehicle can truly be an "under-achiever" for a mission to Saturn. The IPS system would simply "cover-up" for this deficiency.

Now, we size the Ion Propulsion System (IPS) components one by one, and define their required parameters. This includes the power requirement levied on solar arrays as well, as the IPS is the *major* driver in this design (this will become clear as we compare the IPS power requirements with the on-board subsystem power consumption - kilowatts versus watts). The initial vehicle mass is obtained for the parameters given above. First, the payload mass fraction is

$$\mu_{LSEP} := \exp\left(\frac{-\Delta V_{1SEP}}{v_{e,SEP}}\right) - \left(1 - \exp\left(\frac{-\Delta V_{1SEP}}{v_{e,SEP}}\right)\right) \cdot \frac{\beta_T \cdot v_{e,SEP}^2}{2 \cdot \eta_T \cdot \tau_{SEP}} = 0.905$$

Hence the initial mass is

$$m_i := \frac{m_{pay}}{\mu_{LSEP}} = 1.327 \times 10^3 \text{ kg}$$

The propellant mass is obtained from

$$m_{Xe} := m_i \cdot \left(1 - \exp\left(\frac{-\Delta V_{1SEP}}{v_{e,SEP}}\right)\right) = 97.76 \text{ kg}$$

The propellant (tank) volume is computed from the properties of Xe gas at 247 K, assuming a required tank pressure of 3000 psi. It should be noted that the temperature will change depending on several factors, including amount of shading, tank thermal properties, and heat input.

$P_{\text{tank}} := 3000\text{psi}$	Tank pressure
$T_{\text{Xe},2.3} := 247\text{K}$	Tank temperature
$R_{\text{gas,Xe}} := 63.324 \frac{\text{J}}{\text{kg}\cdot\text{K}}$	Gas constant

From the perfect gas law, the gas density is

$$\rho_{Xe} := \frac{P_{\text{tank}}}{R_{\text{gas,Xe}} \cdot T_{\text{Xe},2.3}} = 1.322 \times 10^3 \text{ m}^{-3} \cdot \text{kg}$$

With the Xe mass given above, the tank volume is then

$$V_{\text{Xe,t}} := \frac{m_{Xe}}{\rho_{Xe}} = 0.074 \text{ m}^3$$

Assuming a spherical tank, the tank radius is then

$$r_{se} := \sqrt[3]{\frac{3}{4 \cdot \pi} \cdot V_{\text{Xe,t}}} = 0.26 \text{ m}$$

The surface area of the spherical tank is

$$A_{ts} := 4 \cdot \pi \cdot r_{se}^2$$

As before, a composite Graphite fiber tank with an epoxy resin matrix is assumed. then the wall thickness is

$$t_{ts} := \frac{m_{tc}}{A_{tc} \cdot 1550 \text{ gm} \cdot \text{cm}^{-3}} = 0.012 \cdot \text{mm}$$

The inner (ID) and outer (OD) tank diameters are then

$$ID_{ts} := 2 \cdot r_{se} = 0.521 \text{ m}$$

$$OD_{ts} := ID_{ts} + 2 \cdot t_{ts} = 0.521 \text{ m}$$

From which the tanks can be draw to properly size the layout.

The propellant flow rate is

$$m_{Xe.rate} := \frac{m_{Xe}}{\tau_{SEP}} = 3.394 \times 10^{-6} \text{ kg} \cdot \text{s}^{-1}$$

The *required electric power source* (system power) is then

$$P_{sr} := \frac{\frac{1}{2} \cdot m_{Xe.rate} \cdot v_{e.SEP}^2}{\eta_T} = 2.664 \times 10^3 \cdot \text{W}$$

The NSTAR IPS system is currently rated to 130 kg of propellant throughput, and 2.3 kW power⁹. Since those parameters represent the maximum performance capability of the IPS system under consideration, one NSTAR thruster is marginally sufficient to accomplish the mission from a maximum thruster processed power, with 2.3 kW versus 2.7 kW. A two NSTAR thruster system would provide sufficient to accomplish the mission. The heritage of this thruster gives confidence in the SEP implementation. A third thruster may be added as a spare and for two-level redundancy, and safeguards against a very early thruster failure.

The combined mass of the thruster and power processing unit is obtained from their respective specific mass and the solar array power output:

$$m_{th.ppu} := (\beta_{ppu} + \beta_{th} \cdot \eta_{ppu}) \cdot P_{sr} = 20.183 \text{ kg}$$

Now compute the mass of the thermal management system. The power lost to heat is equal to the system total (source) power minus the power leaving in the thruster exhaust. Hence

$$m_{Xe.ion} := 2.19 \cdot 10^{-25} \text{ kg}$$

$$e_c := 1.602 \cdot 10^{-19} \text{ C} \quad \text{is the charge of one electron}$$

$$W_k := \frac{1}{2} \cdot m_{Xe.ion} \cdot v_{e.SEP}^2 \cdot \frac{1}{e_c} = 631.708 \cdot \text{V} \quad \text{electron Volt (eV)}$$

where W_k is the kinetic energy of a X_e ion with the specified exhaust speed.

The part of the ion's energy spent in its ionization (12.1 eV) is proportional to its exhaust power, whereas the thrust power is proportional to its kinetic energy. Hence the exhaust power is

$$\left(1 - \frac{12.1\text{V}}{W_k}\right) = 0.981 \quad \text{percent higher than the thrust power. The power loss to heat is then}$$

$$P_H := P_{sr} - \eta_T \cdot P_{sr} \left[1 + \left(1 - \frac{12.1\text{V}}{W_k}\right) \cdot \frac{1}{100}\right] = 1.08 \cdot \text{kW}$$

The radiator mass is

$$m_H := \beta_H \cdot P_H = 0.432 \text{ kg}$$

The propellant and power system (solar array) dry masses are now computed. The propellant system dry mass (tank and feed system) is obtained from the tankage fraction:

$$m_{pr} := f_{tk} \cdot m_{Xe} = 14.664 \text{ kg}$$

The solar array mass is

$$m_{sa} := \beta_s \cdot P_{sr} = 28.505 \text{ kg}$$

The SEP system inert mass is then given by

$$m_{SEP.inert} := m_{th.ppu} + m_H + m_{pr} + m_{sa} = 63.784 \text{ kg}$$

Finally, the entire *SEP system wet mass* is

$$m_{SEP} := m_{SEP.inert} + m_{Xe} = 161.544 \text{ kg}$$

this does not include the truss structure mass, or the solar array support structure, which are book-kept separately.

Finally, the total vehicle (injected) mass can be computed. This includes the mass of the SEP and chemical propulsion systems, the aeroshell, and the spacecraft itself (including the science payload).

$$M_{total} := m_{pay} + m_{SEP} = 1.362 \times 10^3 \text{ kg}$$

This is the *injected payload mass*, or the mass that must be carried along by the launch vehicle. Figure 9-6 shows the SEP module layout based on the performance parameters developed above. The solar array dimensions are computed next.

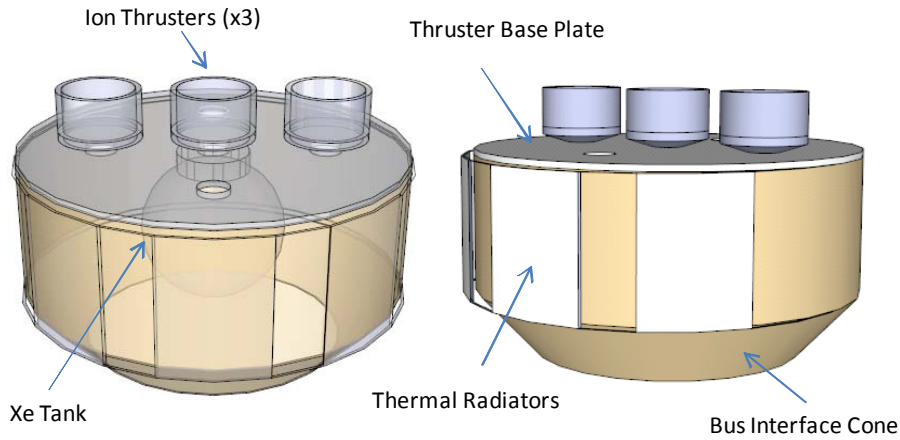


Figure 9-6: SEP Propulsion module (solar arrays not shown)

9.5 Solar Array

The dominant factor in sizing the array will be the Solar Electric Propulsion since the maximum expected loads during flyby will only be about 362W, as opposed to the ~2.7kW needed to drive the SEP system. Furthermore, the array must be functional for two years, at a maximum distance specified by the maximum thruster "on" time. This on-time was given as 8000 hrs to be on the conservative side, and is capable of yielding 2.3 km/s as required. There is sufficient time during the two-year (17,530hrs) SEEGA trajectory to operate the ion thruster the prescribed period of time. In order to constrain the array size however, we also choose that time to be as close to 1 AU as possible, on either side of the trajectory. The transfer ellipse for this constrained 2yr orbit (Section 3.3) is shown in Figure 9-7. Also shown are the points on either side of the ellipse in which the IPS must be on as required. This means the array must supply power to the IPS out to a maximum distance of 1.76 AU. This then constrains the operating distance of the array, and inputs into its size.

The following data is relevant to a triple-junctions solar array,

$$\eta_c := 0.30 \quad \text{Solar cell efficiency (GaInP/GaAs/Ge - 3-junctn, BOL)}$$

$$\text{at } T_\eta := (273.15 + 25)\text{K}$$

The solar cell temperature used for sizing the array is the panel thermal equilibrium temperature at 1.76 AU, the farthest the arrays will be required to operate the IPS. Since the IPS is the design driving parameter ("worst case" power load), sizing the arrays to operate at ~2.2 AU for a load of 362 W is not useful, but instead would be covered by the "worst case" calculations. Assuming a solar panel thermal emissivity of 0.94 and an absorptivity of 0.4, the result is

$$T_{\text{cop}} := 201\text{K}$$

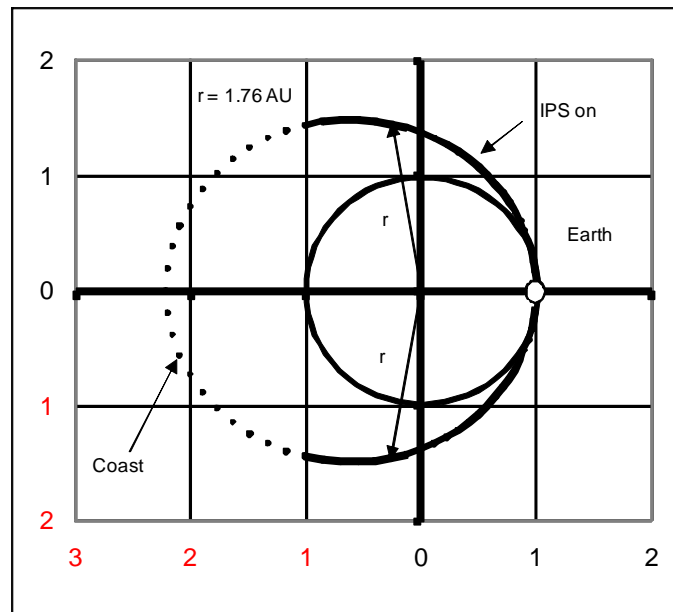


Figure 9-7: IPS "on" time required to provide 2.3 km/s, and maximum array operating distance

The array must be derated based on operating conditions and time. These factors are,

Degradation due to radiation and other effects $D_g := \frac{1.5\%}{\text{yr}}$

Maximum allowable off-normal Sun-Angle $N_{\text{off}} := 10\text{deg}$

The maximum operating distance to the Sun (r_{ops}) is again

$$r_{\text{ops}} := 1.76 \quad \text{AU}$$

Solar intensity at maximum operating distance

$$I_{s,\text{ops}} := \frac{1350 \frac{\text{W}}{\text{m}^2}}{r_{\text{ops}}^2}$$

The temperature coefficient (C_T) is the cell performance variation for operating at temperatures outside its nominal value. It is assumed to be typically ⁸

$$C_T := \frac{0.004}{\text{K}} \quad \text{per } ^\circ\text{C or Kelvin}$$

The cell packing factor is defined as

$$F_p := 0.9$$

The required array life is

$$\tau_{\text{op}} := 2\text{yr}$$

The load on the arrays corresponds to the required IPS system power, or

$$\text{Load} := P_{\text{sr}}$$

The performance change factor due to temperature is

$$E_T := |T_{\text{cop}} - T_{\eta}| \cdot C_T = 0.389$$

The Array Capacity (this is the power at BOL required to account for degradation effects) is then

$$C_A := \frac{\text{Load}}{(1 - D_g \cdot \tau_{\text{op}}) \cdot \cos(N_{\text{off}}) \cdot (1 - E_T)} = 4.561 \times 10^3 \cdot \text{W}$$

The total cell-coverage area is given by

$$A_{\text{cell,tot}} := \frac{C_A}{I_{s,\text{ops}} \cdot \eta_c} = 34.887 \text{ m}^2$$

If each individual cell size is (length x width)

$$l_e := 4\text{cm} \quad \times \quad w := 2\text{cm}$$

then the individual cell area is $A_{\text{per.cell}} := l_e \cdot w = 8 \cdot \text{cm}^2$

and the number of cells required to cover total area is

$$N_{\text{cells}} := \frac{A_{\text{cell.tot}}}{A_{\text{per.cell}}} = 4.361 \times 10^4$$

Given the cell packing factor, then the array size is

$$SA_{\text{size}} := \frac{A_{\text{cell.tot}}}{F_p} = 38.763 \text{m}^2$$

If there are 2 wings in the array, $N_w := 2$, then each array radius would be

$$r_{\text{array}} := \sqrt{\frac{SA_{\text{size}}}{N_w \cdot \pi}} = 2.484 \text{m}$$

This is the most efficient geometry and is appropriate to an Aeroflex type array. The complete SEP module, including solar array is shown in Figure 9-8.

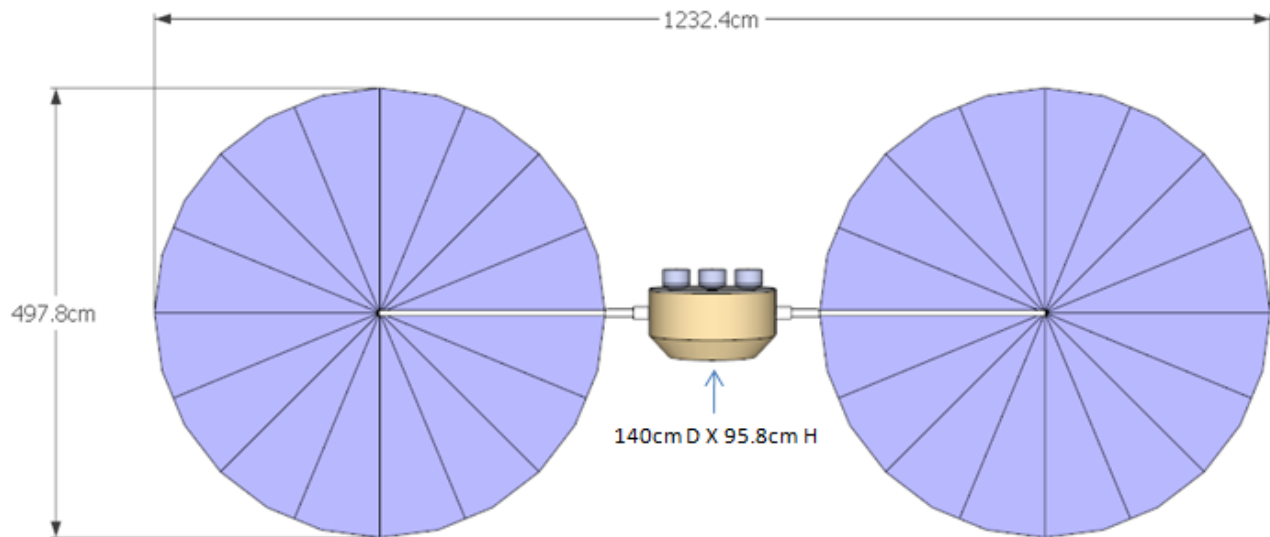


Figure 9-8: SEP Module

10.0 Integrated Space System and Launch Vehicle Selection

All major elements necessary to define the mission and spacecraft are now at hand. The TABS entry probe and the Carrier Spacecraft with its bus and SEP modules have been specified. Table 10-1 shows a summary of all mission-relevant subsystems, including the CS propulsion systems.

Table 10-1: Space system mass and power summary

SUBSYSTEM	MASS (kg)	Peak POWER (Watt)	Cruise POWER (Watt)	Flyby POWER (Watt) - rcv 4 hrs	Flyby POWER (Watt) - xmt 1.3 hr
Payload (TABS Entry Probe)	483.1	16.0			
Structure and Mechanisms	138.4				
Command & Data Handling	20.0	48.0	26.4	48.0	48.0
Communication	21.1	200.0	20.0	20.0	200.0
High-Gain Antenna (parabolic)	7.1				
Spacecraft Transceiver	9.0				
Low-Gain Antennae (2)	1.0				
Amplifiers (2)	4.0				
Power Systems	73.6	14.0	4.2	14.0	14.0
ASRG	38.2				
Power Control Electronics	17.0				
Battery	18.4				
Thermal Control	13.8	10.0	10.0	10.0	10.0
Harness / Fasteners	20.8				
ACS Sensors and Actuators	27.0	30.0	30.0	30.0	30.0
RWA / IMU	17.0				
Star Trackers (2) / Sun Sensors (8)	10.0				
Chemical Thrusters Power (mass below)		6.0			
Total Carrier Spacecraft Power Requirements(w/o SEP Module)		318.0	90.6	122.0	302.0
Spacecraft Dry Mass (w/o CHEM and SEP Module)	797.9				
Add 30% contingency for mass and 20% contingency for power	1037.3	381.6	108.7	146.4	362.4
Chemical Propulsion (incl. 30% cont)	111.5				
Attitude/Reaction Control Thrusters (8)	6.0				
Propellant Tank	17.6				
Propellant Mass (Hydrazine)	87.9				
Solar Electric Propulsion Module (incl. 30% cont)	213.6	2664			
SEP Structure	52.0				
Thruster and Power Processing Unit	20.18				
Propellant Tank and Feed System	14.7				
Propellant (Xenon)	97.76				
Radiator	0.432				
Solar Array	28.5				
Total Spacecraft Injected Mass (w/o Contingency)	1047.9				
Total Spacecraft Injected Mass (Incl. 30% Contingency)	1362.3				
Launch Vehicle Injected Mass Capability (Falcon 9)	1950				
Launch Vehicle Margin	587.7				
Launch Vehicle Margin Percent	30%				

A total injected vehicle mass of 1,362.3 kg which includes the TABS entry probe and delivery system is required. The launch vehicle selection provides for a 30% performance margin. Figure 10-1 shows NASA's ELV performance estimation for relevant vehicles. The Falcon 9 shows capable of injecting the TABS space system into the required transfer orbit. The Falcon 9's user guide⁶³ performance curve provides an even more favorable estimation, and yields the performance margin quoted in Table 10-1.

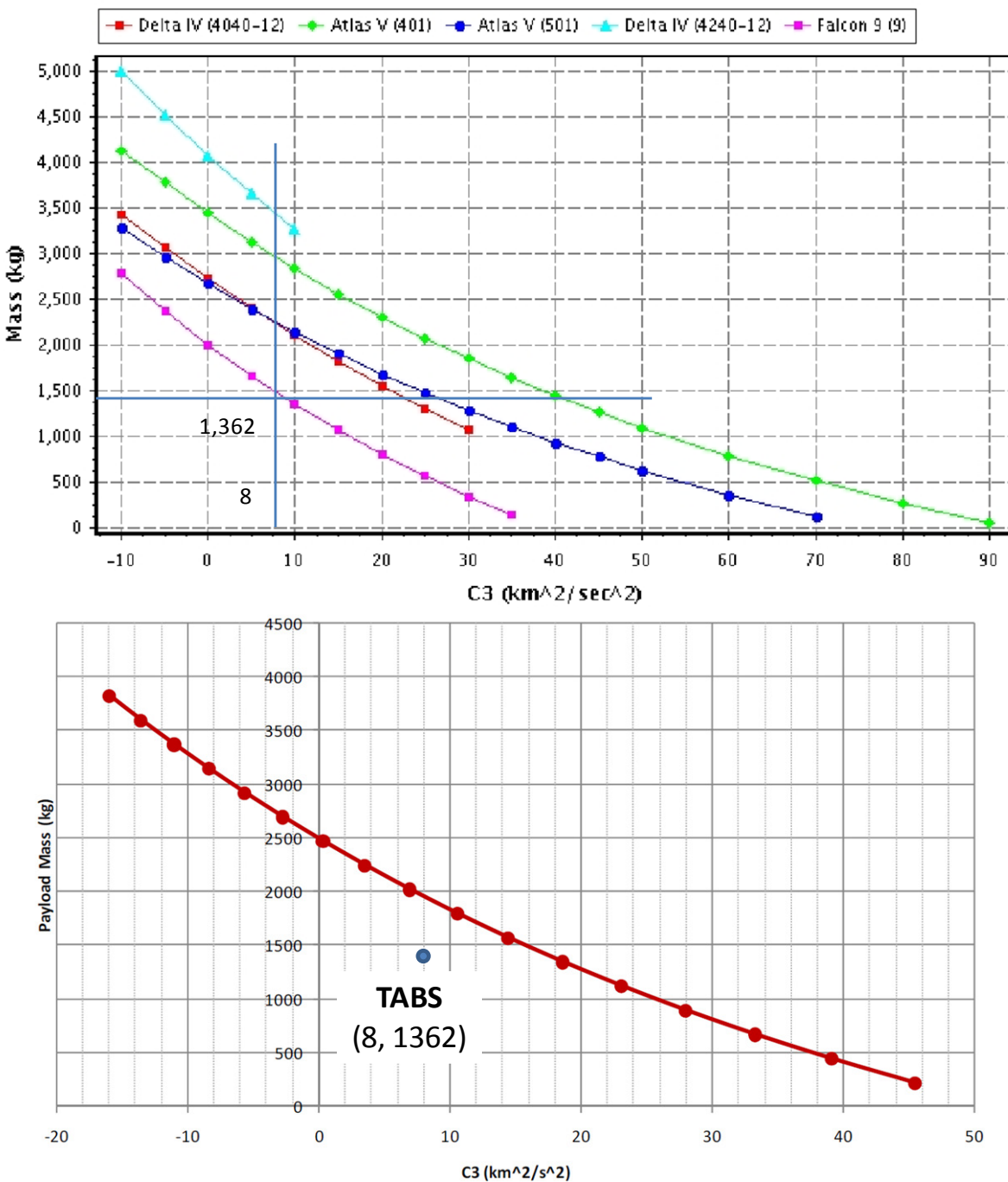


Figure 10-1: NASA ELV and Falcon 9 launch energy performance curves

Figure 10-2 shows the complete space system in deployed configuration. Figure 10-3 shows the overall deployed and launch configurations and dimensions.

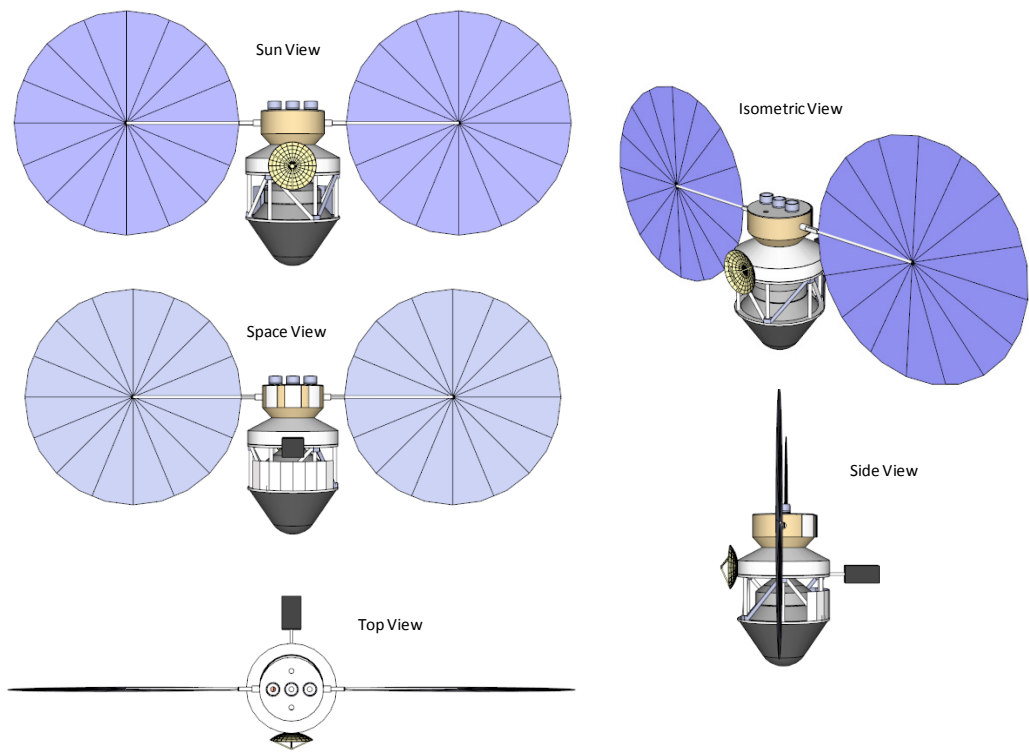


Figure 10-2: Complete Space System perspective views

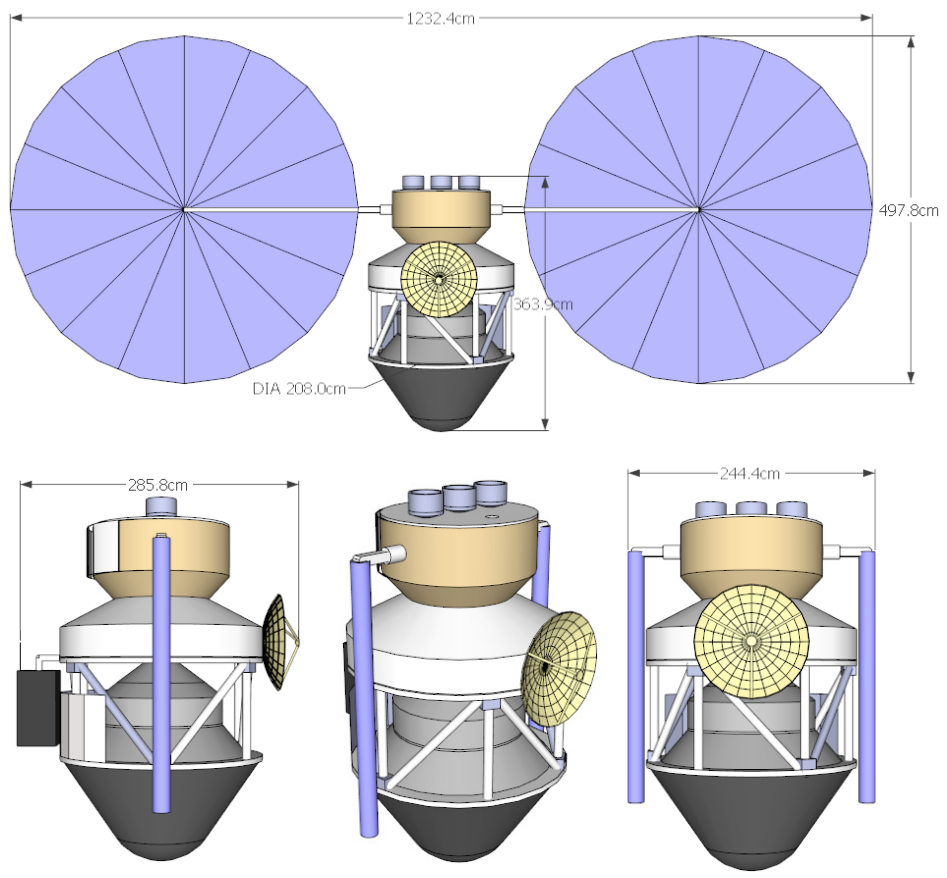


Figure 10-3: Deployed and launch vehicle configurations and dimensions

Figure 10-4 shows the TABS Space System inside the Falcon 9 fairing. As can be seen, there is more than enough volume left, and sufficient mass to co-manifest another space vehicle or additional smaller in-situ probes.

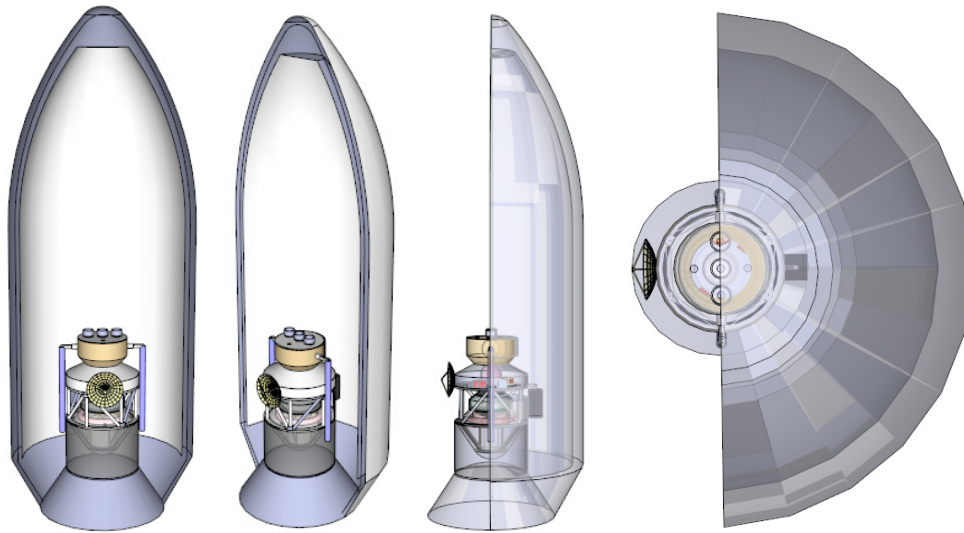


Figure 10-4: The TABS Space System fits well within the volume allocations of Falcon 9

11.0 Conclusion and Future Prospect

This dissertation research set out to demonstrate the feasibility of a Titan Balloon Aerobot, providing an alternative mission implementation as a departure from that documented through numerous studies both in Europe and in the United States. The consensus approach is to float a Montgolfier balloon in Titan’s atmosphere, primarily on the basis of longevity. Nonetheless, as it was demonstrated throughout this work, a Hydrogen-based balloon system not only proves viable, but also presents some important simplifications to the consensus approach. This is particularly the case for the initial deployment scheme. Although no planetary balloon deployment of this size is to be underestimated, adding complicated packaging and deployment schemes of a radiant source (as in the consensus Montgolfier approach) presents an initial and immediate high-risk to the mission. By concentrating on tried and proven technology, and by making some realistic assumptions where developing technologies are needed (mostly in the high-pressure tank and ASRG arenas), TABS gets closer to what is believed to be a lower risk approach to Titan’s atmospheric and in-situ exploration.

The preliminary design baseline is the result of numerous iterations where packaging of instruments, buoyant-gas tanks, decelerator system, balloon, and antenna was such that it ultimately resulted in a feasible buoyant-gas balloon implementation that minimized the size and mass requirements. The final packaging constrained the volume needed and defined the aeroshell and entry probe. It also constrained the carrier spacecraft and the overall space system. Design iterations are shown in Figure 11-1 compared to the selected baseline.

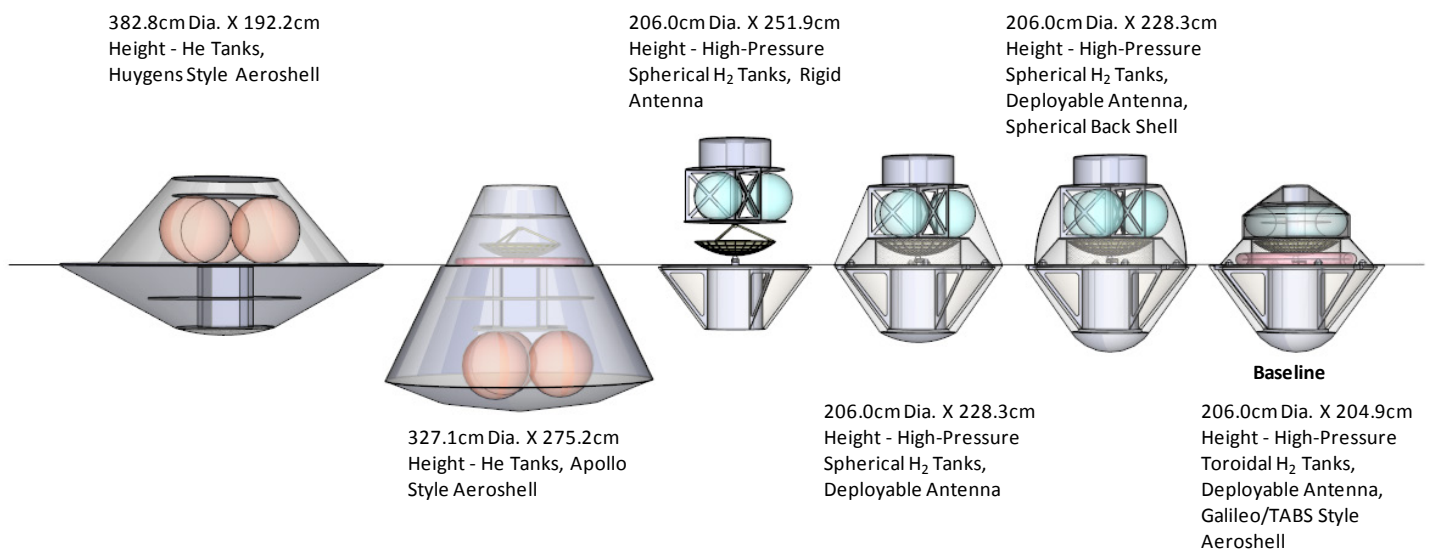


Figure 11-1: Layout and aeroshell configurations leading to the baseline (drawn to scale)

Compared to the TSSM Study entry probe, TABS offers a buoyant-gas alternative at a mass that is not much higher (483 kg versus 398 kg), but with the added advantage of using a balloon system with a far less complicated deployment and operational process, using a “closed” versus an open (atmospheric) gas control system. It is important to note that the use of a buoyant gas (Helium) balloon in another planetary atmosphere has already been demonstrated lending credibility to this approach, albeit with differing size and environmental conditions⁶⁴. Figure 11-2 provides a comparison of TABS and TSSM’s in-situ entry probe size and mass (Huygens added for reference). As can be seen, for the same payload and mission lifetime, the TABS alternative to the Montgolfier consensus is quite competitive, and to this date offers the only known feasible implementation of a Titan buoyant gas entry system for a vehicle in its class.

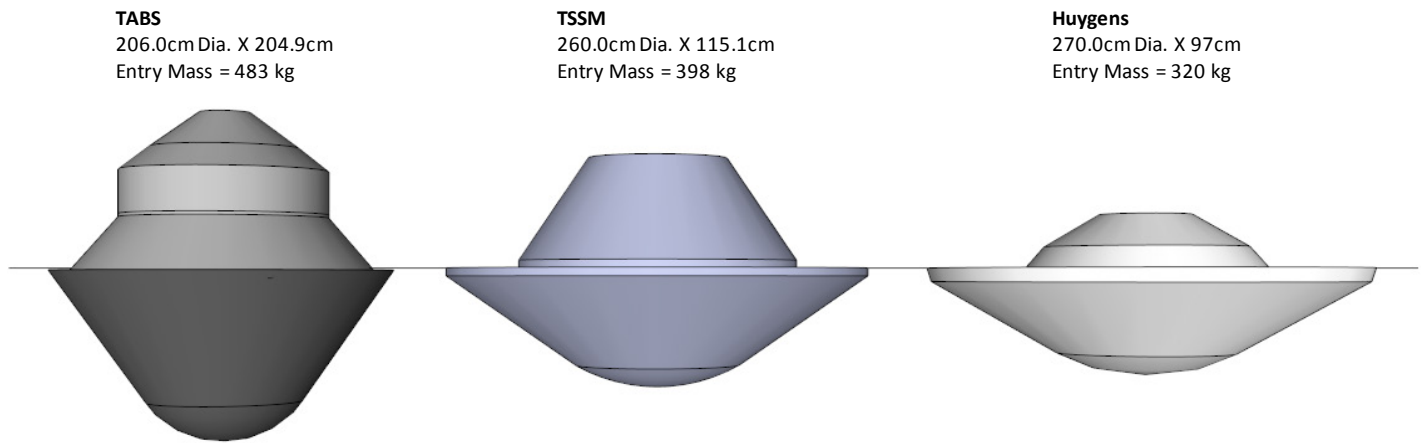


Figure 11-2: Size and mass comparisons for Titan entry systems (drawn to scale)

As part of this work, a new Thermal Protection System (TPS) was also designed, manufactured, and tested successfully at the IRS Plasma Wind Tunnel (PWK1). This new carbon/Phenolic ablator represents an important contribution of TABS not only to planetary entry into Titan's atmosphere, but (as shown as well) as potential use in Earth re-entry missions including planetary sample returns. The Resin Impregnated Carbon Ablator (RICA) developed at the University of Stuttgart will see continuing development over the years to come, but more importantly, hopefully will lead to flight demonstration and scientific application.

In conclusion, this dissertation research has developed a mission that demonstrates the only known and detailed feasible alternative to the Titan Montgolfier consensus, has provided an important empirical contribution to the field of hyperbolic entry ablator research, and through allocation of ample contingencies and margin, has left the door open for international cooperation in an area where pooling institutional and national resources is paramount to any complex mission success.

12.0 References

1. Titan Saturn System Mission (TSSM), Final Report on the NASA Contribution to a Joint Mission with ESA, January 30, 2009, Task Order #NMO710851.
2. Beauchamp, P. M.: "Technologies for Outer Planet Missions: A Companion to the Outer Planet Assessment Group (OPAG) Strategic Exploration White Paper, September 12, 2009.
3. Esper J., "The Neptune / Triton Explorer Mission: A Concept Feasibility Study," Master's Thesis, The George Washington University, Washington, D.C., January 2000.
4. Modified from Surampudi, S.: "Radioisotope Power Systems Technology Programs," presentation to the Radioisotope Power Systems Committee, NASA, Washington, D.C., November 18, 2008.
5. TSSM In Situ Elements, ESA contribution to the Titan Saturn System Mission, ESA-SRE(2008)4, 12 February 2009.
6. Personal contact with the German Mars Society and Hannes Griebel.
7. DISR Movie data available on-line and produced by Erich Karkoschka, the DISR Team, NASA, and ESA. Version 2, University of Arizona 2006.
8. Griffin, M. D., and J. R. French: "Space Vehicle Design," American Institute of Aeronautics and Astronautics, Washington, D.C., 1991.
9. Noca, M., R.W. Bailey: "Titan Explorer Mission Trades from the Perspective of Aerocapture, preprint 2005.
10. Ball, A., J., J. R. C. Garry, R. D. Lorenz, V. V., Kerzhanovich: "Planetary Landers and Entry Probes," Cambridge University Press, Cambridge, 2007.
11. Hall, J. et. al., "Experimental results for Titan aerobot thermo-mechanical subsystem development." *Advances in Space Research* 42 (2008) 1641–1647.
12. Hall, J., et. al.: "A gas management system for an ultra long duration Titan blimp," *Advances in Space Research* 44 (2009) 116–123.
13. Lorenz, R. D." "A Review of Balloon Concepts for Titan," *JBIS*, Vol. 61, pp.2-13, 2008.
14. Samuelson, R. E., et. al.: "Mean molecular weight and hydrogen abundance of Titan's atmosphere," *Nature* 292, 688-693 (20 Aug 1981).
15. Humble, R.W., G. H. Henry, and W. J. Larson, ed.: "Space Propulsion Analysis and Design," McGraw Hill, Inc., New York, 1995.
16. DOE Hydrogen Program, "Low-Cost, High-Efficiency, High-Pressure Hydrogen Storage," Annual Progress Report, FY 2009.
17. US DOD, Handbook, "Metallic Materials and Elements for Aerospace Vehicle Structures," MIL-HDBK-5J, pp. 5-17, 31 January 2003.
18. AIAA: "AIAA Aerospace Design Engineers Guide," American Institute of Aeronautics and Astronautics, Reston, Virginia, 2003.
19. Kawahara, G., S. F. McKleskey: "Titanium-lined, Carbon Composite Overwrapped Pressure Vessel," 32nd AIAA/ASME/SAE/ASEE Joint Propulsion Conference, Lake Buena Vista, FL, July 1996.
20. ARIAN Industrial Control and Automation, "Theory overview of flow measurement using differential pressure devices based on ISO-5167 standard"
21. http://en.wikipedia.org/wiki/Specific_heat_capacity.
22. J. Cui et. al., "Analysis of Titan's neutral upper atmosphere from Cassini Ion Neutral Mass Spectrometer measurements," *Icarus* 200 (2009) 581–615.
23. Gallais, P.: "Atmospheric Re-Entry Vehicle Mechanics," Springer-Verlag, Berlin, 2007.
24. Paul Wercinski, et. al., "Jupiter Deep Probe Design - Entry/Descent System Challenges and Trades," NASA JPL 2003.
25. Burk, T.: "Attitude Control Performance During Cassini Trajectory Correction Maneuvers," AIAA Guidance, Navigation, and Control Conference and Exhibit, San Francisco, California, August 2005.
26. Simons, R., et. al.: "Ultra High Power and Efficiency Space Traveling-Wave Tube Amplifier Power Combiner with Reduced Size and Mass for NASA Missions," NASA/TM-2009-215584, 2009.
27. Coustenis, A., et. al.: "TandEM: Titan and Enceladus mission", *Exp Astron* (2009) 23:893–946.
28. CRC Handbook of Chemistry and Physics 91st edition, 2010-2011
29. M. Fulchignoni, et. al., "In situ measurements of the physical characteristics of Titan's environment," *Nature Articles*, Vol. 438, 8 December 2005.
30. M. Fulchignoni et. al., "The Characterization of Titan's Atmospheric Physical Properties by the Huygens Atmospheric Structure Instrument (HASI)," *Space Science Reviews* 104: 395–431, 2002.
31. Duvall, A., C.G. Justus, and V. W. Keller: "Global Reference Atmospheric Models for Aeroassist Applications," 3rd International Planetary Probe Workshop, Anavyssos, Attiki, Greece, 2005.
32. Yelle, R. V., Strobel, D. F., Lellouch, E., and Gautier, D.: "Engineering Models for Titan's Atmosphere", in *Huygens: Science, Payload, and Mission*, ESA SP-1177, August, 1997.
33. Hirschel, E. H.: "Basics of Aerothermodynamics," Springer-Verlag, Berlin, 2005.
34. Latto, B., and M. W. Saunders: "Viscosity of Nitrogen Gas at Low Temperatures Up to High Pressures: A New Appraisal," *The Canadian Journal of Chemical Engineering*, Vol. 50, December, 1972.

35. Martin, A., and I. D. Boyd: "Non-Darcian Behavior of Pyrolysis Gas in a Thermal Protection System," *Journal of Thermophysics and Heat Transfer*, Vol. 24, No. 1, January–March 2010.
36. Allen and Eggers, "A Study of the Motion and Aerodynamic Heating of Missiles Entering the Earth's Atmosphere at High Supersonic Speeds", NACA TR-1381, 1958.
37. R. W. Detra, H. Hidalgo, "Generalized Heat Transfer Formulas and Graphs for Nose Cone Re-Entry into the Atmosphere". *ARS Journal*, March 1961, pp.318-221.
38. J. A. Fay, F. R. Riddell, "Theory of Stagnation Point Heat Transfer in Dissociated Gas". *Journal of Aeronautical Science*, Vol. 25, No. 2, 1958, pp. 73-85.
39. Barter, N. J. Editor: "Northrop-Grumman Space Data," Northrop Grumman Corp., 5th edition, 2003.
40. Venkatapathy, E., et. al.: "Selection and Certification of TPS: Constraints and Considerations for Venus Missions," Preprint, Supported by NASA's In-Space Propulsion Program.
41. Laub, B., and E. Venkatapathy: "Thermal Protection System Technology and Facility Needs for Demanding Future Planetary Missions," *International Workshop on Planetary Probe Atmospheric Entry and Descent Trajectory Analysis and Science*, Lisbon, Portugal, October 2003.
42. Venkatapathy, E., et. al.: "Thermal protection system development, testing, and qualification for atmospheric probes and sample return missions Examples for Saturn, Titan and Stardust-type sample return", *Advances in Space Research* 44 (2009) 138–150 (table 3).
43. Wright, M. J, and F. S. Milos: "Afterbody Aeroheating Flight Data for Planetary Probe Thermal Protection System Design," *Journal of Spacecraft and Rockets*, Vol. 43, No. 5, September–October 2006.
44. Couzin, P. et. al.: "Huygens Probe Design: Some Lessons Learnt," *Proceedings of the 3rd International Planetary Probe Workshop*, Anavyssos, Attiki, Greece, 27 June – 1 July 2005 (ESA SP-607, April 2006).
45. Walpot, L. M., et. al., "Convective and Radiative Heat Flux Prediction of Huygens's Entry on Titan," *Journal of Thermophysics and heat transfer*, Vol. 20, No. 4, October–December 2006.
46. Bouilly, J-M.: "Thermal Protection System of the Huygens Probe During Titan entry: Flight Preparation and Lessons Learned," *Proceedings of the 3rd International Planetary Probe Workshop*, Anavyssos, Attiki, Greece, 27 June – 1 July 2005 (ESA SP-607, April 2006).
47. Colombatti, G., et., al.: "Huygens probe entry dynamic model and accelerometer data analysis," *Planetary and Space Science* 56 (2008) 601–612.
48. Atkinson, D.H., et. al., "Huygens probe entry and descent trajectory analysis and reconstruction techniques," *Planetary and Space Science* 53 (2005) 586–593.
49. Hollis, B. R., et. al.: "Prediction of the Aerothermodynamic Environment of the Huygens Probe," 38th AIAA Thermophysics Conference, 6-9 Jun 2005, Toronto, Ontario.
50. Wright, M. J., et. al.: "Post-Flight Aerothermal Analysis of the Huygens Probe," *Proceedings of the 3rd International Planetary Probe Workshop*, Anavyssos, Attiki, Greece, 27 June – 1 July 2005.
51. Raynaud, E., et. al.: "Huygens Aerothermal Environment: Radiative Heating," Preprint.
52. NASA Engineering and Safety Center (NESC): "Cassini/Huygens Probe Entry, Descent, and Landing (EDL) at Titan Independent Technical Assessment," May 26, 2005.
53. Underwood, J.: "Parachute System Design Case Study – Huygens," 3rd International Planetary Probe Workshop, Anavyssos, Attiki, Greece, 27 June – 1 July 2005.
54. Wolf, D. F.: "Parachute Inflation and Opening Shock," 3rd International Planetary Probe Workshop, Anavyssos, Attiki, Greece, 27 June – 1 July 2005.
55. Wolf, D. F.: "Parachute Design Examples," 3rd International Planetary Probe Workshop, Anavyssos, Attiki, Greece, 27 June – 1 July 2005.
56. Jajpat R. Utreja, "Prediction of the Drag Coefficient of a 20-degree Conical ribbon Parachute," NASA TN-230-1523, 1975.
57. Taylor, A. P.: "An investigation of the Apparent Mass of Parachutes Under Post-inflation Dynamic Loading Through the use of Fluid Structure Interaction Simulations," AIAA preprint.
58. Ewing, E. G., H. W. Bixby, and T. W. Knacke: "Recovery Systems Design Guide," Technical Report, AFFDL-TR-78-151, 1978.
59. Williams, R. B., et., al.: "Minimum Mass Design of Large-Scale Space Trusses Subjected to Thermal Gradients", AIAA Preprint, Table 2, pp.16.
60. Henry, C. A.: "An Introduction to the Design of the Cassini Spacecraft," *Space Science Reviews* 104: 129–153, 2002.
61. Sovey, J., et. al.: "Development Status of the NASA 30-cm Ion Thruster and Power Processor," NASA Technical Memorandum 106740, 1994.
62. Oleson, S.R.: "An Analytical Optimization of Electric Propulsion Orbit Transfer Vehicles," NASA Contractor Report 191129, May 1993.
63. Space Exploration Technologies Corp.: "Falcon 9 Launch Vehicle Payload User's Guide," SCM 2008-010 Rev. 1, 2009.
64. Sagdeev, R. Z.: "An overview of the Soviet Vega balloon experiment and studies of the atmosphere of Venus," NASA-TM-88516, 1986.

Abridged Curriculum Vitae

Jaime Esper

NASA Goddard Space Flight Center
Greenbelt, MD 20771
E-Mail: Jaime.Esper@nasa.gov

Current Education

- M. S. Mechanical (Aerospace) Engineering, The George Washington University, 2000.
- M. S., Astronomy, University of Florida, 1987.
- B. S., Physics, University of Florida, 1984.

Capabilities Highlights

- *Research Project Manager & Principal Investigator.* Responsible for the technical and programmatic management of Modular, Adaptive, Reconfigurable (MARS) system-level research at NASA GSFC (October 2002 – Present: NASA).
- *Chief Engineer, Minotaur Launch, NASA Wallops Flight Facility.* The Minotaur 1 expendable launch vehicle carrying the TacSat-2 spacecraft was successfully launched into orbit on December 16th, 2006 with nominal NASA Range performance (June 2006 – December 2006: NASA)
- *Deputy Chief Engineer, Robotic Lunar Exploration Program Lander.* Technical leadership of a multi-center team, with project management at NASA MSFC (November 2005 – June 2006: NASA).
- *Senior Aerospace Engineer, Flight System Design.* Exploration Systems Research & Technology Program (NASA HQ) Technical Point of Contact for GSFC (November 2003 – November 2005: NASA).
- *Associate Head, Earth Science Missions Branch, Systems Engineering and Advanced Concepts Division.* Responsible for planning, implementing, directing, and coordinating a comprehensive program for all activities of the Division related to mission systems engineering (February 2002 – February 2004: NASA).
- *Space Technology 5 Mission Systems Engineer.* Carry the responsibilities of the Mission Systems Engineer for the New Millennium Program mission (1998 –2001: Swales Aerospace).
- *Member of the post-launch test team of the Geostationary Operational Environmental Satellite (GOES-10) launched in May 1997.* Worked to redefine the materials and methods for obtaining and processing radiometric data for image navigation and registration (1997 – 1998: Swales Aerospace).
- *Flight Systems Engineering Lead for the Fine Guidance System (FGS) replacement during the 1997 Hubble Space Telescope (HST) Second Servicing Mission.* As Lead Systems Engineer, coordinated activities relating to instrument hardware modifications, I&T, and flight systems (1993 – 1997: AlliedSignal Aerospace).
- *Flight Systems Engineering Lead for HST's Optical Telescope Assembly.* Activities included the support of the Hubble Space Telescope's optical collimation campaign. Led the *implementation* of corrections needed to refocus the instrument for performance optimization (1990 – 1997: AlliedSignal Aerospace).
- *Pointing Control System Engineer, HST.* Supported the development of activities leading to the successful launch of the Hubble Space Telescope (1989 – 1990: AlliedSignal Aerospace).
- *International Ultraviolet Explorer (IUE) spacecraft controller.* In charge of executing real-time commands required to start and stop science observations (1988 – 1989: Computer Sciences Corporation).
- *Master of Science Research Work* at The George Washington University centered on developing an advanced concept for a Neptune-Triton mission (1996 – 1999: The George Washington University).
- *Master of Science Research Work* at the University of Florida included the participation in the research, design, and development team of an automated photometric telescope, installed in the Amundsen-Scott, South Pole station (1984-1987: University of Florida).

Select Publications

1. "Small Rocket/Spacecraft Technology (SMART) Platform", Small Satellite Conference, Logan Utah, August 2011.
2. "Resin Impregnated Carbon Ablator (RICA): A new Thermal Protection System Material for High-Speed Planetary Entry Vehicles", 8th Annual International Planetary Probe Workshop, Portsmouth VA, June, 2011. With Hans-Peter Röser and Georg Herdrich.
3. "Linking and Combining Distributed Operations Facilities Using NASA's GMSEC System Architecture", SpaceOps 2008 Conference, Heidelberg, Germany, May 2008. With D. Smith, T. Grubb.
4. "Outcomes and Visions of the International Study on Cost-Effective Earth Observation Missions", 57th International Astronautical Congress, Valencia, Spain, October 2006. With R. Sandau, L. Paxton.
5. "Modular, Adaptive, Reconfigurable Systems: Technology for Sustainable, Reliable, Effective, and Affordable Space Exploration," Proceedings of the Space Technology and Applications International Forum, American Institute of Physics, 2005.
6. "Modular, Reconfigurable, and Rapid Response Space Systems: the remote sensing advanced technology microsatellite," AIAA 2nd Responsive Space Conference, El Segundo CA, April 2004. With Jim Andary, John Oberright, Maria So, Peter Wegner, Alok Das, Joe Hauser.
7. "The Neptune / Triton Explorer Mission: A Concept Feasibility Study," Proceedings of the 5th IAA International Conference on Low-Cost Planetary Missions, ESTEC, Noordwijk, The Netherlands, 24-26 September 2003, ESA SP-542, November 2003.
8. "Spectral Considerations for the Measurement of Carbon in the Visible and Near Infrared," ASPRS Annual Conference, Anchorage, May 2003. With Janette C. Gervin, Robert W. Knox, Charles R. McClain, Forrest G. Hall.
9. "Low Density Biomass & Coastal Ocean: A Carbon Cycle Mission," 4th International Academy of Astronautics, Symposium on Small Satellites for Earth Observation, Berlin, Germany, April 2003. With Jan Gervin, Frank Kirchman, Betsy Middleton, Robert Knox, Charles McClain, Forrest Hall.
10. "Technology for Earth Science Missions: the Next Generation Small Spacecraft," 52nd International Astronautical Congress, Toulouse, France, October 2001. With S. Neeck.
11. "Nano/Micro Satellite Constellations for Earth and Space Science," 3rd International Academy of Astronautics, Symposium on Small Satellites for Earth Observation, Berlin, Germany, April 2001. With S. Neeck, James A. Slavin, Jesse Leitner, W. Wiscombe, Frank Bauer.
12. "Leonardo-BRDF: A New Generation Satellite Constellation," 51st International Astronautical Congress, Rio de Janeiro, Brazil, October 2000. With W. Wiscombe, S. Neeck, S. Hughes, Si-Chee Tsay, M. Ryschkewitsch.
13. "NASA-GSFC Nano-Satellite Technology for Earth Science Missions," Acta Astronautica Vol. 46, Nos. 2-6, pp. 287-296, 2000. With P. Panetta, M. Ryschkewitsch, W. Wiscombe, S. Neeck.
14. "VOLCAN: A Mission to Explore Jupiter's Volcanic Moon Io," 4th IAF Conference on Low Cost Planetary Missions, Columbia, MD April 2000. With P. Panetta, M. Concha, P. Coronado, S. Scott, J. Soldner.
15. "Advanced Geosynchronous Studies Imager: Scanning Star Detection," The International Symposium on Optical Science, Engineering, and Instrumentation, SPIE July 1999, Denver, Colorado. With D. Chu, J. Carr, J. Bremer, R. Kindsfather.
16. "Advanced Geosynchronous Studies Imager (AGSI): Image Navigation and Registration (INR) System," The International Symposium on Optical Science, Engineering, and Instrumentation, SPIE July 1999, Denver, Colorado. With J. Le Moigne, J. Carr, D. Chu.
17. "Opportunities for the Application of New Millennium Concepts and Technologies," IAF Specialists Symposium on Novel Concepts for Cheaper, Faster, Better Space Missions, Redondo Beach CA, April 1999. With M. Cully, M. Perry.
18. "Enabling Technologies for Nano-satellite Constellations," IAF Specialists Symposium on Novel Concepts for Cheaper, Faster, Better Space Missions, Redondo Beach CA, April 1999. With P. Panetta.
19. "New GOES Landmark Selection and Measurement Methods for Improved On-Orbit Image Navigation and Registration Performance," European Symposium on Remote Sensing, Barcelona, Spain, September 1998. With W. Bryant, J. Carr, and J. Harris.
20. "Space Telescope Fine Guidance Sensor Bearing Anomaly," 30th Aerospace Mechanism Symposium, NASA Langley Research Center, May 15-17, 1996. With S. Loewenthal, J. Pan, and J. Decker.
21. "Optimum Focusing Conditions for the International Ultraviolet Explorer (IUE) Spectral Cameras at Low Resolution," Report 3 Agency Meeting, NASA Goddard Space Flight Center, November 1989. With M. R. Perez, and L. F. Huber.
22. "An Automated South Pole Stellar Telescope," Proceedings of the 118th symposium of the International Astronomical Union, Christchurch, New Zealand, December 1985. With K-Y. Chen, J. D. McNeill, J. P. Oliver, G. Schneider, and F. B. Wood.

Professional Awards

- Robert H. Goddard Award, NASA Goddard Space Flight Center, “Exceptional Achievement Award for Engineering”, August 2010
- Exceptional Achievement Award, NASA Goddard Space Flight Center, GREAT Project, “For outstanding engineering of a remotely-controlled, autonomous robotic vehicle for testing flight avionics, by a team of university and Goddard engineers”, December 2007.
- Performance Award, NASA Goddard Space Flight Center, “In recognition and appreciation for exceptional service in the performance of official duties”, July 2007.
- Group Achievement Award, NASA, Space Technology 5 Team, “For outstanding accomplishment in building, testing, launching, and operating the Space Technology 5 mission, enabling future NASA science missions”, May 2007.
- Team time Off Award, NASA Goddard Space Flight Center, “TacSat-2 Time-Off Award”, December 2006.
- Performance Award, NASA Goddard Space Flight Center, “In recognition and appreciation of exceptional service in the performance of official Duties,” March 2005.
- Performance Award, NASA Goddard Space Flight Center, “In recognition and appreciation of exceptional service in the performance of official Duties,” April 2004.
- NASA Medal for Exceptional Service, “In recognition of your outstanding dedication to the development of new Earth Science technologies and mission formulation,” August 2003.
- Special Act Award, NASA Goddard Space Flight Center, Sun Earth Connection Roadmap Missions Definition Team, September 2002.
- Special Act Award, NASA Goddard Space Flight Center, “In recognition of services in the area of Advanced Concepts,” July 2002.
- NASA Engineering Excellence Group Award, Hubble Space Telescope Second Servicing Mission, Systems Engineering Group, March 1999.
- NASA Recognition, “In appreciation of your outstanding contributions to the Hubble Space Telescope Project Second Servicing Mission,” February 1997.
- NASA Group Achievement Award, Comet Shoemaker-Levy Jupiter Impact Observation Team, May 30, 1996.
- NASA/Goddard Space Flight Center, Group Achievement Award, Hubble Space Telescope First Servicing Mission, Observatory Verification Team, June 3 1994.
- NASA Group Achievement Award, Hubble Space Telescope First Servicing Mission, Contingency Development Team, June 3 1994.
- NASA/Goddard Space Flight Center, Group Achievement Award, Hubble Space Telescope Mission Operations, Flight Systems Engineering Team, June 3 1994.
- NASA/Goddard Space Flight Center, Group Achievement Award, Hubble Space Telescope Mission Operations, Systems Engineering Group, April 30 1992.
- NASA/Goddard Space Flight Center, Certificate of Recognition, Hubble Space Telescope Program, November 1 1991.
- NASA Group Achievement Award, Hubble Space Telescope Mission Operations Team, March 26 1991.